Numerical Modeling of Segmented Flows at Microscales

By:
© Vandad Talimi

A thesis submitted to the School of Graduate Studies
in partial fulfillment of the requirements for the degree of

Doctor of Philosophy

Faculty of Engineering and Applied Science
Memorial University of Newfoundland

May 2014

St. John's Newfoundland

ABSTRACT

Enhancement in heat transfer at micro scales is an active area of study, followed by many researchers. Use of non-boiling two phase flows in the form of segmented flows has become one of the interesting methods for achieving higher cooling (or mass transfer) capacities. Segmented flows (also known as slug flows, plug flows, or Taylor flows) is a series of moving liquid segments which are separated by gas bubbles or another liquid slugs. These flows are known as gas-liquid or liquid-liquid two phase flows, respectively. The effective phenomenon in heat transfer enhancement is internal circulations inside the liquid slugs, which helps to mix the liquid.

The main focus of the present thesis is on heat transfer of gas-liquid segmented flows, using numerical simulations based on the concepts of Computational Fluid Dynamics (CFD). As shown in the literature review, large gaps exist in research which need further studies. The target of this research is providing details on hydrodynamics and heat transfer in gas-liquid two phase flows, which can be helpful in understanding the whole process better. Based on the literature reviewed, the numerical modeling can be conducted using single phase or two phase simulations. Both single phase and two phase numerical simulations have been performed in this research. The research has also been conducted using fixed and moving frames of reference.

It has been shown that slug flows with shorter slugs provide greater cooling capacities compared with long slugs. Furthermore, it has been shown that liquid film around bubbles reduces the intensity of circulations in liquid slugs and hence reduces the cooling capacity. Therefore, using hydrophobic wall materials has been suggested. The key finding of the present research is how the liquid film around bubbles affects heat transfer, and it has been suggested to include this parameter in the correlations in the future. The comparison of the results with experimental data and/or exact analytical solutions throughout the thesis show good agreements.

ACKNOWLEDGMENTS

I would like to express the deepest appreciation to my supervisor, Dr. Yuri S. Muzychka, who has the attitude and the substance of a great mentor. Without his guidance and persistent help this dissertation would not have been possible.

I would also like to express my gratitude to Dr. Serpil Kocabiyik, the co-supervisor of this thesis, for her useful comments, remarks and engagement.

Last but not the least, I would like to thank my lovely wife, Shabnam. This work could not have been possible without her continuous support and encouragement.

Contents

List of Tables

List of Figures

NOMENCLATURE

A	=	area, m^2
b	=	body force per unit mass, N/kg
Bo	=	Bond number, $\equiv gD_h^2(\rho_l - \rho_g)/\sigma$
C	=	fraction function
Ca	=	Capillary number, $\equiv \mu U/\sigma$
Co	=	Courant number, $\equiv u\Delta t/\Delta x$
C_p	=	specific heat capacity, $J/kg.K$
d, D	=	diameter, m
D_h	=	hydraulic diameter, m
Eo	=	Eotvos number,$\equiv gD^2\left(\rho_l - \rho_g\right)/\sigma$
Fr	=	Froude number,$\equiv U^2/g/D$
f	=	Fanning friction factor
F_s	=	surface tension force, N
g	=	gravitational acceleration, m/s^2
G	=	mass flux, $kg/s/m^2$
h	=	convective heat transfer coefficient, W/m^2K
h_∞	=	film thickness over half channel size

H = distance between two parallel plates, m

k = thermal conductivity, W/mK

k = interface curvature

Kn = Knudsen number, $\equiv \lambda/l$

L = microtube length, m

La = Laplace number,$\equiv \sqrt{\sigma/gD^2\left(\rho_l - \rho_g\right)}$

L_s = length of liquid slug, m

$L^\star$ = dimensionless tube length,$\equiv L/D_h/Pe$

$L_s^\star$ = dimensionless slug length,$\equiv L_s/H$

m = relative velocity of two phases, $\equiv \left(U_b - U_l\right)/U_b$

$\dot{m}$ = mass flow rate, kg/s

Mo = Morton number, $\equiv We^3/FrRe^4$

n = normal vector

N = number of liquid slugs

Nu = Nusselt number, $\equiv hD_h/k$

p = pressure, Pa

p = perimeter, m

P = slug pitch, m

Pe = Peclet number,$\equiv RePr$

Pr = Prandtl number, $\equiv \mu C_p/k$

q = wall heat flux, W/m^2K

$\overline{q}$ = mean wall heat flux, W/m^2

$q^\star$ = dimensionless wall heat flux

Q = total heat transfer rate, W

$r^\star$ = dimensionless radial position

R = microtube radius, m

Re = Reynolds number, $\equiv UD_h/\nu$

$\dot{s}$ = energy (heat) generation, W/m^3

t = time, s

T = temperature, K

T = stress tensor

u, U = velocity, m/s

u = actual phase velocity, m/s

u = internal energy per unit mass, j/kg

$u^\star$ = dimensionless velocity

U = superficial velocity, m/s

V = volume,m^3

W = channel width, m

We = Weber number, $\equiv \rho U^2 D/\sigma$

x = distance from entrance, m

x = two phase flow quality

$x^\star$ = dimensionless axial (horizontal) position, $\equiv x/D_h/Pe$

$y^\star$ = dimensionless distance in y-direction, $\equiv y/H$

z = horizontal distance, m

$z^\star$ = dimensionless horizontal distance, $\equiv z/D_h/Pe$

Greek Symbols

α = void/liquid fraction

α = thermal diffusivity, m^2/s

β = slip coefficient

δ = liquid film thickness, m

Δ = thermal boundary layer thickness, m

ϵ = roughness, m

ϵ = channel aspect ratio

λ = mean free path, m

Λ = slip length, m

μ = dynamic viscosity, Ns/m^2

ν = kinematic viscosity, m^2/s

ρ = fluid density, kg/m^3

θ = contact angle, ^{o}

τ = shear stress, Pa

$\tau^\star$ = dimensionless wall shear stress

σ = surface tension, N/m

Superscripts

* = dimensionless

$\overline{(\cdot)}$ = mean value

Subscripts

A = advancing

b = bubble

c = cross section

f = fluid

g, G = gas

GS = gas slug

i = inlet

int = interface

l, L = liquid

LO = liquid only

LS = liquid slug

m = mean

N = number of slugs

o = outlet

R = receding

s = slug

s = static

SP = single phase

t = traveled

T = total

TL = triple line

TP = two phase

w = wall

w = water

Abbreviations

AR = Aspect Ratio

BL = Boundary Layer

CFD = Computational Fluid Dynamics

CSF = Continuum Surface Force

$EWOD$ = Electro Wetting On Dielectric

FFR = Fixed Frame of Reference

LS = Level Set

MFR = Moving Frame of Reference

$PISO$ = Pressure Implicit with Splitting of Operators

$PRESTO!$ = PREssure STaggered Option

RMS = Root Mean Square

$SIMPLE$ = Semi-Implicit Method for Pressure Linked Equations

VOF = Volume Of Fluid

1 TWO PHASE FLOW AT SMALL SCALES

Development of electronic and computer devices, miniature mechanical systems, and MEMS (Micro-Electro-Mechanical-Systems) during the past decades has increased the demand for heat removal processes. Using microchannel heat sinks is one of the early methods suggested by Tuckerman and Pease [1] for thermal management of electronic cooling. The idea was using fluid flow in small parallel channels called as "microchannels" to remove heat generated by an electronic device as shown in Fig. 1.1. The dimensions of microchannels have been optimized by Tuckerman and Pease [1] based on surface temperature and maximum allowable pressure drop. They reported that a single phase water flow microchannel heat sink is able to remove heat up to 790 (W/cm^2).

Single phase internal flows in microchannels are generally laminar, with limited Nusselt numbers in case of long microchannels (much longer than entrance length) [2]. Therefore, researchers have started to investigate different ways to overtake these limits. Some researchers have tried to increase the heat transfer surface area using ge-

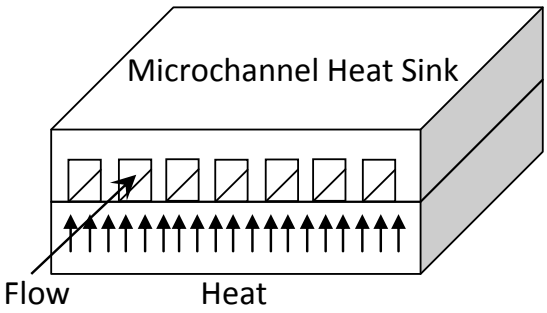

Figure 1.1: A typical microchannel heat sink.

ometrical hindrances [3]. Using tree-like bifurcating microchannels is another example [4, 5]. Non-straight microchannels have also been studied in order to increase mixing and convective heat transfer [6, 7, 8, 9]. Other examples are using short microchannels (compared to entrance length) [10, 11, 12], using nanofluids in order to enhance thermal capacity of the fluids [13, 14, 15], and two phase flows [16, 17, 18, 19, 20]. Figure 1.2 shows some examples of the aforementioned methods.

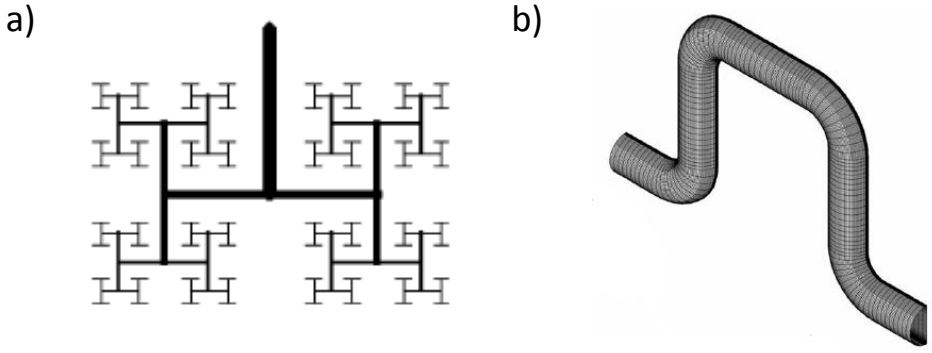

Figure 1.2: Examples of microchannel heat sinks, a) tree-like bifurcating [5], b) non-straight microchannel [6].

Using non-boiling two phase flows in mini and microscales has attracted researchers

soon after the mini and microchannels emerged as an interesting approach in designing small heat sinks and heat exchangers. The number of published literature on two phase flow fundamentals and applications is increasing dramatically as this kind of flow can give higher heat (or mass) transfer rates compared with single phase flows (Fig. 1.3).

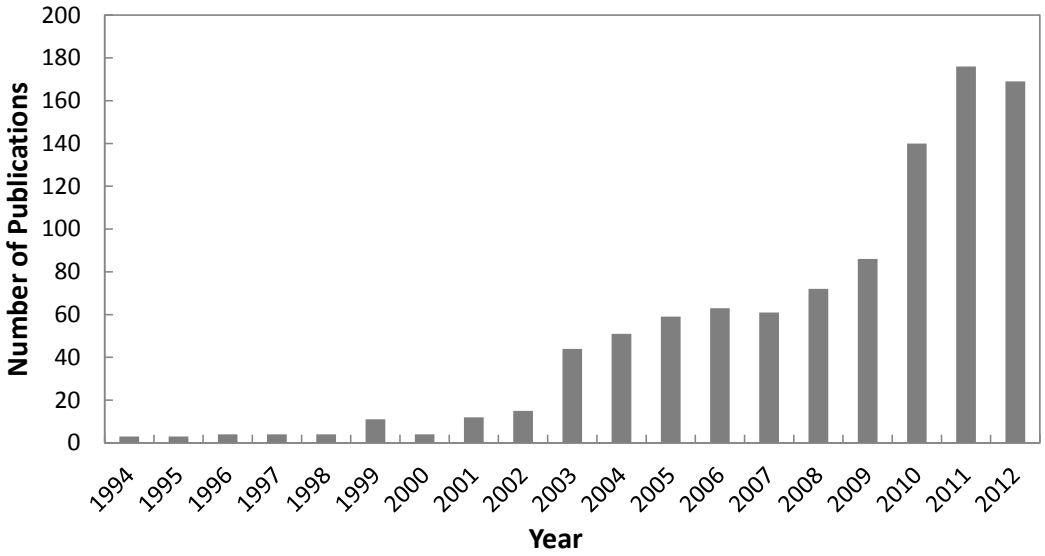

Figure 1.3: Two phase flow research at micro scales during the past two decades (only journal papers with respect to non-boiling two phase flows, excluding phase change).

1.1 Two Phase Flow Patterns

Non-boiling two phase flows are categorized into three types: gas-liquid, liquid-liquid, and solid-liquid two phase flows. The gas-liquid two phase flow has a potential to enhance heat transfer while it could be easily generated (compared with liquid-liquid and solid-liquid flows), so many researchers have focused on the fundamentals of this kind of two phase flows including slug formation, flow pattern, pressure drop, and heat

transfer. The gas-liquid two phase flow in small scales have different modes which are bubbly, slug, churn, slug-annular, and annular flows. Figure 1.4 and Fig. 1.5 show the different types of gas-liquid two phase flows in horizontal and vertical (upward) capillaries.

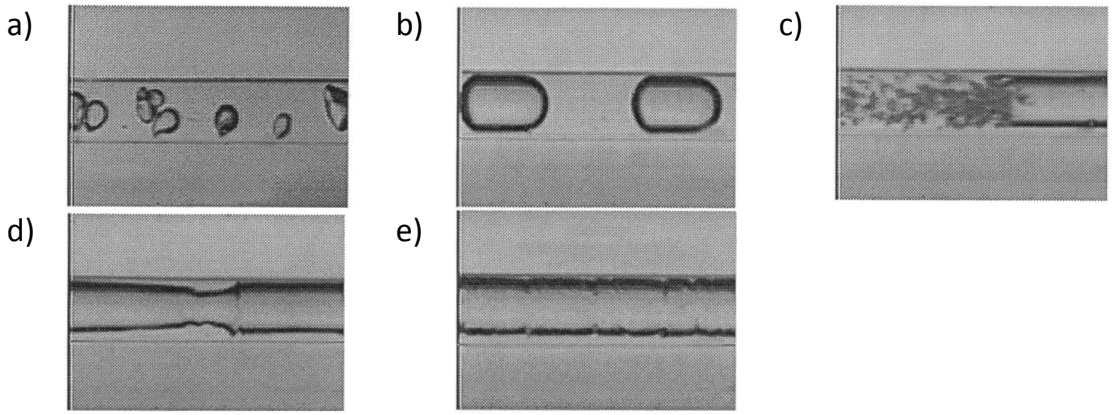

Figure 1.4: Two phase flow regimes in horizontal small tubes, D=1.097 mm, Triplett [22], a) bubble flow, b) slug flow, c) churn flow, d) slug-annular flow, e) annular flow.

Different flow maps have been published for large and small tube diameters which show the type of two phase flow based on the velocities or superficial velocities of two phases. Since there are some differences between the two phase flows in macroscales and microscales, the flow maps generated for macroscales can not accurately predict the flow regime at the microscale. For example, the two phase flow in microchannels is mainly laminar due to small characteristic length but turbulent in large pipes. Furthermore, the liquid slugs in large scale slug flows usually contain small bubbles but this is not the case in slug flow in microchannels. While flow maps are useful

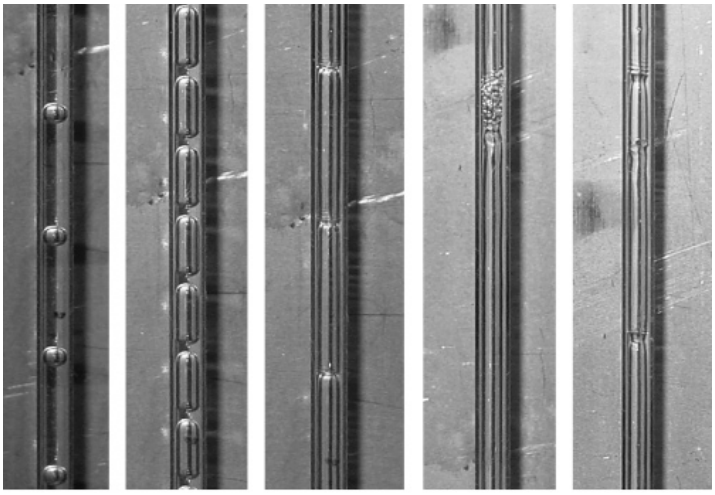

Figure 1.5: Two phase flow regimes in vertical small tubes, Liu and Wang [23].

tool to predict the flow pattern, care must be taken when using them since they are not universal. A sample is shown in Fig. 1.6 for a tube diameter of 1.097 (mm) by Triplett [22]. Recently, some researchers [24, 25] compared the existing flow maps for different microchannel sizes in order to unify flow transition boundaries in the flow maps. For example, Sur and Liu [25] developed a new flow map using the modified Weber numbers as the coordinates. Figure 1.7 shows this flow map.

Typically, microchannels are the channels (or capillaries) with a characteristic length of less than 1 (mm). However different extensions exist in the literature, the following criterion, i.e. the Laplace constant, is one of the mostly used criteria (Galbiati and Andreini [26] and Triplett et al. [22]):

$$D_h \leq \sqrt{\frac{\sigma}{g\left(\rho_L - \rho_G\right)}} \tag{1.1}$$

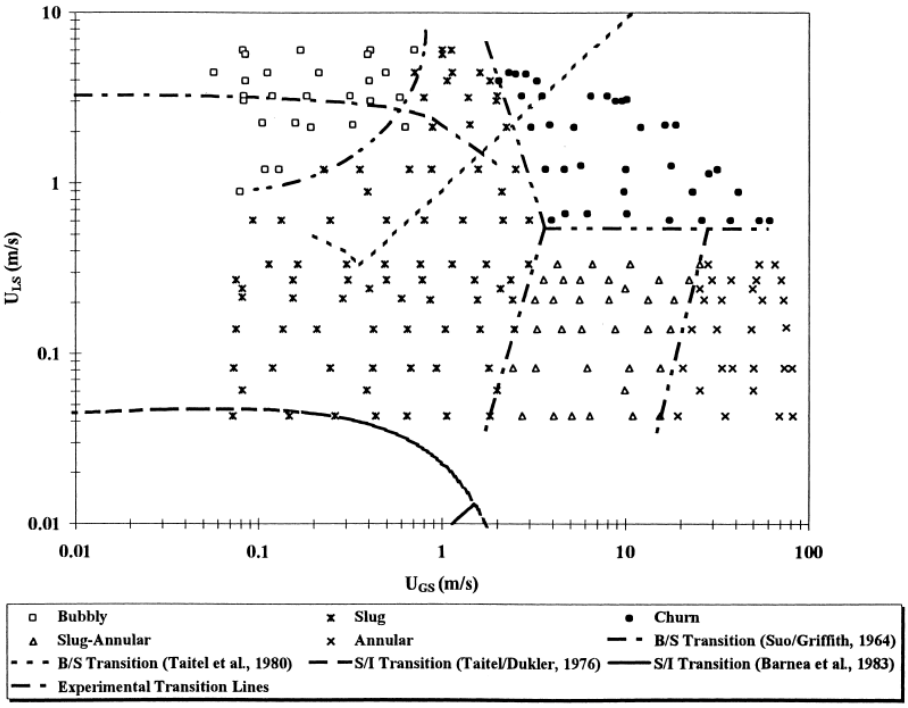

Figure 1.6: Flow map, D=1.097 mm, Triplett [22].

where σ and ρ are the surface tension between the two phases and density, respectively. The indexes L and G denote liquid and gas, respectively. A rough estimation of the Laplace constant for air and water at room temperature is around 2.7 (mm).

Gas-liquid slug flows are of interest in the present research as it could lead to a great enhancement in heat transfer and consequently help to design smaller heat sinks/exchangers. A slug flow contains elongated gas bubbles, usually with a length more than the hydraulic diameter of the microchannel, which separate liquid phase into plugs of liquids. These gas bubbles are often, but not always, surrounded by a thin liquid film which acts like a lubrication layer and let the bubbles move faster

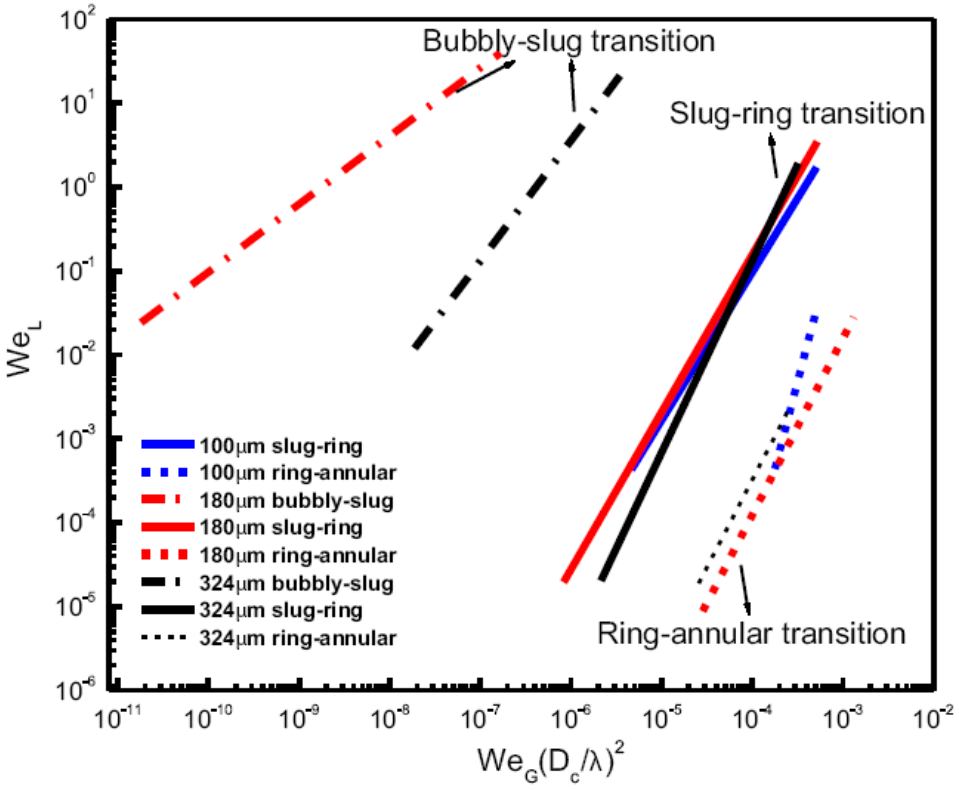

Figure 1.7: Two phase flow map reconstructed with the proposed dimensionless parameters as the coordinates, Sur and Liu [25].

than the average velocity of the liquid phase. Slug flows are sometimes called as Taylor flow (Taylor [27]), Plug flow, Bolus flow (Prothero and Burton [28]), or segmented flow (Horvath et al. [29]). Figure 1.8 shows gas-liquid slug flows with different slug lengths.

1.2 Mechanism of Heat Transfer Enhancement

Two effects have been introduced as responsible factors in enhancement of heat transfer rate in non-boiling two-phase flows: 1) internal circulations in the slugs, leading to a

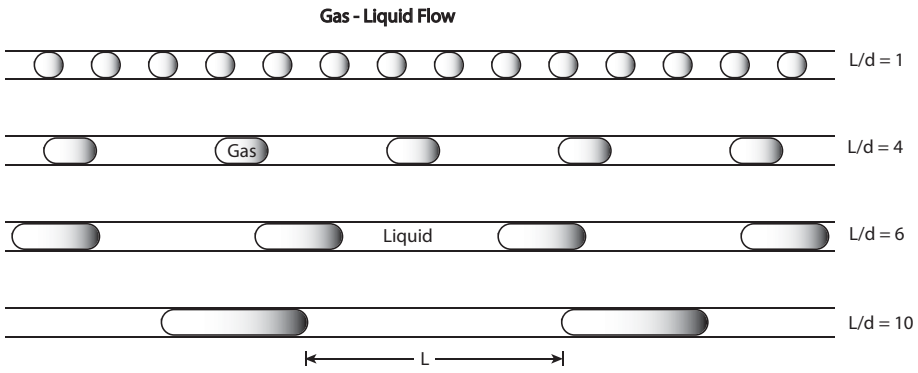

Figure 1.8: Gas-liquid slug flows for different slug lengths.

greater radial heat transfer rate, and 2) increased slug velocity when compared with the same single phase mass flow rate, which is a consequence of reduced phase fraction. Muzychka et al. [30] recently showed that only the first one is valid. As they argued, increasing the convective heat transfer coefficient, h, does not necessarily lead to a greater heat transfer since a segmented flow has smaller contact area compared with a single phase flow. Figure 1.9 shows the internal circulations caused by shear forces in the moving plugs.

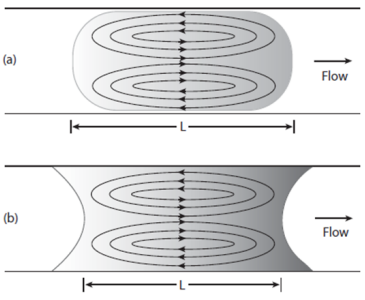

Figure 1.9: Internal liquid plug circulation a) hydrophobic surface b) hydrophilic surface.

The internal circulations inside liquid slugs bring fresh liquid from center of the slug to the wall, where heat transfer process occurs. This provides a renewal mechanism to the thermal boundary layer and increases heat transfer. However, diffusion is important in this process as well, so the boundary layer grows until the circulation center (circulation eye) receives the heat. Figure 1.10 shows effects of the internal circulations on heat removal process for a constant wall temperature.

1.3 Dimensionless Groups

A significant number of dimensionless groups exist to assist two-phase flow researchers developing more general results and models. Reynolds number, Re, Capillary number, Ca, Weber number, We, Nusselt number, Nu, and Prandtl number, Pr, are a few examples. Only a brief description would be presented here. More details of definitions and physical interpretations can be found in literature [2, 21, 32]. Different velocities (true phase velocity or superficial velocity) have been used in the literature to define these dimensionless numbers, so it is necessary to note the definitions when one decides to use data reported in different papers.

Reynolds number

The Reynolds number, Re, is traditionally defined as:

$$Re = \frac{\rho U D_h}{\mu} \tag{1.2}$$

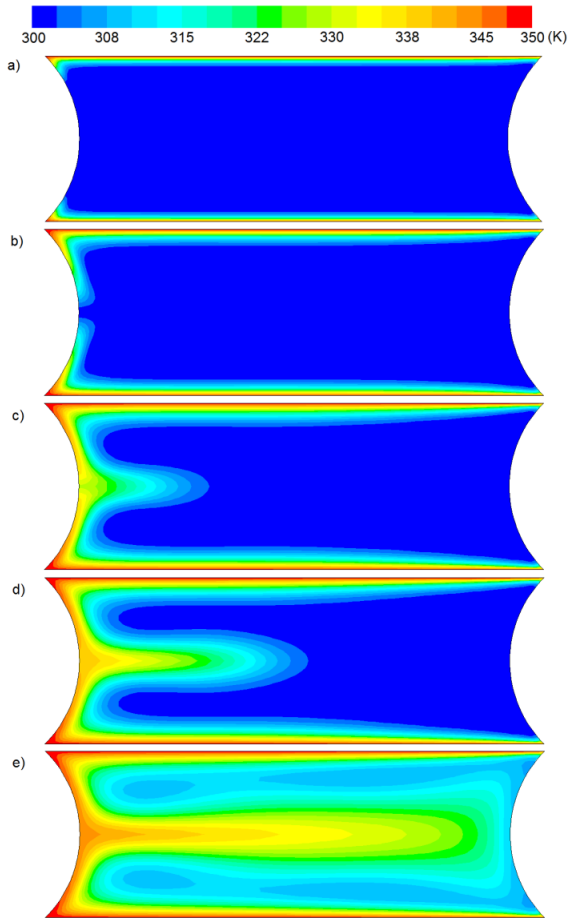

Figure 1.10: Internal circulation effects on heat transfer in a moving liquid slug, a) $x^\star = 9.77 \times 10^{-5}$, b) $x^\star = 2.93 \times 10^{-4}$, c) $x^\star = 6.84 \times 10^{-4}$, d) $x^\star = 1.07 \times 10^{-3}$, e) $x^\star = 3.03 \times 10^{-3}$, (Talimi et al. [31]).

and shows the ratio between inertial and shear stress forces. In the above equation ρ is the fluid density, μ is the fluid viscosity, U is velocity, and D_h is the hydraulic diameter which is identical to the diameter in circular tubes. One of the initial and important steps in numerical simulation of a fluid flow is to examine whether laminar or turbulent conditions exist. Re is mostly used for this decision. The critical Re

corresponding to the onset of turbulence is 2300 for single phase flows in tubes with diameters as small as 50 μm (Incropera et al. [32]). The critical Re has been reported to be of $\approx$ 1000 for single moving droplets (Ren et al. [33]) which could be more applicable in non-boiling two-phase slug flows in microscale.

Decrease in length scale (microtube diameter) and consequently increase in relative roughness (ϵ/D) affects transition Reynolds number range. As summarized in Table 1.1 from Ghajar et al. [34], the transition Reynolds range becomes narrower with a decrease in tube diameter.

Table 1.1: Summary of transition Reynolds number ranges for various stainless steel tube sizes [34]

Tube I.D. (μm)	Transition range
2083	$1500 < Re < 4000$
1600	$1700 < Re < 4000$
1372	$1900 < Re < 4000$
1067	$2000 < Re < 4000$
991	$2000 < Re < 4000$
838	$2200 < Re < 4000$
732	$2200 < Re < 3000$
667	$2200 < Re < 3000$
559	$1900 < Re < 2500$
508	$1700 < Re < 2100$
413	$1500 < Re < 1900$
337	$1300 < Re < 1700$

Capillary number

The Capillary number, Ca, is defined as follows:

$$Ca = \frac{\mu U}{\sigma} \tag{1.3}$$

and is the ratio between viscous and surface tension forces. In the above equation σ is the surface tension between the two phases, which cause a Capillary pressure difference between the two phases at curved interfaces.

Ca/Re number

A combination of Ca, Re, slug length, and hydraulic diameter of the microchannel make a very important dimensionless group in two-phase slug flow pressure drop analyzing (Muzychka et al. [21], Kreutzer et al. [58], Walsh et al. [59]). The ratio of the Capillary number and the Reynolds number is a dimensionless group without any specified name and is independent of flow velocity as follows:

$$\frac{Ca}{Re} = \frac{\mu^2}{\sigma \rho D} \tag{1.4}$$

As showed by Walsh et al. [59] the above dimensionless group - when combined with the slug length and microtube diameter - can illustrate the effects of the slugs on the total pressure drop as follows:

$$\frac{L_s}{D}\left(\frac{Ca}{Re}\right)^{1/3}\begin{cases} << 1 & \text{Taylor flow (two phase flow)} \\ >> 1 & \text{Poiseuille flow (single phase flow)} \end{cases} \tag{1.5}$$

Bond, Eotvos, and Laplace numbers

Using these dimensionless groups one can compare the gravitational and capillary forces. The definitions are different in term of characteristic length scales.

The Bond number, Bo, is defined as:

$$Bo = \frac{gR^2\left(\rho_l - \rho_g\right)}{\sigma} \tag{1.6}$$

The Eotvos number, Eo, is defined as:

$$Eo = \frac{gD^2\left(\rho_l - \rho_g\right)}{\sigma} \tag{1.7}$$

The Laplace number, La, is defined as:

$$La = \sqrt{\frac{\sigma}{gD^2\left(\rho_l - \rho_g\right)}} \tag{1.8}$$

The three dimensionless groups above are related as follows:

$$Eo = 4Bo = \frac{1}{La^2} \tag{1.9}$$

Weber number

The Weber number, We, is defined as:

$$We = \frac{\rho U^2 D_h}{\sigma} \tag{1.10}$$

and is the ratio between inertial and surface tension forces. In mini and micro scales the interaction between two fluids at their interface can be important. The importance of surface tension effects is determined based on Re, Ca, and/or We. The quantity of interest is Ca or We for low Re and high Re flows, respectively.

Froude number

The Froude number, Fr, is defined as:

$$Fr = \frac{U^2}{gD} \tag{1.11}$$

and is a ratio of inertial and gravitational forces. Some researchers also defined the Froude number as: $Fr = U/\sqrt{gD}$.

Fanning friction factor and dimensionless wall shear stress

The average shear stress over a specified channel length, $\overline{\tau}_w$, can be nondimensionalized in two ways. The first model usually denoted as Fanning friction factor, f, is:

$$f = \frac{\overline{\tau}_w}{\frac{1}{2}\rho U^2} \tag{1.12}$$

which gives $fRe = 24$ for laminar flows in plane channels when $D_h = 2H$. In the second model, the dimensionless mean wall shear stress is defined as follows:

$$\tau^\star = \frac{\tau_w D_h}{\mu U} = \frac{fRe}{2} \tag{1.13}$$

The dimensionless mean wall shear stress, $\tau^\star$, has also been named as Poiseuille number by some researchers (Churchill [35]) and has the value of 12 for a fully developed fluid flow in a plane channel. In this study, the shear stress of the two-phase slug flow is presented using the second model since it has more physical meaning than f (Muzychka et al. [21]).

Prandtl number

The Prandtl number, Pr, is defined as follows:

$$Pr = \frac{\nu}{\alpha} = \frac{\mu C_p}{k} \tag{1.14}$$

and is the rate of momentum diffusion versus the rate of thermal diffusion. In the above equation, ν is the momentum diffusion, α is the thermal diffusion, C_p is the specific heat capacity, and k is the thermal conductivity.

Nusselt number and dimensionless heat transfer ($q^\star$)

The Nusselt number, Nu, is defined as:

$$Nu = \frac{hD_h}{k} = \frac{qD_h}{k\left(T_w - T_m\right)} \tag{1.15}$$

and is a dimensionless heat transfer rate, defined based on the difference between wall temperature, T_w, and fluid bulk temperature, T_m. In the above equation h is convective heat transfer coefficient, and q is heat flux. Another approach exists for defining a dimensionless heat transfer, which is based on the difference between wall temperature and inlet temperature, leading to a dimensionless wall flux, $q^\star$, as follows:

$$q^\star = \frac{qD_h}{k\left(T_w - T_i\right)} \tag{1.16}$$

where T_i is the inlet temperature. The first approach is more applicable in heat exchangers and the second one is useful in heat sinks. More details are available in Muzychka et al. [30] and Shah and London [2]. The dimensionless heat transfer and the Nusselt number are related as follows:

$$q^\star = \frac{1}{4L^\star}\left[1 - exp\left(-4\overline{Nu}_{D_h}L^\star\right)\right] \tag{1.17}$$

where $L^\star$ is dimensionless tube length:

$$L^\star = \frac{L/D}{RePr} = \frac{L/D}{Pe} \tag{1.18}$$

1.4 Other Important Parameters

Fig. 1.11 schematically shows a typical slug flow i.e. a train of liquid moving plugs separated by elongated gas bubbles in microchannel. In general the bubbles nose and tail have different curvatures and the difference between them depends on flow

parameters such as Reynolds number. In most slug flows gas bubbles are separated from the microchannel wall by a thin liquid layer around them. The thickness of this layer, known as δ, depends on two phase flow Capillary number, Ca, and will be discussed in section 2.1. The length of the liquid slugs and gas bubbles are normally shown by L_s and L_b, respectively. The pitch, P, is nose to nose or tail to tail distance.

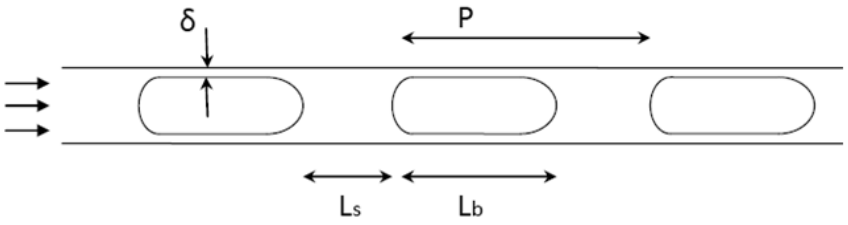

Figure 1.11: Typical slug flow.

The slug flow void fraction is defined as the ratio of the gas volume to the total two phase volume in certain length of mircotube i.e. control volume. That is:

$$\alpha_g = \frac{V_g}{V} \tag{1.19}$$

and liquid fraction is:

$$\alpha_l = \frac{V_l}{V} \tag{1.20}$$

The void and liquid fractions of two phase flows are related as follows:

$$\alpha_l + \alpha_g = 1 \tag{1.21}$$

The mass flux, G, is the mass flow rate per unit cross sectional area which can be calculated as follows:

$$G_g = \frac{\dot{m}_g}{A} = \rho_g U_g \tag{1.22}$$

and

$$G_l = \frac{\dot{m}_l}{A} = \rho_l U_l \tag{1.23}$$

where U is superficial velocity i.e. the velocity of each phase in the microtube if that phase occupied the total cross sectional area. The actual phase velocities can be defined using phase void (or liquid) fraction as follows:

$$u_g = \frac{U_g}{\alpha_g} = \frac{G_g}{\rho_g \alpha_g} \tag{1.24}$$

and

$$u_l = \frac{U_l}{\alpha_l} = \frac{G_l}{\rho_l \alpha_l} \tag{1.25}$$

Finally, the quality of the two phase flow is:

$$x = \frac{G_g}{G_g + G_l} \tag{1.26}$$

and takes a value of 0 for single phase liquid flows and 1 for single phase gas flows.

2 LITERATURE REVIEW

Most studies in this area are experimental. As a result of this and many other reasons, there are significant gaps in numerical simulation analysis. One of the most important reasons can be the time-expense of the numerical methods. Numerical simulation as a method for predicting the heat and mass transfer characteristics has gained popularity due in part to the developments in the computational hardware and software.

A few review articles exist in this area which mostly contain experimental works (Shao et al. [37], Kreutzer et al. [19], Angeli and Gavriilidis [17], and Gupta et al. [18]). Recently, Talimi et al. [20] reviewed numerical studies on hydrodynamics and heat transfer in non-boiling two phase flows in microscales. They gathered and categorized much of the work conducted in recent years into two major sections: gas-liquid and liquid-liquid two phase flows. These sections are categorized further into two subcategories including circular or non-circular channels. While from the numerical point of view there is no difference between the gas-liquid and liquid-liquid two-phase

flow simulations, the role of the gas phase in heat transfer is mostly ignored due to its much lower heat capacity. This further leads to another simplification i.e. using a single phase moving frame technique for simulations. This will be discussed in the later sections. In the case of liquid-liquid two phase flow for heat removal applications both of the phases are shown to play significant roles. Figure 2.1 shows the structure of the review conducted by Talimi et al. [20]. The main focus was on flow patterns, slug formation, film thickness, and bubble shape in the literature and less consideration on heat transfer and pressure drop. Numerical simulation is a very powerful tool which gives much detail on the hydrodynamics and heat transfer and hence it helps a lot in giving deeper insight in two phase slug flows in microchannels.

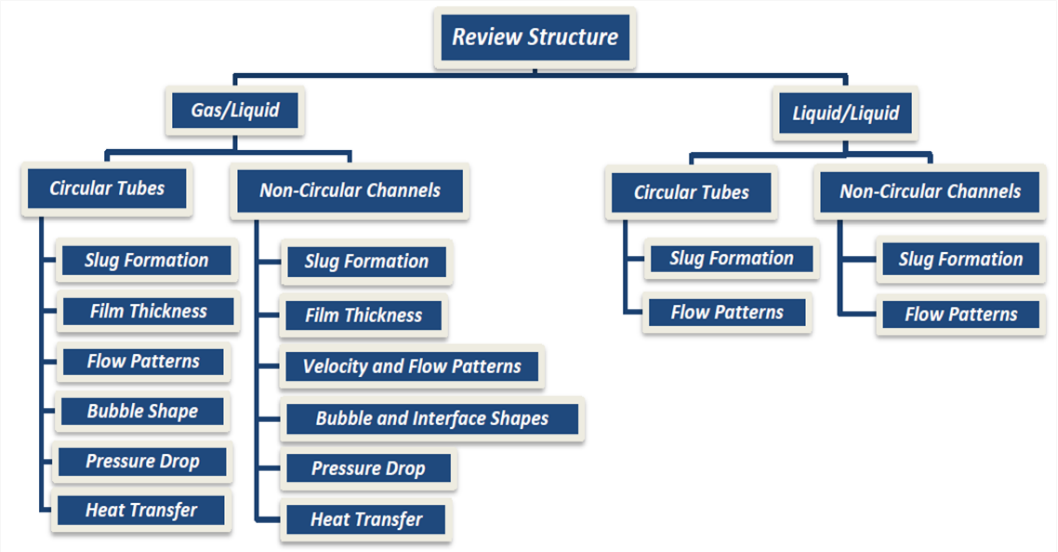

Figure 2.1: Review structure, (Talimi et al. [20]).

In this section a brief review of the existing literature (experimental and numerical) is presented. The film thickness, pressure drop, and heat transfer are the three

important aspects which are going to be considered in the present research. The importance of the film thickness on the internal circulations has been shown by Taylor [27]. As Fig. 2.2 illustrates the streamlines in the liquid slug depends on the Capillary number, Ca, and a dimensionless number, m, which is a relative velocity between the two phases, as follows:

$$m = \frac{U_b - U_l}{U_b} \tag{2.1}$$

where b and l denote the bubble and liquid phase, respectively. Figure 2.2 shows that for high Ca values a complete bypass occurs through the liquid film around the bubbles, and in the slug flows with low Ca number internal circulations exist. As presented in the following sections the film thickness is a function of Ca, so the film thickness is an important parameter which governs the flow pattern i.e. internal circulations and this way the film thickness might have strong effects on heat transfer process. In the following sections, the experimental and numerical studies on the film thickness will be reviewed along with pressure drop and heat transfer.

2.1 Film Thickness

The film thickness has been calculated experimentally using two different approaches. In the first approach, the thickness of the liquid film around the bubbles is measured directly from the images (Aussilous and Quere [38] and Han and Shikazono [52]). In the second approach, the film thickness is calculated based on the bubble velocity and

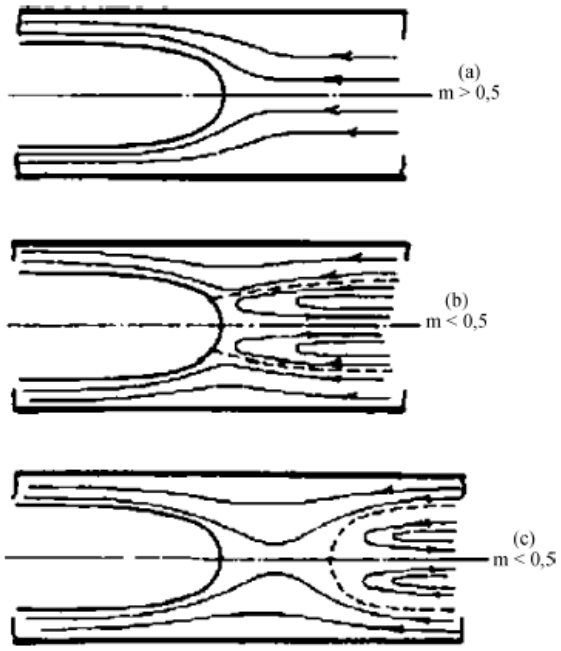

Figure 2.2: Streamlines in liquid slugs in front of a Taylor bubble, (Taylor [27]).

continuity equation. Some researchers assumed a stagnant film (Warnier et al. [40]) and some assumed a fully developed annular flow velocity profile and zero shear stress at the interface in their calculations (Thulasidas et al. [41]). The following correlations have been suggested for film thickness calculation in slug flows:

Fairbrother and Stubbs [42]:

$$\frac{\delta}{R} = 0.5Ca^{1/2} \tag{2.2}$$

for $5 \times 10^{-5} < Ca < 3 \times 10^{-1}$.

Bretherton [43]:

$$\frac{\delta}{R} = 1.34Ca^{2/3} \tag{2.3}$$

for $10^{-3} < Ca < 10^{-2}$.

Taylor [27]:

$$\frac{\delta}{R} = \frac{1.34Ca^{2/3}}{1 + 3.35Ca^{2/3}} \tag{2.4}$$

for $10^{-3} < Ca < 1.4$. In the correlations above δ and R are the liquid film thickness and microchannel radius, respectively.

The effects of a few different parameters on liquid film thickness have been studied numerically. These parameters are Ca, Re, Fr, bubble length, and flow direction (with gravitational effects).

Gupta et al. [44] compared the numerically calculated liquid film thickness with different empirical correlations and showed that the best agreement is with Betherton's prediction at low Ca (similar results were reported by Martinez and Udell [116]). Chen et al. [46] calculated the liquid film thickness around the bubble for $Ca \approx 0.006$ and 0.008, and compared their results with the Bretherton correlation. Their results show some differences from Bretherton's prediction. While Taha and Cui [47] reported the independence of liquid film thickness around a rising bubble on the bubble length in

vertical microtubes, Chen et al. [46] argued that since the bubble length in their study was smaller than three times the microtube diameter, the results show some difference from Bretherton's prediction. Shen and Udell [48] reported an over prediction of Bretherton's theory for Ca higher than 0.005.

Fig. 2.3 shows the results of numerical study performed by Giavedoni and Saita [49] on the liquid film thickness. As one can see in Fig. 2.3, Re has some effect on liquid film thickness for high values of Ca. Aussillous and Quere [38] suggested a correlation for liquid film thickness at high Ca as a function of Ca and Re or Ca and We. Edvinsson and Irandoust [50] (and also Taha and Cui [51]) showed that the liquid film thickness increases with Ca, Re and Fr. They argued that for small microchannels it is sufficient to correlate the liquid film thickness with Ca. As flow rates and diameters increase, the effects of inertial forces as well as gravitational forces become more pronounced.

Same was reported by Han and Shikazono [52] who examined effects of different parameters on film thickness in microtubes with diameters from 0.3 (mm) to 1.3 (mm). They confirmed that film thickness is only a function of Capillary number when Capillary number is small, and by an increase in Ca the effects of inertial force is important. They suggested the following correlations at different Reynolds numbers:

$$\frac{\delta}{D} = \frac{0.670Ca^{2/3}}{1 + 3.13Ca^{2/3} + 0.504Ca^{0.672}Re^{0.589} - 0.352We^{0.629}} \tag{2.5}$$

when $Re < 2000$, and:

$$\frac{\delta}{D} = \frac{106.0\left(\frac{\mu^2}{\rho\sigma}\frac{1}{D}\right)^{2/3}}{1 + 497.0\left(\frac{\mu^2}{\rho\sigma}\frac{1}{D}\right)^{2/3} + 7330\left(\frac{\mu^2}{\rho\sigma}\frac{1}{D}\right)^{0.672} - 5000\left(\frac{\mu^2}{\rho\sigma}\frac{1}{D}\right)^{0.629}} \tag{2.6}$$

when $Re > 2000$. As Ca approaches zero, Eq. 2.5 follows Bretherton's theory (Eq. 2.3).

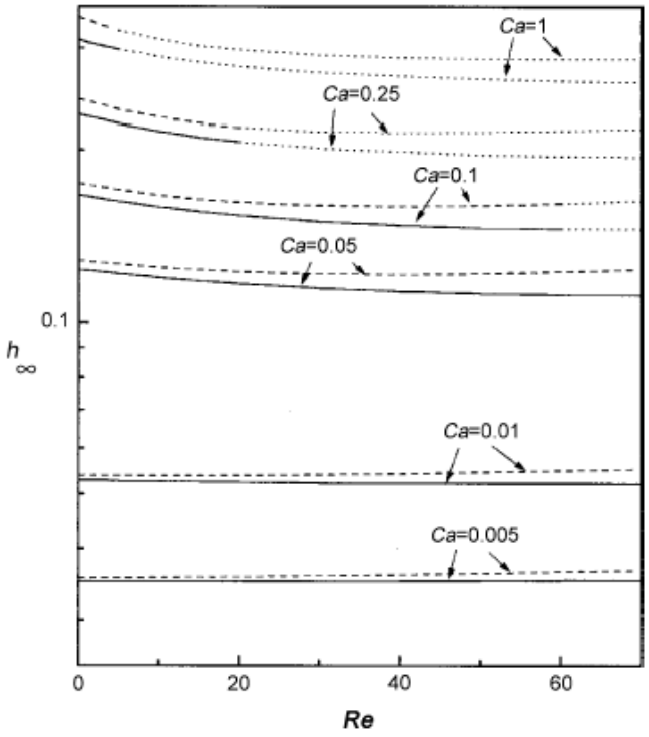

Figure 2.3: Film thickness over half channel size, (h_∞), for channels (dashed lines) and circular capillaries (solid lines). The situations which may not be feasible are presented by dotted lines, Giavedoni and Saita [49].

Fig. 2.4 shows the range of Ca in which numerical studies on the liquid film thickness have been conducted. As this figure shows, Ca lower than 0.001 have been neglected in the numerical simulation. Assuming water as liquid phase and air as gas

phase, this value represents a superficial velocity of 0.07 (m/s). As lower velocities are applicable in the microfluidics, numerical studies for low Ca could be performed in future research.

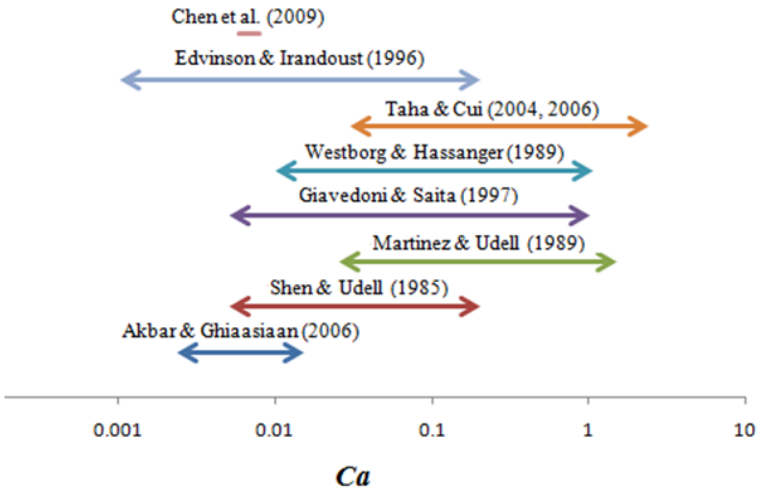

Figure 2.4: Ca range in which liquid film thickness has been studied numerically for gas-liquid flows in circular microtubes.

Film Thickness in Non-Circular Microchannels

The effects of different parameters including Ca, gravity effects, channel shape and geometry, and bubble length on the thickness of liquid film around the bubble have been of interest in recent research. Ghidersa et al. [53] reported that in square microchannels, the liquid film thickness around the Taylor bubbles increases with increases in the Ca.

Taha and Cui [54] showed that there is a difference between the liquid film thickness for upward and downward flows in square microchannels, for $Ca = 0.009$. According to their results, for this low Ca, the film thickness around the bubbles rising in a

microchannel (upward flow) is higher than downward flow, and they argued that this is because of gravity forces.

Onea et al. [123] considered a cylindrical bubble in square and rectangular minichannels with the same hydraulic diameters and flow parameters. They showed that the bubble in the square channel has a circular cross section while in the rectangular channels the bubble is squeezed between the long walls. Therefore, the thickness of the liquid film relative to the smaller dimension is decreasing while the other is increasing.

Liu and Wang [56] reported a thinner liquid film thickness at the side walls in equilateral triangular microchannels as compared with square microchannels for the same hydraulic diameters and initial volume of Taylor bubbles. They also showed that liquid film thickness in square microchannels is less than that in circular microtubes over the full range of Ca. They presented the reasons as follows: the symmetry of the circular microchannel leads to a uniform liquid film between Taylor bubbles and the wall, but in square and equilateral triangular microchannels most of the liquid is squeezed into the corners which results in thinner liquid films on side walls.

According to Yu et al. [57], the liquid film around the bubbles could become very thin or even partially dry-out in small microchannels with width of around 50 micrometers. They reported that the film thickness depends on the magnitude of the surface tension, the bubble length, the bubble velocity and the surface property. The range of Ca in which numerical studies on the liquid film thickness have been conducted for non-circular microchannels is showed in Fig. 2.5. As shown, most of

the research was performed for square cross sectional microchannels. Only Yu et al. [57] carried out simulation for rectangular microchannels and only for aspect ratio of 2. Therefore, a gap exists for Ca lower than 0.006 for rectangular microchannels with the aspect ratio of 2, and also for other aspect ratios in all values of Ca. Similar to rectangles, the only triangles shape which has been studied numerically was equi-lateral triangles by Liu and Wang [56].

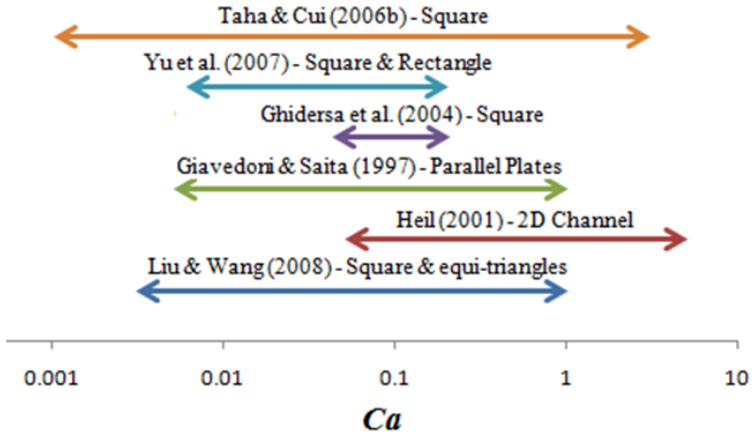

Figure 2.5: Ca range in which liquid film thickness has been studied numerically for gas-liquid flows in non-circular microchannels.

2.2 Pressure Drop

Pressure drop in two-phase slug flow increases as a result of circulations inside the slugs and the hydrodynamic effects of a two-dimensional velocity field near the wall. Based on the analysis presented by Kreutzer et al. [58] and Han and Shikazono [52] the two phase pressure drop in slug flows is a result of three components:

$$\Delta P = \Delta P_{slug} + \Delta P_{film} + \Delta P_{cap} \tag{2.7}$$

ΔP_{slug} is the pressure drop in the liquid slug and is assumed to be a summation of a fully developed laminar flow pressure drop in the liquid and an additional effect due to the internal circulations. ΔP_{film} is the pressure drop in the film and is usually very small compared to the slug pressure drop (Kreutzer et al. [58]). ΔP_{cap} is the pressure drop in the bubble front and end noses and according to Bretherton [43] can be calculated as follows for slug flows in circular microtubes and with a small Ca:

$$\Delta P_{cap} = 7.16 \left(3Ca\right)^{2/3} \frac{\sigma}{d} \tag{2.8}$$

As reported by Kreutzer et al. [58] and Walsh et al. [139] the ratio between Ca and Re is a prominent parameter in pressure drop modeling of gas-liquid two phase slug flow. They also included slug length effects on the pressure drop in their analysis. Walsh et al. [139] suggested the following model for pressure drop calculation:

$$fRe = 16 + \frac{1.92}{L^{\star}} \left(\frac{Re}{Ca}\right)^{1/3} \tag{2.9}$$

where $L^{\star} = L_s/D$ is the dimensionless liquid slug length and the Reynolds number is based on the liquid phase velocity and properties. As discussed earlier the two phase flow can be assumed as a fully developed single phase laminar flow (Poiseuille flow) when:

$$\frac{L}{D}\left(\frac{Re}{Ca}\right)^{1/3} >> 1 \tag{2.10}$$

Numerical studies on slug flow pressure drop have been also published recently. Table 2.1 shows that most of the numerical studies on pressure drop have been conducted for gas-liquid two phase slug flows in circular microtubes and other useful channel shapes have not been studied yet.

Kreutzer et al. [58] and Gupta et al. [44] showed that in a computational unit cell including a Taylor bubble and two half liquid slugs ahead and behind the bubble, the pressure distribution along the axis in the bubble is constant and higher than that of the liquid phase. Similar results have also been reported by Taha and Cui [51]. Kreutzer et al. [58] argued that there is a difference between pressure drops resulted from numerical simulations and experiments due to impurities in the real fluid which is not accounted for in numerical studies. They suggested modeling the pressure drop as sum of two elements. Firstly, the pressure drop in the slug (liquid phase) as a single phase, and secondly, the effects of gas phase or interface as a function of Re and Ca. The model proposed by Kreutzer et al. [58] for numerical simulations is as follows:

$$f = \frac{16}{Re}\left[1 + 0.07\frac{1}{L_s^\star}\left(\frac{Re}{Ca}\right)^{0.33}\right] \tag{2.11}$$

According to Kreutzer's results, pressure in the liquid slug decreases along the axis, and an oscillation was found right behind the bubble. Kreutzer et al. [58] argued that oscillation happens because of an inundation on the interface. Gupta et al. [44]

reported a complex pressure distribution in this region because of numerical effects.

Table 2.1: Numerical studies on pressure drop in circular microtubes and non-circular microchannels

Duct shape	Fixed frame	Moving frame
Circle	Gupta et al. [44, 64]	Kreutzer et al. [58]
	Akbar and Ghiaasiaan [36]	Fries and Rohr [62]
	Chen et al. [46]	He and Kasagi [61]
	Qian and Lawal [65]	Mehdizadeh et al. [63]
	Kashid et al. [128], (Liquid/Liquid)	
Parallel plates	—	Baird [66]
		Talimi et al. [31]
Square, Rectangle	Yu et al. [57]	Taha and Cui [54]
Other	—	—

Chen et al. [46] showed that pressure drop increases rapidly with decreasing slug length or increasing bubble length. Therefore, using different gas injector systems e.g. nozzles, can affect pressure drop by influencing gas slug length.

Taha and Cui [51] observed fluctuations in the wall shear stress ahead of and behind the slug, and nearly zero pressure drop in the central region. Based on their results, these fluctuations decrease with an increase in Ca. They also reported that the pressure drop across the bubble front increases with increasing Ca. He et al. [60] and He and Kasagi [61] stated that increasing in bubble frequency and decreasing in slug length will increase pressure drop in both flow conditions of with and without liquid film. He and Kasagi [61] reported that at one microtube diameter away from gas bubble, shear stress is almost equal to the single phase Poiseuille flow. In the other words, the increasing effect of two-phase flow on shear stress is significant near

the interface.

Slug flow pressure drop in curved microchannels was studied numerically by Fries and von Rohr [62]. They reported channel curvature and width as effective parameters and stated that as these parameters decrease, the pressure drop of the gas-liquid Taylor flow increases.

Pressure Drop in Non-Circular Microchannels

The pressure drop or wall shear stress for the slug flow inside non-circular microchannels has not been studied extensively and only the effects of Ca and flow direction (gravity effects) were of interest in recent years. Yu et al. [57] shows similar trend in pressure across the centerline to the centerline pressure distribution of circular microtubes, and showed that pressure is distributed almost constantly along the bubbles with an effective pressure drop inside the liquid slugs.

Taha and Cui [54] investigated wall shear stress of Taylor flow in square microchannels for two opposite directions (upward and downward). According to their results, the side wall shear stress distributions are the same for both flow directions at low Ca. They also showed that similar to circular capillaries at low Ca, there are some fluctuations in shear stress profile and that the central region of the profile (related to bubbles body) has near-zero value. They argued that the corner wall shear stress for upward flow is higher than the downward flow, because of different liquid film thicknesses in these two cases.

2.3 Heat Transfer

Non-boiling two phase slug flows or Taylor flows (Taylor [27]) have been studied widely for enhance in heat (or mass) transfer in microscales in recent years. Heat (or radial mass) transfer increases using this type of flows due to the internal circulations inside the moving slugs (Muzychka et al. [30]). The heat transfer process in slug flows has been examined experimentally and numerically but there are still large gaps in research (Shao et al. [37], Kreutzer et al. [19], and Angeli and Gavriilidis [17]).

Early experiments on heat transfer in slug flows have been conducted by Oliver and Wright [68] and Oliver and Young-Hoon [69, 70]. They investigated using slugs in heat transfer enhancement focusing on the effects of internal circulations and the void fraction. A correlation based on the data presented by Oliver and Wright [68] has been introduced by Hughmark [71] as follows:

$$\frac{h_{TP}D\sqrt{\alpha_L}}{k} = 1.75\left(\frac{\dot{m}C_p}{\alpha_L kL}\right)^{1/3}\left(\frac{\mu}{\mu_w}\right)^{0.14} \tag{2.12}$$

The effect of slug length on mass transfer has been investigated by Horvath et al. [29] at different Reynolds numbers but a fixed void fraction of $\alpha = 0.5$. The effects of slug length on Nusselt numbers has been experimented also by Vrentas et al. [72] but this time for a solid-liquid two phase slug flow using steel spheres to segment the liquid stream.

Numerical simulations of heat transfer in slug flows have been appeared in the literature more recently. Table 2.2 presents the different numerical studies of slug flow

heat transfer in circular and non-circular microchannels and the conditions employed in these simulations. Ua-arayaporn [73], He et al. [60], and Gupta et al. [64] showed that the Nusselt number, Nu, is large in the region where bubbles exist in gas-liquid slug flows. This is mainly because the difference between the mean temperature in the thin liquid film around the bubble and the wall temperature is very small. Lakehal et al. [74] and Narayanan and Lakehal [75] simulated the heat transfer process in gas-liquid slug flows and presented the following correlation for the Nusselt number using a combination of laminar and turbulent Nusselt numbers:

$$Nu_D \approx 3.67 + 0.022 {Re_D}^{4/5} Pr^{0.4} \tag{2.13}$$

where Re_D is based on the gas bubble velocity. Gupta et al. [64] reported that Nu in gas-liquid slug flows increases by a factor of 2.5 compared with laminar and fully developed single phase flow in both constant wall temperature and constant wall heat flux boundary conditions.

Narayanan and Lakehal [75] reported a substantial increase in the Nusselt number, Nu, with increasing gas slug length. They obtained an average Nu of 15 for slug flows and indicated that using slug flows may lead to an overall enhancement in heat transfer by a factor between 3 and 4 compared to single phase flows. They also showed that gravity has some effects on heat transfer in slug flows, and in particular the down-flow case where the direction of gravity is the same as direction of flow, the average Nu is about 4% higher compared to the zero gravity cases. As it is common in approximately

all of the numerical studies that have been reviewed, the fluid properties are assumed to be constant at an appropriate temperature. Fei et al. [76] is one of the rare studies in which two-phase flow was numerically studied using temperature dependent properties.

Leung et al. [77] studied gas liquid heat transfer of Taylor flows in vertical upward direction under constant wall heat flux thermal boundary condition. They used circular capillaries with 2.00 (mm) diameter and examined effects of slug length, mixture velocity, and homogeneous void fraction on the heat transfer process. Based on what they reported, Taylor flow heat transfer increases by a decrease in slug length and an increase in mixture velocity. These results were based on a wide range of slug lengths ($1 - 220D$) with controlled mixture velocities ($0.11 < U_{tp} < 0.53(m/s)$, $200 < Re_{tp} < 1100$), and homogeneous void fractions ($0.03 < \alpha < 0.90$). Finally, they suggested that slug flow heat transfer under constant wall temperature boundary condition is approximately 15% lower than slug flow heat transfer under constant wall heat flux boundary condition. They extended this research [78] (in 2012) and suggested the following empirical correlation for the apparent slug Nusselt number, $Nu_{L^\star}$, in slug flows under constant wall heat flux boundary condition:

$$Nu_{L^\star} = Nu_{LO} + 0.13\,(L_s^\star)^{-0.46}\,(Ca)^{-0.30} \tag{2.14}$$

and argued that slug flows with lower Capillary numbers have greater heat transfer rates due to stronger circulations inside the moving slugs. However, as stated by

Leung et al. [78] using Eq. 2.14 is possibly safe for slug flows with long liquid slugs and/or large Ca, and should be used with care when slugs are short ($L_s^\star < 10^{-4}$) or the slug flow has a low Capillary number ($Ca < 10^{-3}$). In the present Ph.D. research, these effects have been focused numerically and reasons have been discussed.

Muzychka et al. [30] suggested a heat transfer predictive model based on an asymptotic analysis and the available data in the literature. They suggested to use the slug length instead of the tube length as the length scale when nondimensionalizing heat transfer data. Their model is as follows:

$$q^\star = \left[\left(\frac{1.614}{L_s^{\star 1/3}} \right)^{-3/2} + \left(\frac{1}{4L_s^\star} \right)^{-3/2} \right]^{-2/3} \tag{2.15}$$

where

$$q^\star = \frac{Q/\left(\alpha_L \pi D L\right) D}{k\left(T_w - T_i\right)} \tag{2.16}$$

and

$$L_s^\star = \frac{\pi \alpha_L L_s k}{4 \dot{m} C_p} \tag{2.17}$$

The correlation above is applicable when a system includes more than five liquid slugs.

Combining the Graetz slug flow and Poiseuille flow asymptotes, Walsh et al. [59] proposed the following model for two phase slug flow heat transfer in circular capillaries under constant wall heat flux:

$$Nu_x = \left[\left(\frac{1.302}{x^{\star 1/3}} + \frac{D}{L_s} \left[\frac{0.886}{x^{\star 1/2}} - \frac{1.302}{x^{\star 1/3}} \right] \right)^{10} + \left(4.36 + \frac{25}{\sqrt{L_s/D}} \right)^{10} \right]^{1/10} \tag{2.18}$$

where

$$Nu_x = \frac{q_w D}{\alpha_L k \left(T_{w,x} - T_{m,x} \right)} \tag{2.19}$$

and

$$x^\star = \frac{x}{DPe_D} = \frac{\pi \alpha_L x k}{4 \dot{m} C_p} \tag{2.20}$$

where α_L is the liquid fraction and $\dot{m}$ is the liquid mass flow rate.

Asadolahi et al. [84, 85, 86] evaluated numerical modeling of Taylor flow hydrodynamics and heat transfer using two phase moving frame of reference numerical simulations (see Fig. 3.8b). They compared the bubble shape, film thickness, bubble velocity, and homogeneous void fraction with existing correlations and experimental results and reported good agreement. They also compared pressure drop and heat transfer from numerical simulations to experimental results, and discussed that overall using a two phase moving frame of reference numerical simulation can be a valid approach in prediction of slug flow behavior.

Table 2.2: Numerical simulations of slug flow heat transfer in microtubes and microchannels

Authors	Conditions	Geometry	Boundary condition
Ua-arayaporn et al. [73]	$14 < Re < 435$ $0.4 < We < 130$	Circular Moving frame of reference $D = 10, 20(\mu m), L = 2D$	Constant heat flux
Fukagata et al. [83]	$0.0087 < Ca < 0.27$ $16 < Re_L < 490$	Circular Moving frame $D = 20(\mu m), L = 2D$	Constant heat flux
He et al. [60]	$Re = 90$ $We = 11$	Circular Moving frame $D = 10(\mu m)$	Constant heat flux
Narayanan and Lakehal [75]	$Ca = 0.0154$ $We = 17$ $Re = 1110$	Circular Fixed frame $D = 1(mm), L = 40D$	Constant temperature
Lakehal et al. [74]	$U_G = 0.66(m/s)$ $U_L = 1.11(m/s)$	Circular Fixed frame $D = 1(mm), L = 40D$	Constant temperature
Gupta et al. [64]	$Re = 280$ $Ca = 0.006$ $\alpha = 0.51(water - air)$	Circular Fixed frame $D = 0.5(mm), L = 40D$	Constant heat flux
Mehdizadeh et al. [81]	$Ca = 0.0031$	Circular Fixed frame $D = 1.5(mm), L = 40D$	Constant heat flux (Conjugated simulation)
Baird [66]	$Re = 1, 10, 50, 100$ $Pe = 0.2, 50$	Parallel plates Moving frame $L = 0.5, 1, 2, 3, 4, 5H$	Constant temperature
Young and Mohseni [79]	$Re = 100$ $\theta = 90^o$	Parallel plates Moving frame $L = 0.5, 1, 2, 4, 8H$	Constant temperature & Constant heat flux
Oprins et al. [80]	$Re_H = 50, 100$ $Pr \approx 7.5$	Parallel plates Moving frame $L = 2.8(mm), H = 1(mm)$	Constant temperature
Talimi et al. [31, 82]	$Re = 375$ $\theta = 45^o, 60^o, 90^o, 135^o$	Parallel plates Moving frame $L = 1, 2, 3, 5, 10, 20H$	Constant temperature
Asadolahi et al. [84, 85, 86]	$22 < Re < 1189$ $0.003 < Ca < 0.160$ $(water - nitrogen)$	Circular Moving frame $2.74 < L_s/D < 6.43$	Constant heat flux

Howard et al. [87] investigated effects of Prandtl and Capillary numbers on heat transfer of Taylor flows in a 1.5 (mm) diameter circular microtube under constant wall heat flux boundary condition. Different slug lengths ($0.88 < L_s/D < 32$) and Prandtl numbers ($6.8 < Pr < 912.5$) have been considered in their experiments. They showed that a change in Prandtl number can cause a significant change in the transition region from entrance to fully developed flows. Furthermore, Nusselt number oscillates when a low Prandtl liquid is used in generating Taylor flow, and these oscillations are damped out when Prandtl number increases. Another important parameter on heat transfer is the film thickness, and it has to be considered when calculating void fraction of a Taylor flow. The effect of film thickness on heat transfer in slug flows is studied further in the present thesis.

Leung et al. [89] studied the effects of gravitational force on slug flow pattern and heat transfer in circular microtubes ($1.12 < d < 2.12(mm)$ giving Bond numbers of $0.287 < Bo < 1.028$) experimentally, and reported insignificant effect of gravity on heat transfer in Taylor flow regime. However, as they showed, flow pattern and bubble velocity depend on the Bond and Capillary numbers, but this dependency vanishes for small value of Bo and/or Ca, or as $Ca \to \infty$.

Heat Transfer in Non-Circular Microchannels

While non-circular microchannels include a variety of geometries like square, rectangle, parallel plates, triangle, and ellipse, only a few numerical studies were found for moving plugs or droplets between parallel plates. This may be due to the necessity of

using three dimensional computational domains in the cases other than parallel plates in non-circular microchannels which makes the numerical studies time consuming. The prominent parameters which affect heat transfer in non-circular channels have been reported as slug length, channel geometry, interface shape (contact angle), and flow pattern (internal circulations).

Baird [66] showed that shorter droplets moving between two parallel plates have higher values of Nu, and as the length of the droplets increases the heat transfer characteristics moves toward the single phase heat transfer, because the main mechanism of increasing convective heat transfer i.e. internal circulations in the droplet has less effect. Baird [66] also mentioned that important parameters in heat transfer modeling for moving droplets between parallel plates are Pe, droplet length, distance between two parallel plates, and meniscus curvature effects i.e. contact angle. As a result, the reports of Nu versus position of droplets should include all of the aforementioned parameters.

Young and Mohseni [79] reported higher Nu (after initially oscillating) for various droplet sizes moving between parallel plates compared with continues Graetz flow. They argued this is because of the circulating internal flows inside the moving droplets. They also showed that as the droplets become shorter, the Nu increases because there is relatively more cool fluid inside the droplet which can be brought into contact with the heated wall in comparison to the longer droplets. They reported that Nu begins to decrease (before being constant) when the first circulation completes and

the previously heated fluid is brought back to the heated walls. They also reported a locally higher value of Nu before stabilization and argued this as follows. In long droplets the dominant heat transfer process is diffusion from the wall into the liquid in radial direction, but in short droplets the diffusion in wall-tangent direction has the main role. The highest peak in Nu occurs when these two diffusion times become near equal in magnitude.

Oprins et al. [80] studied numerically the internal flow patterns and heat transfer inside electrostatic actuated droplets moving between two parallel plates. They carried out steady and time-dependent simulations, assumed laminar flow and constant fluid properties. They also proposed a lumped model by dividing the droplet into four cells for steady state case, and then expanded it in order to make it capable of predicting unsteady heat transfer inside the moving droplet, before it becomes thermally saturated. They reported that the heat transfer increases to twice that as compared to the minimum heat transfer only by heat conduction in the liquid.

Sammarco and Burns [143] performed a finite difference analysis to investigate the effect of different parameters on microfabricated devices heat transfer behavior using a moving droplet. They suggested a new optimized value for a dimensionless parameter which is useful in design purposes. In addition, they showed that for $Pe \leq 0.1$, one can achieve more uniform interface temperatures.

Suzuki et al. [144] investigated experimentally the flow pattern of a sliding droplet between two parallel plates on a slope and reported the droplet shape, solid-liquid

molecular interaction, and the gravitational force as the important parameters in order to determine the sliding mode on a solid surface. They observed that water droplets slid down with interfacial rotation flows and slipping motion at the solid-liquid interface. This observation is very important and can be helpful in numerical simulations where the boundary conditions should be applied e.g. at moving walls. The slip rates are dependent on the combination of the chemical compositions and the coating material of the top and the bottom walls.

Walker and Shapiro [149] studied hydrodynamics of a moving droplet between two parallel plates for EWOD purposes. They modeled the problem using Hele-Shaw equations as a two-dimensional problem due to small spacing between the plates and consequently small Reynolds number.

Zeng and Korsmeyer [150] and Jang et al. [151] performed three dimensional simulations of moving droplet hydrodynamics for lab-on-a-chip applications using Flow3D and CFD-ACE+, respectively. However, their main focus was on electrohydrodynamics, electric potential distribution, droplet fission, etc.

More recently Kumari and Garimella [146] carried out one of the rare three dimensional numerical studies on moving droplets hydrodynamics and heat transfer and presented three dimensional motion effects on convective heat transfer inside the droplet using temperature profiles at the different locations inside the droplet. They conducted their simulations for two different situations: a moving droplet on a single plate and between two parallel plates, using hemispherical and cylindrical computa-

tional domains, respectively.

Talimi et al. [31] compared two approaches for integrating the heat transfer for a specified number of slugs in a channel when the single phase moving frame computational domain is used. The first approach includes summing up the local heat transfer rates for all of the moving slugs in the channel from entrance to exit. This requires that one knows the exact position of all the slugs. The second approach, on the other hand, is based on the heat received by a slug while it moves through the channel and liquid volume fraction of the two phase flow. They showed that the second approach is more straightforward. Based on this approach Talimi et al. [31] presented some graphs of dimensionless heat transfer for different slug lengths and contact angles. They assumed same values for advancing and rear contact angles and as they mentioned the effects of the difference between these two contact angles will be examined in the future studies.

2.4 Other Aspects

2.4.1 Slug formation

The process of slug formation in circular channels has been reported as a strong function of type of mixing zone and studied for different mixing zone shapes: T-junctions (Qian and Lawal [65], Kumar et al. [103], Dai et al. [113]), Y-junctions (Kumar et al. [103], Ilnicki et al. [114]), pre-mixed inlets (Qian and Lawal [65], Kumar et al. [103]), and annular nozzles (Shao et al. [37], Gupta et al. [64], Chen et al. [46],

Goel and Buwa [108], Narayanan and Lakehal [75]). The parameters of interest which have been studied by researchers are diameter of the mixing zone, channel curvature (for meandered channels), and superficial velocities of the two phases. The forces which have been studied by recent researchers include surface tension, viscous friction, inertial, and gravitational forces. The effects of these forces can be presented using the different dimensionless groups such as the Reynolds number, Re, and Capillary number, Ca.

Wall adhesion and contact angle play a prominent role in slug/bubble formation as reported in some recent literatures. For example Cherlo et al. [109] reported an increase in slug length with a decrease in contact angle. On the other hand, Gupta et al. [44] reported that the wall contact angle plays no role when the mesh is fine enough near the walls because the thin liquid film around the bubbles can be captured using this fine mesh. This could be true when the channel material is hydrophilic and there is no gas/liquid/solid contact angle. In the case of hydrophobic materials, the wall contact angle is still important. However the mesh resolution in the numerical simulations conducted by Cherlo et al. [109] is much coarser than what Gupta et al. [44] used. This seems to be unavoidable (especially in 3D cases) since using fine mesh like what Gupta et al. [44] suggested is very time consuming.

T-Junction:

Dai et al. [113] performed a highly detailed numerical study on slug formation in T-junction. They showed three stages in slug formation: expansion, collapse, and

pinching off. They also argued that pressure increase in the liquid phase, shear stress, and surface tension are three forces which are involved in the process of slug formation. The different arrangements of liquid and gas inlet directions and their effects on slug formation were studied numerically by Qian and Lawal [65]. They showed that in order to achieve shorter gas slugs, gas and liquid phases should be fed head to head or perpendicular to each other, while the liquid flows parallel to the microchannel. Decreasing the diameter of the mixing zone, leads to a decrease in the gas slug length.

Y-Junction:

Ilnicki et al. [114] showed numerically that liquid slug length increases and gas slug length decreases with a decrease in gas superficial velocity or an increase in liquid superficial velocity for a Y-shape microchannel. Similar trend observed by Kumar et al. [103]. They also reported that slug length ratio has a 20-30% difference compared with the flow rate ratio.

Annular (Concentric) Nozzles:

A three stage process of slug formation using concentric nozzles - consists of expanding, contracting, and necking - was reported by Shao et al. [37], similar to what observed by Dai et al. [113] in T-junction. These stage names refer to the movement of gasliquid interface at the lower end of the gas bubble near the nozzle. At the first stage, expanding, the gas/liquid interface moves toward the microtube wall due to injection of gas. As the bubble grows to a certain level, the interface movement reverses and it moves away from the wall toward axis. This is the contracting stage.

By injecting more gas, the gas bubble grows further in radial direction and leaves only a thin film of liquid to pass. Therefore, liquid pressure makes the relation region between gas bubble and gas inlet stream slender i.e. necking stage. Figure 2.6 shows these three stages.

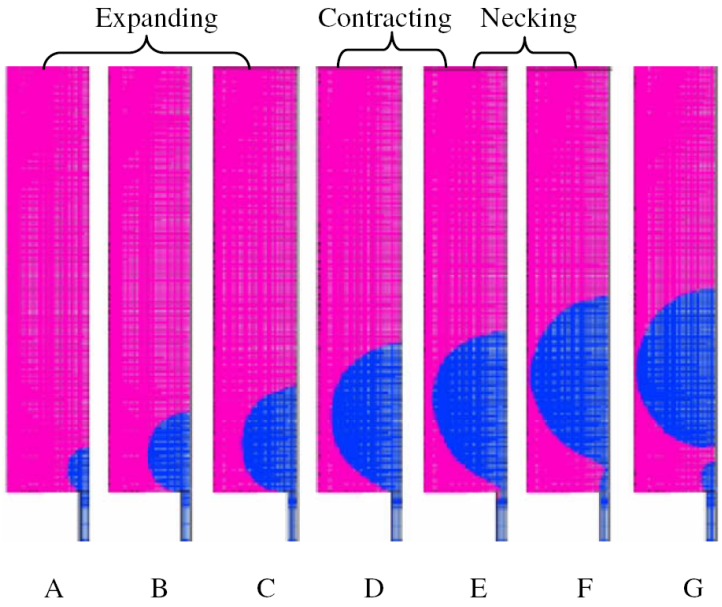

Figure 2.6: Slug formation process (Shao et al. [37]).

Chen et al. [46] stated that bubble departure size (maximum gas slug size just before departure) depends on liquid and gas superficial velocities. By increasing gas superficial velocity (or decreasing liquid superficial velocity), the departure size and the length of the gas slug increase. (The same results were also reported by Kumar et al. [103].) They also showed that under the same liquid and gas superficial velocities (U_L and U_G) i.e. same flow conditions, the size of Taylor bubbles formed inside a given geometry of microtube can vary distinctly using different bubble generation devices.

In other words, for a given set of U_L and U_G, different flow patterns can occur inside the same channel.

Another detailed numerical study on slug formation process using concentric nozzles was performed by Goel and Buwa [108], in which the effect of different parameters such as gas and liquid superficial velocities, Ca number, nozzle geometry, contact angles, and physical properties of liquid were of interest. They showed that wall adhesion is a very important parameter in the process of slug formation and an increase in wall contact angle and a decrease in nozzle wall contact angle would decrease the bubble formation period. Surface tension has a significant effect on this process and the bubble formation period increases with an increase in surface tension.

Narayanan and Lakehal [75] focused on the effect of gravity on the breakup into slugs and according to their results, the slug breakup happens slightly earlier for upflow, which leads to a higher breakup frequency.

Pre-Mixed Inlets:

Qian and Lawal [65] numerically investigated the effect of pre-mixing level and mixing zone geometry on gas slug length. They showed as the two phases (gas and liquid) are mixed better at the inlet of microchannel, the gas slug lengths become shorter (similar results were also reported by Kumar et al. [103]). Kumar et al. [103] also reported that by increasing the curvature ratio (the ratio of coil diameter to tube diameter) the slug length increases for both gas and liquid phases. They proposed the following reasons for this behavior. For low curvature ratios small slugs formed

due to strong centrifugal forces. As the curvature ratio increases, the centrifugal force becomes weaker and slug length increases. They also showed that by decreasing Ca, the gas slug length increases, by showing that when surface tension increases or viscosity decreases, the gas slugs become longer.

Slug Formation in Non-Circular Microchannels

Slug formation process in non-circular microchannels has been widely neglected in the recent numerical simulation. Almost all of the numerical studies on slug formation process in gas-liquid two phase flows have been carried out for circular microtubes. This may be because of applicability of a two dimensional axisymmetric geometry. The studies performed by Santos and Kawaji [119] for square microchannels and Yu et al. [57] for square and rectangular microchannels are exceptions. Based on the results of Santos and Kawaji [119] the length of gas slugs increase with an increase in gas superficial velocity or a decrease in liquid superficial velocity. Yu et al. [57] performed a lattice Boltzmann numerical study on the process of slug formation in non-circular microchannels and reported a dependency of the process on Ca. They showed that for high Ca, small bubbles formed, with a diameter less than microchannel width. So slug flow would not occur. They argued that this is because of weak surface tension forces that cannot dominate shear forces. According to their results, gas inlet pressure is higher than liquid inlet pressure in the expanding stage of slug formation. When the liquid inlet pressure overcomes the gas pressure, the second stage starts. The third stage, necking, is when a peak occurs in the difference between gas and liquid inlet

pressures. The aforementioned procedure can be seen in Fig. 2.7.

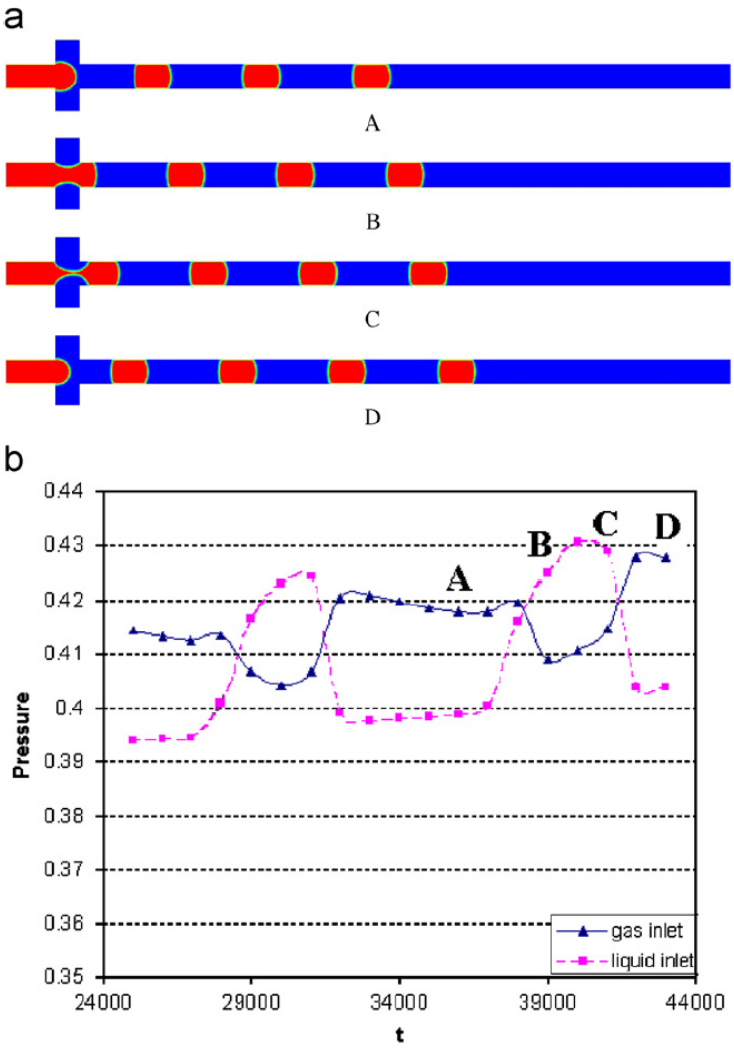

Figure 2.7: (a) Snapshots of the slug formation process and (b) pressure variation at the gas and liquid inlets, time points AD correspond to the four snapshots in (a) (Yu et al. [57]).

Using 2D simulations for rectangular microchannels Guo and Chen [120] reported some critical contact angles above which the Taylor bubble formation will not take place and showed that this critical contact angle depends on Ca. This shows the

important role of the contact angle (i.e. using different wall materials) in controlling the slug formation process in microchannels. Obviously more research can give deeper insight on this subject.

2.4.2 Bubble Shape

Typically, Taylor bubble shape depends on different parameters such as Ca and Re and has a meniscus front nose and a relatively flattened bottom. The length of the Taylor bubbles depends strongly on the mixing configuration. The liquid film formed between the bubble and the wall is uniform at the middle portion. The film thickness of the liquid around the gas bubble increases continuously towards the front nose (as it is shown schematically in Fig. 3.8), while it shows somewhat wavy behavior towards the bottom portion.

Kreutzer et al. [58] and Chen et al. [46] reported a change in the front and rear shapes of the departed Taylor bubbles with Re (defined based on the two-phase velocity $U = U_L + U_G$). According to Chen et al. [46], at low Re, both the front and rear sides of Taylor bubbles show a hemispherical cap shape. As Re increases, the curvature radius of the bubble tip become smaller and the rear cap becomes flattened (similar results are reported by Kreutzer et al. [58]). The dependency of bubble shape on Re is showed in Fig. 2.8. Chen et al. [46] also showed that when the liquid superficial velocity is small enough as compared to the gas superficial velocity, long Taylor bubbles can be formed by merging a growing bubble with the departed Taylor

bubble in front of it. This approach is called Taylor-pairing or doubling.

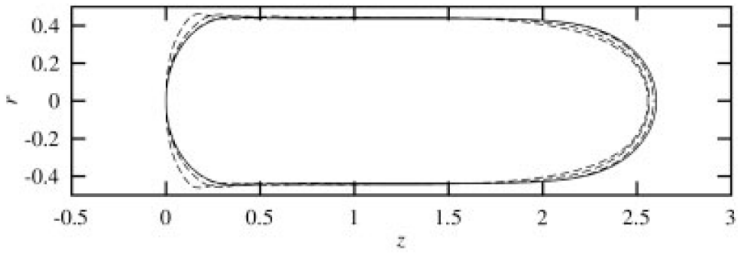

Figure 2.8: Taylor bubble shape for $Re = 1, 10, 100, 200$ at $Ca = 0.04$ (Kreutzer et al. [58]).

Edvinsson and Irandoust [115] showed that as Ca increases, the rear side of the bubble becomes less convex and inverted gradually. They also reported that as Re increases, a multiple wavelet appears in the film near the rear side of the bubble and its amplitude increases with Re.

Taha and Cui [51] reported almost similar curvature of Taylor bubble ends at low Ca and nearly identical streamlines at both ends of the bubble. They also showed that as Ca increases, the bubble nose becomes more slender and liquid film flowing around the bubble is thicker (similar results reported by Martinez and Udell [116]). They discussed three separate regions in the leading edge of the bubble: the bubble cap region, the liquid film region and the transition region between them. According to their results, increase in Ca result in an increase of the liquid film thickness and the sharpness of the bubble nose. This results in smaller bubble caps and larger transition regions.

Taha and Cui [47] found that by decreasing the Morton number, Mo, under a

constant value of Eotvos number, Eo, the curvature of the bubble nose increases and the bubble tail flattens, which results in an increment of the liquid film thickness around the bubble. Also the curvature of bubble nose increases as Eo goes up.

The length of the Taylor bubbles has been studied numerically by Shao et al. [37] and Kumar et al. [103]. Shao et al. [37] reported the bubble size increases with increasing gas and decreasing liquid superficial velocities. Also, bubble size is mainly affected by surface tension and only slightly by density and viscosity. They reported an increase in bubble size with increasing nozzle size, and argued the reason is due to the decrease in gas flux when using larger nozzles, while keeping the same gas flow rate. The surface tension force increases as nozzle becomes larger. Former has a detaching effect and later has an attaching effect, therefore the bubble formation time and consequently its size increases. A dependency on bubble length on inlet conditions was also reported by Kumar et al. [103] for pre-mixed inlet configuration in meandering microtubes.

Ua-arayaporn et al. [73] studied the effect of pressure gradient on the shape of bubbles in a slug flow through microtubes and found that the bubbles are nearly spherical under the low pressure gradients.

Bubble Shape in Non-Circular Microchannels

The main parameters, which are reported to have strong effects on the bubble shape and interface between the two phases, are Ca and superficial velocity ratio.

According to the numerical research on bubble shape in square microchannels, the

bubble shape is nonaxisymmetric and flatten out against the wall for low Ca and axisymmetic, i.e. the bubble cross section at any axial position remains circular, for high Ca. Ghidersa et al. [53] and Taha and Cui [54] reported that the bubble shape remains circular even up to $Ca = 0.043$, which they argued is in agreement with other published studies. However the generally accepted minimum value of the Ca is 0.04. There are several different reports on transition Ca limit from 0.1 to 0.04 (Taha and Cui [54], Raimondi et al. [121]).

Taha and Cui [54] showed that at low Ca, both the front and rear ends of the bubbles are nearly spherical. When Ca increases, the convex bubble end inverts gradually to concave. As the Ca increases, the bubble becomes longer and more cylindrical. At higher Ca numbers, we have cylindrical bubbles.

Liu and Wang [56] carried out a numerical study on bubble shape with respect to Ca through square and equilateral triangular microchannels and (similar to Taha and Cui [54] and Raimondi et al. [121]) argued that because the liquid film thickness in corners is larger than side walls, the liquid flows more slowly in the corners. They also reported the transition Ca limit of 0.1 for square microchannels and discussed two potential causes for differences between this limit and the value of 0.04 reported by other researchers. Firstly, the inertial effect was considered in their study and second, they simulated a finite long bubble in their work.

Yu et al. [57] reported that a larger gas to liquid flow ratio leads to longer gas bubbles in square and rectangular microchannels. Under the same flow rate ratio, a

smaller Ca number results in a longer bubble. According to their results, the geometry of the mixing section also affects the bubble size and the spacing between the bubbles.

Reznik and Yarin [122] simulated numerically the change in the contact angle of a droplet squeezing between two moving walls and reported that the free surface deviates from circularity at the beginning of the squeezing process and after sufficiently strong squeezing, the contact angle gradually goes up toward the value of π. According to their results, the free surface becomes more similar to the circular shape during the final steps of squeezing.

2.4.3 Flow Patterns

Bubble length, Peclet number Pe, Bodenstein number Bo, Capillary number Ca, pressure gradient, flow direction (gravitational effects), channel curvature (for curved microchannels), and superficial velocities of the two phases have been reported by many researchers as the main factors influencing flow patterns and consequently heat and mass transfer. Another important factor is whether the bubble touches the channel walls, i.e. dry-out condition, or not.

Giavedoni and Saita [49] and Martinez and Udell [116] reported different flow patterns for high and low Ca. Based on their results, circulation regions inside the liquid slugs become smaller as Ca increases and showed that these results agree with Taylor [27].

Slip ratio between bubbles and liquid has been studied numerically (Edvinsson and

Irandoust [50], Ua-arayaporn et al. [73], He et al. [60]). He et al. [60] found that for Taylor flow when the wall is perfectly wetted by liquid, the gas bubble to liquid velocity ratio is approximately 1.2, which agrees well with the Armand correlation (Armand and Treschev [117]) but when the gas bubbles contact with the wall directly i.e. a dry-out patch, the gas bubble flows with the same velocity as liquid slugs (slip ratio of 1). Ua-arayaporn et al. [73] reported higher ratios of gas velocity to liquid velocity for higher pressure gradients and argued this is because the change in bubbles shape for higher pressure gradients. At higher pressure gradients, the bubble is elongated in the central region of the tube or pipe and less is influenced by the no-slip wall condition. Edvinsson and Irandoust [50] argued that for small microchannels it is sufficient to correlate the relative velocity of gas plugs with Ca. As flow rates and diameters increase, the effects of inertial forces as well as gravitational forces become more pronounced. In addition, the size of the circulation regions within the liquid plug decreases rapidly with increases in liquid film thickness. Ilnicki et al. [114] reported that for high values of overall velocities ($U_G + U_L > 0.4(m/s)$) the time necessary to reach a steady Taylor flow increases significantly if the slip ratio (U_G/U_L) is higher than 1. On the other hand, for the overall velocity lower than 0.4 (m/s) this necessary time increases only if the slip ratio is higher than 2.5.

Axial transport phenomena (considering mass transfer) between liquid slugs through the liquid film around the bubbles have been studied by Salman et al. [118] and Muradoglu et al. [104]. Salman et al. [118] investigated numerically the effect of axial

mixing in liquid phase of Taylor flows for low Bo, where diffusion is sufficiently large, and reported an increase in axial mixing in liquid slugs with increasing Ca and argued this is because of a thicker liquid film around the bubbles and better communication between slugs. They also showed that axial mixing increases with an increase in bubble and slug length and suggested using short bubble and slug lengths in order to have reduced axial mixing.

Muradoglu et al. [104] studied the effects of Pe on the axial mass transfer (dispersion) in the liquid slugs. They found that "convection" and "molecular diffusion" control the axial dispersion for different Peclet numbers, Pe. They introduced three different regimes of Pe:

1) Convection-controlled regime when $Pe > 10^3$.

2) Diffusion-controlled regime when $Pe < 10^2$.

3) Transition regime when $10^2 \leq Pe \leq 10^3$.

Curved microtubes have been studied by Fries and von Rohr [62]. They showed that the symmetrical velocity profile of straight microtubes changes to an asymmetrical one for the meandering channel configuration. Therefore radial mass transfer inside the liquid slug increases and mixing length reduces. A smaller radius of curvature provides more mixing rather than larger radii. They argued this is because of larger centrifugal forces. According to their discussion, the optimal slug length for fast mixing depends on the bend geometry. While longer slug lengths provide an enhanced mass

transfer due to the bending angle of the slug, shorter liquid slugs have smaller turning angles, providing an enhanced asymmetrical flow pattern.

Taha and Cui [51] reported that at low Ca, the shape of streamlines at the front and end of the bubble are almost the same, bending sharply in the path of circulation. They also mentioned that this localized effect of the bubble can be seen only within a bubble diameter from the bubble nose. According to their results, the circulation region in the liquid slugs becomes smaller and the center of the circulation zone shifts toward the axis, as Ca increases. Also, by increasing Ca, the thickness of liquid film flowing around the bubble increases, and complete bypass flow occurs around $Ca = 0.5$. They observed two stagnation points in the liquid plug: one on the bubble tip and the second inside the liquid plug.

Flow Patterns in Non-Circular Microchannels

According to the published literature, velocity field and flow patterns of gas-liquid two phase flow in non-circular microchannels are both affected by Ca, channel shape and geometry, slug length, and local pressure gradient. There is also a reported critical Ca in which a complete bypass occurs. This critical value has been reported for a few channel shapes such as squares and triangles.

As presented in Table 2.3 most of the recent attention on velocity field and flow pattern of two phase flow inside non-circular microchannels was on square microchannels. Rectangular microchannels were of interest by Yu et al. [57] and Onea et al. [123]. Liu and Wang [56] is one of the rare numerical studies on flow pattern inside

triangular microchannels. Therefore rectangular and triangular geometries need more numerical focus.

Zaloha et al. [124] investigated flow patterns and circulations inside liquid slugs in gas liquid Taylor flows in straight and meandering rectangular microchannels using micro Particle Image Velocimetry ($\mu - PIV$). According to their report, the internal circulations inside moving liquid slugs are symmetrical about the center line of the straight rectangular microchannels, but more complex in the meandering microchannels. They quantified the recirculation motion inside moving slugs for slug lengths of $L_s/w < 1.5$, and showed that the product of the liquid slug residence time and the recirculation rate is independent of the two phase velocity, U_{tp}, when $8 < Re_{tp} < 32$ and $1.1 \times 10^{-3} < Ca_{tp} < 4.5 \times 10^{-3}$.

Worner et al. [105] reported that the velocity profile in the liquid slug has the same parabolic form for different lengths of computational domain in square microchannels.

Taha and Cui [47] showed numerically that the behavior of dimensionless bubble velocity of Taylor flow in square microchannels is similar to circular microtubes, except for low Ca where it increases with Ca. They also showed that the transition to complete bypass occurs around $Ca = 0.4$. According to their results, two separate circulation regions exist in front of and behind the bubble at low Ca. As Ca increases, similar to the circular microtubes, the center of circulations moves away from walls and shifts toward the symmetry line. At high Ca, recirculation regions vanish and a complete bypass occurs. They showed that the liquid flow field is not axisymmetric

Table 2.3: Numerical studies on hydrodynamics and heat transfer in gas liquid two phase flows in non-circular microchannels.

Authors	Flow conditions	Geometry	Research aspects
Liu and Wang [56]	$0.003 < Ca < 1$	MFR Square and equi-triangle $D_h = 1mm, L = 16D_h$	Bubble shape, flow patterns, and film thickness
Yu et al. [57]	$0.006 < Ca < 0.2$ Air-silicon oil	FFR Square and rectangular $125\mu m \times 125 or 250\mu m$	Pressure drop, flow patterns, slug formation, and film thickness
Ghidersa et al. [53]	$Re = 76.3$ $Ca = 0.043, 0.205$	MFR Square duct (3D) $2mm \times 2mm \times 2mm$	Bubble shape, flow patterns, and film thickness
Worner et al. [105]	$Ca = 0.2$	MFR Square duct (3D) $2mm \times 2mm \times 2mm$	Bubble shape and flow patterns
Taha and Cui [54]	$0.001 < Ca < 3.4$	MFR Square duct (3D) $2mm \times 2mm \times 2mm$	Bubble shape, flow patterns, pressure drop, and film thickness
Young and Mohseni [79]	$Re = 100, 400$	MFR Single droplet between parallel plates $0.125 < H/L < 1$	Heat transfer (isothermal and isoflux boundary conditions)
Onea et al. [123]	$Mo = 0.0004926$ $H = 0.03, 3$ Air/methyl chloride water	MFR Square and rectangular $D_h = 2mm$ (3D)	Bubble shape, flow patterns, and film thickness
Oztaskin et al. [135]	$0.11 < Ca < 0.23$	MFR Square ducts (3D) $2mm \times 2mm$	Velocity and flow patterns, flow stability
Santos and Kawaji [119]	$0.018 < U_G < 0.791 m/s$ $0.042 < U_L < 0.757 m/s$ Air-water	FFR Square ducts (3D) $D_h = 113\mu m$	Slug formation and flow patterns
Oprins et al. [80]	$U = 0.1 m/s$ Water	MFR Single droplet between parallel plates $L = 2.8mm$, $H = 1mm$	Flow patterns, heat transfer (isothermal wall)
Heil [138]	$0.05 < Ca < 5$ $0 < Re < 280$	MFR 2D channel	Film thickness and flow patterns
Giavedoni and Saita [49]	$0.005 < Ca < 1$ $0 < Re < 70$	MFR Circular tubes and parallel plates	Film thickness and flow patterns
Guo and Chen [120]	$6.4 \times 10^{-4} < Ca < 0.017$	FFR Rectangular ducts (2D)	Slug formation and flow patterns

at low Ca by presenting two different positions of the vortex eye from the side and diagonal views.

Ghidersa et al. [53] reported that for the cross section with the smallest film thickness, in the liquid film surrounding the bubble a back flow region exists. They argued this flow corresponds to a local high positive pressure gradient due to the rapid change in film thickness.

Liu and Wang [56] like other researchers (Taha and Cui [54], Raimondi et al. [121]) reported that with increases in Ca, the distribution of the vortex centers transferred from walls into the circle gradually, and become smaller and smaller. They argued that as the vortex centers shifted toward the centerline, more liquid flows towards the bubble and this forms a thicker film. Finally at critical Ca, at which the bubble velocity is equal to the maximum liquid velocity, there is a complete bypass and no circulation in liquid plug. They obtained a critical Ca of 0.8 and 1.0 in square and equilateral triangular shapes, respectively.

2.4.4 Liquid-Liquid Slug Flow

Numerical studies on liquid-liquid two phase flows have not been considered widely and the articles found in this field are much less than what can be found in gas-liquid field. Table 2.4 shows the numerical studies on liquid-liquid two phase flows. As one can see in Table 2.4, many of research aspects are still untreated, including slug shape, film thickness of continuous phase around slugs of dispersed phase, pressure

drop, and heat transfer. Based on the thermal diffusivity of the liquids, both phases could contribute in the heat transfer process. The ability of liquid-liquid two phase flows to increase heat transfer as compared with gas-liquid two phase flows can be a future research subject. Curved microchannels are another gap in research.

Table 2.4: Numerical studies on hydrodynamics and heat transfer in liquid-liquid two phase flows.

	Circular microtubes	Non-circular microchannels	Meandering microchannels
Slug formation	Kashid et al. [101, 125, 126, 127, 128]	Wu et al. [102, 129]- Rectangle Kumar et al. [103]- Rectangle Aliasghar Zadeh and Radspiel [130]- Rectangle Cherlo et al. [109]- Rectangle Raj et al. [131]	No studies found.
Slug shape	No studies found.	Raj et al. [131]	No studies found.
Flow pattern	Kashid et al. [101, 125, 126, 127]	Wu et al. [129]- Rectangle Raimondi et al. [107, 121] (Square)	No studies found.
Film thickness	No studies found.	No studies found.	No studies found.
Pressure drop	Kashid et al. [128]	No studies found.	No studies found.
Heat transfer	No studies found.	No studies found.	No studies found.

Liquid-Liquid Slug Formation in Circular Microchannels

The effects of a small number of parameters on the slug formation process in liquid-liquid flows have been studied in the recent years. These parameters are wall adhesion, wall confinement, and Ca.

Kashid et al. [101] simulated slug formation in a Y-junction mixer using two liquids and reported that the wall adhesion plays a very important role in formation

of the plugs. According to their simulation results, the two liquids travel through the microtube, after the Y-junction, as two parallel flows to a certain distance. After that, slugs form due to the wall adhesion.

Liquid-Liquid Slug Formation in Non-Circular Microchannels

The liquid-liquid two phase flows in non-circular microchannels have not been considered extensively in the numerical simulations. Only a few studies have considered the effects of some general parameters such as Ca and Re on the slug formation process and flow patterns.

Aliasghar Zadeh and Radespiel [130] argued that the mechanism of slug formation depends on Ca. For high Ca, shear stress forces play the prominent role, and for low Ca, a force balance between phases pressure difference and Laplace pressure is important.

The effects of Ca on slug length have been studied by Aliasghar Zadeh and Radespiel [130] and Wu et al. [102]. According to Aliasghar Zadeh and Radespiel [130], slug length decreases initially and flattens as Ca increases. Wu et al. [102] reported the strong dependence of plug size on Ca. They showed that (for their case) by increasing Ca, droplets become shorter. They also showed that for $Ca < 0.005$, droplet length is only influenced by Ca and that for higher Ca, it is influenced by both Ca and Re.

Wu et al. [129] showed that the distance between two neighboring droplets increases with a decrease in Ca. Another result of their work is that the size of the formed slugs increases when Ca decreases. For small Ca, the diameter of formed

droplets becomes larger than the width of the channel and slugs are generated. For larger Ca, small droplets generated and do not touch the wall and therefore the effect of the channel geometry decreases.

Raj et al. [131] showed the strong effect of wall contact angle on slug formation in rectangular microchannels. They performed 3D simulations for different contact angles from 60^o to 180^o and observed that an increase in the wall contact angle makes the slugs smaller and more stable.

Liquid-Liquid Flow Patterns in Circular Microchannels

Kashid et al. [101, 125, 126, 127] have carried out a number of numerical simulations on the flow pattern inside the slugs. The effect of different parameters including Re, interface shape, and circulation intensity were of interest in their works. The effects of Ca and We were also studied recently by Wu et al. [129].

Kashid et al. [101] performed numerical simulations for a liquid-liquid plug flow in microtubes considering two liquid plugs separately. They considered two cases for the second liquid plug: with and without a thin film around the computational domain. According to their results two flow patterns exist in each slug: a recirculation zone at the center and in the wall proximity and two stagnant zones in between them. Thus, there is a parabolic velocity profile showing the maximum velocity at the center of the slug, zero velocity at some radial position and negative velocity at the wall surface.

Kashid et al. [125] mentioned that for long liquid slugs in which slug length is larger than slug diameter, the radial position of the stagnant zones are located at roughly

half the microtube radius. These stagnant zones shift slightly toward the center of the slug with increasing liquid flow velocity. On the other hand, for shorter slugs, the radial position of the stagnant zones observed between the center of the slug and the walls at low velocities goes towards the center rapidly, with increasing velocity. They also reported that in the case of a slug in contact with the walls (without film) and a length longer than its diameter, the normalized circulation time is not influenced significantly by the flow velocity. But for the slugs with a length smaller than their diameter, at low liquid velocity, the circulation time is constant, but with an increase in the flow velocity, the circulation time decreases and subsequently remains constant.

Kashid et al. [126] showed that in liquid-liquid flows, while the viscosities of two liquids are different, both of the slugs show similar velocity profiles, and argued this is due to very low Re in which the velocity profiles are independent of viscosity.

Kashid et al. [127] observed that there are four stagnant zones within each slug on the upper and lower parts and at the front and rear ends. According to their results, in some slugs, the stagnant rear zone does appear if the rear side is a perfect hemisphere.

Liquid-Liquid Flow Patterns in Non-Circular Microchannels

Raimondi et al. [121] categorized the liquid-liquid slug flows in square microchannels into three main categories: when Ca is higher than 0.01, internal circulations exist in both continuous and dispersed phases, and a thin film of continuous phase observed between dispersed phase slugs and the wall. For low Ca and Re, several recirculation regions exist in the slugs, and for low Ca and high Re, no circulations

exist in the continuous phase.

Wu et al. [129] reported that for small Ca, the flow patterns are the same for different We. This is due to the relatively larger influence of Ca on the flow. But when the inlet velocity is large, the flow pattern is not only influenced by Ca but also We, because of the squared velocity term.

2.5 Research Gaps

Based on the literature reviewed large gaps is research exist in the field of slug flow and its application in heat transfer in small scales. The gaps which can be addressed numerically are discussed in the following sections.

2.5.1 Flow Patterns

One of the most important issues in this subject would be presence of a thin liquid film around the gas phase or the second liquid phase. Numerical researchers can focus on the appearance of a real dry-out condition, not because of a poor mesh resolution which could lead to nonphysical results.

2.5.2 Slug Formation

From a geometrical point of view, circular microtubes were of interest by numerical researchers much more than other channel shapes. Therefore the principal research gap is slug formation in non-circular microchannels and the different parameters which are important in this process and their effects, for example, the effects of different merging

geometries including T-junctions, Y-junctions, and concentric nozzles. The effects of different phase velocities, Re, and Ca on the process of slug formation can be studied. Another gap in this area is liquid-liquid flows in all of the channel shapes. While from a numerical point of view there is no difference between gas and liquid (as long as they are immiscible), liquid-liquid two phase flows could be investigated by applying the proper dimensionless groups such as Ca.

2.5.3 Film Thickness

The investigation on thickness of the liquid film around the gas phase has been neglected for low Ca in circular microtubes and a wide range of Ca in non-circular microchannels such as triangular and/or rectangular microchannels with aspect ratios other than two. Additionally, no numerical investigation was found for the film thickness around the second liquid phase in liquid-liquid two phase flows. As discussed in the literature review, the film thickness might play a role in controlling heat transfer and this could be investigated numerically in the future.

2.5.4 Pressure Drop

Pressure drop plays a significantly important role as a parameter against heat (or mass) transfer. In most of the situations an increase in heat transfer results in increasing the pressure drop as well. Therefore, in optimization of heat sinks or heat exchangers, pressure drop has to be considered carefully. Like slug formation, most of the numerical studies focused on pressure drop were in circular microtubes and this leaves a large

gap for non-circular microchannels. Again liquid-liquid flows have been neglected as well. As another suggestion, the effects of existing liquid film around bubbles in gas-liquid flows or three phase interface, when dry-out condition happens, in all channels shapes, can be studied numerically in the future.

Table 2.5: Numerical studies on heat transfer in gas-liquid two phase flows

Duct shape	Constant temperature	Constant heat flux	Non-symmetrical boundary conditions
Circle	Gupta et al. [64]	Gupta et al. [64]	—
	Narayanan and Lakehal [75]	Ua-arayaporn et al. [73]	—
	Lakehal et al. [74]	He et al. [60]	—
		Mehdizadeh et al. [81]	—
		Fukagata et al. [83]	—
		Asadolahi et al. [84, 85, 86]	—
Parallel plates	Young and Mohseni [79]	Young and Mohseni [79]	—
	Baird [66]		—
	Oprins et al. [80]		—
	Talimi et al. [31, 82]		—
Square,	Talimi et al. [88]	—	—
Rectangle	—	—	—
Other	—	—	—

2.5.5 Heat Transfer

Based on the literature review, more effort is necessary in this field. Only a few experimental or numerical simulations have been found in the literature, especially for non-circular microchannels. A very important issue is that, while the flow can be symmetrical (or axysimetrical) from the hydrodynamics point of view, the thermal boundary conditions can be non-symmetrical. For example, different thermal condi-

tions can be applied on the different walls of a rectangular microchannel. This issue may be considered in addition to the isothermal or isoflux wall boundary conditions in the future research. As presented in Table 2.5, significant research gaps exist in the channel shapes other than circle and parallel plates. Non-symmetrical thermal boundary conditions have been neglected as well.

2.5.6 Curved Microchannels

All of the aforementioned suggestions may be of interest in meandering microchannels as well. The effects of curved path on heat transfer and flow patterns have been shown in single phase flows widely. Except a few literature reported in the present review, this field has been neglected in the past. Heat transfer characteristics and pressure drop could be numerically investigated in the future.

2.6 Summary

A few of the research gaps discussed in section 2.5.5 have been considered in the present research for numerical simulations. Starting with moving frame of reference two dimensional cases (see section 3.3.1) for parallel plates and circular microchannels, heat transfer in moving liquid slugs have been studied. Validity of two dimensional simulations for moving droplets between parallel plates has been investigated by comparing two dimensional with three dimensional simulations. After that, heat transfer in square microchannels geometries have been considered, using three dimensional simulations. A comparison between moving and fixed frames of reference has also

been performed and the results show possible effects of liquid film around bubbles on heat transfer process. Finally, some simulations using fixed frame of reference for circular microchannels have been carried out in order to investigate the effects of film thickness on heat transfer.

3 OBJECTIVES AND METHODOLOGY

3.1 Objectives

Numerical simulation is a powerful tool to approach the fluid dynamics and heat transfer problems. The high amount of detail produced by a CFD study provides the researchers a deep insight of the process. Performing numerical simulations along with experiments also provides the opportunity to examine whether there has been any parameter missed in the correlations based on the experimental studies. The main objectives of the present research are as follows:

3.1.1 Implementation of The Moving Wall Technique

There are two different methods for simulation of two phase slug flows: 1) fixed frame of reference, and 2) moving frame of reference. These methods are explained in detail in section 3.3.1. In terms of heat transfer, the heat flux results from moving frame

of reference should be integrated along the channel with respect to the number of slugs inside the channel. Two different approaches for the integration will be examined and compared in this thesis. The methodology of implementation of these two approaches will be presented in section 3.3.2. The numerical simulations, results, and the comparison of these two approaches has been conducted and presented in section 4.1.

3.1.2 Three Dimensional Effects on Heat Transfer in a Moving Liquid Slug Between Two Parallel Plates

Moving slugs between two parallel plates have been mostly simulated using two dimensional domains. These two dimensions are the direction of the slug motion and the direction normal to the walls. This way the system and moving slugs are assumed with a unit depth. However, the reality is different. The moving slug has a three dimensional shape, and the contact area between the slug and walls is a finite area. This simplification will be examined in the present thesis using both 2D and 3D simulations for similar geometries, and the results will be compared, in section 5.1.

3.1.3 Potential Effects of Liquid Film on Heat Transfer in Slug Flows

As reported in earlier sections, the internal circulations in moving slugs is the mechanism that enhances convective heat transfer in two phase slug flows. The thickness of liquid film around bubbles has effects on the flow pattern inside the liquid phase, and hence internal circulations as showed by Taylor [27] (see Fig. 2.2). In channels

with hydrophobic walls, there might be no film around bubbles i.e. a special case. The film thickness, δ, is governed mostly by the Capillary number, Ca, as discussed in section 2.1. In most of the existing correlations for heat transfer in two phase slug flows, the Capillary number has no effects (see Eqs. 2.15 and 2.18 for example). In this research, the heat transfer in slug flows with and without film (in hydrophilic and hydrophobic channels) will be examined and compared to each other in section 6.2. The heat transfer in slug flows with different film thicknesses will also be simulated to determine whether the film has any potential effects on heat transfer (section 6.3).

3.2 Numerical Simulation

The non-linear Navier-Stokes equations will be solved numerically in this research using Computational Fluid Dynamics (CFD) in order to understand the hydrodynamics and heat transfer process in slug flows inside microchannels. A brief description of points of direct relevance to the computations will be provided in this section and further details of the implementation can be found in the literature. Versteeg and Malalasekera [90] provided an excellent description of the finite volume method on which the ANSYS Fluent package is based.

3.2.1 Governing Equations

The commonly solved equations in numerical simulations of slug flows are the continuity equation, the momentum equation and the energy equation (Versteeg and

Malalasekera [90]).

Conservation of mass:

$$\nabla \cdot \vec{U} = 0 \tag{3.1}$$

Conservation of momentum:

$$\rho \frac{D\vec{U}}{Dt} = \rho\vec{g} - \nabla p + \mu\nabla^2\vec{U} + \vec{F_s} \tag{3.2}$$

Conservation of energy:

$$\rho C_p \frac{DT}{Dt} = k\nabla^2 T + \dot{s} \tag{3.3}$$

The equations above should be expanded regarding the Cylindrical or Cartesian coordinate systems when the cross section is circular or non-circular, respectively.

3.2.2 Spatial Discretization

In fluid flow problems, diffusion and convection are linked and should be considered in calculation of the quantities of interest. The value of each quantity at each node depends on the values of neighbor nodes with respect to the convection and diffusion. Different schemes have been suggested for spatial discretization of the governing equations. The following schemes are used in the present research.

Second-Order Upwind Scheme

The second-order upwind scheme provides second order accuracy by using a multidimensional linear reconstruction approach [91] to evaluate quantities at cell faces. The higher accuracy of this scheme is because of using a Taylor series expansion of the cell-centered solution about the cell centroid as discussed in [92]. In the second-order upwind scheme the face value, ϕ_{face}, is calculated as follows:

$$\phi_{face} = \phi + \nabla\phi \cdot \vec{r} \tag{3.4}$$

where ϕ is the cell-centered value, $\nabla\phi$ is the gradient of ϕ in the upstream cell, and $\vec{r}$ is the center to center displacement vector from the upstream cell to the cell face. The use of upwind quantities provides a very stable scheme [90].

Power Law Scheme

The power law differencing scheme was invented by Patankar [93] in 1980. In this scheme, the flux is calculated using a polynomial expression when $0 < Pe < 10$ and is set to zero when $Pe > 10$. For example, the net flux per unit area at the west face of a control volume is evaluated as follows:

$$q_w = \begin{cases} (\rho u)_w \left[\phi_W - \frac{(1-0.1Pe_w)^5}{Pe_w}(\phi_P - \phi_W)\right], & \text{if } 0 < Pe < 10 \\ (\rho u)_w \phi_W, & \text{if } Pe > 10 \end{cases} \tag{3.5}$$

The power law differencing scheme is more accurate for one dimensional problems

as discussed in [90].

QUICK Scheme

The QUICK scheme (Quadratic Upstream Interpolation for Convective Kinetics) was introduced in 1979 by Leonard [94]. In this scheme, a three-point upstream-weighted quadratic interpolation is used for calculation of cell face values. Each face value, ϕ, is calculated using a quadratic function including two neighbor nodes and a node on the upstream side. In a uniform grid, the Quick scheme provides each ϕ_{face} as follows:

$$\phi_{face} = \frac{6}{8}\phi_{i-1} + \frac{3}{8}\phi_i - \frac{1}{8}\phi_{i-2} \tag{3.6}$$

where the nodes i and $i-1$ are the neighbor nodes and the node $i-2$ is the upstream node. The QUICK scheme is typically more accurate in structured grids aligned with the flow direction [92].

3.2.3 Temporal Discretization

The implicit temporal discretization scheme has been used in the present thesis. In this scheme, the quantity ϕ at the next time step (n+1) is evaluated as follows [92]:

$$\frac{\phi^{n+1} - \phi^n}{\Delta t} = F\left(\phi^{n+1}\right) \tag{3.7}$$

where the function F incorporates any spatial discretization, n is the current time step (t), and $n+1$ is the next time step ($t+\Delta t$). This scheme is referred to as *implicit* since

the quantity ϕ^{n+1} at the right hand side is calculated using the neighbor values at the new time step, $n+1$. The implicit temporal discretization scheme is unconditionally stable, however large time steps may lead to less accurate results.

3.2.4 Pressure-Velocity Coupling

The velocity field, $\vec{U}$, can be calculated using the discretized momentum equations if one knows the pressure field, p. Because the pressure field, p, is unknown in CFD simulations, a method for calculation p is required. The following pressure-velocity coupling algorithms have been used in the present research.

SIMPLE

The SIMPLE algorithm (Semi-Implicit Method for Pressure-Linked Equations) by Patankar and Spalding [95] is a procedure for evaluation of pressure based on a guess-and-correct method on the staggered grid arrangement. The process starts with a guessed pressure field, p^*. Then the momentum equations are solved using the p^* and the velocity components, u^* and v^*, are obtained. Then the pressure correction equation is solved which yields to the correction pressure, p'. Then the new pressure and velocity fields, p and $\vec{U}$, are calculated using p'. The process will be repeated using the new pressure field as p^*, and is continued until the answers are converged. Figure 3.1 shows the SIMPLE sequence of operations.

SIMPLEC

Van Doormal and Raithby [96] introduced the SIMPLEC (SIMPLE-Consistent)

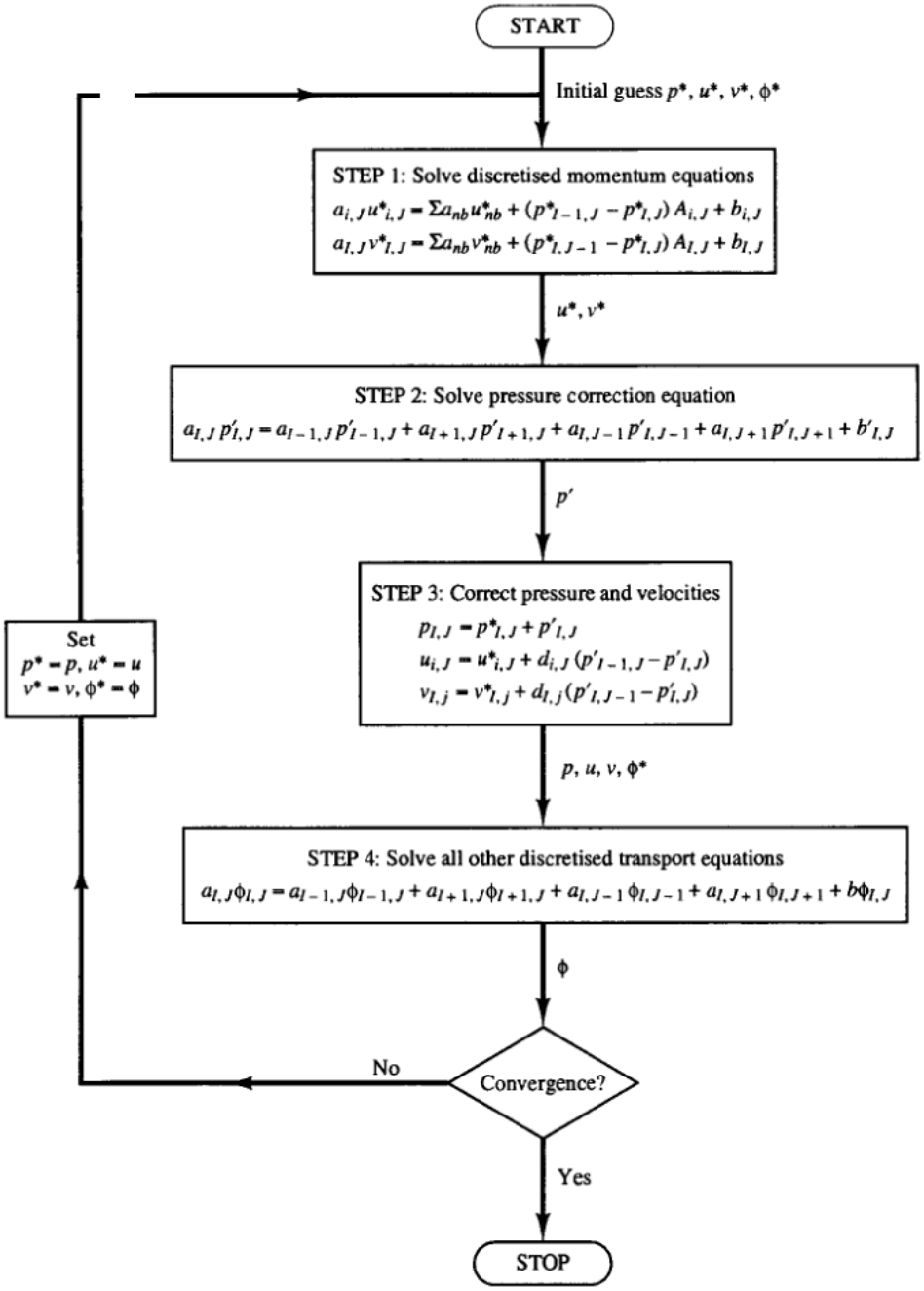

Figure 3.1: The SIMPLE algorithm, [90].

algorithm in 1984. This algorithm has the same sequence of operations as the SIMPLE algorithm. The difference between SIMPLEC and SIMPLE is that the momentum equations are modified and the terms that are less significant than those in SIMPLE are neglected.

PISO

The PISO (Pressure Implicit with Splitting of Operations) was introduced by Issa [97] in 1986. While this procedure was developed originally for non-iterative computation of unsteady compressible flows, it has also been adopted for iterative computation of steady state flows. The PISO algorithm is an extension of SIMPLE, starts with initial guess, ϕ^*, with two correction steps, ϕ' and ϕ''. Figure 3.2 shows the PISO sequence of operations.

3.2.5 Interface Capturing Methods

In the present research the volume of fluid method (VOF), developed by Hirt and Nichols [98], will be employed to model the two phase flow in microchannels. In this method, the two phases are assumed as incompressible and not penetrating each other. The advantage of using VOF method (among the available methods such as Level Set (LS)) is that the continuity equation is more precisely satisfied, as reported by Carlson et al. [99]. Selecting between the methods also depends on the software availability, for example ANSYS Fluent gives the opportunity to implement the VOF method. In the case of two phase flows, the Reynolds Transport Theorem [136], which is the basis

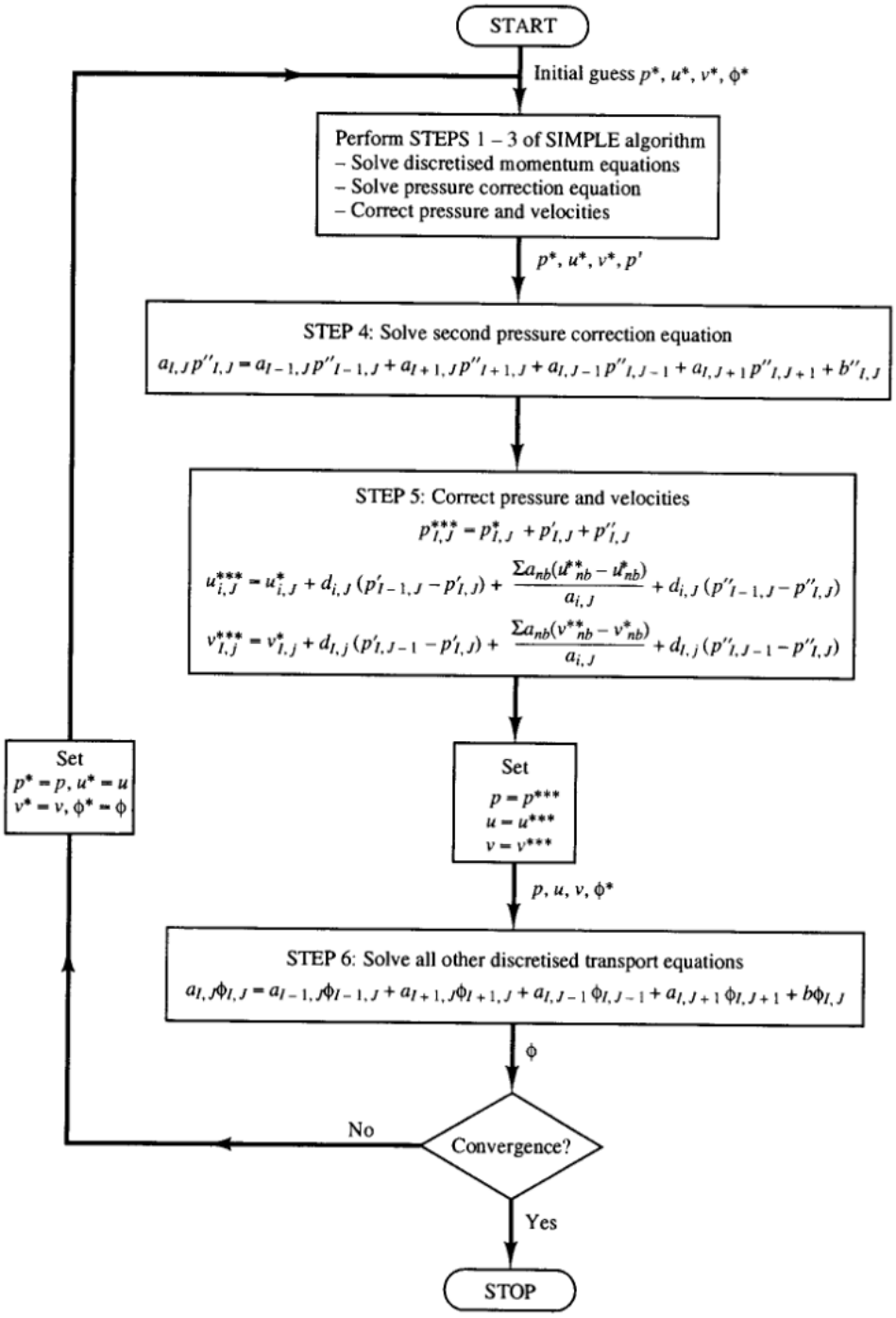

Figure 3.2: The PISO algorithm, [90].

for conservation laws, gives the following conservation equations (see Fig. 3.3):

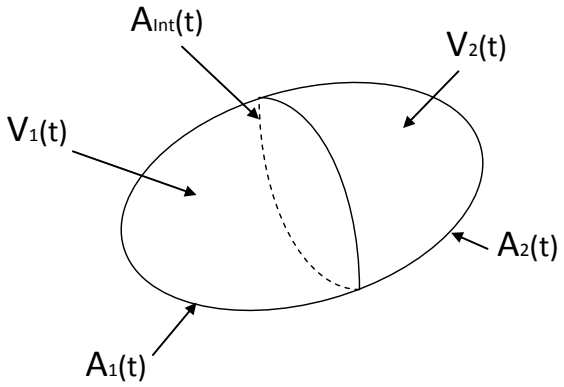

Figure 3.3: Control volume cut by an interface.

Conservation of mass (two phase):

$$\frac{d}{dt}\int_{V_1}\rho_1\,\mathrm{d}V+\frac{d}{dt}\int_{V_2}\rho_2\,\mathrm{d}V=-\int_{A_1}\rho_1U_1\cdot n_1\,\mathrm{d}A-\int_{A_2}\rho_2U_2\cdot n_2\,\mathrm{d}A \tag{3.8}$$

Conservation of momentum (two phase):

$$\begin{aligned}\frac{d}{dt}\int_{V_1}\rho_1U_1\,\mathrm{d}V+\frac{d}{dt}\int_{V_2}\rho_2U_2\,\mathrm{d}V=&-\int_{A_1}\rho_1U_1(U_1\cdot n_1)\,\mathrm{d}A-\int_{A_2}\rho_2U_2(U_2\cdot n_2)\,\mathrm{d}A\\&+\int_{V_1}\rho_1b\,\mathrm{d}V+\int_{V_2}\rho_2b\,\mathrm{d}V+\int_{A_1}n_1\cdot T_1\,\mathrm{d}A+\int_{A_2}n_2\cdot T_2\,\mathrm{d}A\end{aligned} \tag{3.9}$$

where b is the external force per unit mass and T in the stress tensor.

Conservation of energy (two phase):

$$\begin{aligned}
&\frac{d}{dt}\int_{V_1}\rho_1\left(\frac{1}{2}U_1^2+u_1\right)\,\mathrm{d}V+\frac{d}{dt}\int_{V_2}\rho_2\left(\frac{1}{2}U_2^2+u_2\right)\,\mathrm{d}V=\\
&-\int_{A_1}\rho_1\left(\frac{1}{2}U_1^2+u_1\right)U_1\cdot n_1\,\mathrm{d}A-\int_{A_2}\rho_2\left(\frac{1}{2}U_2^2+u_2\right)U_2\cdot n_2\,\mathrm{d}A\\
&+\int_{V_1}\rho_1 b\cdot U_1\,\mathrm{d}V+\int_{V_2}\rho_2 b\cdot U_2\,\mathrm{d}V+\int_{A_1}(n_1\cdot T_1)\cdot U_1\,\mathrm{d}A\\
&+\int_{A_2}(n_2\cdot T_2)\cdot U_2\,\mathrm{d}A-\int_{A_1}q_1\cdot n_1\,\mathrm{d}A-\int_{A_2}q_2\cdot n_2\,\mathrm{d}A
\end{aligned}\tag{3.10}$$

where u is the internal energy per unit mass and q in the heat flux.

In the VOF method, all the conservation equations are examined using a single value for each property in the computational cell. This way, the governing equations above, will be simplified to the Eqs. 3.1 , 3.2, and 3.3. Figure 3.4 shows a typical computational domain used in the VOF method cut by an interface. At each simulation time step, each computational cell could be filled by phase 1, phase 2, or both of them, based on the location and shape of the interface.

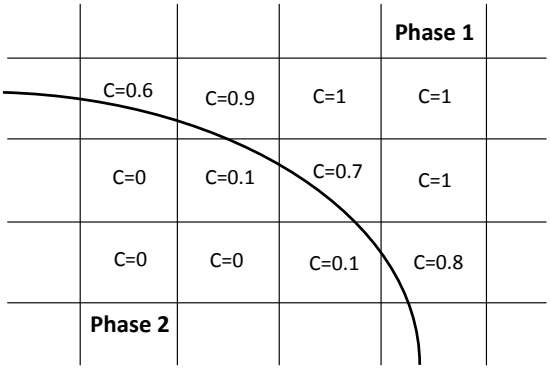

Figure 3.4: Computational domain cut by an interface in the VOF method.

The VOF method is based on the idea of a fraction function, C, which has a value between 0 and 1. Basically, C is one when the cell is full of the main phase, is zero if the cell is full of the secondary phase, and $0 < C < 1$ when the interface of two phases exists in the cell. The equation to be solved is (Hirt and Nichols [98]):

$$\frac{\partial C}{\partial t} + U.\nabla C = 0 \tag{3.11}$$

The density and viscosity in each cell will be calculated based on the volume weight fraction of each phase in the cell as follows:

$$\rho = \alpha_G \rho_G + \alpha_L \rho_L \tag{3.12}$$

and

$$\mu = \left(\frac{\alpha_G \rho_G}{\alpha_G \rho_G + \alpha_L \rho_L} \right) \mu_G + \left(\frac{\alpha_L \rho_L}{\alpha_G \rho_G + \alpha_L \rho_L} \right) \mu_L \tag{3.13}$$

In order to model the parameters like the pressure jump across the interface or the surface tension force, one needs to know the shape and curvature of the interface. The normal vector to the interface is calculated using the derivatives of the function C. In the present research, the Geometric Reconstruction Scheme [137] has been used to calculate the interface shape. This scheme uses a piecewise linear approach to represent the interface between the two fluids. In the Geometric Reconstruction Scheme, the interface is assumed to have a linear slope inside each cell, and the fluxes through the cell faces are computed using this linear shape, as shown in Fig. 3.5.

In this scheme, the position of the linear interface is calculated relative to the center of each partially filled computational cell, using the volume fraction, C, in that cell and the neighbor cells. Then fluxes through cell faces are calculated, and finally, the volume fraction, C, will be updated based on these fluxes.

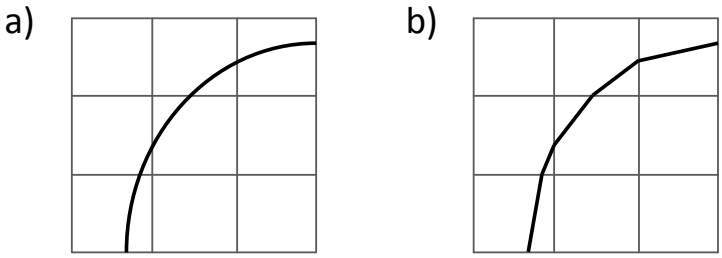

Figure 3.5: Interface shape using the Geometric Reconstruction Scheme, a) actual interface shape, b) interface shape represented by the geometric reconstruction (piece-wise linear) scheme.

The force $\vec{F_s}$ in the momentum equation (Eq. 3.2) is caused by surface tension on the interface between the two phases. This is a result of interactions between the molecules in a fluid and at the interface. Details on calculating the surface tension force, $\vec{F_s}$, has been provided by Brackbill et al. [100]. The surface tension force is important when capturing the interface shape between two immiscible fluids is of interest. This force has not been taken into account in the single phase moving frame simulation in the present research since it is a single phase simulation and interface shapes have been fixed as explained in the following sections. In the present research the surface tension force will be calculated using the Continuum Surface Force (CSF) model proposed by Brackbill et al. [100] as follows (see Fig. 3.6):

$$\vec{F_s} = \sigma k \hat{n} \left[\frac{\alpha_l \rho_l + \alpha_g \rho_g}{0.5 \left(\rho_l + \rho_g \right)} \right] \tag{3.14}$$

where $\hat{n}$ is the surface normal vector:

$$\hat{n} = \vec{\nabla} \alpha_l \tag{3.15}$$

and k is the surface curvature and calculated based on the local surface vector gradients:

$$k = - \left(\vec{\nabla} . \hat{n} \right) = \frac{1}{|\hat{n}|} \left[\left(\frac{\hat{n}}{|\hat{n}|} . \vec{\nabla} \right) |\hat{n}| - \left(\vec{\nabla} . \hat{n} \right) \right] \tag{3.16}$$

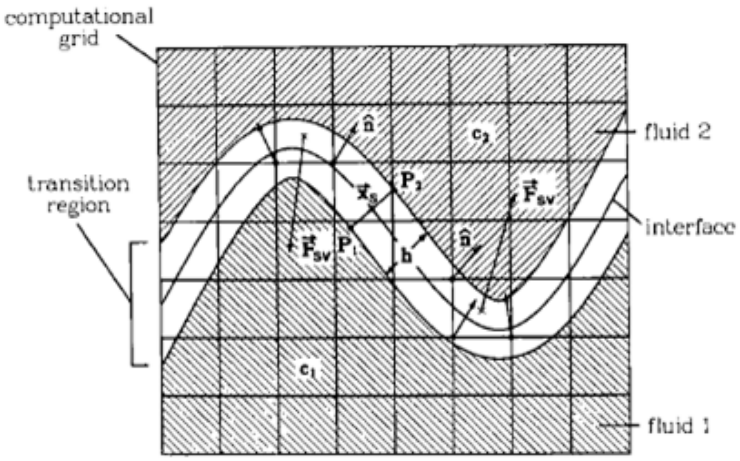

Figure 3.6: Calculation of the surface tension force on the interface [100].

3.2.6 Wall Shear Stress

The wall shear stress in Newtonian fluids under laminar flow condition is proportional to velocity gradient in normal direction to the wall as follows:

$$\tau_w = \mu \frac{\partial u}{\partial n} \tag{3.17}$$

where viscosity, μ, is based on the average fluid temperature. In three dimensional flows where there are two velocity components parallel to the wall, as shown in Fig. 3.7, the wall shear stress has two components as follows [152]:

$$\tau_{w,1} = \mu \frac{\partial u}{\partial n} \tag{3.18}$$

and

$$\tau_{w,2} = \mu \frac{\partial w}{\partial n} \tag{3.19}$$

However in symmetrical internal flows with respect to XOY the second component takes the value of zero when integrated over the surface and the wall shear stress can be calculated using Eq. 3.17.

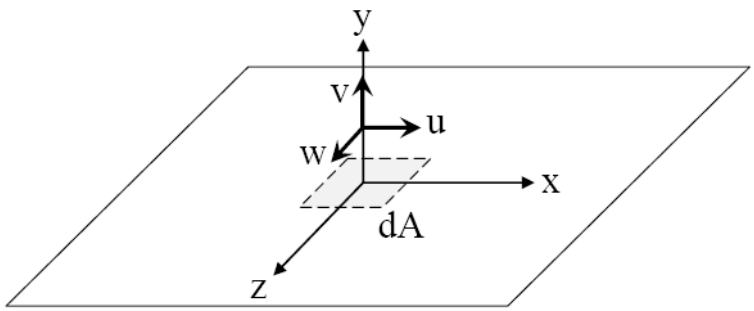

Figure 3.7: Three dimensional velocity components in boundary layer flow.

3.2.7 Wall Heat Flux

The wall heat transfer is the parameter of interest when a constant temperature is used as the thermal boundary condition. The wall heat flux can be calculated as follows:

$$q = k_f \left(\frac{\partial T}{\partial n} \right)_{wall} \tag{3.20}$$

where n is the coordinate normal to the wall.

3.3 Notes on Numerical Simulation

3.3.1 Computational Domain Extensions

Computational domains commonly used by researchers can be categorized into two main groups: fixed frames and moving frames. The numerical simulations using moving frame computational domains are also on two types: two-phase moving frame simulations and single-phase moving frame simulations. These types of computational domains are briefly reviewed in this section.

Fixed frame of reference:

A fixed frame of reference computational domain generally includes a junction and a part of microtube or microchannel after the junction. Figure 3.8a shows this type of computational domain. The two phases meet at the junction and form a two phase flow afterward. Many researchers have used the first type of computational domains to simulate two-phase flows in microtubes and microchannels (Shao et al. [37], Qian

and Lawal [65], Chen et al. [46], Kashid et al. [101], and Liu and Wang [56]). They mainly set up the computational domain as shown in Fig. 3.8a with some differences. In this way, one should consider the minimum ratio of length to diameter (L/D) or length to width (L/W) of domain to let the slugs be formed and the flow become fully developed. This ratio should be at least 40 according to the various reports (Lakehal et al. [74]). This long domain requires a large number of iterations especially when the heat transfer is of interest, therefore the CPU time will be large. Note that the domain shown in Fig. 3.8a is typical and researchers may use it with some differences. For example the geometry of junction could be a T-junction (Wu et al. [102] and Yu et al. [57]), Y-junction (Kashid et al. [101] and Kumar et al. [103]), concentric nozzles (Shao et al. [37], Chen et al. [46], and Gupta et al. [44]) or even premixed inflow (Kumar et al. [103]). Furthermore, some researchers used 3-dimensional domains (Liu and Wang [23] and Ghidersa et al. [53]) or curved domains (Kumar et al. [103]). The length of two-phase formation region shown in Fig. 3.8a depends on many conditions like the type of the two-phase flow. This length is reported up to four diameters for bubbly flow and seven diameters for slug flow (Lakehal et al. [74]).

Two phase moving frame of reference:

In the second type of computational domains only one cell is considered and the computational domain is smaller than the fixed frame domains. The unit cell generally includes one slug and two half slugs before and after. Figure 3.8b shows a two phase moving frame computational domain which has been widely used to analyze steady

state slug or bubble shape and film thickness. Some researchers have used this type of computational domains to pursue a particular part of the flow in order to increase the ease of simulation and reduce simulation time (Muradoglu et al. [104], Worner et al. [105], Taha and Cui [47, 54], and Fries and von Rohr [62]).

Single phase moving frame of reference:

This type of computational domains has been mostly used for gas-liquid two phase flows includes only the liquid slug and fixed (or flexible in few studies for bubble shape e.g. Kreutzer et al. [58] i.e. moving mesh technique) interfaces. The liquid-gas-solid contact angle can be controlled by interface shape. Figure 3.8c schematically shows this type of computational domains. Mostly a zero shear stress has been applied at the interfaces since the gas phase viscosity is much less than the liquid phase viscosity. Single phase moving frame is a simplified computational domain which gives faster results and could be appropriate when there is no liquid film around the bubbles or dry-out condition. This can be the case for hydrophobic microchannel materials. In this case there is no convective heat or mass transfer between the neighbor liquid slugs through liquid film and all the liquid is circulating inside the slugs. Baird [66], Young and Mohseni [79], and Talimi et al. [31] have used the single phase moving frame simulations to analyze convective heat transfer in discrete droplets. Rosengarten et al. [106] showed that contact angle plays a significant role on the plug dynamics and whether or not the dry-out condition appears. The domain presented in Fig. 3.8c is typical of many studies and may be used in different ways, including 3-dimensional

domains (Ghidersa et al. [53], Worner et al. [105]) and curved paths (Fries and von Rohr [62]).

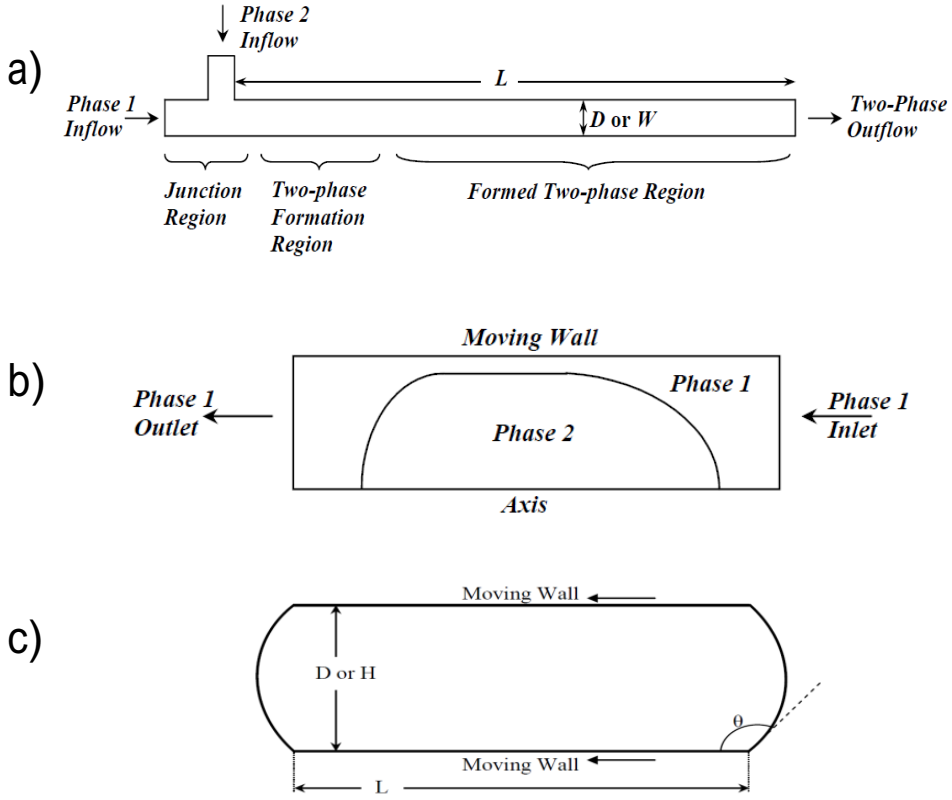

Figure 3.8: Typical computational domains frequently used for slug flow numerical simulations, a) fixed frame two phase, b) moving frame two phase, c) moving frame single phase.

3.3.2 How to Integrate Moving Frame of Reference Results?

Heat Transfer (1st approach)

In the problems with a constant wall temperature, using the dimensionless heat transfer, $q^{\star}$, is more applicable than the Nusselt number, Nu, because the Nu depends on the local mean temperature which should be calculated. Detailed discussion can

be found in Muzychka et al. [134]. On the other hand the $q^\star$ depends on the wall and inlet temperatures which are known. The dimensionless mean wall heat flux $q^\star$ is defined as follows [2]:

$$q^\star = \frac{\overline{q} D_h}{k\left(T_w - T_i\right)} \tag{3.21}$$

The dimensionless heat flux in a single phase slug flow can be expressed as a function of dimensionless axial position:

$$q^\star = g_1\left(x^\star\right) \tag{3.22}$$

where $x^\star$ is the dimensionless axial distance:

$$x^\star = \frac{x/D_h}{Pe_{D_h}} \tag{3.23}$$

Muzychka et al. [134] proposed the following compact model for the function g_1 in Eq. 3.22 for thermally developing single phase slug flow in plane channel with constant wall temperature:

$$q^\star = \left[\left(\frac{1.128}{\sqrt{x^\star}}\right)^{-11/2} + \left(\frac{1}{4x^\star}\right)^{-11/2}\right]^{-2/11} \tag{3.24}$$

As one can see in Fig. 3.9a, the dimensionless heat transfer in two phase segmented flow can be affected by three parameters other than $x^\star$. These are the liquid slug length, liquid-gas-solid contact angle, and the number of liquid slugs per unit length of the channel.

$$q^{\star} = g_2\left(x^{\star}, \frac{L_s}{D_h}, \theta, N\right) \tag{3.25}$$

where N is the number of liquid slugs and is known once L_s and P are known.

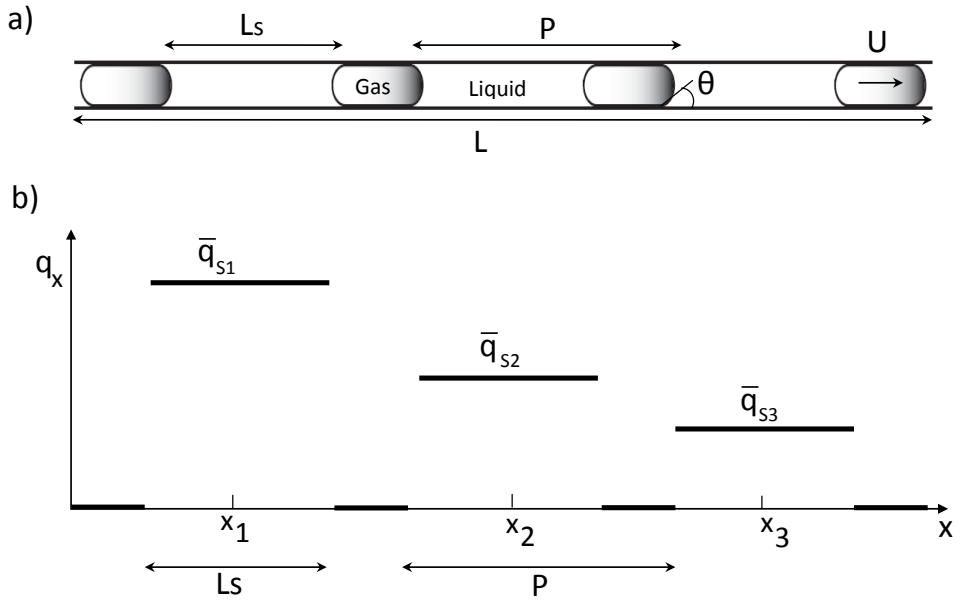

Figure 3.9: a) Slugs arrangement in a typical slug flow, b) Ideal heat flux of a typical slug flow along a channel including 3 slugs.

The local dimensionless heat transfer at the wetted area (where a liquid slug exists) is not a function of the number of slugs per unit length of the tube. Therefore:

$$q_x^{\star} = g_3\left(x^{\star}, \frac{L_s}{D_h}, \theta\right) \tag{3.26}$$

When the local heat flux is known, one could integrate along the channel length to calculate total heat flux.

$$q^{\star}_{0-L} = \frac{1}{A}\int_{0}^{L} q^{\star}_{x} dA \tag{3.27}$$

Fig. 3.9b schematically shows the dimensionless local heat transfer along the channel. In the intervals where a liquid slug exists, heat is transfered by convection and as the liquid slugs travel further, their ability to remove the heat decreases. The heat transfer into gas slugs are neglected here, due to much lower typical thermal capacities of gases compare to liquids. Knowing L_s and P, the locations of all the liquid slugs $(x_1, x_2, ..., x_N)$ are known.

According to Fig. 3.9b the total heat flux can be calculated as follows:

$$q^{\star}_{0-L} = \frac{1}{A}\sum_{n=1}^{N} \overline{q}^{\star}_{s_n} A_s \tag{3.28}$$

where A_s is the wetted area of each liquid slug and $\overline{q}^{\star}_{s_n}$ is dimensionless mean liquid slug heat transfer for each slug. Canceling the perimeter of arbitrary channel shape and assuming all of the liquid slugs are at the same length, one can find:

$$q^{\star}_{0-L} = \frac{L_s}{L}\sum_{n=1}^{N} \overline{q}^{\star}_{s_n} \tag{3.29}$$

In the present study we simulate a moving slug to find the function g_3 in Eq. 3.26. Once the function g_3 is known, the function g_2 over a known length of the duct can be calculated using the frequency of the liquid slugs.

Heat Transfer (2nd approach)

In the previous section, the mean dimensionless heat flux along each liquid slug in a two phase flow was the parameter of interest. The overall heat transfer along the channel was calculated based on the integration of all the slugs included. In the 2^{nd} approach, the overall energy balance along the channel is used. The energy balance over the entire length of the channel is:

$$Q = \dot{m} C_p (T_o - T_i) \tag{3.30}$$

where $\dot{m}$ is mass flow rate and defined as follows:

$$\dot{m} = \rho U A_c \tag{3.31}$$

in single phase flows, and:

$$\dot{m} = \rho U A_c \alpha_L \tag{3.32}$$

in two phase flows, where α_L is liquid fraction, A_c is cross sectional area, and U is the mean velocity and slug velocity in single phase and two phase flows, respectively. The convective heat transfer to the gas phase was neglected. Hence, once the exit temperature of the liquid slugs is known, one can calculate the convective heat transfer of the heat sink according to the system's liquid fraction. Note that liquid fraction is a function of L_s, P, and θ.

The dimensionless heat transfer is defined using Eq. 3.21 based on the total accepted thermal energy by a liquid slug, from entrance of to exit of the channel, instead of $\overline{q}_s$. Therefore the dimensionless heat transfer is:

$$q^\star = \frac{(Q/A_t)D_h}{k(T_w - T_i)} \tag{3.33}$$

where A_t is the traveled area of the liquid slug from the channel entrance to the present slug location. For example, A_t for a system with two parallel plates is (both sides):

$$A_t = 2x = 2Ut \tag{3.34}$$

based on the unit width of the channel. Assuming the liquid slug is about to exit the channel, A_t is equal to the total area of the channel.

3.3.3 Two-Dimensional versus Three-Dimensional Simulation

When a two-phase slug flow in a circular microtube is of interest, one can use a two-dimensional computational domain with one boundary as an axis. This is applicable in straight microtubes without any bends and curvature. The 2D assumption is not appropriate if a junction is going to be used to generate slugs in circular microtubes. Furthermore, some researchers have used 2D computational domains for two phase flows inside square or rectangular microchannels (for example Raimondi and Prat [107]). Using a 2D computational domain with or without a symmetry line means a flow between two parallel plates or through a rectangular microchannel with a very

large aspect ratio. Talimi et al. [82] focused on the differences between 2D and 3D heat transfer simulation results for a moving droplet between two parallel plates and discussed that in some cases care must be taken when using 2D simulations. Goel and Buwa [108] showed that even for a circular microtube, axisymetric simulations will not give same results compared to 3D simulation when bubble generation is of interest in gas-liquid two-phase flows. Cherlo et al. [109] compared 2D and 3D simulation results for generated slug lengths in a liquid-liquid two phase flow in a rectangular microchannel and showed that they are comparable. Generally, more computations are required when a 3D simulation is performed. Adding this to a very time consume nature of two phase flow simulations, researchers may still be interested in using 2D computational domains. This issue may be less important by developing computers in the future.

3.3.4 Boundary Conditions

In this section some important notes on inlets, walls, and exit boundary conditions have been reported. These notes might be considered when setting a numerical simulation.

Inlet and Exit:

The most used boundary condition at the inlet is specified velocity. When constant velocity is considered along with simulating a junction, care should be taken on the length of each phase path before the junction in order to maintain fully developed

velocity profile.

While using a specified pressure as the exit boundary condition has been suggested for these numerical simulations (in which there is not a fully developed flow which is the case in two phase flows, because the phases alternate and the fluid circulates inside the slugs) some researchers recently reported reliable results using outflow boundary condition (ANSYS Fluent) at the exit (Cherlo et al. [109] and Goel and Buwa [108]).

Periodic boundary conditions can be applied at inlet and outlet with some limitations when using two phase moving frame computational domains (Shao et al. [37] and van Baten and Krishna [110]). For example if heat transfer (or mass transfer) is desired, then pressure and enthalpy is not the same at inlet and outlet due to wall shear stress and heat receiving, respectively.

Walls:

At microscales, the no-slip boundary condition can be applied in most of situations. Deciding on slip or no-slip boundary condition depends on a dimensionless group which is called Knudsen number, Kn, for gas flows:

$$Kn = \frac{\lambda}{l} \tag{3.35}$$

where λ is the mean free path of the fluid molecules and l is a characteristic length e.g. hydraulic diameter. The following generalized dimensionless slip coefficient, β, is used when there is a liquid flow in a channel with a superhydrophobic surface:

$$\beta = \frac{\Lambda}{l} \tag{3.36}$$

where Λ is an arbitrary slip length . Furthermore, a slip condition, Navier slip condition, (for example Chen et al. [46]) can also be applied in order to avoid numerical clutches where there is a moving contact line. More fundamental details can be found in Renardy et al. [111] and Spelt [112].

3.3.5 Grid Resolution

In two phase numerical simulations there is a need for a very fine mesh near the walls in the computational domain in order to get accurate shear stress distribution on the wall and heat transfer from the walls to the flow or capturing the thin liquid film around the bubbles. A coarse mesh cannot predict the thin film in hydrophilic microchannels and consequently failed to give a valid shear stress and heat transfer distribution. Even if both phases touch the wall, i.e. a dry-out condition, a fine mesh is needed to simulate interface moving and/or the shear stress at the corners if a single phase moving frame technique is used. Gupta et al. [44] discussed this in detail, and suggested a criterion for mesh refinement near the wall based on film thickness, which is a function of Capillary number. Some numerical simulations using coarse mesh can be found in the literature as well. This could be accepted for purposes other than what mentioned above e.g. slug length. Qian and Lawal [65] is an example.

Talimi et al. [31] reported that very fine mesh is required at the corners in order to

reach grid independent results when the wall shear stress is of interest in single phase moving frame simulations. The grid refinement at the corner has been reported to about 0.066 % of the channel spacing in their study due to high shear stress gradients at the corners.

3.3.6 Transient Time Step Setting

A very important step in transient numerical simulation is time step sizing. The time step can be adjusted using a dimensionless group, Courant Number, which is defined as follows:

$$Co = \frac{u\Delta t}{\Delta x} \tag{3.37}$$

and is a comparison between the particle moving distance during the assumed time step and control volume dimension. A high Co value leads to an unstable numeric approach and a low Co value means a small time step size and consequently a large simulation time, so there is a need to optimize Co using appropriate time step size. Furthermore, as the mesh becomes finer the time step should be decreased as well in order to hold Co in its safe range. A typical time step order of magnitude of $1\times10^{-5}(s)$ or $1 \times 10^{-6}(s)$ has been used by the researchers (see the three-dimensional simulation performed by Cherlo et al. [109] for example).

A wiser time step adjustment is using a variable time step by implementing a fixed Courant number which is available in ANSYS Fluent (for example Gupta et al. [44]).

In this method, the time step is being modified based on critical cell size and local velocity components to hold the maximum Courant number to a fixed value.

3.4 Single Phase Slug Flow in Circular and Non-Circular Microchannels

This section provides models for single phase dimensionless heat transfer, which will be used in the present study as a reference to evaluate heat transfer enhancement using segmented (slug) two phase flows. The models presented in this section have been recently published by Muzychka et al. [134]. Figure 3.10 shows typical and simplified thermal boundary layer and velocity profile in a single phase slug flow in an arbitrary cross section. This is the case for low Prandtl number fluids such as liquid metals where thermal diffusion is much faster than momentum diffusion.

There are two different ways to calculate dimensionless wall heat transfer in internal flows when wall temperature is constant. They are based on different temperature difference calculations as follows:

- wall to inlet $T_w - T_i$
- wall to bulk mean $T_w - T_m$

The best choice is based on the application. In heat exchangers, where there are two fluid streams, the best choice is wall to bulk mean temperature difference. But in heat sinks, where there is only one fluid stream, it is more straightforward to use wall to inlet temperature difference.

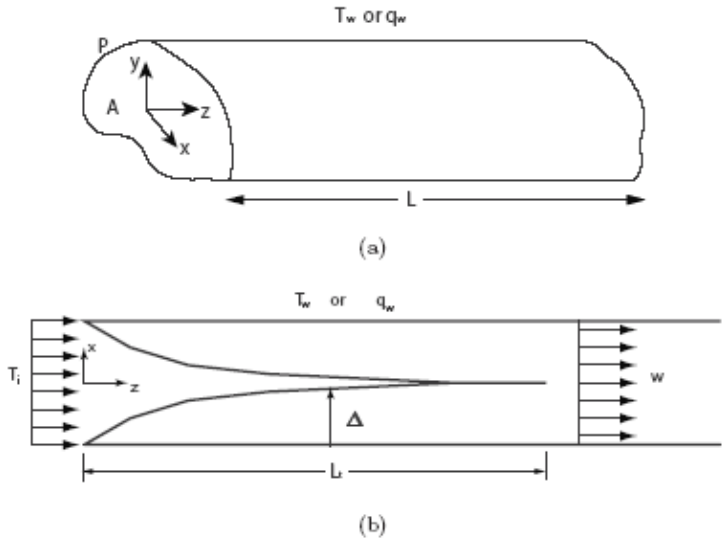

Figure 3.10: a) Graetz slug flow in an arbitrary shaped channel or duct, b) corresponding thermal boundary layer development [134].

3.4.1 Parallel Plates

In the case of single phase slug flow between parallel plates (plane channel), the mean Nusselt number for isothermal wall boundary condition based on the wall to bulk mean temperature difference, $(T_w - T_m)$, is as follows [134]:

$$\overline{Nu}_{D_h} = \left[\left(\frac{1.128}{\sqrt{L^\star}} \right)^2 + (9.87)^2 \right]^{1/2} \tag{3.38}$$

with a root mean square (rms) error of approximately 2.3%. The dimensionless heat transfer, $q^\star$, for isothermal wall boundary condition based on wall to inlet temperature difference, $(T_w - T_i)$, is [134]:

$$q^{\star} = \left[\left(\frac{1.128}{\sqrt{L^{\star}}} \right)^{-11/2} + \left(\frac{1}{4L^{\star}} \right)^{-11/2} \right]^{-2/11} \tag{3.39}$$

with a root mean square (rms) error of approximately 0.8%.

In the case of isoflux wall boundary condition, the Nusselt number based on wall to bulk mean temperature difference, $(T_w - T_m)$, is [134]:

$$Nu_{D_h} = \left[\left(\frac{0.886}{\sqrt{z^{\star}}} \right)^{12/5} + (12)^{12/5} \right]^{5/12} \tag{3.40}$$

with a root mean square (rms) error of approximately 3.8%. The Nusselt number for isoflux wall boundary condition based on wall to inlet temperature difference, $(T_w - T_i)$, is [134]:

$$Nu_{D_h} = \left[\left(\frac{0.886}{\sqrt{z^{\star}}} \right)^{-3} + \left(\frac{1}{4z^{\star}} \right)^{-3} \right]^{-1/3} \tag{3.41}$$

with a root mean square (rms) error of approximately 1.3%.

3.4.2 Circular Microchannels

In the case of single phase slug flow inside circular channels, the mean Nusselt number for isothermal wall boundary condition based on the wall to bulk mean temperature difference, $(T_w - T_m)$, is as follows [134]:

$$\overline{Nu}_D = \left[\left(\frac{1.128}{\sqrt{L^{\star}}} \right)^{2} + (5.783)^{2} \right]^{1/2} \tag{3.42}$$

with a root mean square (rms) error of approximately 2.5%. The dimensionless heat transfer, $q^\star$, for isothermal wall boundary condition based on wall to inlet temperature difference, $(T_w - T_i)$, is [134]:

$$q^\star = \left[\left(\frac{1.128}{\sqrt{L^\star}} \right)^{-5/2} + \left(\frac{1}{4L^\star} \right)^{-5/2} \right]^{-2/5} \tag{3.43}$$

with a root mean square (rms) error of approximately 3.8%.

In the case of isoflux wall boundary condition, the Nusselt number based on wall to bulk mean temperature difference, $(T_w - T_m)$, is [134]:

$$Nu_D = \left[\left(\frac{0.886}{\sqrt{z^\star}} \right)^2 + (8)^2 \right]^{1/2} \tag{3.44}$$

with a root mean square (rms) error of approximately 4.4%. The Nusselt number for isoflux wall boundary condition based on wall to inlet temperature difference, $(T_w - T_i)$, is [134]:

$$Nu_D = \left[\left(\frac{0.886}{\sqrt{z^\star}} \right)^{-2} + \left(\frac{1}{4z^\star} \right)^{-2} \right]^{-1/2} \tag{3.45}$$

with a root mean square (rms) error of approximately 2.2%.

3.4.3 Square Microchannels

In the present research, heat transfer in two phase slug flows inside square microchannels have been studied numerically. In the case of single phase slug flow inside square channels, the mean Nusselt number for isothermal wall boundary condition based on

the wall to bulk mean temperature difference, $(T_w - T_m)$, is as follows [134]:

$$\overline{Nu}_{D_h} = \left[\left(\frac{1.128}{\sqrt{L^\star}} \right)^2 + (4.935)^2 \right]^{1/2} \tag{3.46}$$

with a root mean square (rms) error of approximately 2.42%. The dimensionless heat transfer, $q^\star$, for isothermal wall boundary condition based on wall to inlet temperature difference, $(T_w - T_i)$, are [134]:

$$q^\star = \left[\left(\frac{1.128}{\sqrt{L^\star}} \right)^{-2.3} + \left(\frac{1}{4L^\star} \right)^{-2.3} \right]^{-1/2.3} \tag{3.47}$$

with a root mean square (rms) error of approximately 4.54%.

4 TWO DIMENSIONAL MOVING FRAME OF REFERENCE SIMULATION

Moving slugs between parallel plates and inside circular channels are considered in this chapter using two dimensional moving frame of reference simulations. The heat transfer process, integration approaches for moving frame simulations, and effects of slug length and contact angle on heat transfer are discussed. The assumption of similar advancing and receding contact angles is also assessed with a direct comparison with simulation results with respect to real dynamic contact angles.

4.1 Moving Slugs Between Parallel Plates

In this section, the shear stress and heat transfer of a moving liquid slug for constant wall temperature are studied numerically. The problem is considered as a non-boiling 2D problem, and simulations are carried out for different slug lengths and interface shapes.

4.1.1 Numerical Modeling

Fig. 4.1 schematically shows geometry of the computational domain used in this section. H is the distance between the plates and has been fixed to $1(mm)$. θ is the contact angle of the liquid phase and the wall. The advancing and receding contact angles are generally deferent and depend on the flow circumstances [132]. In this section, the advancing and receding contact angles have been assumed to be equal due to lack of information and correlations for dynamic contact angle versus fluids and flow conditions between parallel plates. The effects of the difference between advancing and receding contact angles on heat transfer will be analyzed in the next section. Concave and convex interface shapes have been considered using $\theta = 45^o, 60^o, 90^o, 120^o$.

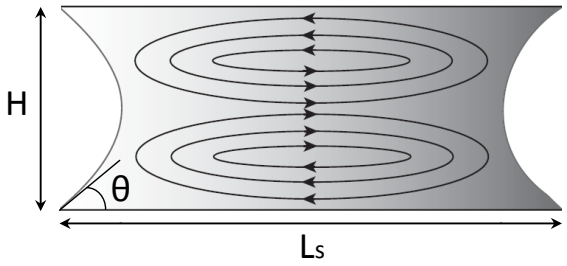

Figure 4.1: Schematic of the domain used in simulation of moving slugs between parallel plates.

In the real situations, the slug moves with the nominal mean velocity U. In the present model, the slug is considered as a stationary slug and the top and bottom walls are considered as moving walls with the velocity of $-U$. A constant velocity of -0.1 (m/s), no-slip condition, and constant temperature of 350 (K) are applied to the top and bottom walls. Zero shear stress and zero heat flux are applied to the

front and rear interfaces in order to simulate interface between liquid and gas. The model is solved as a steady state flow in order to gain a fully developed hydrodynamic solution showing internal circulations. After that, the energy equation is solved using unsteady solver and thermal boundary conditions are applied. The initial temperature of the fluid is set to 300 (K). The fluid properties are assumed to be constant at the temperature of 325 (K) i.e. average of the initial and the wall temperature. These properties are as follow:

- $\rho = 987(kg/m^3)$
- $\mu = 0.000528(kg/m.s)$
- $k = 0.645(W/m.K)$
- $C_p = 4182(J/kg.K)$
- $Pr = 3.42$

The Reynolds number based on these properties and the hydraulic diameter is 374, much lower than the critical Reynolds value of turbulent flow. The critical value has been reported to 2300 for continuous flows [32] or 1000 for a single droplet [33] so, the flow regime is considered laminar. The gravitational effects are neglected based on the Bond number limit reported by Bretherton [43] i.e. 0.842. The Bond number is equal to 0.034 in this section.

4.1.2 Grid Independency and Validation Study

A structured mesh is used in this section. The grid resolution is increased in the vicinity of the walls and interfaces until the results became independent of the grid size. Figure 4.2 shows the final grid at the corner generated for a liquid slug with $L_s/H = 2$ and $\theta = 60^o$. The coarsest and finest mesh sizes are $0.025H$ and $0.00066H$, respectively.

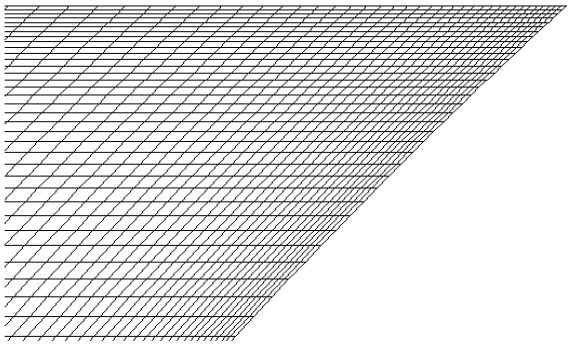

Figure 4.2: Generated mesh at the corner of a liquid slug with $L_s/H = 2$ and $\theta = 60^o$.

It is expected that as the length of the liquid slugs increases, the velocity profile at the middle vertical line approaches to the analytical velocity profile of the Poiseuille flow between two parallel plates, with the maximum of $1.5U$ at the center. Figure 4.3 shows the numerical results are accurate enough with the mean and maximum errors of 0.053% and 0.056%, respectively.

As another validation test, the simulation was conducted for the domain with $L_s/H = 1$ and $\theta = 90^o$ using the same conditions of the classic lid driven cavity problem at Re=100 and the results showed a very good agreement with the results

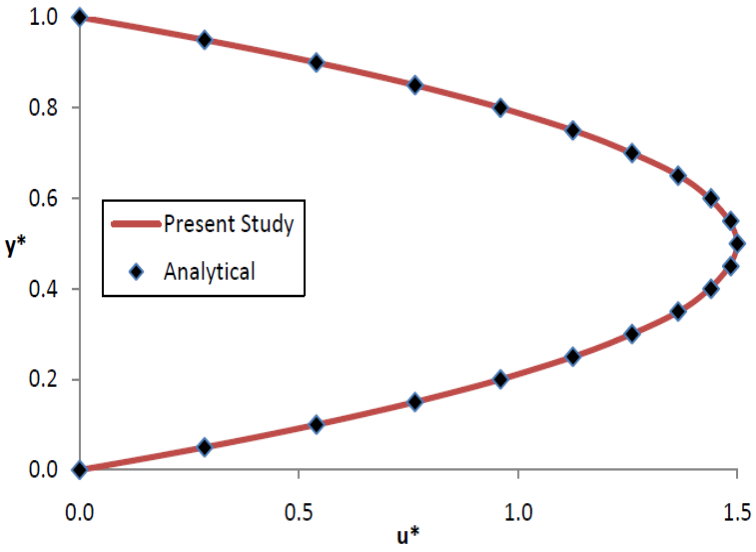

Figure 4.3: Comparison between the velocity profile at the middle vertical line of the liquid slug and the analytical velocity profile.

of Ghia et al. [133]. Figure 4.4 compares the horizontal component of the velocity at the middle vertical line and the results published by Ghia et al. [133].

4.1.3 Heat Transfer Prediction

Fig. 4.5 shows the streamlines inside a liquid slug with $L_s/H = 3$ and $\theta = 45^o$ and the ratio of local dimensionless shear stress to Poiseulle flow dimensionless shear stress along the contact region. As one can see, the core of the circulations are not located at the middle, but near the rear interface. Similar flow patterns were reported by Oprins et al. [80], Baird [66] for parallel plates and Mehdizadeh et al. [63] for circular tubes. The local shear stress increases dramatically in the front and rear regions which is the effect of two-dimensional flow in the corners. The local minimum represents the location of the circulation eye.

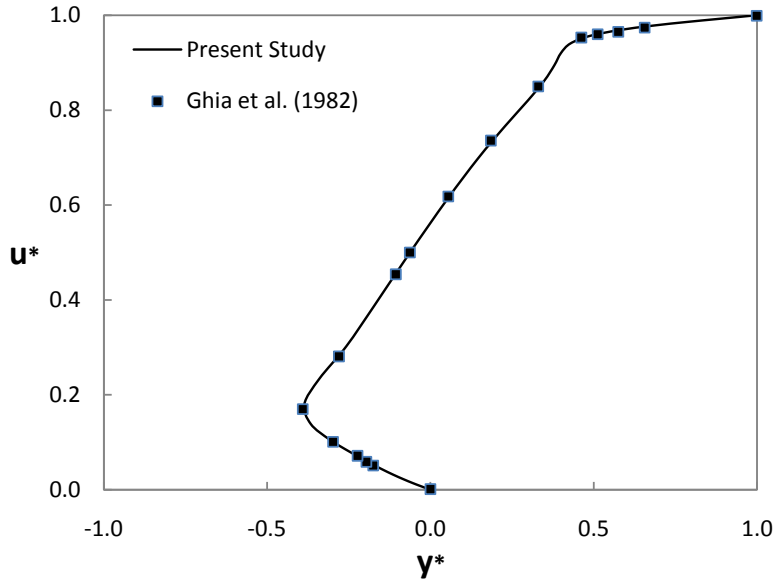

Figure 4.4: Comparison between the horizontal component of the velocity at the middle vertical line and the results of Ghia et al. [133], $L_s/H = 1$, $\theta = 90^o$, $Re = 100$.

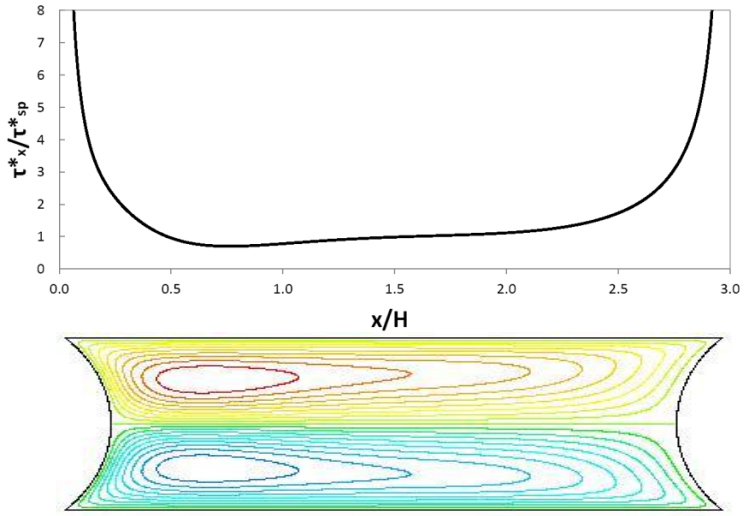

Figure 4.5: Shear stress distribution along contact area (top) and streamlines (bottom) of a moving slug between parallel plates, $L_s/H = 3$ and $\theta = 45^o$.

Fig. 4.6 shows the effect of contact angle on the local wall shear stress distribution. As can be realized from the location of the minimum, the circulation eye goes toward the middle of the slug as θ decreases. Besides, with a decrease in θ, the shear stress increases in the front and rear regions, so one can expect larger average shear stress for two phase flows with concave interface shape. The average shear stress along the slug is shown in Fig. 4.7 for different slug lengths and contact angles. According to Fig. 4.7, shorter slugs and slugs with smaller contact angles lead to greater shear stress at the wall.

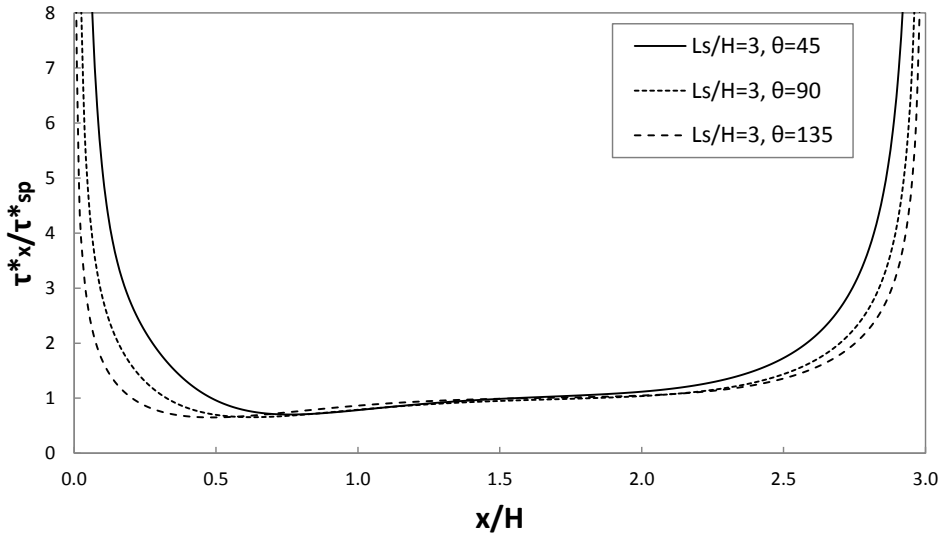

Figure 4.6: The effect of contact angle on the normalized shear stress distribution along contact area of moving slugs between parallel plates, $L_s/H = 3$.

Heat Transfer (1st approach from section 3.3.2):

Fig. 4.8 shows how heat is transferred by the twin circulations toward the center of the slug and fresh water is transferred towards the wall. In early steps, Fig. 4.8a,

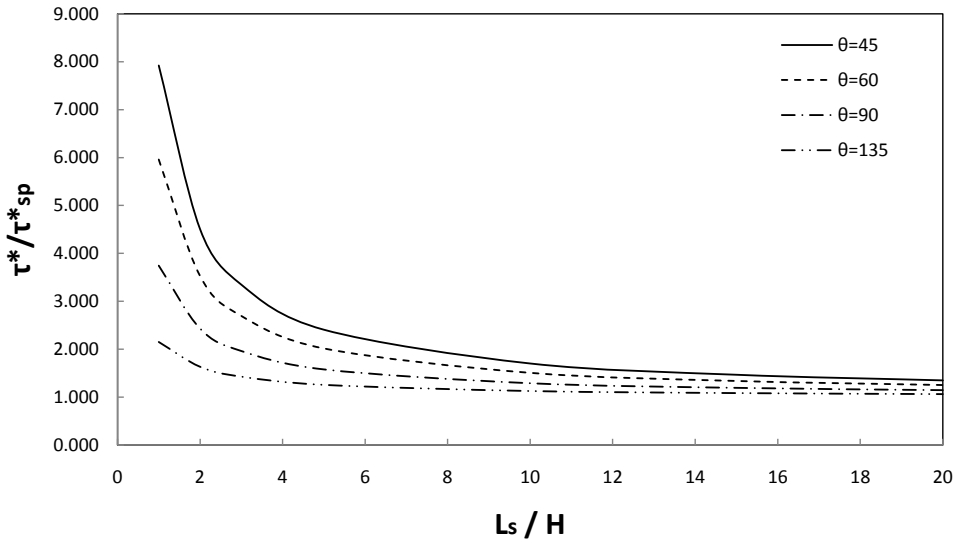

Figure 4.7: Average shear stress for moving slugs with different lengths and contact angles.

the thermal boundary layer is very thin and the dominant heat transfer process is heat diffusion into the slug normal to the wall. In Fig. 4.8b, the thermal boundary layer has just started to grow and some heat is transferring toward the center close to the receding interface, due to the circulation. In Figs. 4.8c and 4.8d, the center feels the heat transfer process after accepting the heated liquid. Finally, Fig. 4.8e is after one complete circulation, and all the liquid is now feeling the heat transfer.

The distribution of local heat flux along the contact area is shown in Fig. 4.9 for a moving slug with $L_s/H = 3$ and $\theta = 45^o$ at different times. The graph has the same time steps as Fig. 4.8 and enables one to see what exactly happens. As shown, there is a peak near the front corner where the thermal boundary layer is thin, because of refreshing with fresh liquid. At early steps of the process when fresh liquid touches

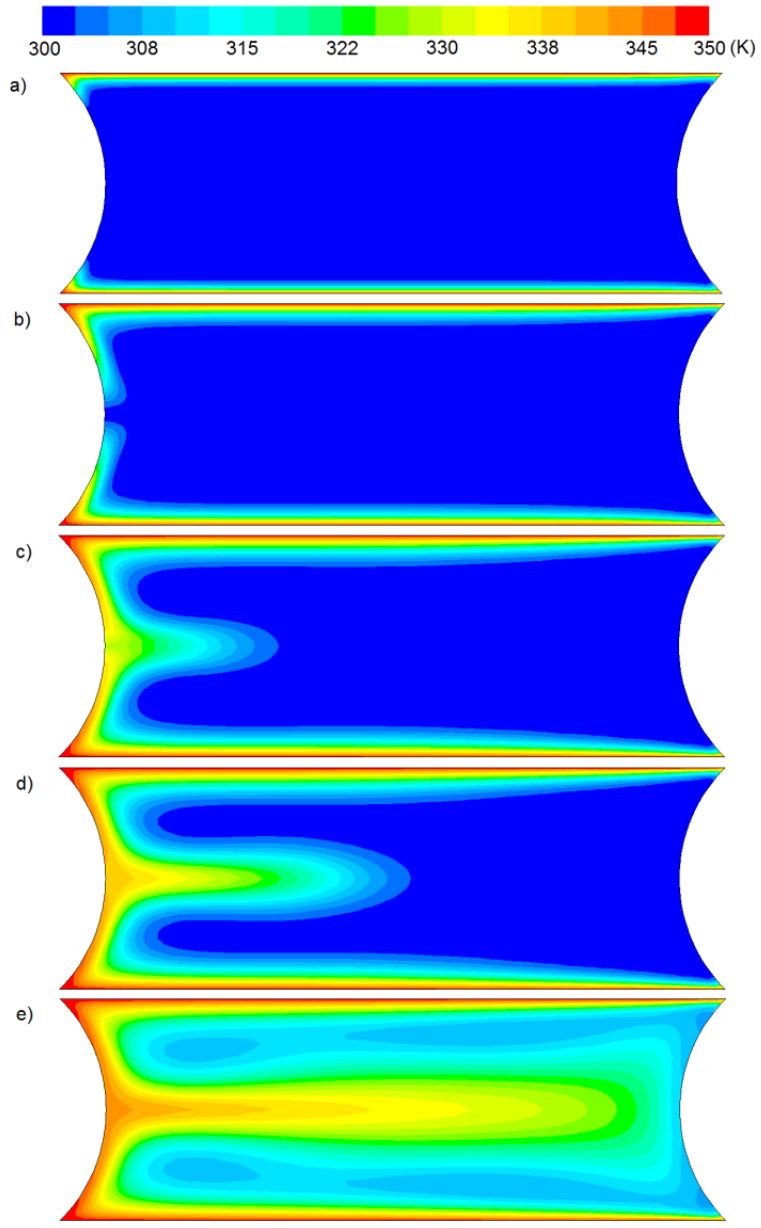

Figure 4.8: Temperature distribution in a moving slug between two parallel plates with $L_s/H = 3$ and $\theta = 45^o$ at different times: a)t=0.0025s (x=0.25mm), b)t=0.0075s (x=0.75mm), c)t=0.0175s (x=1.75mm), d)t=0.0275s (x=2.75mm), e)t=0.0775s (x=7.75mm).

the wall, the heat transfer is almost constant along the slug due to almost uniform thermal boundary layer (except tiny regions near the front and rear interfaces), and the prominent heat transfer phenomenon is heat diffusion into the liquid normal to the wall. As the slug travels further, the heated liquid is transferred toward the center and fresh liquid is replaced by the circulation (Fig. 4.8), the heat transfer rate decreases overall due to thickening of the thermal boundary layer, and a slope appears in the graphs which reveals the convection heat transport phenomenon.

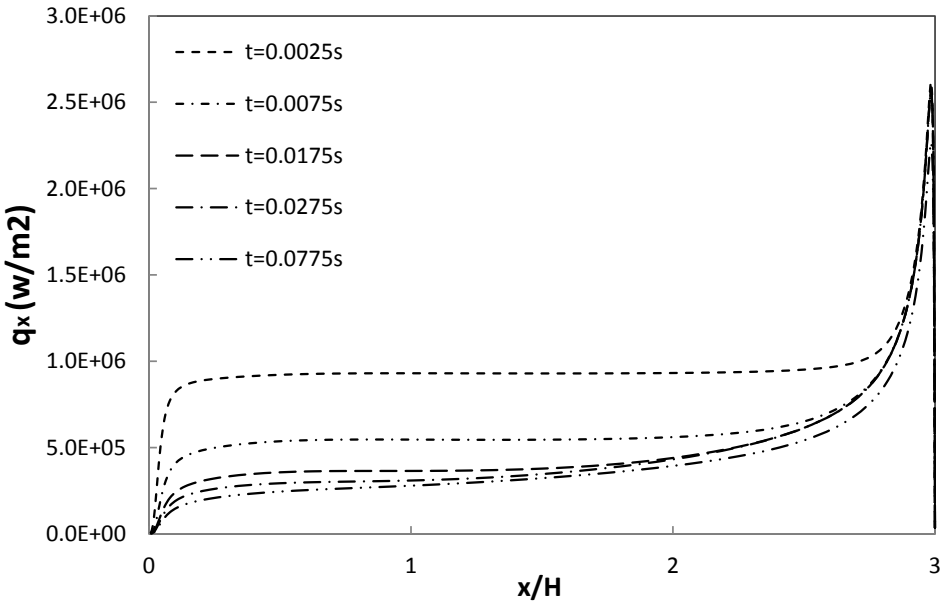

Figure 4.9: Distribution of local heat transfer rate (W/m^2) along the contact area of a moving slug with $L_s/H = 3$ and $\theta = 45^o$ at different times (same as Fig. 4.8).

According to Eq. 3.26, simulations were carried out for different slug lengths from $L_s/H = 1$ to 5 and contact angles from $\theta = 45^o$ to $\theta = 135^o$ to include the effects of these parameters on the heat transfer process.

Fig. 4.10 shows the dimensionless mean liquid slug heat transfer, $\overline{q}_s^\star$, for slugs with the same lengths ($L_s/H = 3$) but different contact angles of $45^o, 60^o, 90^o, 135^o$. As shown, the heat removal capacity decreases gradually in the entrance region, and then starts a fast decrease afterward. This dramatic decrease is due to the fact that the slugs are becoming thermally saturated. In other words, the mean temperature of the slug approaches the wall temperature. The point in which the two streams meet is around $x^\star = 0.01$. This means the distance of about 25 (mm) for simulation conditions of this section, and may include 4 or 5 slugs assuming a void fraction of 0.5 approximately (a pitch twice of the slug length). This distance has another meaning as well. Due to the slug's dimensions, each slug completes its third circulation before being thermally saturated. As it was expected, a slug with higher contact angle (more convex interface shapes) has a higher heat removal capacity in the region where convection is dominant, due to its greater mass.

Figures 4.11 and 4.12 present the dimensionless heat flux for various slug lengths with contact angles of 45^o and 135^o, respectively. Overall, shorter slugs show higher heat removing performance rather than longer slugs before becoming thermal saturated. One should notice that this does not necessarily mean that slug flows with shorter slug lengths have more heat removing capacity, but the pitch (liquid fraction) plays a prominent role here. There is also an abrupt decrease in heat transfer for short slugs at around $x^\star = 0.001$ as can be observed from Fig. 4.11. The reason is at this position, the first circulation is just finished and the front section of thermal boundary

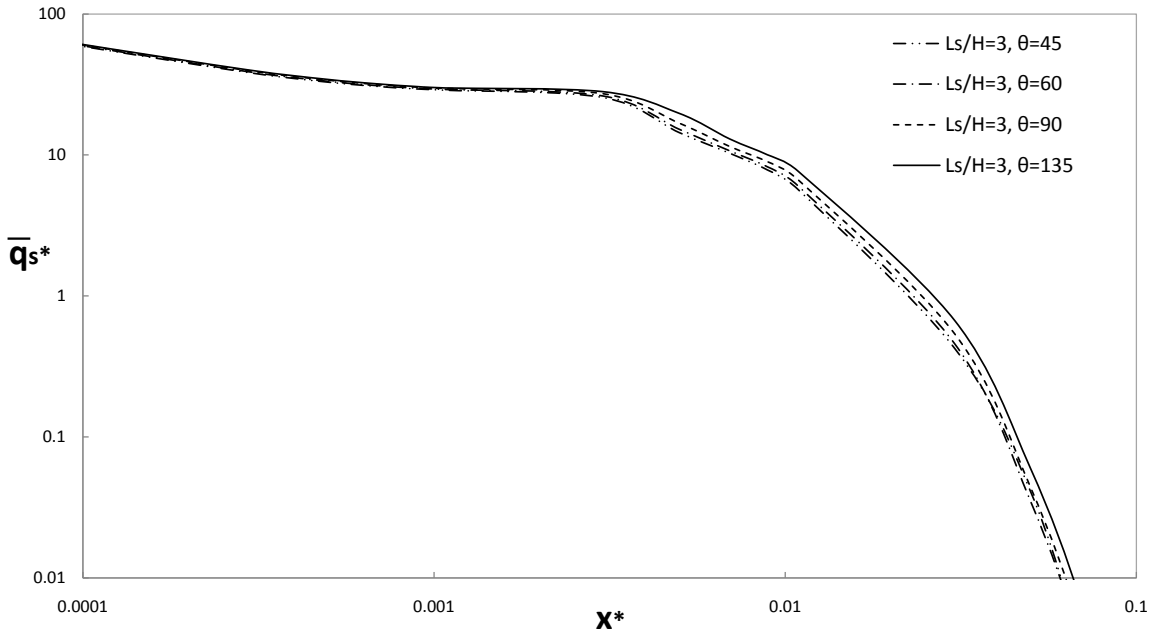

Figure 4.10: Dimensionless mean liquid slug heat transfer for slugs with the same lengths ($L_s/H = 3$) and different contact angles ($45^o, 60^o, 90^o$, and 135^o).

layer is now experiencing warm liquid from the previous circulation. These graphs can be used to read the dimensionless mean liquid slug heat flux, $\overline{q}_s^\star$, at the location of each liquid slug (the function g_3 in Eq. 3.26) and integrate over the channel length with respect to the total number of liquid slugs and the pitch (see Eq. 3.29 and Fig. 3.9).

Heat Transfer (2nd approach)

Figures 4.13 and 4.14 show the dimensionless heat transfer for liquid slugs based on the total accepted thermal energy by slugs with different lengths (from $L_s/H = 1$ to 5) and the same contact angle (45^o and 135^o, respectively). The horizontal axis is dimensionless channel length, $L^\star$. As can be seen, shorter slugs can accept more heat

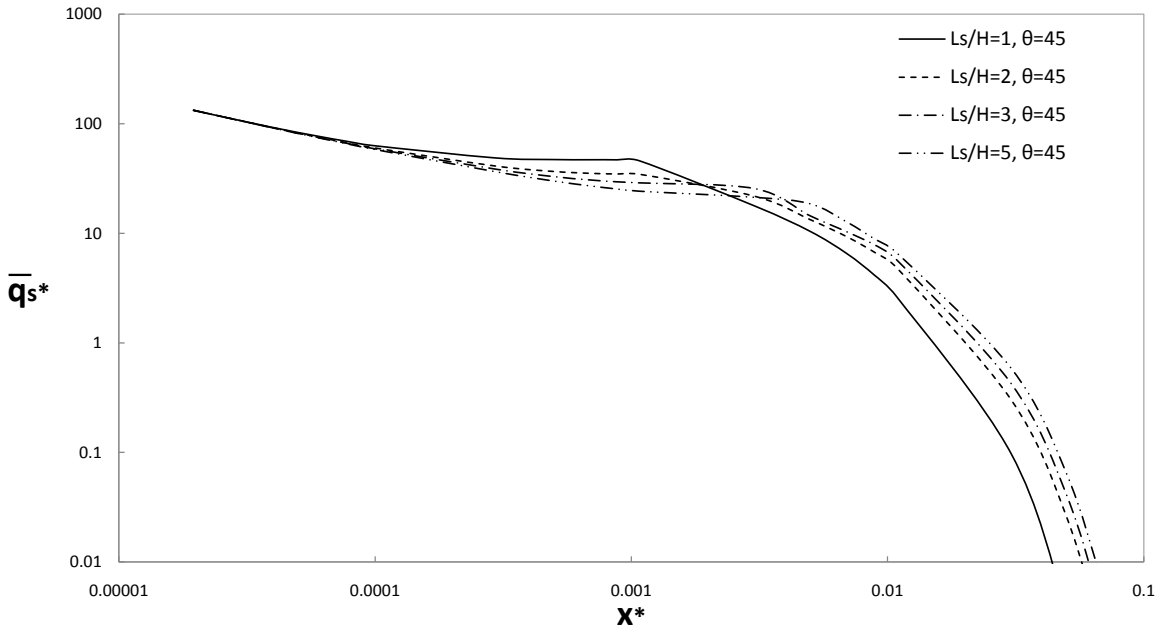

Figure 4.11: Dimensionless mean liquid slug heat transfer for slugs with different lengths (from $L_s/H = 1$ to 5) and the same contact angle (45^o).

from the channel walls compare with single phase Poiseuille flow before being thermally saturated. The thermal behavior of liquid slugs match on the single phase slug flow (Eq. 3.24) for short duct asymptote. The liquid slugs show more heat removal capacity after a while of traveling which is because of the internal circulations. shorter slugs, show better performance. As shown, the asymptotic thermal behavior of liquid slugs are not same as in single-phase slug flow for all of the liquid slugs. The dimensionless heat transfer read from figures 4.13 and 4.14 can be used to calculate exit temperature of the slugs and convective heat transfer using Eq. 3.30 and Eq. 3.33, respectively. As can be seen, using the present approach to calculate thermal performance of the heat sink is straightforward as compared with the 1^{st} approach, because it only needs

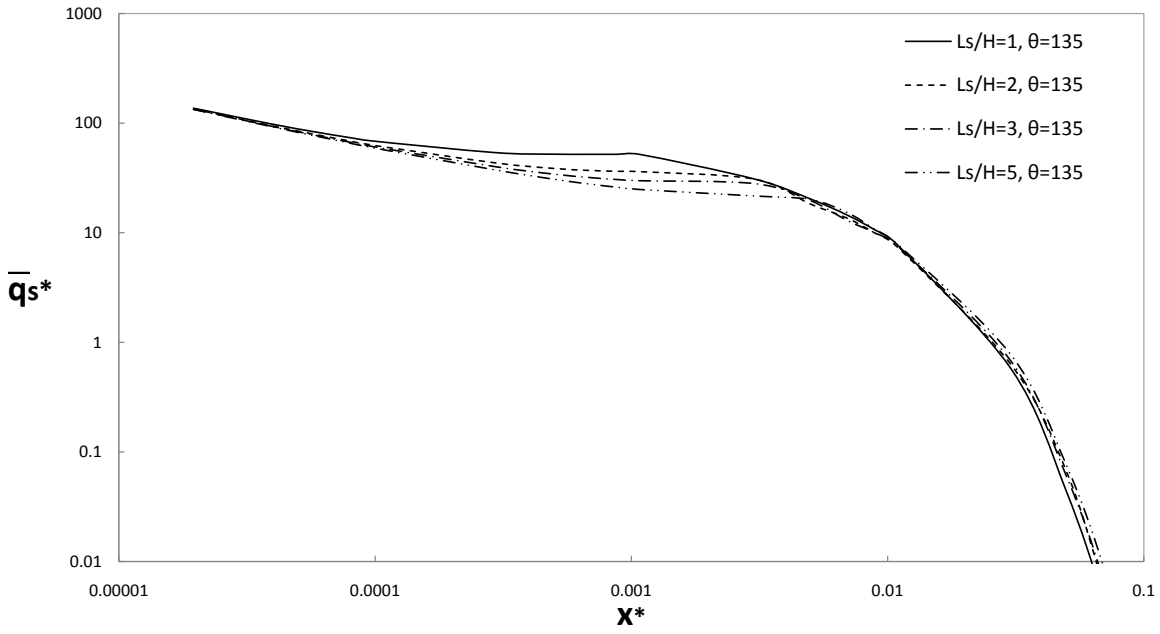

Figure 4.12: Dimensionless mean liquid slug heat transfer for slugs with different lengths (from $L_s/H = 1$ to 5) and the same contact angle (135^o).

reading one data point from the graphs.

4.1.4 Assessment of the Two Integration Approaches

So far, two approaches (section 3.3.2) have been used for presenting the dimensionless heat transfer for segmented flow. An example can be used in order to compare these two approaches. The following values have been assumed in this section:

- $L = 18mm$
- $L_s = 3mm$
- $P = 6mm$
- $H = 1mm$

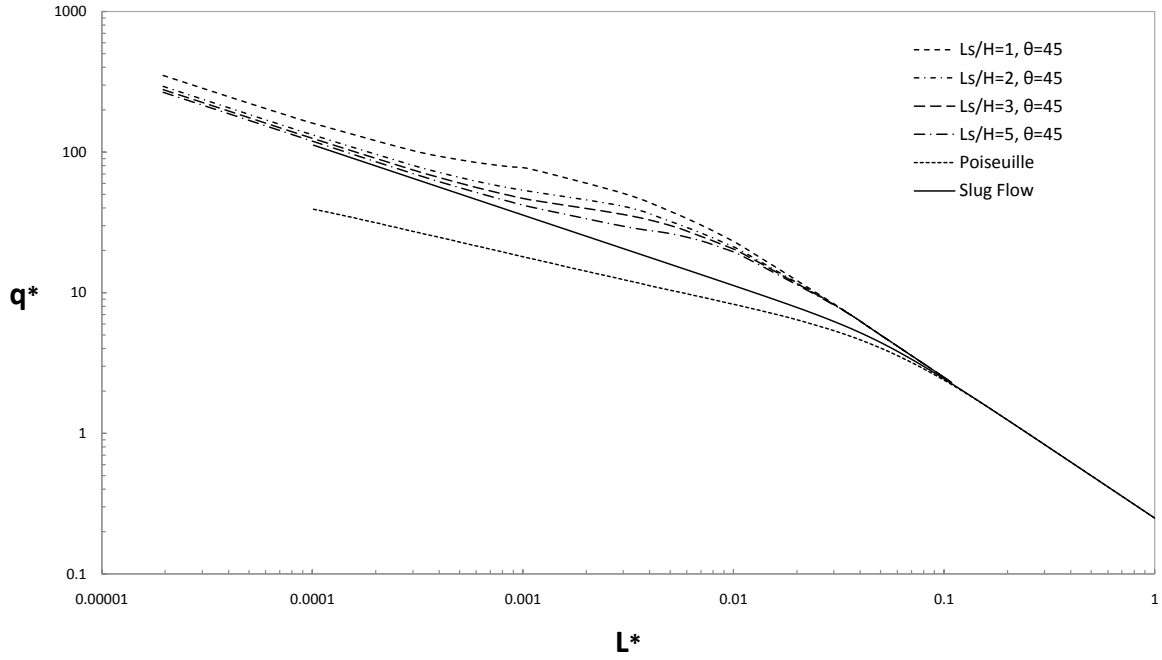

Figure 4.13: Dimensionless heat transfer for slugs with different lengths (from $L_s/H =$ 1 to 5) and the same contact angle (45^o).

- $\theta = 90^o$

Based on the above information $\alpha_L = 0.5$. Other parameters including thermophysical, transport, and flow parameters are the same as what have been defined in the section 4.1.1.

If one wants to implement the first approach, the exact locations of all of the liquid slugs are important, so different situations exist. In the present example three scenarios have been assumed as shown in Fig. 4.15. In the first scenario, the new liquid slug has just entered the channel, and in the last scenario the oldest liquid slug is about to exit the channel. The liquid slugs are in midways in the second scenario. Greatest heat transfer may be expected in the first scenario and lowest heat transfer

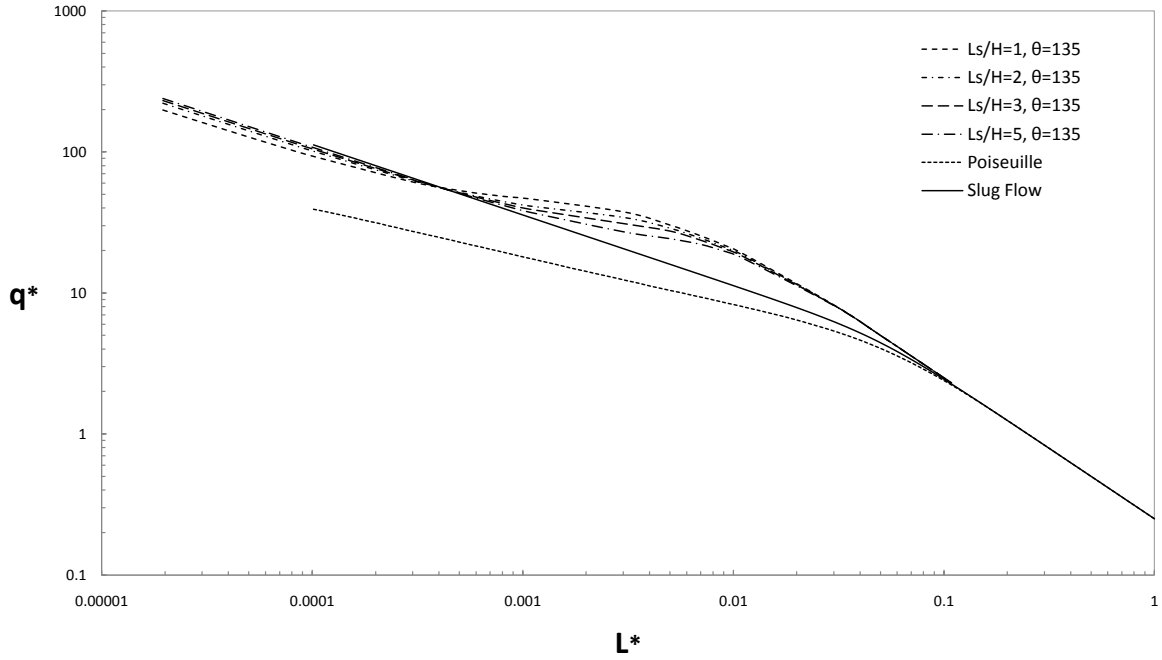

Figure 4.14: Dimensionless heat transfer for slugs with different lengths (from $L_s/H =$ 1 to 5) and the same contact angle (135^o).

rate in the last scenario, since as slugs proceed inside the channel they become more thermally saturated. In order to use the first approach, the dimensionless mean liquid slug heat flux, $\overline{q}_s^\star$, at each location must be read from the plots, and then the integral in Eq. 3.29 is needed to calculate total dimensionless heat transfer, $q^\star$, in the channel. Table 4.1 presents the results.

As presented in Table 4.1, one can expect the dimensionless heat transfer, $q^\star$, oscillating between 12.676 and 10.502. Total heat flow, $\overline{q}$, can be calculated now using Eq. 3.21. As can be seen nine datapoints have been read from the $\overline{q}_s^\star$ plots, and finally a range of heat transfer was calculated. Based on the total length of the channel, hydraulic diameter, and Pe_{D_h} one can use the plots of the 2^{nd} approach and read the

value of $q^\star = 24.341$ for $L_s/H = 3$ and $\theta = 90$. Knowing the liquid fraction, $\alpha_L = 0.5$, the total dimensionless heat transfer will be 12.171 which falls well in the previous range concluded from the 1^{st} approach. It is obvious that the 2^{nd} approach is more straightforward because only one datapoint has to be read from the plots.

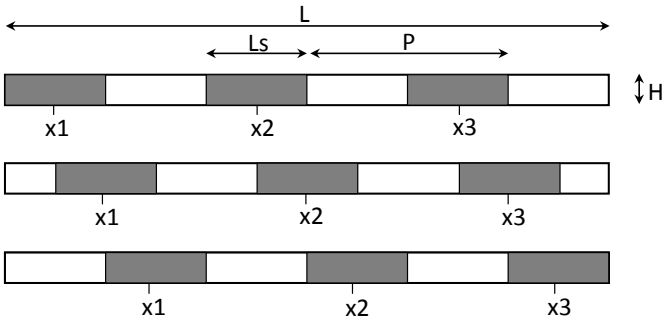

Figure 4.15: Different scenario assumptions used for the example (top: first scenario, middle: second scenario, bottom: third scenario).

Table 4.1: Dimensionless mean liquid slug heat flux, $\overline{q}^\star_s$, and dimensionless heat transfer, $q^\star$, for the example of Fig. 4.15.

	$1^{st} scenario$	$2^{nd} scenario$	$3^{rd} scenario$
$\overline{q}^\star_{s1}$	32.779	29.467	28.737
$\overline{q}^\star_{s2}$	27.278	24.569	21.464
$\overline{q}^\star_{s3}$	16.001	14.412	12.815
$q^\star$	12.676	11.408	10.502

4.1.5 Summary

In this section, the shear stress and heat transfer for moving liquid slugs between parallel plates (plane channels) under constant wall temperature boundary condition were studied numerically and the effects of slug length and contact angle were focused.

It was shown that the increase in shear stress is due to two-dimensional flow at the slug corners, where the triple interface line exists, caused by circulations. Further, the shear stress decreases with an increase in contact angle or slug length. It was also shown that heat flux is higher in shorter slugs, but one should evaluate the thermal capacity of the heat sink by calculating the overall heat flux including the effects of liquid fraction. A second approach was assessed as an alternative, and it was shown that evaluating the thermal cooling capacity is more straightforward using the 2^{nd} approach, because there is a need for reading only one data point from the relevant plots.

4.2 Moving Slugs Inside Circular Tubes

As stated by Eq. 3.26, the total dimensionless heat transfer, $q^{\star}$, in two phase slug flows depends on $x^{\star}$, slug length, and contact angle. Throughout this research, the dimensionless heat transfer has been (and will be in the next chapters) reported versus dimensionless channel length, $L^{\star}$, for different slug lengths and contact angles. However, as mentioned in section 4.1.1, there are not enough correlations to predict advancing and receding contact angles for different flow conditions, but Circular microchannel is an exception. Yu et al. [147] have reported dynamic contact angles (both advancing and receding) and triple line pressure drop for moving liquid slugs in hydrophobic circular microchannels, where both gas and liquid touch the microchannel wall. They reported enough information for predicting advancing and receding contact angles,

θ_A and θ_R, for a moving slug when Reynolds number is known. For this geometry only, difference between advancing and receding contact angles has been considered, and computational domains have been adjusted for different Reynolds number. The Reynolds number considered in this section are 100 and 500. Furthermore, the effects of neglecting dynamic contact angels on heat transfer will also be focused in this section.

Yu et al. [147] has defined the total pressure drop in a two phase slug flow as a combination of three components. As shown in Fig. 4.16, these components are liquid slug pressure drop, ΔP_{LS}, gas phase pressure drop, ΔP_{GS}, and the pressure drop due to motion of the triple line, ΔP_{TL}. The last component, ΔP_{TL}, is a function of advancing and receding contact angles as shown by Eq. 4.1 [147].

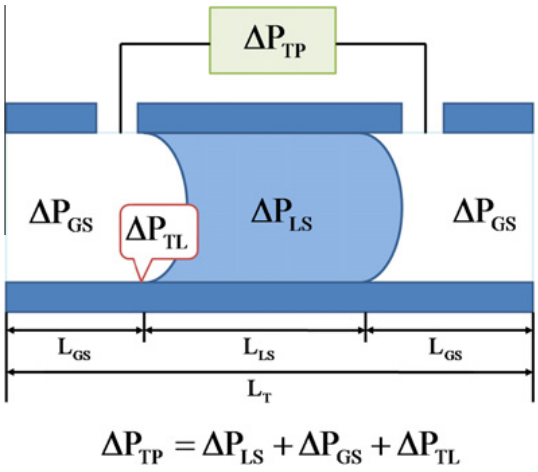

Figure 4.16: Components of pressure drop of a slug flow with triple line [147].

$$\Delta P_{TL} = -\frac{4\sigma_L}{D}\left(\cos\theta_A - \cos\theta_R\right) \tag{4.1}$$

They assumed that the difference between advancing and static contact angles is approximately equal to the difference between static and receding contact angles as follows [147]:

$$\theta_A - \theta_S \approx \theta_S - \theta_R \tag{4.2}$$

They derived the following equation from Eqs. 4.1 and 4.2, which gives the advanced contact angle based on the triple line pressure drop, ΔP_{TL}, and static contact angle, θ_S, which is a function of fluid properties [147].

$$\theta_A = \arccos\left[-\frac{C_1 C_2}{C_2^2 + C_3^2} \pm \sqrt{\left(\frac{C_1 C_2}{C_2^2 + C_3^2}\right)^2 - \left(\frac{C_1^2 - C_3^2}{C_2^2 + C_3^2}\right)}\right] \tag{4.3}$$

where:

$$C_1 = \frac{\Delta P_{TL} D}{\sigma_L} \tag{4.4}$$

and:

$$C_2 = 4\left(1 - \cos\theta_S\right) \tag{4.5}$$

and:

$$C_3 = 4\sin\theta_S \tag{4.6}$$

Once ΔP_{TL} and θ_S are known, one can calculate the advancing contact angle, θ_A,

using Eq. 4.3. In their experiments, Yu et al. [147] measured the triple line pressure drop versus Capillary number for different fluids as shown in Fig. 4.17.

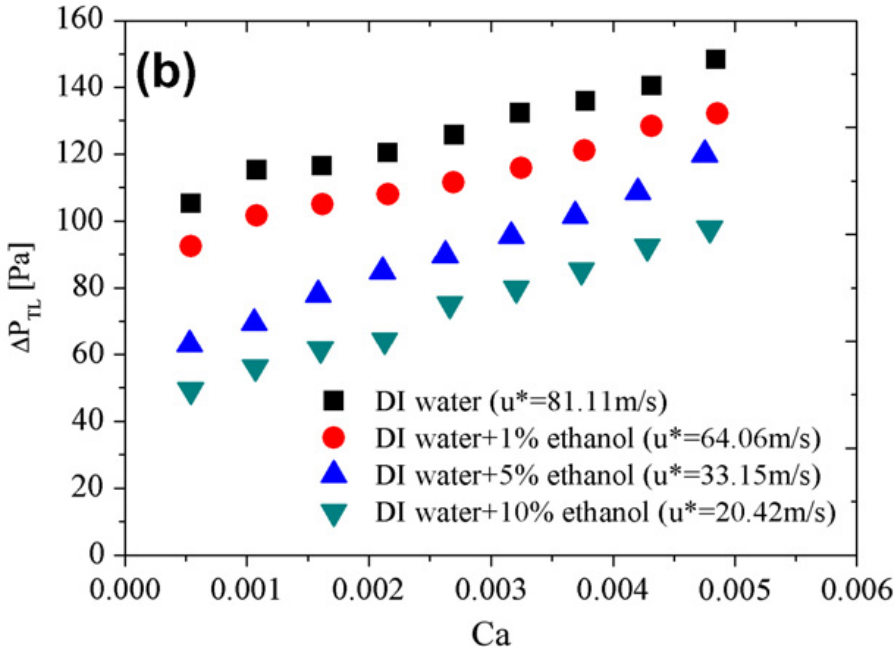

Figure 4.17: Triple line pressure drop of various fluids versus Capillary number (D=1.555 (mm)) [147].

Fig. 4.18 can also be used instead of Eq. 4.3. Once a Reynolds number is assumed, the Capillary number can be derived and then the triple line pressure drop, ΔP_{TL}, and the advancing contact angle, θ_A, can be read from Fig. 4.17 and Fig. 4.18, respectively. The receding contact angle, θ_R, can then be calculated using Eq. 4.1.

4.2.1 Numerical Modeling

As described in the previous section, the computational domain for moving slugs in circular microchannels has been adjusted based on the known advancing and receding

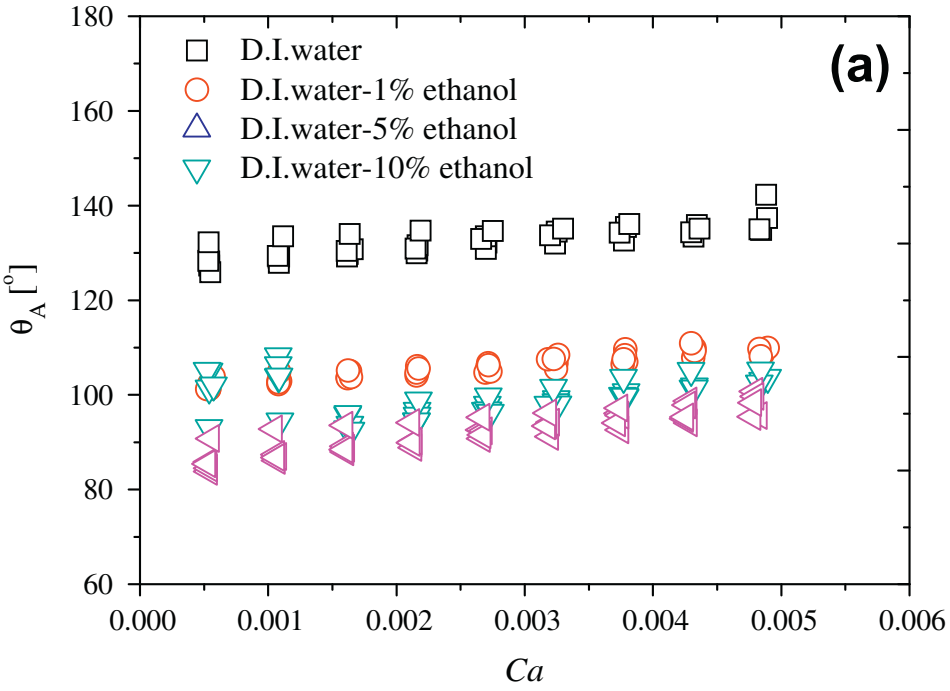

Figure 4.18: Advancing dynamic contact angle versus Capillary number [147].

contact angles based on two Reynolds numbers of 100 and 500, which are both in laminar flow range (see Table 1.1). As other sections, slugs are assumed to be at around room temperature, 300 (K), at the microchannel inlet, and the microchannel wall has been assumed to be at 350 (K). The fluid properties were assumed to be constant at the temperature of 325 (K) i.e. average of the initial and the wall temperature. These properties are as follow:

- $\rho = 987(kg/m^3)$
- $\mu = 0.000528(kg/m.s)$
- $k = 0.645(W/m.K)$
- $C_p = 4182(J/kg.K)$

- $Pr = 3.42$

Table 4.2 presents advancing and receding contact angles for $Re = 100$ and 500. The data reported by Yu et al. [147] have been used to calculate θ_A and θ_R, as mentioned in the previous section (Eqs. 4.1 and 4.2).

Table 4.2: Advancing and receding contact angles for $Re = 100$ and 500 (assuming water) used for generating computational domains of moving slugs in circular microchannels.

Re	Ca	θ_A	θ_R
$(-)$	$(-)$	$(^o)$	$(^o)$
100	0.00025	128	92
500	0.0013	130	90

The simulations have been performed using the moving frame of reference described in section 3.3.1. The slug velocity has been adjusted and applied to the wall to provide Reynolds numbers of 100 and 500. No-slip condition and constant temperature of 350 (K) were applied to the wall. The simulations have been performed using 2D computational domains using circular microchannel axis. Zero shear stress and zero heat flux were applied to the front and rear interfaces in order to simulate interface between liquid and gas. The model was solved as a steady state problem in order to gain a fully developed solution showing internal circulations. Next, the energy equation was solved using the unsteady solver and thermal boundary conditions were applied.

4.2.2 Grid Independency and Validation Study

Two dimensional structured mesh was used in the simulations of this section. As the first attempt, 10 mesh points were used in the radial direction of a slug with $L_s/D = 2$. The mesh number in axial direction has been adjusted to give square mesh shape in order to increase computation accuracy. The mesh size has then be doubled for four times, giving 20, 40, 80, and 160 mesh in the radial direction. Table 4.3 presents total mesh number and numerical results for these cases.

Table 4.3: Different mesh sizes examined for moving slugs in circular microchannels (D=1.555 (mm), Re=500, L_s/D=2).

Mesh size	Mesh number	Iterations	τ_w (Pa)	Change in τ_w %	Change in $q^\star$ %
$\frac{1}{10}$	400	116	0.5156	—	—
$\frac{1}{20}$	1600	214	0.5694	10.4 %	11.2 %
$\frac{1}{40}$	6400	470	0.6177	8.5 %	5.6 %
$\frac{1}{80}$	25600	1141	0.6669	8 %	1.9 %
$\frac{1}{160}$	102400	4652	0.6980	4.7 %	0.4 %

As presented in Table 4.3, required iterations increases by increase in the mesh resolution which means higher simulation time. The average wall shear stress has also been reported in Table 4.3. Based on these values, there is around 4.7% change in the average wall shear stress when one uses 160 grids instead of 80 grids. It seems that approaching to an insignificant change requires much more mesh resolution, due to the singularities close to the corners as reported by Talimi et al. [31]. While

τ_w still increases using finer mesh sizes, the heat transfer results show perfect grid independency. This is due to the fact that the flow in the corners do not contribute significantly in the heat transfer process. However, wall shear stress and pressure drop is not in the scope of the present work. Therefore, based on Table 4.3, the $\frac{1}{80}$ mesh size has been selected as the appropriate mesh resolution, since it gives grid independence heat transfer results, $q^\star$, (using Eq. 1.16) with reasonable amount of computational efforts. Since $q^\star$ has been calculated for different simulation times (slug positions through the channel length), they have not been reported in Table 4.3. The change in $q^\star$ in Table 4.3 is average of dimensionless heat transfer differences for all the simulation times.

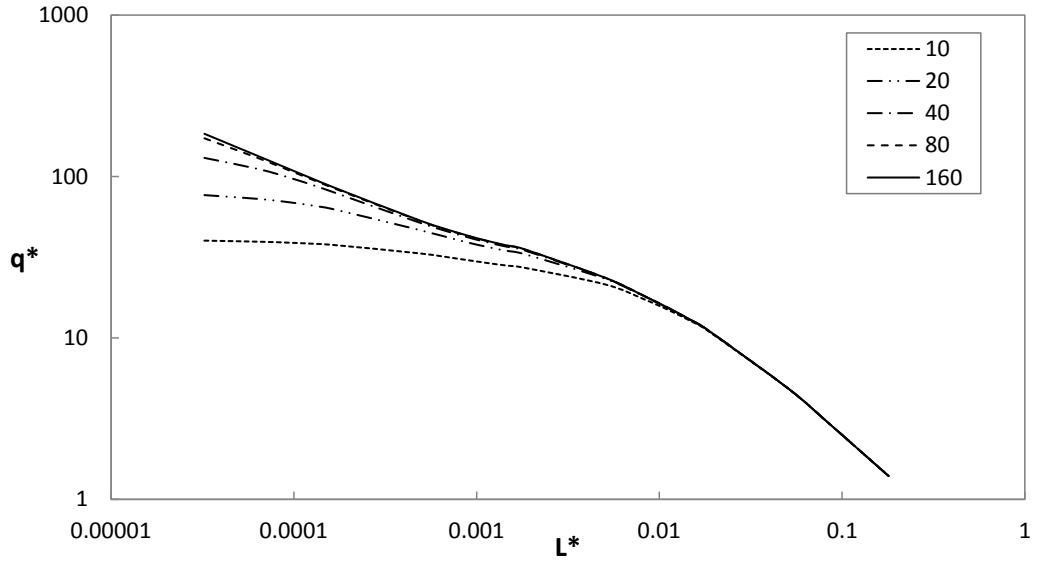

Figure 4.19: Dimensionless heat transfer for a slug flow with $L_s/D = 2$ for different grid numbers in the radial direction.

Fig. 4.19 shows dimensionless heat transfer, $q^\star$, versus dimensionless channel

length, $L^{\star}$, for the different grid size simulations of Table 4.3. As shown in Fig. 4.19, the grid dependency is large in the initial part of the channel, which can be assumed as very short channels, while all the simulation results show the same dimensionless heat transfer after being fully developed. By increasing the mesh resolution, the difference in the initial part is also decreases and approaches to an insignificant order of 0.4% (see Table 4.3), when using $\frac{1}{160}$ mesh instead of $\frac{1}{80}$. This makes using of 80 grids in the radial direction a reasonable choice, when heat transfer is of interest.

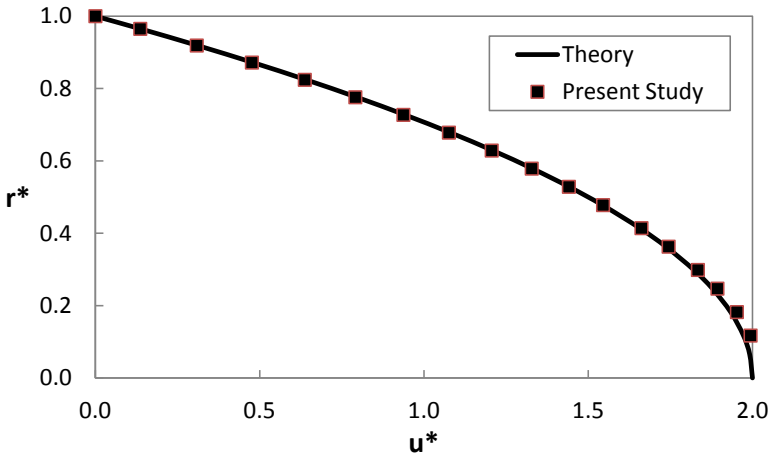

Figure 4.20: Comparison between the velocity profile at the middle radial line of the moving liquid slug and the analytical velocity profile of a laminar single phase Poiseuille flow in a circular pipe.

It is expected that as the length of a liquid slug increases, the velocity profile across the cross section of the slug approaches to a single phase laminar Poiseuille velocity profile, i.e. a parabolic profile. Figure 4.20 shows analytical and numerical velocity profile for a long slug ($L_s = 6.5D$) along radial direction. As can be seen, there is a good agreement and the mean and maximum differences are 0.1% and 1%,

respectively.

4.2.3 Heat Transfer Prediction

Fig. 4.21 shows circulations and streamlines inside a moving slug with $L_s/D = 2$ at the Reynolds number of 100. This flow pattern is axisymetric and the bottom line is axis, so fresh fluid from the slug center is brought to the contact region with the microchannel wall (top wall in Fig. 4.21), which renew the thermal boundary layer and increases the heat transfer. This unsteady process has been shown in Fig. 4.22, at different simulation times.

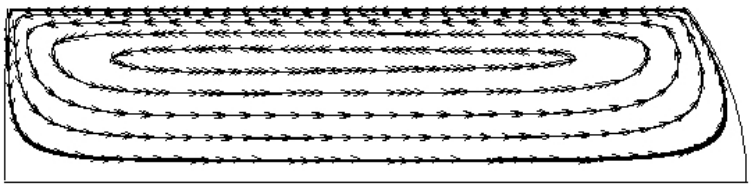

Figure 4.21: Streamlines inside a moving liquid slug with $L_s/D = 2$ in circular microchannel at $Re = 100$.

As shown in Fig. 4.22a, at the beginning of the process, the heat transfer is through heat diffusion into the liquid slug, through growing of the thermal boundary layer normal to the microchannel wall. In Fig. 4.22b and c, the heated portion of the fluid which passed through the thermal boundary layer, has just started to circulate due to the flow pattern shown in Fig. 4.21, and fresh liquid is renewing the thermal boundary layer from the nose of the moving liquid slug (the front interface). In Fig. 4.22d, the thermal boundary layer has become thicker and visible, and the

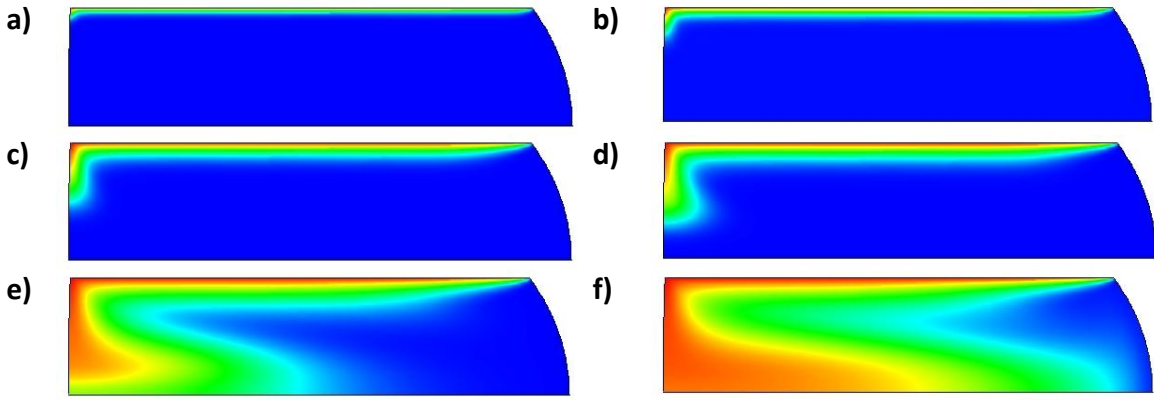

Figure 4.22: Temperature distribution inside a moving liquid slug with $L_s/D = 2$ in circular microchannel ($Re = 100$) at different simulation times, a) t=0.0025 (s), b) t=0.0075 (s), c) t=0.0175 (s), d) t=0.0275 (s), e) t=0.0775 (s), f) t=0.1275 (s).

center is about to feel the heat by the hot liquid entering from the tail. Finally, in Fig. 4.22f, the first circulation is about to finish, and the slug center close to the slug nose is being warm. This process continues until all the slug approaches to the microchannel wall temperature. Once this happens, the slugs no longer remove heat from the microchannel wall, and approaches the fully developed asymptote as shown in the next figures.

The dimensionless heat transfer, $q^\star$, versus dimensionless channel length, $L^\star$, is shown in Figs. 4.23 and 4.24 for slug flows with different slug lengths from $L_s/D = 1$ to 5 at Reynolds numbers of 100 and 500, respectively. The dimensionless heat transfer for single phase slug flow (see section 3.4) is also shown in these figures for direct comparison. As shown in these figures, there is a potential increase in heat transfer (with respect to α_L) when using two phase slug flows mostly in the middle range

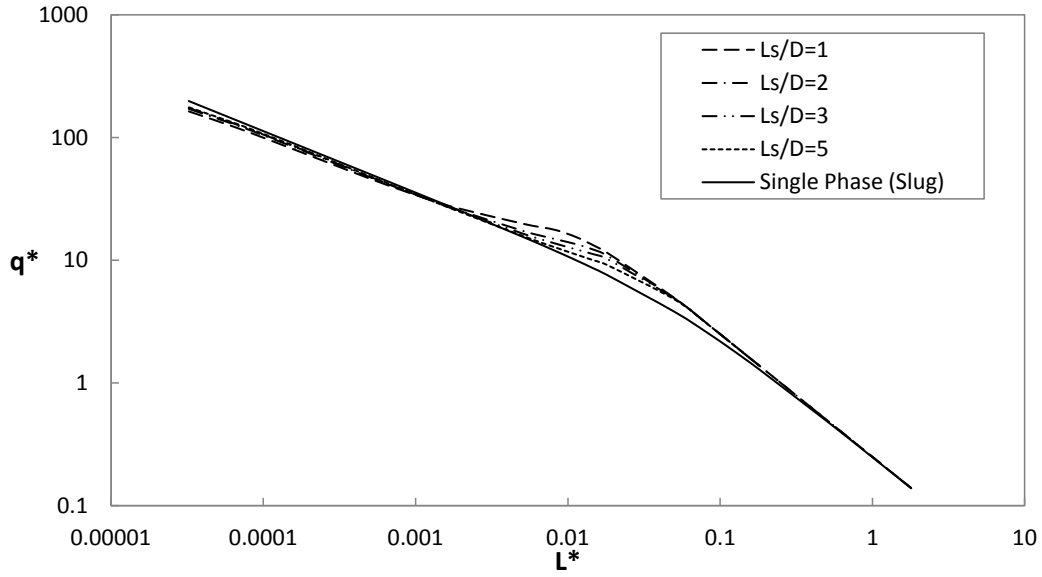

Figure 4.23: Dimensionless heat transfer, $q^{\star}$, for moving liquid slugs for different slug lengths (L_s/D =1, 2, 3, and 5) at same Reynolds numbers ($Re = 100$).

of the horizontal axis. This covers short channels in which the flow is not yet fully developed (thermally). This region is a bit wider and starts earlier in higher Reynolds numbers, if one compares Fig. 4.24 for $Re = 500$ to Fig. 4.23 for $Re = 100$. Besides, approaching the fully developed flow asymptote happens earlier in the two phase slug flows with $Re = 500$ compared to $Re = 100$. This is due to the fact that in two phase slug flows with higher Re, the mixing process is greater, so the slugs are going to become thermally saturated sooner. Shorter slugs remove heat more than longer slugs (with similar α_L) as shown in both Figs. 4.23 and 4.24. In fact, very long slugs behave like a single phase flow, and by using two phase slug flows with shorter slugs, one can increase the number of circulations in microchannel, and hence increase the heat transfer process.

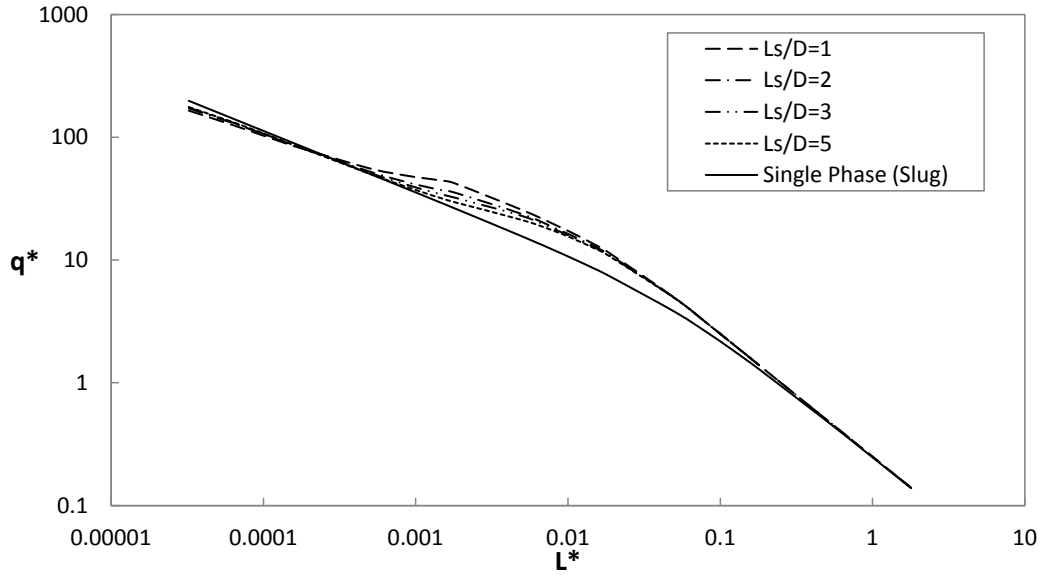

Figure 4.24: Dimensionless heat transfer, $q^{\star}$, for moving liquid slugs for different slug lengths (L_s/D =1, 2, 3, and 5) at same Reynolds numbers ($Re = 500$).

4.2.4 Effects of Dynamic Contact Angles on Heat Transfer

The real advancing and receding contact angles of the moving liquid slugs inside circular microchannels have been considered in the previous section. Models for calculation of θ_A and θ_R based on flow conditions are not available in all channel geometries. The main question here is: *"To what extent the change in contact angles affects the heat transfer process in moving liquid slugs?"* Fig. 4.25 shows the static liquid slug shape (slug at rest, dashed lines for the static interface) and the dynamic shape (solid lines) when $\theta_A > \theta_S > \theta_R$. In this section, same moving slugs (same properties, length, and Reynolds number) in circular microchannels with static and dynamic contact angles (see Table 4.2) are simulated and the flow patterns and heat transfer are compared. The simulations have been performed for $L_s/D = 1$ and 5, and $Re = 100$ and 500.

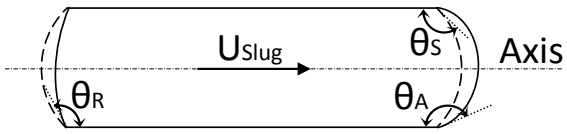

Figure 4.25: Schematic view of a moving slug with different advancing and receding contact angles vs. the static slug shape, ($\theta_A > \theta_S > \theta_R$).

The internal circulations inside moving liquid slugs with $L_s/D = 1$ at $Re = 100$ assuming equal advancing and receding contact angles ($\theta_A = \theta_R = \theta_S$) and dynamic contact angles ($\theta_A > \theta_S > \theta_R$) are shown in Fig. 4.26. The internal circulations and flow patterns seem approximately similar in two cases with a slight difference in the corners i.e. due to the difference in the contact angles. Knowing that the liquid mass of the two slugs are equal, the convective heat transfer process into the moving slugs should depend on the flow patterns. To examine the change in the heat transfer process, one needs to see the temperature distributions in both slugs at different simulation times.

The temperature distribution at different simulation times (slug locations) inside the microtube are shown in Fig. 4.27. As shown in these two figures, while assuming the real advancing and receding contact angles in the simulation leads to a slight change in the flow pattern, the difference in temperature distribution seems to be insignificant. The convective heat transfer is a function of liquid slug mass and internal circulations. Since the liquid mass is the same between the two cases, and the streamlines are almost similar, the convective heat transfer does not change signifi-

cantly when one simplifies the computational domain assuming ideal contact angles (equal to the static contact angle).

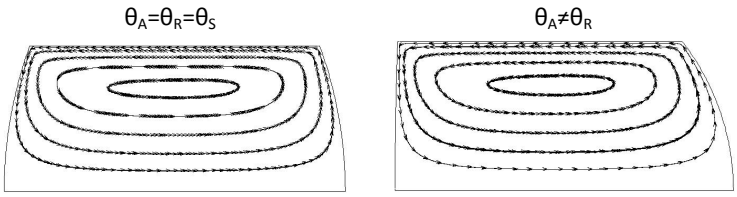

Figure 4.26: Flow pattern inside moving liquid slug with $L_s/D = 1$ at $Re = 100$. Left is the simulation assuming static contact angle ($\theta_A = \theta_R = \theta_S$), and right is the simulation considering contact angle hysteresis ($\theta_A > \theta_S > \theta_R$).

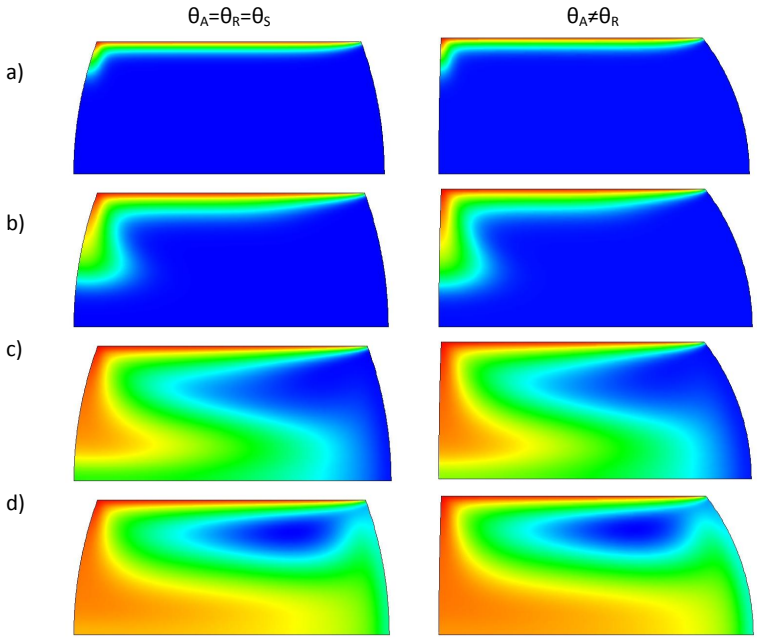

Figure 4.27: Temperature distribution inside moving liquid slug with $L_s/D = 1$ at $Re = 100$, with static (left) and dynamic (right) contact angles, at different simulation times, a) t=0.0075 (s), b) t=0.0275 (s), c) t=0.0775 (s), d) t=0.1275 (s).

The dimensionless wall heat transfer, $q^\star$, for slugs with $L_s/D = 1$ and 5 at $Re = 100$

and 500 are shown in Figs. 4.28 and 4.29, respectively. As shown, the dimensionless heat transfer curves are almost identical when plotted versus channel dimensionless length. The average differences between $q^\star$ for $L_s/D = 1$ to 5 and $Re = 100$ and 500 are presented in Table 4.4. As one can see, the differences are insignificant (less than 1%) in all cases.

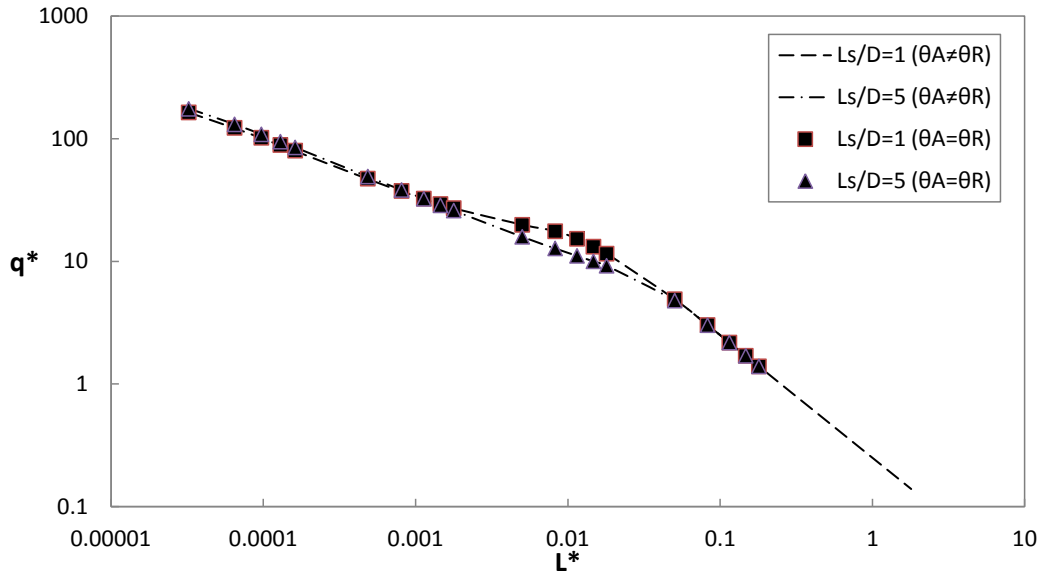

Figure 4.28: Dimensionless wall heat transfer for $L_s/D = 1$ and 5 using static and dynamic contact angles at $Re = 100$.

Table 4.4: Difference between dimensionless wall heat transfer assuming static and dynamic contact angles for $L_s/D = 1$ and 5 at $Re = 100$ and 500.

	$Re = 100$	$Re = 500$
$L_s/D = 1$	0.58 %	0.52 %
$L_s/D = 5$	0.67 %	0.78 %

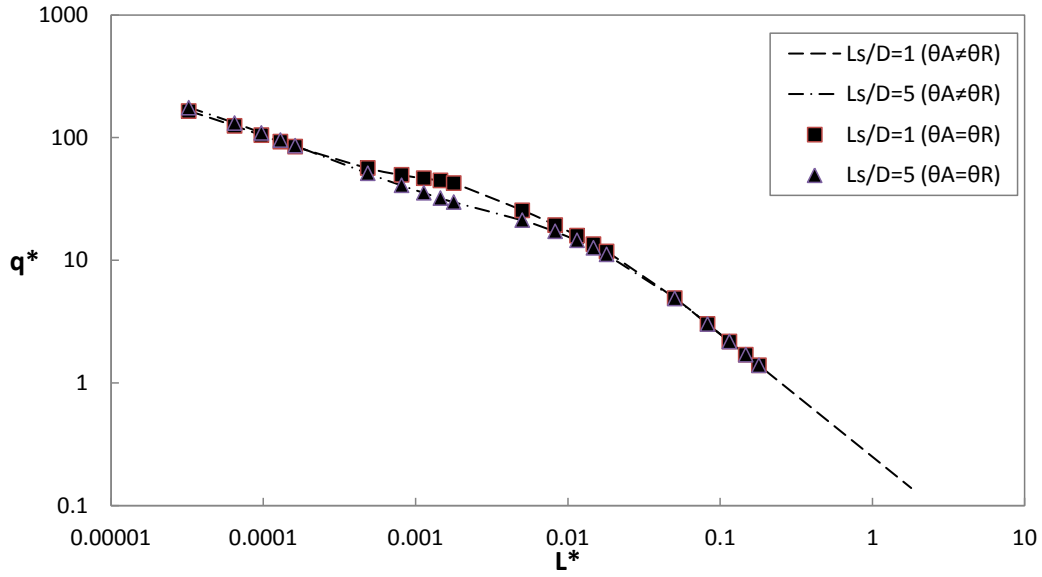

Figure 4.29: Dimensionless wall heat transfer for $L_s/D = 1$ and 5 using static and dynamic contact angles at $Re = 500$.

4.2.5 Assessment of the Two Integration Approaches

In section 3.3.2, two approaches for heat transfer integration along the channel have been discussed. These approaches are assessed using an example of two phase slug flow in circular microtubes in this section, assuming the following values (see Fig. 4.30 for more information):

- $N = 7$ (number of slugs)
- $D = 1.555mm$
- $L_s = 2D$
- $L = 48mm$
- $Re = 500$

- $\theta_A = 130^o$ and $\theta_R = 90^o$ (see Table 4.2)

Based on the information above $\alpha_L = 0.47$. Other parameters including thermophysical, transport, and flow parameters are the same as the defined values in section 4.2.1.

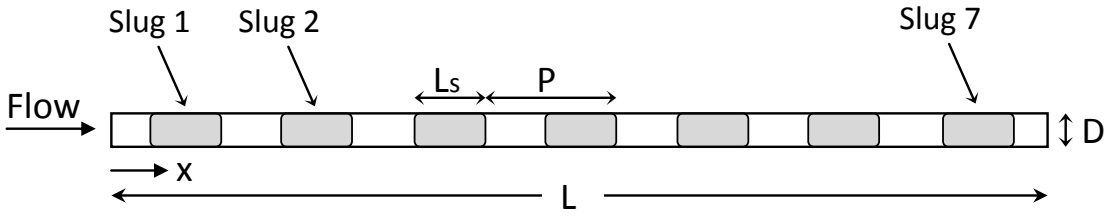

Figure 4.30: Schematic view of the two phase slug flow used for assessment of the integration approaches in circular microtubes.

The total dimensionless heat transfer based on the first approach is reported to $q^\star = 5.19$ in Table 4.5. Using $\alpha_L = 0.47$ and Fig. 4.24, the dimensionless heat transfer is calculated as $q^\star = 5.35$. The $q^\star$ values from the two approaches are in a good agreement with a difference only around 3%. Again both methods provide same results, but as discussed earlier, using the second approach might be more straightforward, since it requires reading of only one data point from the graphs and α_L.

4.2.6 Summary

In this section, the computational domains have been generated using existing correlations for advancing and receding contact angles of moving slugs in circular microchannels, reported by Yu et al. [147]. These correlations have been found for circular

Table 4.5: Dimensionless mean liquid slug heat flux, $\overline{q}_s^\star$, and dimensionless heat transfer, $q^\star$, for the example of Fig. 4.30.

	$q\ (W/m^2)$	$\overline{q}_s^\star$
Slug 1	611625.94	29.49
Slug 2	319732.09	15.42
Slug 3	217407.56	10.48
Slug 4	169558.05	8.17
Slug 5	135864.69	6.55
Slug 6	109996.58	5.30
Slug 7	89218.52	4.30
$q_{0-L}^\star$		5.19

hydrophobic microchannels only, in which both phases touch the wall.

In total, heat transfer could be enhanced using two phase slug flows, provided that the microchannel length is in a certain range. Microchannels with much shorter or much longer lengths are not compatible with the two phase slugs flows, if one aims to increase heat transfer. This optimal length also depends on the fluid parameters and flow conditions through Pr and Re numbers, respectively, since they have been used in calculations of the dimensionless channel length, i.e. the horizontal axis in the presented figures. Furthermore, the circulation intensity increases as slug length decreases since the fluid must traverse the slug at a rate proportional to the slug speed and length. In other words, the residence time for one circulation is lower in short liquid slugs. Therefore, using shorter slugs at same α_L helps achieving higher heat transfer rates.

The assumption of equal advancing and receding contact angles in simulation of moving slugs in microchannels has been assessed, and it is shown that the thermal

effects are insignificant. The reason is that the convective heat transfer process is a strong function of slug mass and internal circulations. The slug mass remains the same when a slug starts to move inside a channel, although the contact angles change. The internal circulations have been shown almost the same in the two cases. Therefore, it is reasonable to assume same advancing and receding contact angles (same to the static contact angle) when correlations of advancing and receding contact angles are not available.

The two approaches for heat transfer integration when using the moving frame of reference technique have been assessed using an example of two phase slug flow inside circular microtubes. Both approaches provide similar results with only a small difference. Using the second approach has been suggested since it requires reading of only one data point from $q^\star$ graphs.

5 THREE DIMENSIONAL MOVING FRAME OF REFERENCE SIMULATION

In the previous chapter, two dimensional numerical simulations have been carried out, including moving slugs between parallel plates and in circular channels. In this chapter, three dimensional simulations, in which all the three coordinates need to be considered, will be performed, and the validity of using only two dimensions in parallel plates geometry is examined. After that, square channels will be examined as the most prominent channel shape in heat sink design. Other channel shapes will be left for future studies.

5.1 3-Dimensional vs. 2-Dimensional Simulation of Moving Slugs Between Parallel Plates

Using moving slugs (or discrete droplets) between two parallel plates has been investigated widely for lab-on-a-chip applications and cooling purposes at small scales in

recent years [140, 80, 66, 141, 142, 79, 143, 144, 145, 146, 148]. Application of moving droplets in cooling process has been of a great interest since one can effectively remove heat from hot spots [140]. Besides, numerical simulations have been performed to investigate the hydrodynamics and thermal behavior of this new cooling method in detail. Most of the numerical studies were performed using 2D computational domains [80, 66, 141, 142, 79, 143, 144], and only a few considered the 3D slug shapes [145, 146]. While a number of studies on this kind of flow have been published recently, large gaps in research exist [20]. Section 2.3 includes a literature review of numerical simulations of moving slugs between two parallel plates.

While the real shape of the slug moving between two parallel plates is three dimensional, most of the numerical studies found in the literature are two dimensional as reviewed in literature review. In the two dimensional simulations, the depth of the domain is assumed to be unity, which is not realistic. Figure 5.1 shows the two situations schematically. The length of the domain in a 2D simulation, L_s, is actually the slug diameter (along the moving direction) from the top view. In this section, both 2D and 3D numerical simulations were carried out and compared to each other, in order to investigate the accuracy of predicting thermal behavior of a moving slug using 2D simulations. The presented results could provide a deeper insight of moving slug hydrodynamics and convective transport phenomena (heat and mass transfer) for EWOD, lab-on-a-chip, and microcooling applications.

As discussed in section 1.3, in the convection problems in heat sinks with a constant

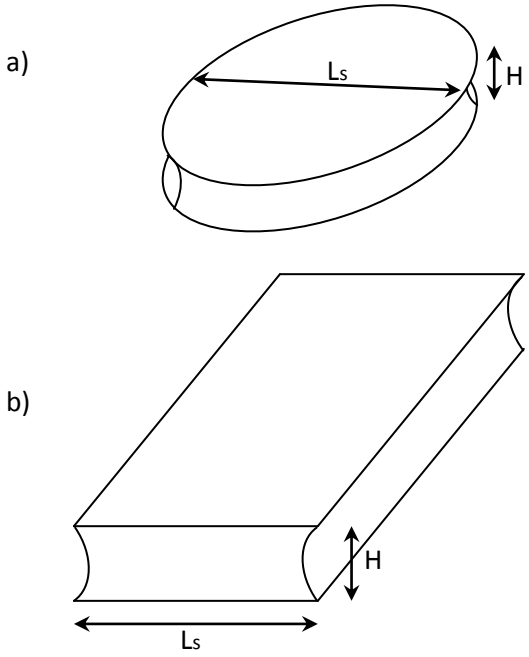

Figure 5.1: a) Real shape of a liquid slug between two parallel plates, b) two-dimensional assumption with unit depth.

wall temperature, using the dimensionless heat transfer, $q^\star$, is more applicable than the Nusselt number, Nu, because the Nu depends on the local bulk temperature which should be calculated. On the other hand $q^\star$ depends on the wall and inlet temperatures which are known and fixed. The dimensionless mean wall flux q^* is defined as follows: [2]

$$q^\star = \frac{\overline{q} D_h}{k\left(T_w - T_i\right)} \tag{5.1}$$

where, in this section, $\overline{q}$ will be calculated using energy balance based on the mean enthalpy of the moving slug at time t. So, the dimensionless heat transfer is: [31]

$$q^{\star} = \frac{C_p(T - T_i)\rho V D_h}{tAk(T_w - T_i)} \tag{5.2}$$

where V is the slug volume which is obviously different for 2D and 3D cases. For example for $\theta = 90^o$:

$$V = L_s H \tag{5.3}$$

for unit depth of the droplet in 2D case, and:

$$V = \pi \frac{L_s^2}{4} H \tag{5.4}$$

in the 3D case. A is the wetted area (both sides) which is:

$$A = 2L_s \tag{5.5}$$

for unit depth of the slug in 2D case, and:

$$A = 2\pi \frac{L_s^2}{4} \tag{5.6}$$

in the 3D case. For slugs with contact angles different from 90^o, true area and volume are used in this section based on the slug shape and contact angle, θ.

The dimensionless heat transfer is usually presented versus dimensionless axial distance, $x^{\star}$, in the literature, which is:

$$x^{\star} = \frac{x/D_h}{Pe_{D_h}} \tag{5.7}$$

where x is the slug location in the moving direction and is calculated using slug velocity and simulation time.

5.1.1 Numerical Modeling

Fig. 5.2 schematically shows the geometry of 2D and 3D computational domains used in this section. H is the distance between the plates and is fixed to $1(mm)$ in the simulations of this section. θ is the contact angle between the slug and the wall. Two different contact angles have been implemented to investigate both convex and concave interface shapes which are 45^o and 135^o.

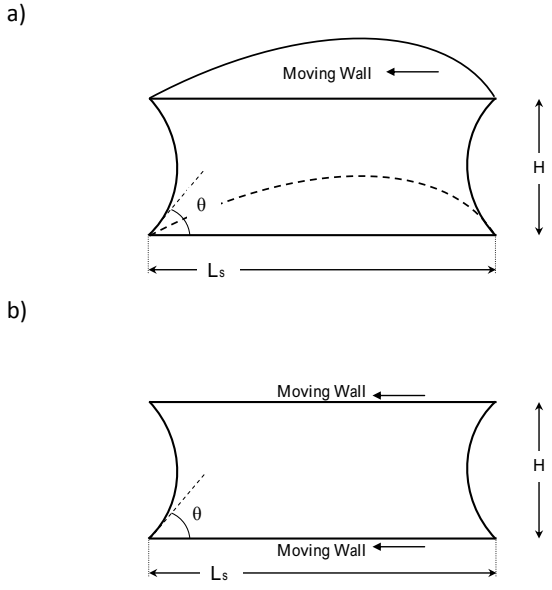

Figure 5.2: Schematic of the domains used in the simulations, a) 3D computational domain using symmetry in the direction of motion, b) 2D computational domain.

In the real situations the slug moves with the nominal mean velocity U. In the moving wall technique, the slug is considered as a stationary slug and the top and bottom walls are considered as moving walls with the velocity of $-U$. The moving wall velocity is setup to give different Reynolds numbers (10, 100, 375, 500, and 1000). No-slip condition and constant temperature of 350 (K) are applied to the top and bottom walls. Zero shear stress and zero heat flux are applied to the interfaces in order to simulate interface between liquid and gas. The model is solved as a steady state flow in order to gain a fully developed solution showing internal circulations. Next, the energy equation is solved using the unsteady solver and the thermal boundary condition is applied. The initial temperature of the fluid is set to 300 (K). The fluid properties are assumed to be constant at the temperature of 325 (K) i.e. average of the initial and the wall temperature. These properties are as follow:

- $\rho = 987(kg/m^3)$
- $\mu = 0.000528(kg/m.s)$
- $k = 0.645(W/m.K)$
- $C_p = 4182(J/kg.K)$
- $Pr = 3.42$

The Reynolds numbers considered in this section are lower than the critical Reynolds value of turbulent flow. This critical value has been reported to 2300 for continues flows [32] or 1000 for a single droplet [33]. Therefore, the flow regime was considered

laminar. The gravitational effects have been neglected since the Bond number is low in this study.

5.1.2 Grid Independency and Validation Study

Structured and unstructured mesh are used in this section for the 2D and 3D simulations, respectively. The grid resolution is increased in the vicinity of the walls and the corners until the results become independent of the grid size. Figure 5.3 shows the final grid at the corner generated for a droplet with $L_s/H = 3$ and $\theta = 45^o$ in both 2D and 3D simulations. After a grid independency study, 150 and 60 grids have been used in vertical direction in 2D and 3D simulations, respectively.

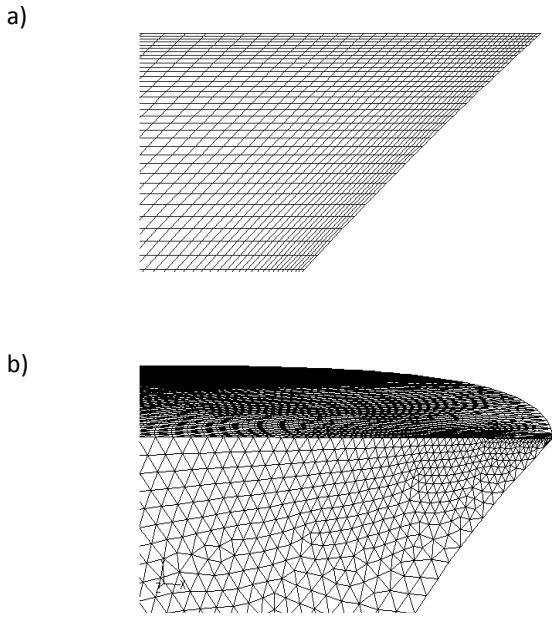

Figure 5.3: Generated mesh at corner of a droplet with $L_s^* = 3$, $\theta = 45^o$, a) structured mesh for 2D simulation, b) unstructured mesh for 3D simulation using symmetry.

As shown in Fig. 5.2b only half of the moving droplet in the 3D case is simulated in order to reduce computational efforts. In the following section, the 3D numerical results (pathlines and contours) will be presented on this symmetry plane and another plane (parallel to the plates and halfway between them) which will be called as "mid plane" in this section.

It is expected that as the length of the liquid slugs increases, the velocity profile at the middle vertical line approaches to the analytical velocity profile of the Poiseuille flow between two parallel plates, with the maximum of 1.5U at the center. Figure 5.4 shows that the numerical results are accurate enough with the mean and maximum differences of 0.053% and 0.056%, respectively.

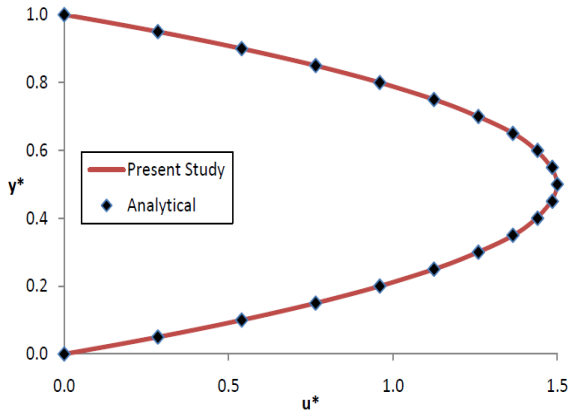

Figure 5.4: Comparison between the velocity profile at the middle vertical line of the liquid slug and the analytical velocity profile.

As another validation test, a simulation is conducted for a domain with $L_s/H = 1$ and $\theta = 90^o$ using the same conditions of the classic lid driven cavity problem at $Re = 100$ and the results showed a very good agreement with the results of Ghia et

al. [133]. Figure 5.5 compares the horizontal component of the velocity at the middle vertical line and the results published by Ghia et al. [133].

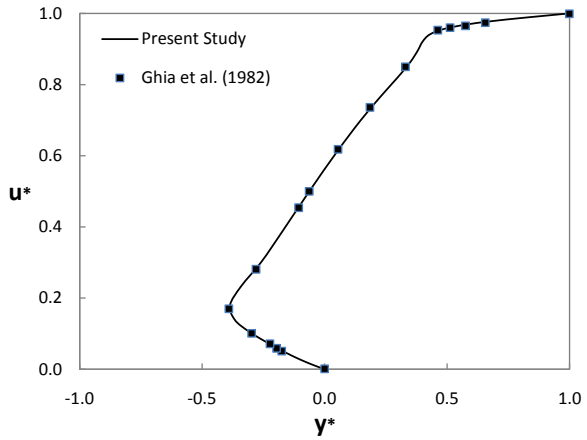

Figure 5.5: Comparison between the horizontal component of the velocity at the middle vertical line and the results of Ghia et al. [133], $L_s/H = 1$, $\theta = 90^o$, $Re = 100$.

5.1.3 3D vs. 2D Hydrodynamics and Flow Pattern

In this section, the differences between hydrodynamics and flow patterns of the 2D and 3D simulations are discussed. The simulations have been carried out for different Reynolds numbers, droplet dimensions, and contact angles, as mentioned in the previous section.

Fig. 5.6 shows the particle paths (streamlines for 2D case) for 2D and 3D cases at different Reynolds numbers. As can be seen in Fig. 5.6, at low Re the pathlines at the mid plane are somehow parallel and the location of circulation core are not very different in 2D and 3D simulations. As Re increases, the circulation core tends to move toward the rear interface in 3D simulation and the pathlines at the mid plane start to

deviate from their former regular harmony. At a higher Reynolds number ($Re = 375$), 3D effects of flow motion transfer the core of the internal circulations toward the rear corner which cannot be predicted using 2D simulation. The pathlines in the 3D simulation are more parallel to the wall in the front half of the slug (symmetry plane) compared with 2D simulation results and this is obviously because of the change in the location of the circulation eye. More three dimensional effects can be seen in mid plane pathlines. The pathlines are not parallel in the rear half of the moving slug and this may affect the convective heat transfer in the slug, which can not be predicted in 2D simulations. Interestingly, a sink and source appears at $Re = 375$ where the pathlines separate from each other and merge again. This might show a secondary circulation near the side of a moving slug at this Reynolds number. By increasing in the Reynolds number to $Re = 500$ these sink and source points spread and turn into two lines. The flow pattern is more complicated and the difference between 2D and 3D simulations become larger.

The pathlines at four vertical slices including the symmetry plane are presented in Fig. 5.7. Figure 5.7a shows the position of the vertical slices, starting from the symmetry plane with steps of 0.4 (mm). The circulation eye close to the rear corner of the slug exists only in the symmetry plane, and not in other sections. This means that the width of the circulation is limited and it does not extent to the sides. Furthermore, the flow patterns are very different in other slices which indicates a fully three-dimensional flow pattern in moving slugs between two parallel plates.

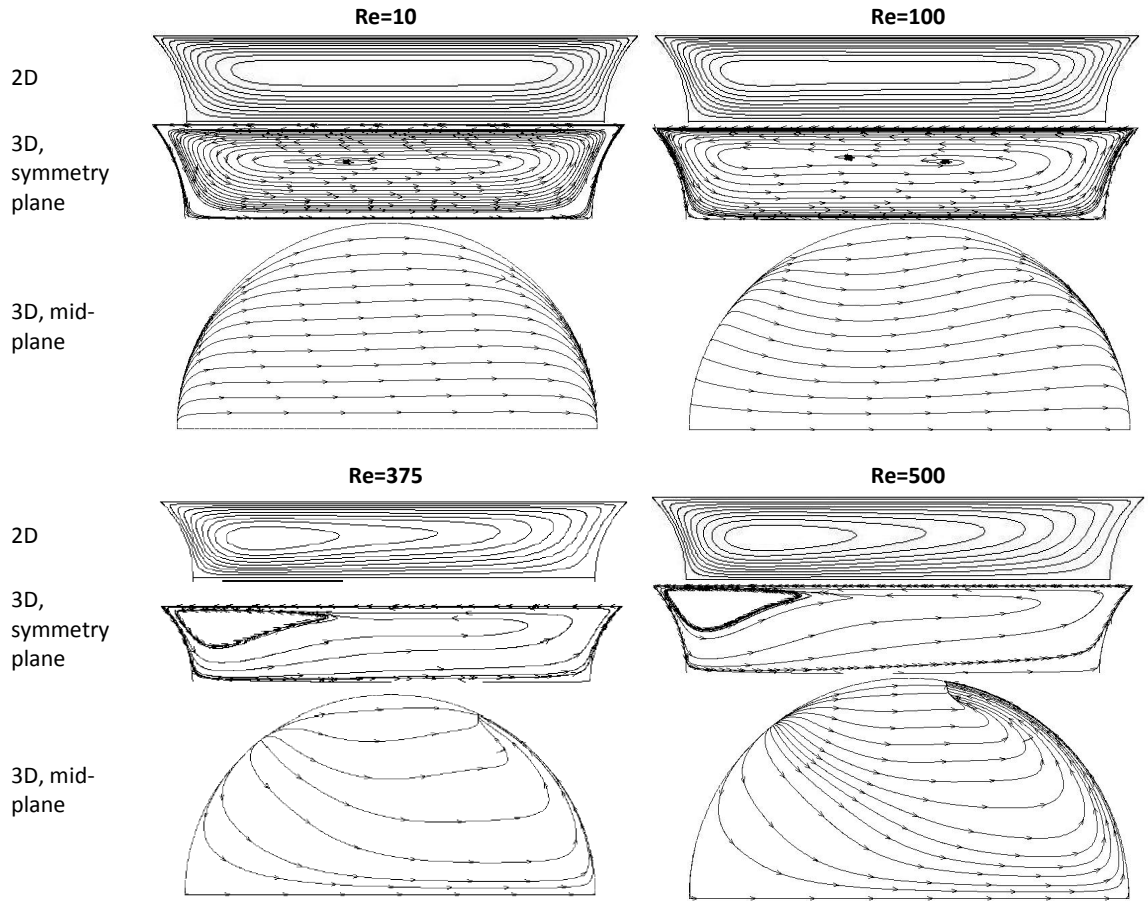

Figure 5.6: Stream functions for 2D and 3D simulations (symmetry plane and mid plane) at different Reynolds numbers: 10, 100, 375, and 500.

At higher Reynolds numbers, the flow pattern becomes even more complicated. Figure 5.8 shows the pathlines at the mid plane when Reynolds number is 1000. This might show the onset of turbulence and is in a good agreement with the critical Re reported by Ren et al. [33]. Simulating the flow using laminar assumption must be performed with more care. Judging these high Reynolds flows will be postponed to the future when more experimental evidences are available. In this section, the Reynolds numbers of $Re = 10, 100, 375$, and 500 will be discussed.

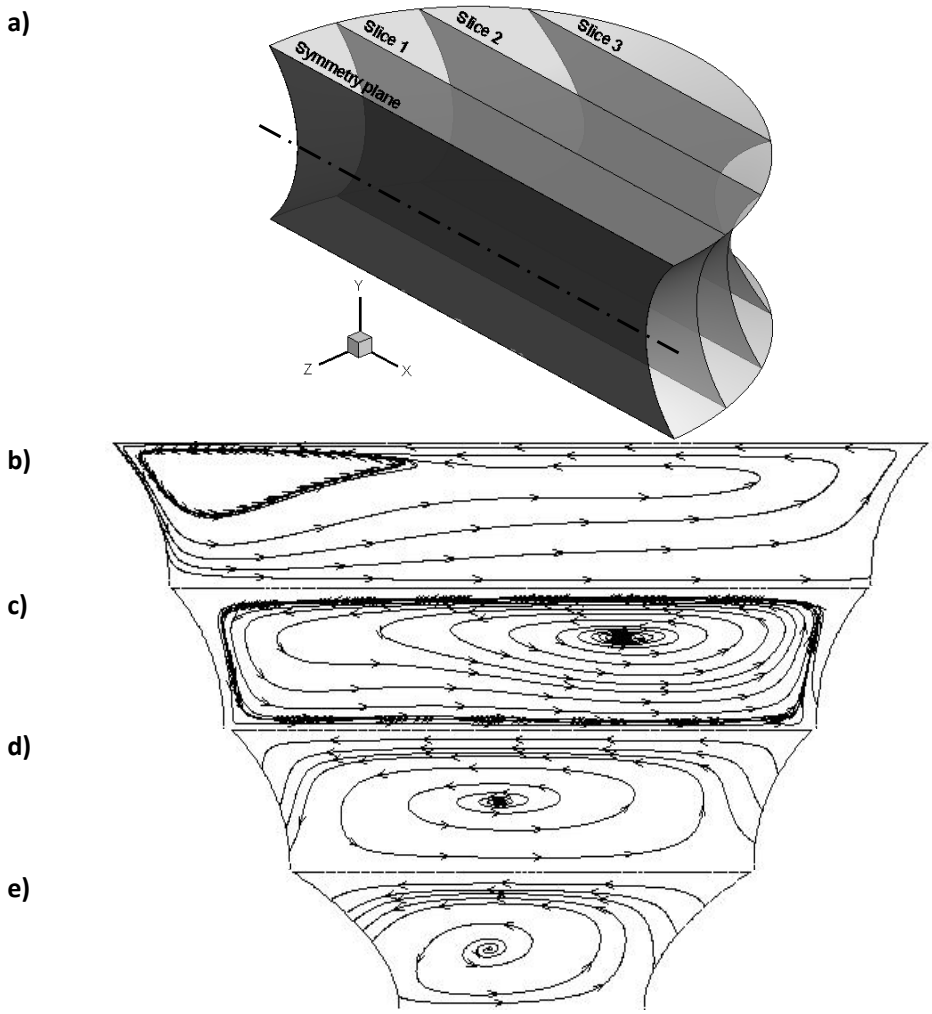

Figure 5.7: Stream functions at different vertical positions of the 3D moving slug with $L_s/H = 3$, $\theta = 45^o$, and $Re = 375$, a) Slice positions, starting from the symmetry plane and steps of $0.4(mm)$, b) symmetry plane, c) slice 1, d) slice 2, e) slice 3.

5.1.4 3D vs. 2D Heat Transfer

Temperature distributions inside a moving slug with $Re = 375$, $L_s/H = 3$, and $\theta = 45^o$ are presented in Fig. 5.9. The temperature contours are presented for 2D and 3D simulations at the same simulation times in order to make a direct comparison.

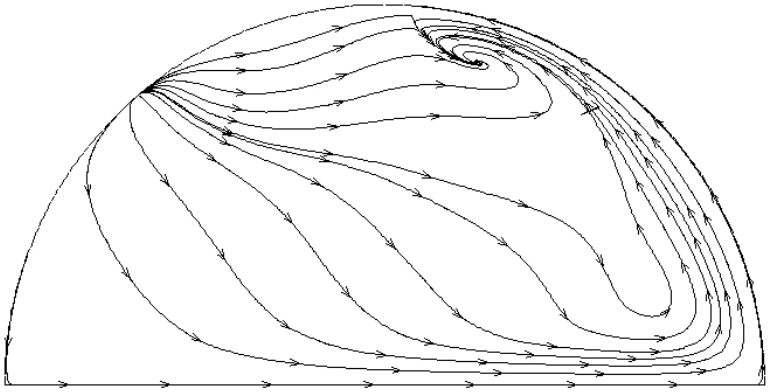

Figure 5.8: Streamlines at the symmetry plane at Re=1000 ($L_s/H = 3$ and $\theta = 45^o$).

As a result of the earlier discussions for flow pattern, the temperature distributions are not identical for 2D and 3D simulations. The difference between the temperature distributions due to the different circulation regions can be observed in the first two columns. It seems that since the circulation region is more compacted and moved toward the rear corner in the 3D case, the circulation process takes less time and brings the heated liquid to be in contact with the wall at approximately half way of the wetted wall region, while the heated fluid will be brought to the wall near the front side of the moving slug in the 2D simulations. The third column in Fig. 5.9 shows the temperature distribution in the mid plane and as shown, the convective heat transfer is not monotonous and parallel to the moving direction or the symmetry plane like what is assumed in 2D simulations, but has the 3D motion effects, which was discussed earlier.

Fig. 5.10 shows temperature distribution at different vertical slices (same slice positions with Fig. 5.7) at the simulation time of 0.0775 (s) (x=7.75 (mm)). As

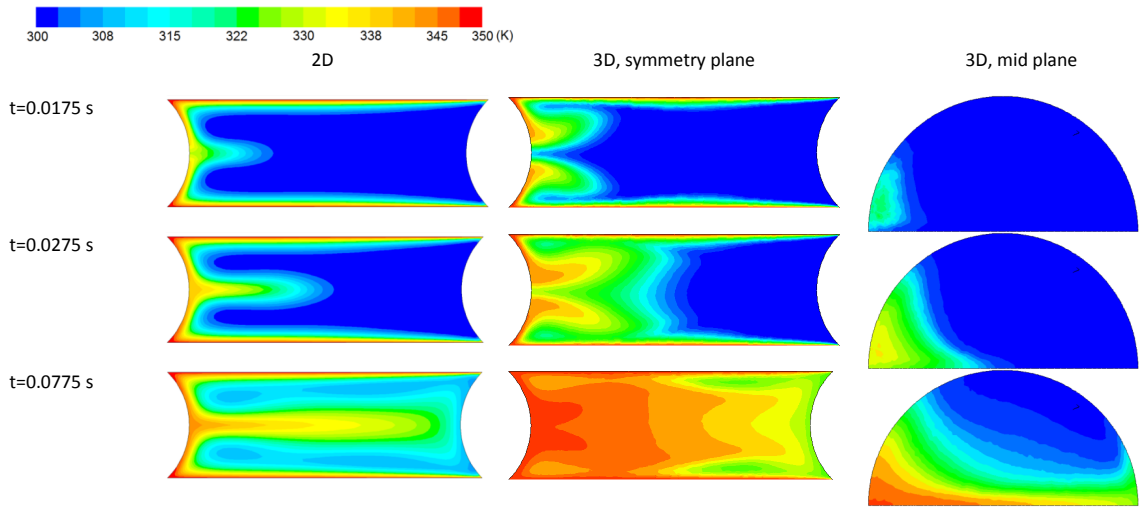

Figure 5.9: Temperature distribution in a moving droplet between two parallel plates with $L_s/H = 3$, $\theta = 45^o$, and $Re = 375$ at different times: a)t=0.0175s (x=1.75mm), b)t=0.0275s (x=2.75mm), c)t=0.0775s (x=7.75mm).

shown, while most of the fluid particles have been heated up in the symmetry plane, most of the fluid is still thermally fresh close to the slug sides. The reason could be what was mentioned about the width of circulation core - the responsible mechanism of heat transfer enhancement - which is limited and not be extended to the sides. This makes the fluid particles close to the symmetry plane to receive heat faster while there is more fresh fluid far from the vertical symmetry plane.

The main question here is: *To what extent neglecting the aforementioned 3D effects can be a source of error in heat transfer modeling, if one applys the 2D assumption?* In order to address this question, the thermal behavior in the two simulations are compared using the dimensionless convective heat transfer, $q^\star$, while the slugs proceed in their path (Eq. 5.2). Two cases were assumed in nondimensionalizing heat transfer

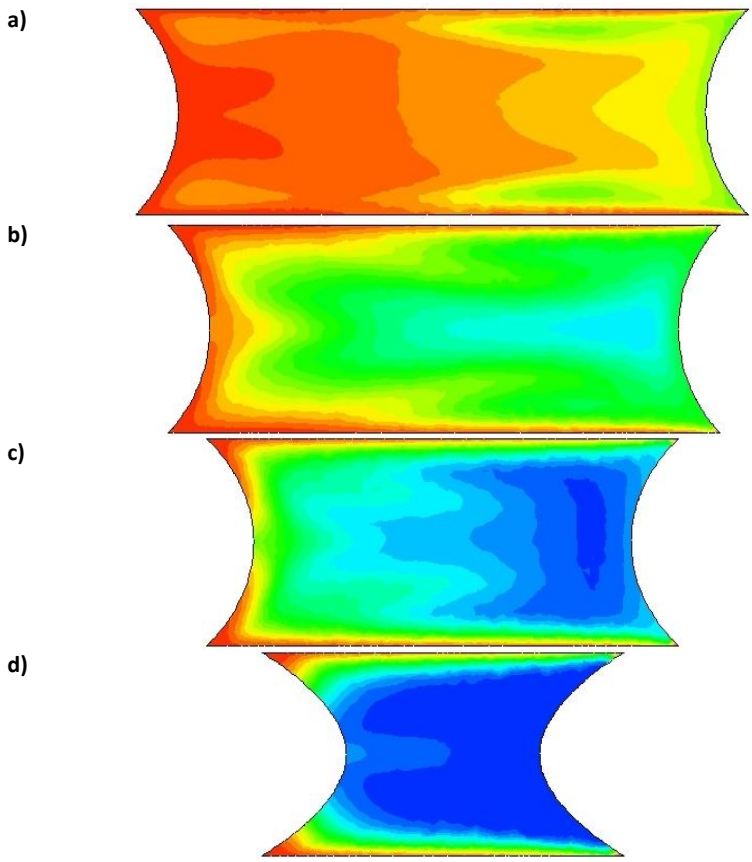

Figure 5.10: Temperature distribution in a moving droplet between two parallel plates with $L_s/H = 3$, $\theta = 45^o$, and $Re = 375$ at different vertical slices (see Fig. 7a for slice positions) a) symmetry plane, b) slice 1, c)slice 2, d) slice 3.

for the results of 2D simulations. In the first case, the slug volume and wetted area are calculated based on the 2D assumption (Eq. 5.3 and Eq. 5.5), and in the second case, the 2D numerical heat transfer results were nondimensionalized using the slug volume and wetted area of a 3D slug with the same size and contact angle (for example Eq. 5.4 and Eq. 5.6 for $\theta = 90^o$). The true volume based on the contact angle is considered in this section for contact angles different from 90^o, as discussed earlier. The results

are then compared with 3D simulation results.

Fig. 5.11 shows the dimensionless heat transfer, $q^\star$, calculated for 2D (both cases) and 3D slugs versus the dimensionless axial distance, $x^\star$, using Eq. 5.7. The graph contains two major horizontal parts which represent two important assymptotes: entrance (boundary layer) region, and fully developed region. As shown, the first case significantly overpredicts the dimensionless heat transfer. On the other hand, the second case is somehow in agreement with the 3D results. The agreement is very good in the fully developed region, but shows some inaccuracy in the boundary layer region. The difference between the 2D (case 2) and 3D simulations in the boundary layer region can be explained referring back to Fig. 5.9. As shown in the first row, which represents boundary layer region, the shape and thickness of the thermal boundary layers are different in 2D and 3D simulations. Overall, the thickness of the boundary layer region in the 3D slug is less than 2D simulation. This means that the actual thermal boundary layer in real moving slugs is thinner than what 2D numerical simulations predict, due to the flow in the third direction which is neglected. The thinner thermal boundary layer in 3D simulation can be the reason of higher dimensionless heat transfers compared with the 2D simulation (second case) in the boundary layer region in Fig. 5.11.

The 3D and 2D (case 2) simulations do not follow the fully developed asymptote of Poiseuille flow between parallel plates in Fig. 5.11, because of the fact that a single moving slug is considered and it does not fill the cross section of the channel. The sim-

ulation of 2D (case 1) follows this asymptote because it has been nondimensionalized using the slug contact area and volume based on a unit depth.

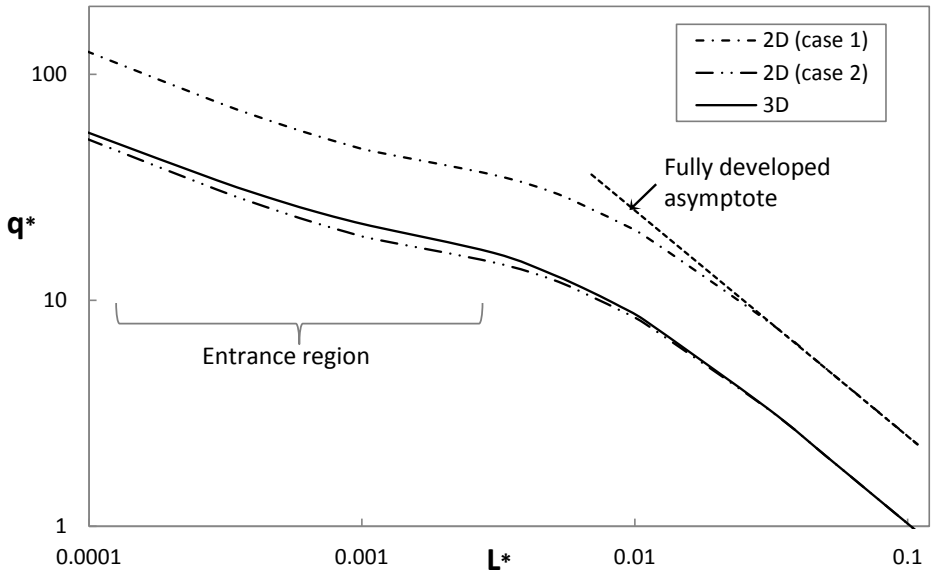

Figure 5.11: Dimensionless heat transfer for a moving slug with $L_s/H = 3$, $\theta = 45^o$, and $Re = 375$ using 2D and 3D simulations. $q^\star$ is calculated using 2D area and volume in case 1, and 3D area and volume in case 2.

Based on the assumptions discussed in section 5.1.1 (page 145), the length of boundary layer region is only a few millimeters ($\sim$ 4 or 5 mm) so the channel length can be an important parameter to decide if one can use the 2D results in predicting the thermal behavior of real moving slugs. The simulations have been carried out for different slug lengths and contact angles as well. The mean difference between q^* of 2D and 3D cases are presented in Table 5.1 for various slug lengths and contact angles. As presented in Table 5.1, overall, the errors decrease as the slug becomes larger and/or has more liquid mass i.e. larger contact angle. Case 1, in which $q^\star$ has been calculated

using 2D area and volume (unit depth), is obviously not appropriate due to its large prediction error. Using case 2 assumptions still make error when small slugs, with diameters (slug length) almost equal to the distance between parallel plates, are of interest. On the other hand, using case 2 assumptions (true area and volume for calculation of $q^\star$) can make small errors for larger slugs, especially when the size of the heat sink/exchanger is much larger than the thermal entrance length.

Table 5.1: The difference between $q^\star$ for various slug lengths and contact angles at Reynolds number of 375.

L/H	θ	Case 1 †	Case 2 * ††	Case 2 **
1	45	137.9%	16.5%	14.0%
3	45	108.7 %	6.3 %	5.4 %
3	135	89.7%	4.4%	4.0%

* Entrance region (boundary layer)
** Total (both entrance and fully developed region)
† 2D results are nondimensionalized using 2D area and volume (unit depth)
†† 2D results are nondimensionalized using 3D (true) area and volume

Table 5.2 presents the difference between dimensionless heat transfer, $q^\star$, for a moving slug with $L/H = 3$ and $\theta = 45^o$ at different Reynolds numbers. Only a slight change can be seen in the errors with an increase in Re from 10 to 500. This might show that the effect of Re on heat transfer simulation using 2D assumption is not significant when the flow is laminar.

5.1.5 Summary

In this section, the potential errors caused by using 2D computational domains for modeling the thermal behavior of moving slugs between parallel plates were examined.

Table 5.2: The difference between $q^\star$ for $L/H = 3$ and $\theta = 45^o$ and different Reynolds numbers.

Re	Case 2, B.L. *	Case 2 **
10	4.9%	4.2%
100	6.3 %	5.3 %
375	6.3 %	5.4 %
500	6.9 %	5.9 %

* Entrance region (boundary layer)
** Total (both entrance and fully developed region)

It was shown that if one performs numerical simulation for small slugs, then using 2D simulations can be a source of significant errors due to the 3D effects which are neglected. However, if larger slugs with diameters (slug lengths) of a few times larger than channel width are desired, one can use 2D simulations with some precautions. First, simulation results must be nondimensionalized using the real contact area and slugs volume/mass representing the real slug dimensions and shape. In addition, this method is recommended for a channel with a length greater than the entrance length (boundary layer region) based on the fluid properties and flow parameters such as velocity, since the errors are becoming smaller in the fully developed region. Finally, as the mass of the slug becomes greater, i.e. larger contact angle, the errors decrease.

This section has some limitations as well, which could be addressed and noticed in the future studies.

- Firstly, the same contact angles have been assumed for front and rear interfaces which is a simplification. As shown and discussed in section 4.2.4 for circular channels, the errors in heat transfer prediction might be insignificant. However,

simulations including the contact angle hysteresis could be performed in the future to examine this effect quantitatively, given that models for prediction of advancing and receding contact angles are available for moving slugs between parallel plates (not for a moving droplet on a plate). For the 3D simulations a model for contact angle all around the slug is required as a continuous function. Again, these effects are insignificant in circular channels as shown in section 4.2.4.

- Secondly, in 3D simulations the shape change in the slug due to its motion has been neglected. In fact, the slug may be elongated in the motion direction and makes an elliptic shape. This way the diameters are not equal in the motion direction and the direction normal to it, when one looks from the top view.
- Finally, the slug path can be curved when controlled by an electric field and the effects of the angular acceleration on heat transfer process can be addressed in the future.

5.2 Moving Slugs Inside Square Ducts

In this section, heat transfer in moving slugs in square microchannels is studied. When one tries to generate a computational domain in a square geometry, the first step is using symmetry planes in order to cut the computational domain and simplify the simulations. Since the simulations will be carried out as a steady state problem (hydrodynamic), and then an unsteady state simulation will be applied for the heat

transfer, the validity of using symmetry planes should be examined in a general unsteady state approach. Therefore, in the first section, a full computational domain of a moving slug in a square microchannel is used and the validity of using symmetry planes is examined.

5.2.1 Test for Symmetry

Fig. 5.12 shows the geometry of the computational domain, including the vertical mid plane, which is examined for the symmetry. Velocity profiles at different time steps will be presented on the mid line in the Fig. 5.12. The microchannel width and depth are both 1 (mm) which gives a hydraulic diameter of 1 (mm). The slug length to hydraulic diameter is 2 (L_s/D_h). The front and rear interfaces are assumed to be straight (with a contact angle of 90 ^{o}), and all the side walls are the microchannel walls. The slug velocity is applied to the walls in reverse direction which gives $Re = 500$.

The simulation is performed as an unsteady state simulation with a very small time step ($\Delta t = 5 \times 10^{-5}(s)$) in order to track the momentum diffusion and any changes in the velocity profiles. No shear stress and no slip boundary condition are applied to the interfaces and walls, respectively.

Fig. 5.13 shows velocity profiles on the mid line (see Fig. 5.12) at different simulation times. The momentum diffusion at initial steps can easily be seen in this figure, and more importantly it is symmetrical. As momentum diffuses into the fluid, the average velocity is also increases which is due to the mass balance inside the compu-

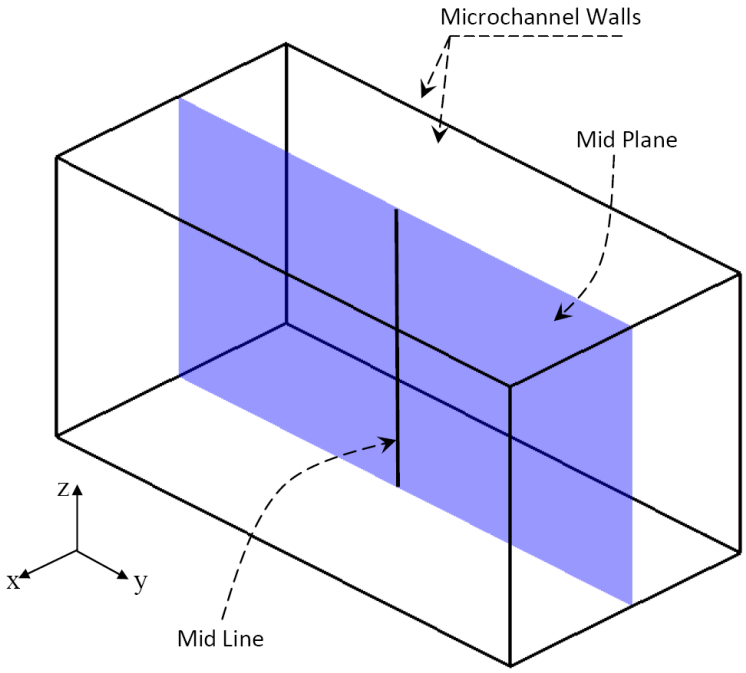

Figure 5.12: Computational domain used in the symmetry test.

tational domain. The fluid particles in the vicinity of the moving walls, are traveling toward the rear interface and have to return toward the center of slug due to the circulations. After a while, the velocity profile on the mid line reaches its steady state shape (see $t = 0.05(s)$ and $t = 0.075(s)$ in Fig. 5.13). As shown, the velocity profile is perfectly symmetrical in all the simulation times presented in Fig. 5.13. The steady state velocity profile in Fig. 5.13 is not parabolic since the slug length is only two times the hydraulic diameter. This will be addressed for longer slugs in section 5.2.3.

Fig. 5.14 shows the velocity vectors on the computational nodes on the mid plane (see Fig. 5.12). This figure also includes contours of the velocity components in the x-direction (u). Again a perfect symmetry is observed and in general one can conclude

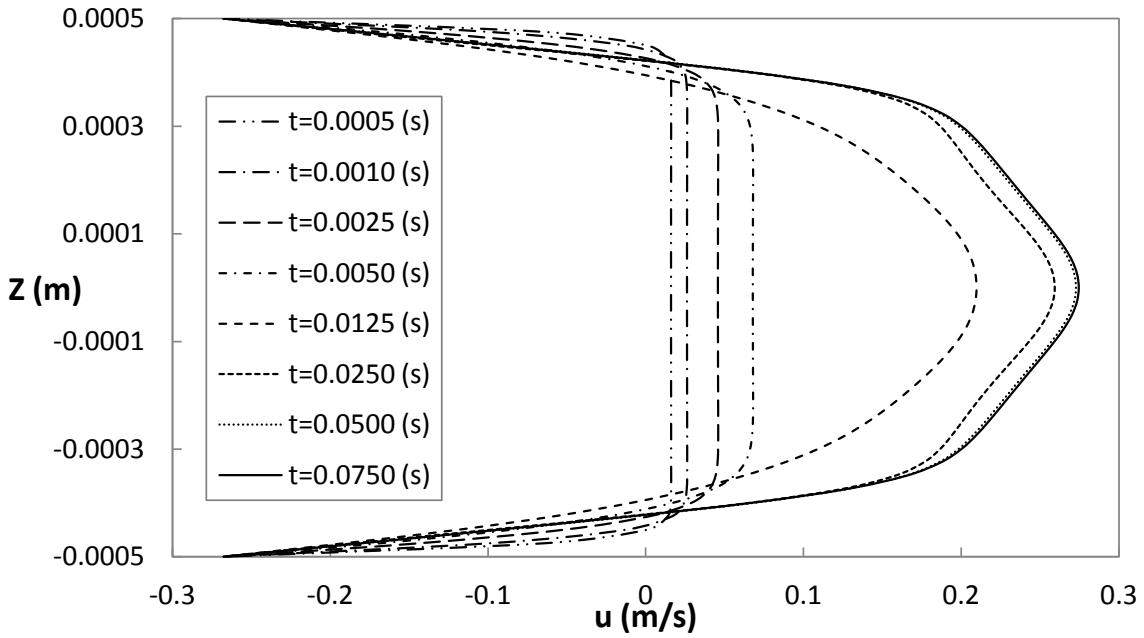

Figure 5.13: Velocity profiles on the mid line (see Fig. 5.12) during the unsteady state simulation.

that using symmetry planes to cut the computational domain for the application of this chapter is valid. In the next sections, these symmetry planes will be used to generate smaller computational domains, and consequently, faster numerical simulations.

5.2.2 Numerical Modeling

A square microchannel with a hydraulic diameter of 0.0005 (m) has been considered in the present study. The microchannel geometry is the same as what Betz and Attinger [153] (explained in detail in section 5.2.5) used in their experiment in order to make a direct comparison. Figure 5.15 shows the computational domain with fixed advancing and receding interfaces. Two symmetry planes in vertical and horizontal directions (X-

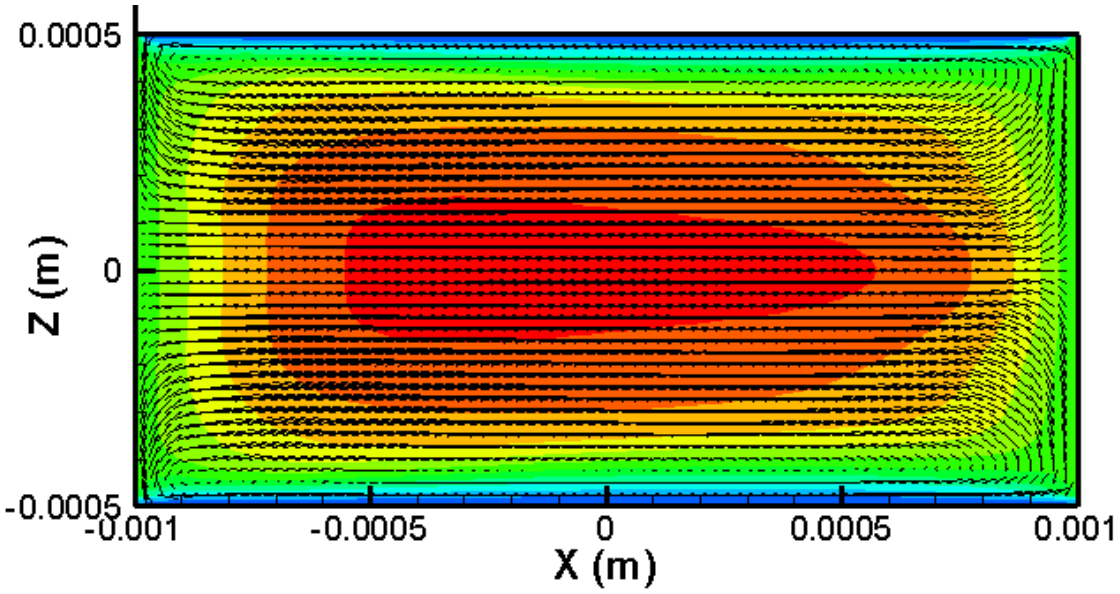

Figure 5.14: Contours of x velocity component and velocity vectors in the mid plane (see Fig. 5.12).

Z and X-Y, respectively) help to make the computational domain smaller, as discussed in the previous section. The top and side walls are moving walls and their velocities are calculated based on the data provided by Betz and Attinger [153], to provide same Reynolds numbers. The fluid is water with fixed physical and transport properties. The fluid properties are examined at the bulk temperature (average of inlet and exit temperatures) of Betz and Attinger experiments [153].

The simulations are performed as steady state simulation in order to gain a fully developed hydrodynamics solution showing internal circulations. Zero shear stress and no slip boundary conditions are applied to the interfaces and walls, respectively. The energy equation (Eq. 3.3) is solved using unsteady state solver and thermal boundary conditions have been applied. Constant wall temperature and no heat transfer are

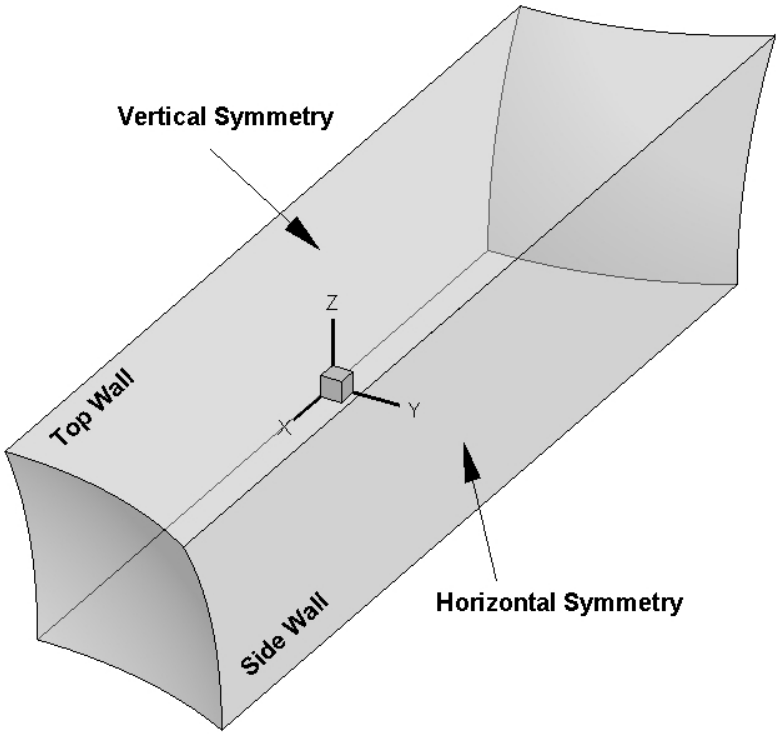

Figure 5.15: The computational domain used in the simulation of moving slugs in square channels.

applied to walls and interfaces, respectively.

The numerical simulations have been performed for the data points provided by Betz and Attinger [153]. They performed a few runs with Reynolds numbers less than 1000 in the laminar flow range. These Re numbers are lower than the critical Reynolds value of turbulent flow. The critical value has been reported to 2300 for continues single phase Poiseuille flows [32] or 1000 for moving single droplets [33] (See also Table 1.1). The gravitational effects are neglected in this section since the Bond number, Bo, is lower than the criterion reported by Bretherton [43].

5.2.3 Grid Independency and Validation Study

Three dimensional structured mesh was used in this section. As reported by Talimi et al. [31] a very high mesh resolution is required in the corners in order to achieve grid independence wall shear stress results. This could lead to very time consuming simulations in three dimensional cases. Three mesh resolutions have been studied first to check if grid independence heat transfer results could be achieved using lower mesh resolutions. The width and height of the computational domain have been divided into 20, 40, and 80 mesh in the three cases. Table 5.3 presents total mesh number and numerical results for these three cases.

Table 5.3: Different mesh sizes examined for moving slugs in square microchannels, $L_s/D_h = 2$.

Mesh size	Mesh number	Iterations	τ_w (Pa)	Change in τ_w %	Change in $q^\star$ %
$\frac{1}{20}$	32,000	291	2.43	—	—
$\frac{1}{40}$	256,000	760	2.76	11.9 %	1.13 %
$\frac{1}{80}$	2,048,000	1918	3.07	10.1 %	0.27 %

As presented in Table 5.3, required iterations increases by increase in the mesh resolution which means higher simulation time. The average wall shear stress has also been reported in Table 5.3. Based on these values, there is around 12% change in the average wall shear stress when one uses the second case instead of the first case. This will be around 10 % using the third case instead of the second case. While the change has not been approached to an insignificant order, there are more than 2 million

elements in the simulations. This is mainly due to the singularities close to the corners as reported by Talimi et al. [31]. While τ_w still increases using finer mesh sizes, the heat transfer results show grid independency. This is due to the fact that the flow in the small corners do not contribute significantly in the heat transfer process. However, wall shear stress and pressure drop is not in the scope of this section. Therefore, based on Table 5.3, the second mesh size has been selected as the appropriate mesh size since it gives grid independence heat transfer results, $q^\star$, (using Eq. 1.16) with reasonable amount of computational efforts.

Since $q^\star$ has been calculated for different simulation times (slug positions through the channel length), they have not been reported in Table 5.3. The change in $q^\star$ in Table 5.3 is average of dimensionless heat transfer differences for all the simulation times, i.e. different channel lengths. Figure 5.16 shows the dimensionless heat transfer, $q^\star$, versus dimensionless channel lengths, $L^\star$. As shown, the difference between the simulations with 40 and 80 grids in the width and height directions (y and z in Fig. 5.15) is insignificant. The maximum differences are 11.2% and 2.8% for mesh refinement from 20 to 40 grids and 40 to 80 grids, respectively.

It is expected that as the length of a liquid slug increases, the velocity profile across the cross section of the slug approaches single phase Poiseuille velocity profile. The single phase Poiseuille velocity profile can be achieved analytically using separation of variables. The Poiseuille flow dimensionless velocity profile as a function of y and z is as follows: [2]

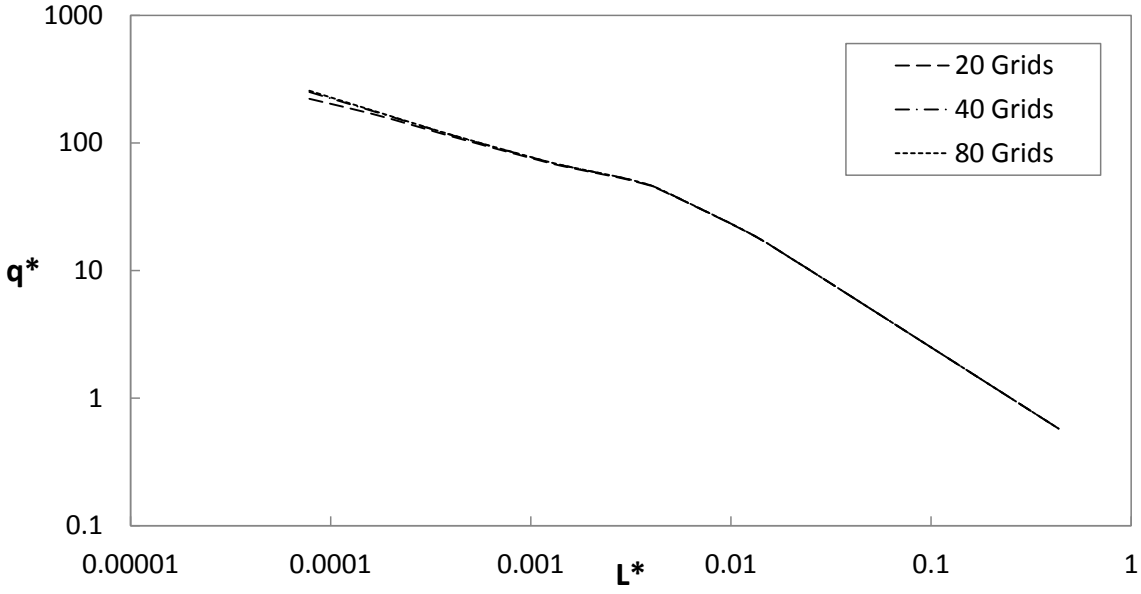

Figure 5.16: Dimensionless heat transfer versus dimensionless channel length for moving slugs in square microchannels ($L_s/D_h = 2$) for different mesh sizes used in the grid independency study.

$$u^{\star}(y,z) = \sum_{n=1,3\ldots}^{\infty} \frac{1}{n^3}(-1)^{\frac{n-1}{2}} \cos\left(\frac{n\pi y}{2Y}\right) \times \left(1 - \frac{\cosh\left(\frac{n\pi z}{2Y}\right)}{\cosh\left(\frac{n\pi Z}{2Y}\right)}\right) \tag{5.8}$$

Figures 5.17 and 5.18 show analytical and numerical velocity profiles for a long slug ($L_s = 10D_h$) along vertical and diagonal directions. The analytical profiles in these figures have been achieved using 50 terms in the series of Eq. 5.8. As shown, there is a good agreement and the mean and maximum differences are 0.3% and 0.7%, respectively.

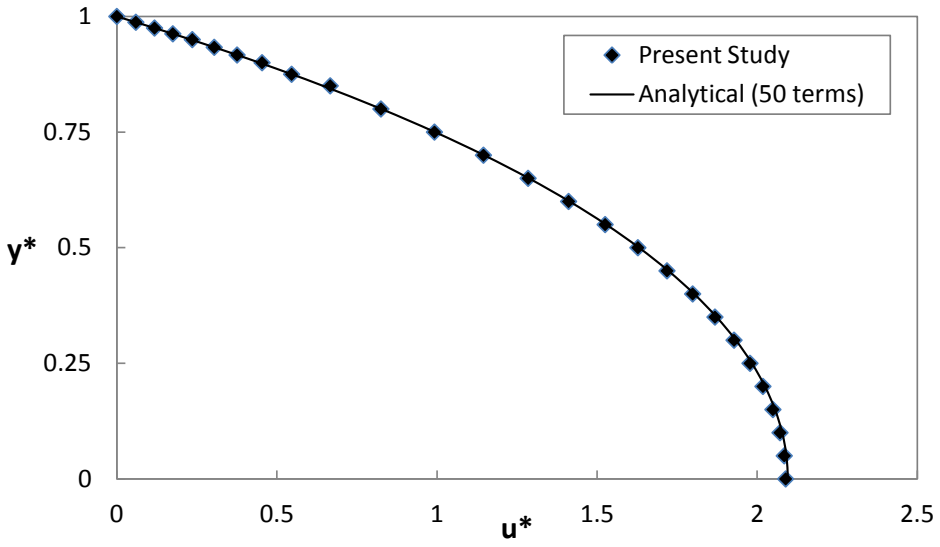

Figure 5.17: Dimensionless velocity along dimensionless vertical axis ($y^\star = y/Y$), numerical and theoretical.

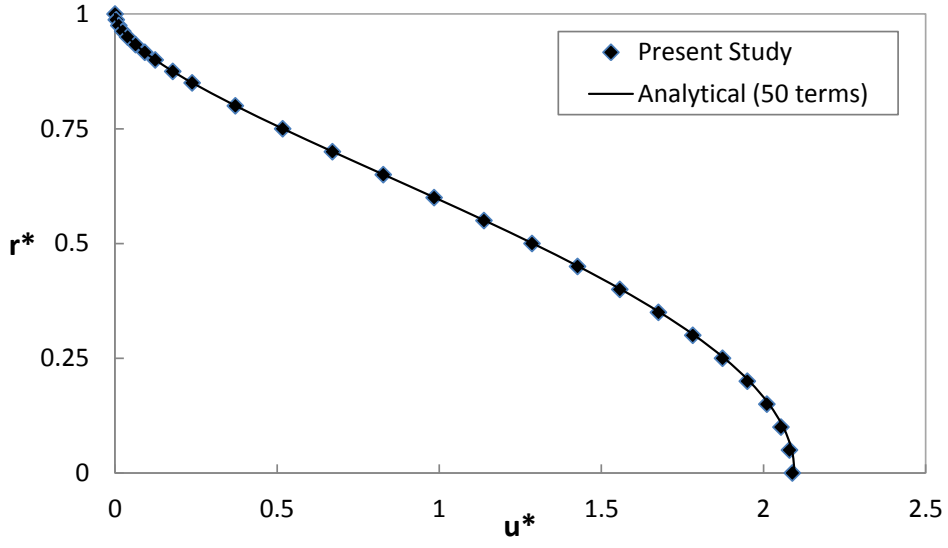

Figure 5.18: Dimensionless velocity along diagonal direction $\left(r^\star = \sqrt{y^2+z^2}/\sqrt{Y^2+Z^2}\right)$, numerical and theoretical.

5.2.4 Hydrodynamics and Flow Pattern

The flow pattern and streamlines at the vertical symmetry plane (see Fig. 5.15) of the simulated moving slug at $Re = 512$ are shown in Fig. 5.19. As shown, the streamlines are approximately parallel in a large portion of front half of the slug. This leads the circulation core toward the receding interface and closer to the microchannel wall. According to Talimi et al. [82] this is expected at Re numbers at the order of 500 and upper.

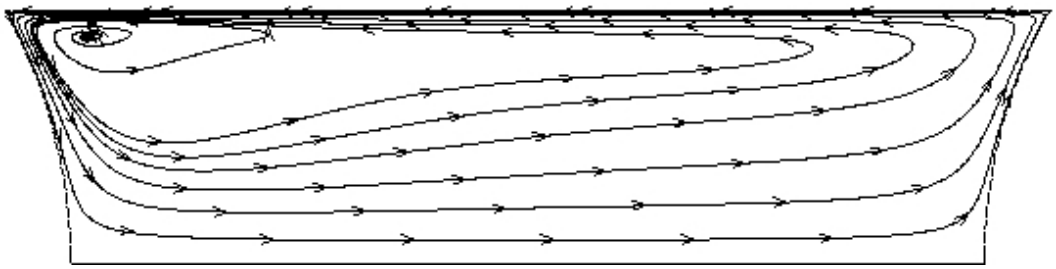

Figure 5.19: Streamlines inside a moving liquid slug at vertical symmetry plane (see Fig. 5.15), $Re = 512$.

The streamlines shown in Fig. 5.19 are different from what has been schematically shown by Taylor in Fig. 2.2. The reason is bypass flow through the thin liquid film around gas bubbles which is not simulated when using moving frame of reference single phase simulations. Therefore, the liquid is completely circulating inside moving slugs in Fig. 5.19. The difference between hydrodynamics and its effects on heat transfer process will be discussed in more details in later sections of this chapter.

Due to the flow pattern shown in Fig. 5.19, as the liquid slug travels inside the microchannel, fresh liquid from the center is brought to the wall and keeps the heat

transfer rate at a high level. Figure 5.20 shows temperature distribution on the vertical symmetry of the moving slug (same view of Fig. 5.19) at different simulation times. As expected, the heated liquid in the thermal boundary layer is moving toward the slug center and the thermal boundary layer remains thin.

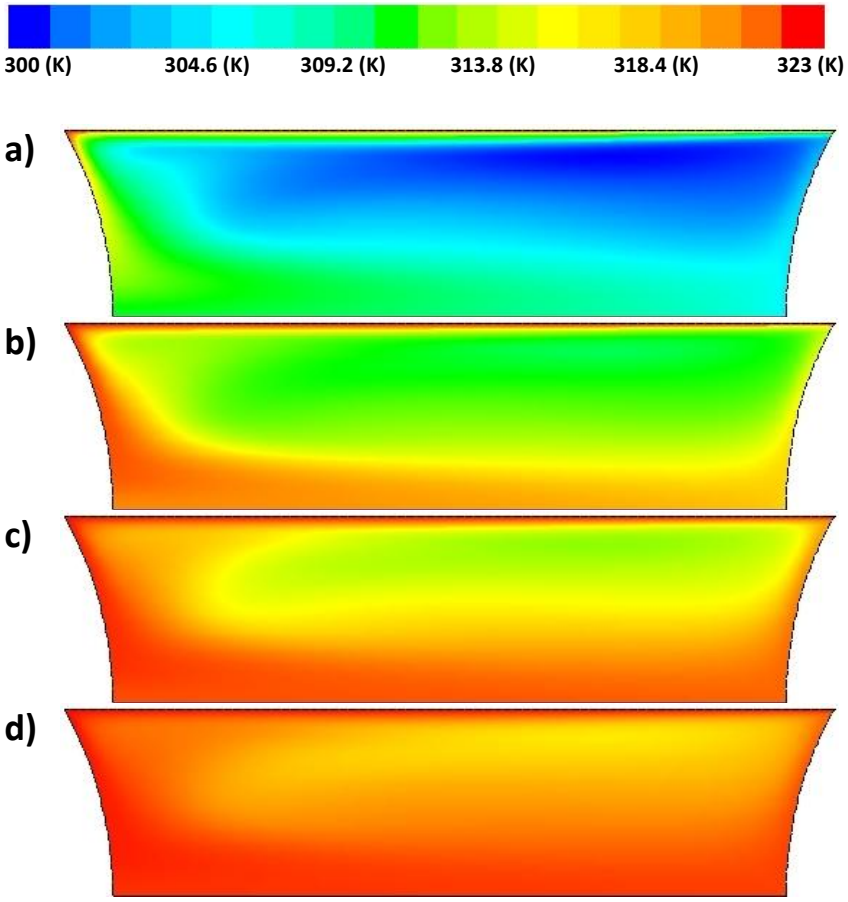

Figure 5.20: Contours of temperature in a moving liquid slug at vertical symmetry for $Re_L = 512$ at different simulation times (positions): a)$t = 0.0034s, (x = 2.5mm)$, b)$t = 0.0102s, (x = 7.5mm)$, c)$t = 0.0171s, (x = 12.5mm)$, d)$t = 0.0239s, (x = 17.5mm)$.

The circulation core can be observed in Fig. 5.20a close to the upper corner at

trailing interface. Since this region is so close to the wall, it will be heated fast due to thermal diffusion process. It can be understood from the boundary between hot and cold regions in Fig. 5.20b, that the temperature contours exactly obeys the streamlines shown in Fig. 5.19. After this time, diffusion of thermal energy from the center of slug toward the wall, helps the heat convection through the streamlines to squeeze the cold region inside the moving slug (Fig. 5.20c). After traveling a distance, the slug is going to be thermally saturated which means that the average temperature of the liquid inside the slug approaches the wall constant temperature. At this time, the heat transfer rate drops due to the small temperature difference between wall and flow temperatures. This is shown in Fig. 5.20d.

5.2.5 Comparison to Experimental Data

The numerical simulation results are compared to the experimental data reported by Betz and Attinger [153] in this section. They reported experimental Nusselt number, Nu, for two phase slug flows. They used segmented two phase flows in a heat sink with square microchannels under a constant wall heat flux boundary condition. However, they measured the local surface temperature at five points along the microchannels. The average surface temperature for non-boiling runs were 50, 75, and 90 (^oC) with the standard deviation less than 0.5 (^oC), due to the fact that the heat sink system was made of Aluminum i.e. highly conductive. Therefore, the equivalent Nusselt number for constant wall temperature boundary condition can be calculated. This

has been reported in Appendix 1, and as shown there, the difference is about 7%. After the comparison, the effects of different parameters (including Reynolds number, contact angle, and slug length) on slug flow heat transfer in square microchannels will be discussed, in the next section.

The simulation time which is the time a slug has traveled inside the microchannel and is about to exit can be determined using the slug velocity and the microchannel length from Betz and Attinger [153]. Heat transfer rates can then be nondimensionalized using Eq. 1.16 (wall to inlet temperature difference) and slugs temperature rise i.e. the difference between initial and final slug temperatures in the transient numerical simulations.

The Nu numbers at different Re numbers from the numerical simulations and Betz and Attinger [153] are shown in Fig. 5.21. The Re numbers less than 1000 have been considered in the comparison in order to ensure that the flow is not turbulent. As can be seen in Fig. 5.21, while there is a same trend, the Nu numbers from the numerical simulations are significantly higher than what experiments show. Different Re numbers lead to different microchannel dimensionless lengths, $L^\star$. The Nu numbers resulted from the present numerical simulations and experiments by Betz and Attinger [153] are presented in Fig. 5.22. This figure also includes "Leveque" limit of Nu [2] (See Eq. A1.1 in Appendix 1) in channels with a constant wall temperature versus microchannel dimensionless length, $L^\star$. As shown, simulation data points show significant enhancement in heat transfer compared to Betz and Attinger [153] data

points. The average difference is around 220% which means that the Nu numbers achieved from the numerical simulations are around three times more than the Nu numbers from the experiments.

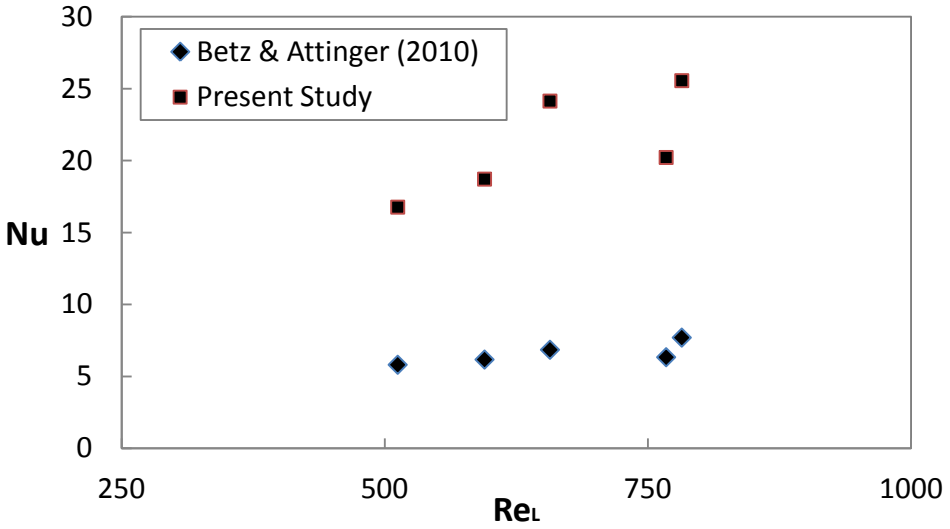

Figure 5.21: Nusselt number as a function of liquid phase Reynolds number.

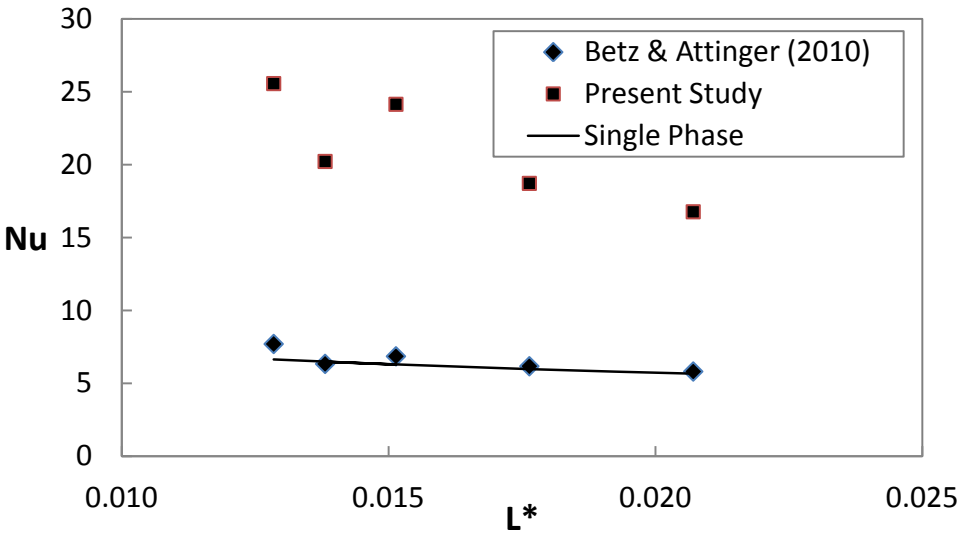

Figure 5.22: Nusselt number as a function of microchannel dimensionless length.

This significant difference could not be only due to numerical or experimental errors. There is one possibility for increase in heat transfer when moving slugs are considered individually in a moving frame of reference numerical simulations: *liquid film effects*. As discussed earlier (Fig. 2.2), a portion of the liquid inside a moving slug bypasses through the thin liquid film around the coming bubble and finally enters the next liquid slug. This bypassing liquid receives heat from the wall and become almost thermally saturated, due to its small mass, when is about to enter the next liquid slug. While this heat receiving process is fast due to the small liquid mass inside the film, it negatively affects the heat removal capacity of the next slug. The other negative effect of liquid film is decrease in the portion of liquid phase circulating inside moving slugs. These effects may be changed by change in the thickness of liquid film around the bubbles. This shows that in spite of what has been argued by some researchers so far, the effect of liquid film on heat transfer enhancement is might be an impediment.

In the numerical simulations of this section, moving slugs have been simulated individually in a moving frame of reference without considering any inlets or outlets to or from the adjacent films. This leads to complete circulation inside the simulated moving slugs. As a result, all the liquid is contributing in internal circulations which are the responsible mechanism for heat transfer enhancement. This may show that more enhancement in heat (or radial mass) transfer can be achieved using slug flows with no liquid film around the bubbles. This type of flows may be generated under certain conditions or using hydrophobic (or super hydrophobic) materials as microchannel wall.

Further studies (numerical and experimental) are required to quantitatively model this effect on the heat transfer process in this type of two phase slug flows in square channels. This can be pursued in the future.

5.2.6 Heat Transfer Prediction

As discussed in the previous section, heat removal process might be enhanced using separate slugs or a slug flow with a very thin liquid film around the bubbles. In this section, effects of different parameters on flow pattern and heat transfer in moving slugs inside square microchannels are studied. These parameters are Reynolds number, contact angle, and slug length.

Fig. 5.23 shows streamlines inside moving slugs (on horizontal symmetry plane) with $L_s/D_h = 3$ and $\theta = 120^o$ for different Reynolds numbers of 100, 200, and 500. As shown in Fig. 5.23a, in low Re slug flows the streamlines are parallel and circulation core is located approximately in the middle of the slug (horizontally). By increasing the Reynolds number, Re, the flow pattern changes and the circulation core moves toward the receding interface close to the microchannel walls. The flow pattern at $Re = 500$ in Fig. 5.23c is quite similar to the flow patterns in Fig. 5.19 for the same Re but a different contact angle.

Effect of Reynolds number on dimensionless heat transfer, $q^\star$, for the two moving slugs of Fig. 5.23 (a and c) is shown in Fig. 5.24. In both slug flows, $q^\star$ begin and end to same asymptotes and the difference is in the region in between. At the beginning

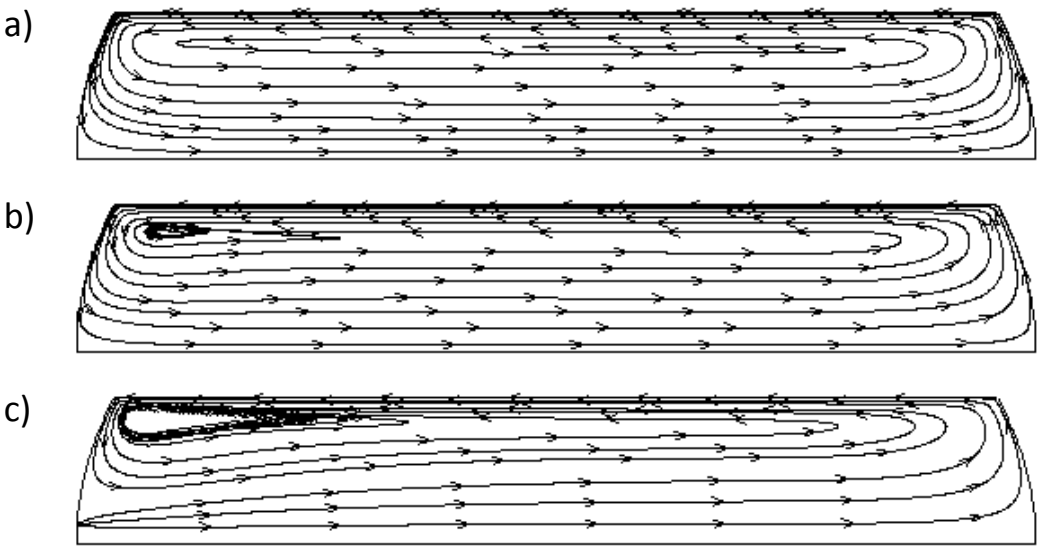

Figure 5.23: Streamlines inside moving liquid slugs with $L_s/D_h = 3$, $\theta = 120$ (horizontal symmetry plane) at different Reynolds numbers: a) $Re = 100$, b) $Re = 200$, and c) $Re = 500$.

of the process, the heat transfer is due to thermal diffusion into the thin thermal boundary layer (see Fig. 5.20a) and the circulations have not started contributing in the cooling process yet. This is why both start from the same asymptote. After a while, the moving slug with higher Re starts to receive more thermal energy and shows higher $q^\star$. This is due to the stronger circulations shown in Fig. 5.23c compared with Fig. 5.23a. Both slugs follow the fully developed asymptote after $L^\star \approx 0.05$.

Fig. 5.25 shows effects of the other parameter of interest, contact angle, on the dimensionless heat transfer in slug flows in square microchannels. As shown, the change in $q^\star$ is not significant when contact angle, θ, varies. The comparison in this figure has been conducted for three slug flows in square microchannels with same slug

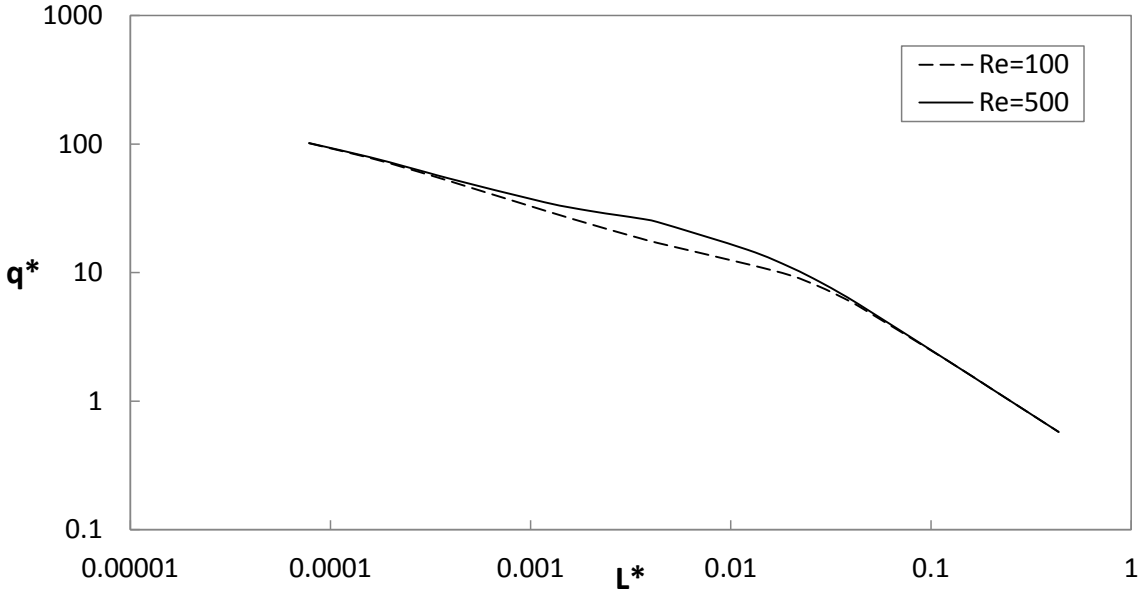

Figure 5.24: Dimensionless heat transfer, $q^\star$, for moving liquid slugs with same lengths and contact angles ($L_s/D_h = 3$ and $\theta = 120$) at different Reynolds numbers ($Re = 100$ and 500).

lengths (L_s/D_h =3) and Reynolds number (Re =500). The different contact angles of 60, 90, and 120 have been considered, and as shown, the difference is visible in the developing region (entrance region) compared to fully developed region. The $q^\star$ for slugs with $\theta = 90$ is 4% higher than the slugs with $\theta = 120$ in the developing region where $x^\star < 0.05$. The difference is around 0.2% in the fully developed region where $x^\star > 0.05$. The $q^\star$ difference in developing and fully developed regions between slugs with $\theta = 60$ and $\theta = 90$ are 9% and 0.5%, respectively. This shows that the dimensionless heat transfer, $q^\star$ for slug flows in square microchannels for different contact angles could be approximated using a right angle slug which is much simpler when developing computational domain for numerical studies. As such, the dimensionless

heat transfer, $q^\star$, are reported for slug flows with right angles for different slug lengths and Reynolds numbers in the rest of this section.

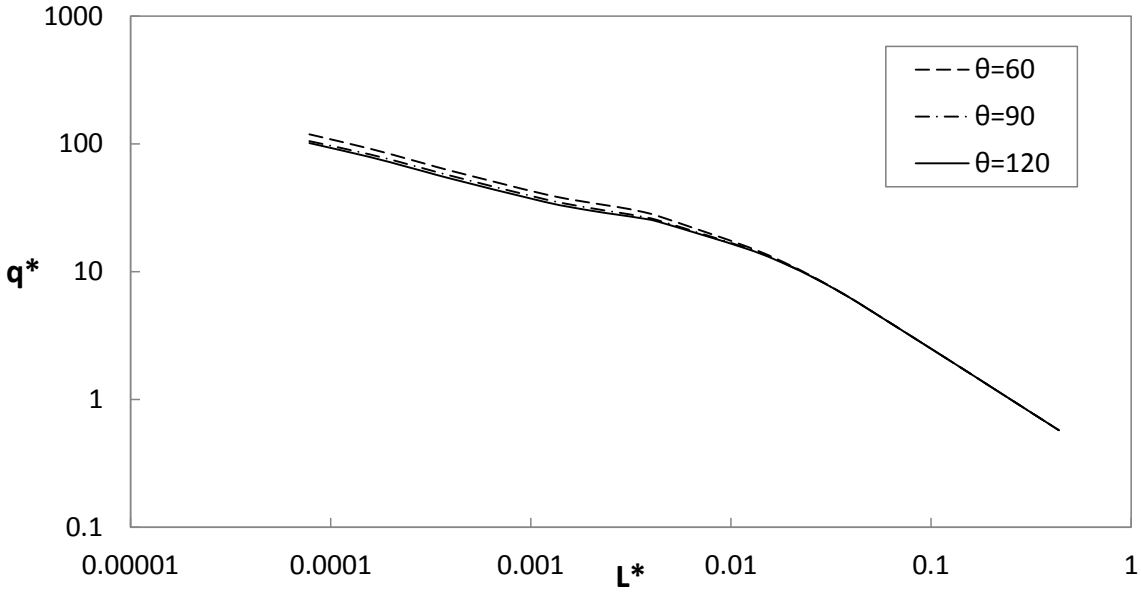

Figure 5.25: Dimensionless heat transfer, $q^\star$, for moving liquid slugs with same lengths and Reynolds numbers ($L_s/D_h = 3$ and $Re = 500$) at different contact angles (θ =60, 90, and 120).

Dimensionless heat transfer, $q^\star$, for slug flows with different slug lengths for two Reynolds numbers of 100 and 500 are shown in Figs. 5.26 and 5.27, respectively. These two figures could be used for heat transfer prediction in slug flows in square microchannels (with respect to α_L as discussed in section 3.3.2), when film thickness is very small or there is no film around the gas phase which is the case in hydrophobic microchannels. The single phase Slug flow $q^\star$ is also presented in these figures to show the potential enhancements in heat transfer using two phase slug flow in microchannels (Eq. 3.46).

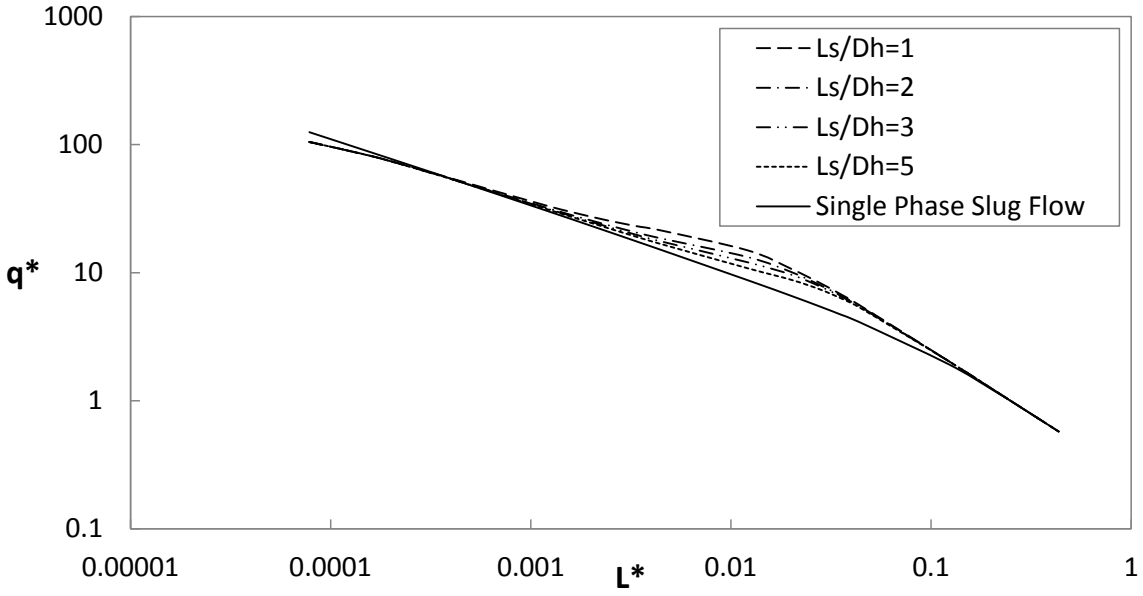

Figure 5.26: Dimensionless heat transfer, $q^{\star}$, for moving liquid slugs for different slug lengths (L_s/D_h =1, 2, 3, and 5) at same Reynolds numbers ($Re = 100$).

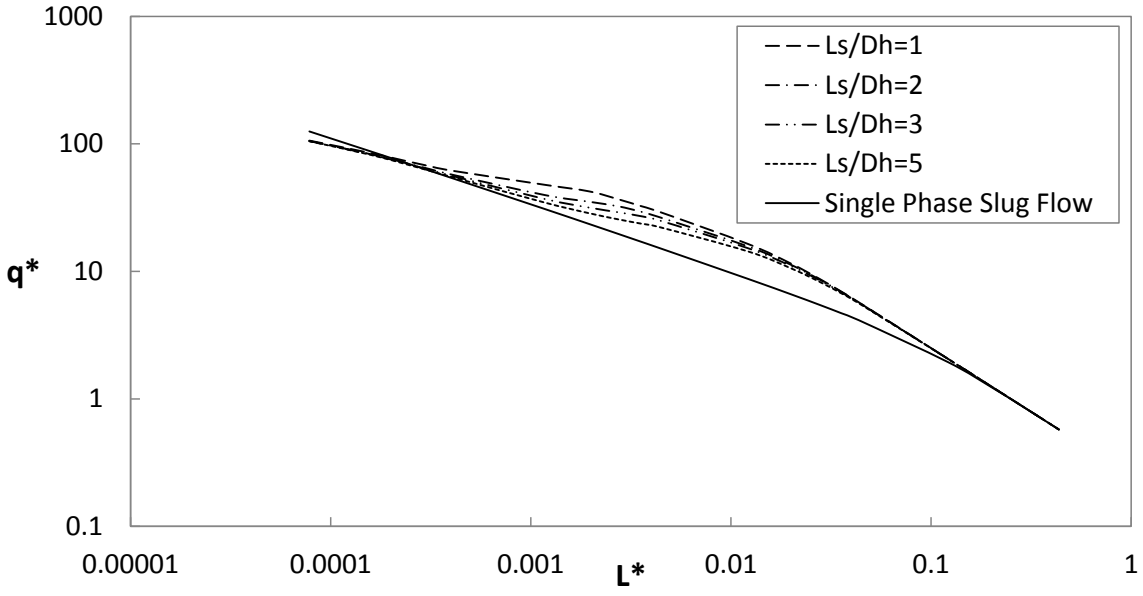

Figure 5.27: Dimensionless heat transfer, $q^{\star}$, for moving liquid slugs for different slug lengths (L_s/D_h =1, 2, 3, and 5) at same Reynolds numbers ($Re = 500$).

As Figs. 5.26 and 5.27 show slug flows with shorter slugs (with same α_L) provide higher heat transfer rates and an increase in slug length leads to a decrease in total heat transfer rate. This is due to increase in internal circulation effects in slug flows with shorter slugs. The fluctuations in the curves are due to fluid circulations inside the moving slugs which are not the case in the single phase slug flow. Furthermore, a slug flow approaches to the thermally saturated situation sooner than a single phase slug flow. This again shows greater heat removal rates from microchannel walls.

5.2.7 Summary

Heat transfer process under constant wall temperature boundary condition in two phase slug flows inside square microchannels has been considered in this section. Individual moving slugs have been simulated numerically and results have been compared to experimental data provided by Betz and Attinger [153]. The numerical Nu numbers showed significantly higher values but similar general trends compared with experimental Nu numbers.

The high difference could not be only a result of errors in numerical simulations or experiments. The film thickness around bubbles may be responsible to decrease total heat transfer in a two phase slug flow inside microchannels. This is due to negative effects of liquid film on thermal boundary layer renewal and amount of liquid in circulations inside moving slugs. This may show that heat transfer could be further increased in microchannel heat sinks using two phase slug flows under dry-out flow

condition i.e. two phases are in direct contact with microchannel wall. This type of slug flow could be generated using hydrophobic or superhydrophobic materials in microchannels.

The effects of Reynolds number, contact angle, and slug length on slug flow heat transfer have also been studied in this section. It has been shown that Reynolds number, Re, has a significant effect on slug flow heat transfer due to a change in flow pattern and circulation shape in moving slugs and with an increase in Reynolds number the heat transfer increases. Contact angle shows some small and negligible effects on slug flow heat transfer and it has been discussed that the hydrodynamics and heat transfer of slug flows might be simulated numerically using right angle computational domains (slugs) which are simpler to be developed. Finally, dimensionless heat transfer has been reported for different slug lengths and Reynolds numbers and the results could be used in prediction of heat transfer rates (with respect to α_L) when there is a very thin liquid film around the gas phase or there is no film which is the case in hydrophobic microchannels.

6 FIXED FRAME OF REFERENCE SIMULATION

This chapter includes numerical simulation of two phase slug flow using the VOF method and the fixed frame of reference. Using the liquid slug shape resulted from the VOF simulation, a moving frame of reference simulation is designed based on the method used in the previous chapters, and results are compared. Since the liquid film around the bubbles is neglected in the MFR single phase technique, one can examine the role of this film on heat transfer. The final section of this chapter includes numerical simulation of two phase slug flows with different film thicknesses, and the heat transfer process is examined.

6.1 Slug Flow in Circular Tubes

In this section, a two phase slug flow is simulated using the VOF method discussed in section 3.2.5. The simulation is carried out for constant wall temperature and constant wall heat flux boundary conditions. The liquid film thickness, pressure drop, and heat

transfer for both boundary conditions are compared to existing correlations.

6.1.1 Numerical Modeling

A FFR two phase simulation has been designed using almost the same method applied by Gupta at al. [44] with some differences. Figure 6.1 shows geometry of computational domain used in the present FFR two phase simulation. Water and air enter the microtube as the liquid and gas phases with a velocity of 0.5 (m/s). The thermal boundary condition (constant wall temperature or constant wall heat flux) has been applied after a sufficient distance from the entrance in order to ensure that a completely formed two phase slug flow is participating in the heat transfer process. Length of the entrance region has been set to $12R$ [74] and total length of the domain is $60R$. The radius of the microtube is 250 (μm). Fluids enter the microtube with a temperature of 300 (K). Simulations have been carried out for two thermal boundary conditions i.e. a constant wall temperature of 350 (K), and a constant wall heat flux of 30000 (W/m^2).

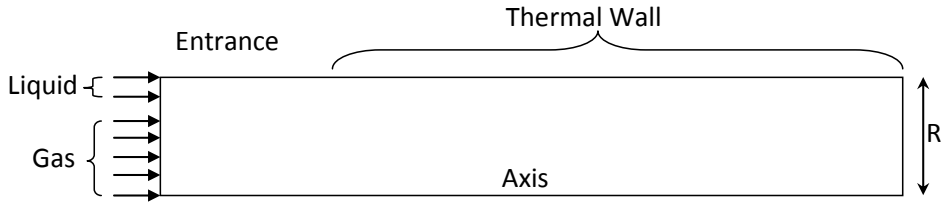

Figure 6.1: Schematic of the domain used in the FFR two phase simulation.

Table 6.1 presents thermophysical and transport properties used for the two phases in the FFR two phase simulation. The Reynolds number, Re, based on these properties

and the two phase stream velocity is around 280, much lower than the critical Reynolds value of turbulent flow. This critical value has been reported to 2300 for continuous internal flows [32] or 1000 for a moving discrete droplets [33], so the flow regime was considered laminar. The Capillary number, Ca, is 6.2×10^{-3}. Gravitational effects have been neglected based on the Bond number limit reported by Bretherton [43] i.e. 0.842. The Bond number is around 0.008 in the present study.

Table 6.1: Thermophysical and transport properties of the two phases used in the present study.

	water	air
$\rho(kg/m^3)$	997	1.185
$\mu(kg/m.s)$	8.899×10^{-4}	1.831×10^{-5}
$k(W/m.K)$	0.6	0.0242
$C_P(J/kg.K)$	4182	1006.43

6.1.2 Grid Independency and Validation Study

In the FFR two phase simulation the suggestion by Gupta et al. [44] has been applied in the grid generation i.e. using at least five finite volumes in the thin liquid layer region around the bubbles. Total number of 69 mesh were used in radial direction. The Taylor film thickness correlation [27] has been used for estimating the thickness of this layer and finer mesh has been used near the wall. The liquid film thickness of the present numerical simulation is 12.5 (μm) which is in a good agreement with existing correlations. Table 6.2 presents the film thickness obtained from different correlations. As expected (and reported by Gupta et a. [44] and Martinez and Udell [116]) the best

agreement is with Bretherton's model with a difference of 10%.

Table 6.2: The film thickness calculated using different correlations.

Correlation	Range	by:	$\delta(\mu m)$
$0.5Ca^{1/2}$	$5 \times 10^{-5} < Ca < 0.3$	Fairbrother and Stubbs [42], Taylor [27]	9.8
$1.34Ca^{2/3}$	$10^{-3} < Ca < 10^{-2}$	Bretherton [43]	11.3
$\frac{1.34Ca^{2/3}}{1+2.5\left(1.34Ca^{2/3}\right)}$	$10^{-3} < Ca < 1.4$	Aussillous and Quere [38]	10.1

As the next part of validation study, pressure drop is compared to the model suggested by Walsh et at. [139] (Eq. 2.9). The fRe group from the present numerical study is 69. The fRe group using the correlation by Walsh et al. [139] (Eq. 2.9) is $fRe = 75$. There is a good agreement between the simulation results and the experimental model, and the difference is around 8%.

Heat transfer under constant wall temperature boundary condition has been calculated as $q^\star = 13.99$ using Eq. 2.16. The heat transfer predictive model suggested by Muzychka et al. [30] for the same flow conditions and channel geometry is $q^\star = 14.86$ (Eqs. 2.15 and 2.17). As can be seen, the agreement is very good and difference is around 5.8%.

The mean Nusselt number, Nu_{0-L}, for constant wall heat flux along the heat transfer simulation section (see Fig. 6.3) has been calculated as $Nu_{0-L} = 27.3$ from the simulation results of this section. The heat transfer based on the correlation by Leung et al. [78] is $Nu_{0-L} = 28.9$. Again, the heat transfer simulation is in good agreement with the experimental data, and the difference is around 5%.

6.1.3 Slug Formation Process

The slug and bubble formation process has been shown in Fig. 6.2. As shown, the time period of slug/bubble formation is around 2 (ms) showing the fast process of slug formation.

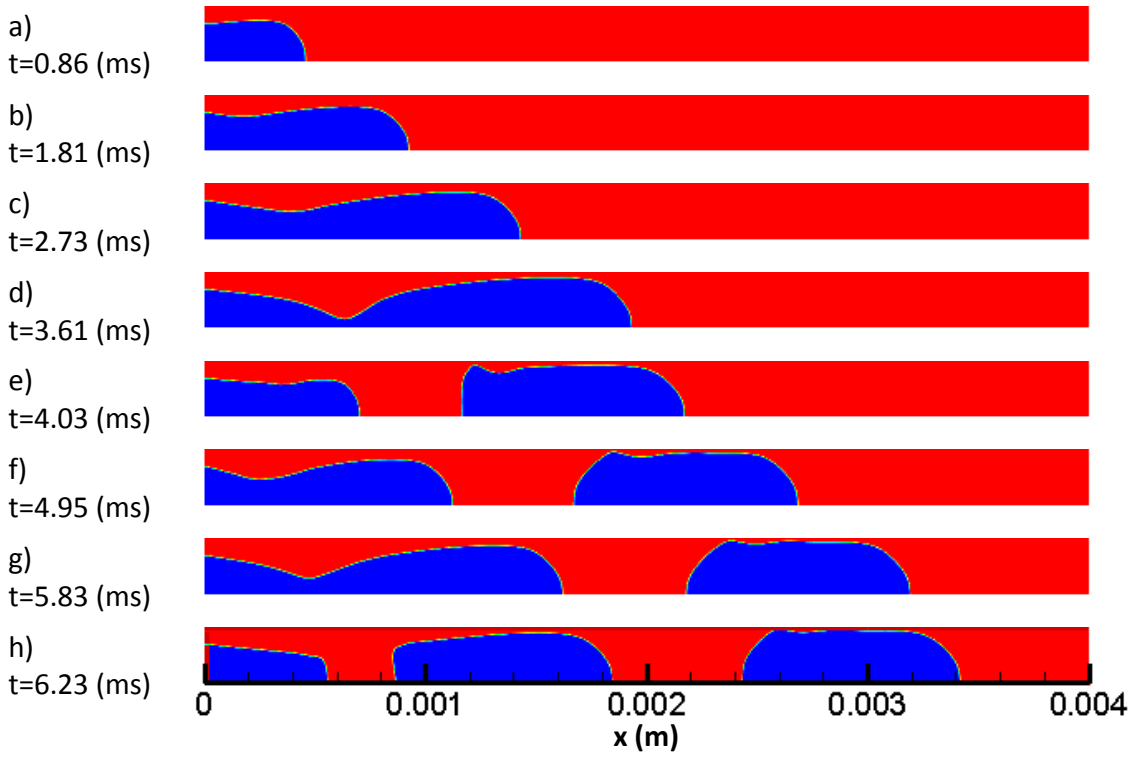

Figure 6.2: Slug formation process at different time steps, blue: air, red: water (with respect to centerline).

The three stage process of slug formation (or Taylor bubble formation) shown in Fig. 6.2 is similar to what has been reported by Shao et al. [37] including expanding, contracting, and necking. In Fig. 6.2a, the gas/liquid interface is moving toward the microchannel wall due to the injection of the gas phase through the concentric nozzle

located on the axis. After that, in 6.2b and 6.2c, the interface is moving away from the microchannel wall toward the axis. This is due to the local liquid phase pressure on the interface. In Fig. 6.2d, the necking stage is occurring and the Taylor bubble is about to separate from the injecting gas phase. This three stage process of bubble/slug formation is repeated from Fig. 6.2e to Fig. 6.2g. The first shaped bubble has its stable shape in Fig. 6.2h, and the liquid slug has just been shaped between the two neighbor Taylor bubbles.

Fig. 6.3 shows the phase contours resulted from the FFR two phase simulation of this section. This figure only shows the portion of the total computational domain that will be used in the next section to compare with the moving frame single phase simulation results (no-film slug flow). The length of aforementioned portion is about 9 mm which contains six liquid slugs at a given simulation time. The bubbles have a stable shape and the liquid film around them has been captured successfully as mentioned earlier.

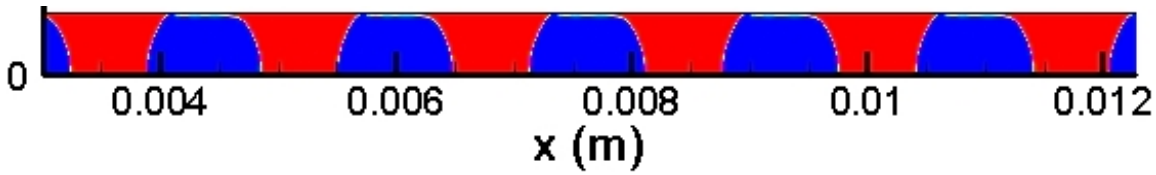

Figure 6.3: Phase contours of the FFR two phase simulation, red: liquid phase, blue: gas phase (with respect to centerline).

6.2 Wall Shear Stress and Heat Transfer Comparison of Slug Flows With and Without Liquid Film

In this section, the two phase slug flow which has been numerically simulated in the previous section will be used. In order to examine the role of liquid film on the wall shear stress and heat transfer process, a MFR single phase simulation is carried out for moving slugs with same length and shape to the liquid slugs simulated in the previous section. Local wall shear stress, local wall heat flux distribution at constant wall temperature, and local wall temperature distribution at constant wall heat flux are compared to each other and the role of liquid film on the aforementioned parameters are discussed.

6.2.1 Numerical Modeling

Fig. 6.4 schematically shows the geometry of computational domain used in the MFR single phase simulation. The computational domain shape and interface curvature of the MFR simulation has been obtained from the shape of liquid slugs in the two phase simulation results. The front and rear curvatures are not the same due to different pressures at the front and back of the bubbles. In typical Taylor flows bubble nose radius is smaller than its tail radius and this has been considered in this section. R is the microtube radius and has been set to 250 (μm), similar to the FFR two phase simulation of section 6.1.

In the MFR simulations, the liquid slug has been considered as a stationary slug

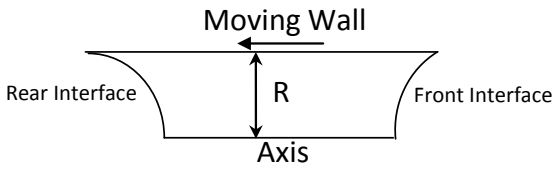

Figure 6.4: Schematic of the domain used in the MFR single phase simulation with real interface shape.

and the wall is moving with the velocity equal to the velocity of liquid slugs measured from FFR two phase simulation results. No-slip condition was applied to the moving wall. Zero shear stress and zero heat flux were applied to the front and rear interfaces in order to simulate interface between liquid and gas. The model was solved as a steady state flow in order to gain a fully developed hydrodynamic solution showing internal circulations. After that, the energy equation was solved using unsteady solver. Isothermal and isoflux thermal boundary conditions, same as the FFR two phase simulation, were applied to the wall. The initial temperature of the fluid was set to 300 (K). The same water thermophysical and transport properties of the two phase simulation were applied.

6.2.2 Grid Independency and Validation Study

After examining different grid sizes for the MFR single phase simulation it has been observed that using 40 nodes in the radial direction and dividing the near wall cells to half for five times gives a grid independence results. This way the finest cells are $\frac{1}{32}$ of the regular cells. Mean wall shear stress have been used to examine the

grid independency for this part. While no significant change in the mean wall shear stress will be obtained, additional iterations will be required for convergence using finer mesh. Figure 6.5 shows the velocities for different radial positions at the middle of the MFR computational domain and the parabolic velocity profile obtained from theory of laminar incompressible flow inside a tube. Agreement is good and mean and maximum differences are 1% and 2%, respectively. Figure 6.5 shows some difference between the numerical and theoretical velocity profiles near the axis which is the effects of circulation inside the moving slug. The reason is that the moving slug is not long enough, thus the flow in the middle is not completely same as the Poiseuille flow.

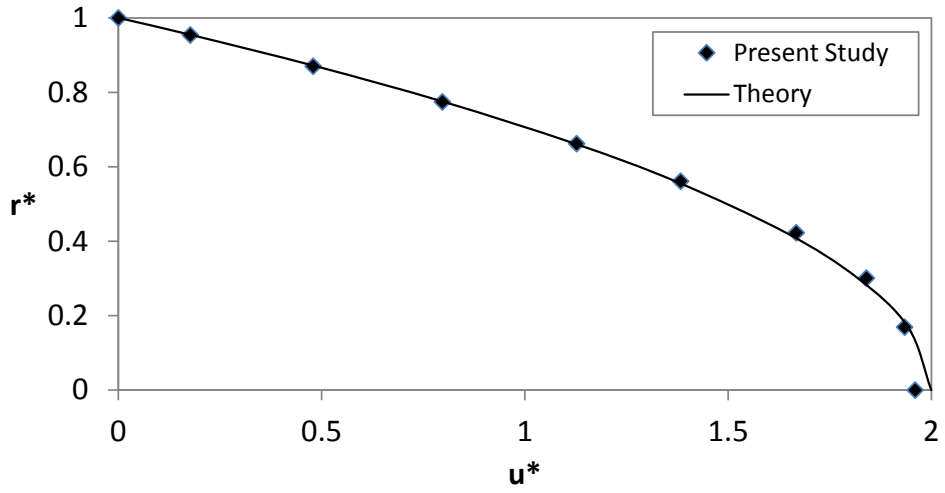

Figure 6.5: Numerical and theoretical dimensionless velocity profiles.

6.2.3 Wall Shear Stress With and Without Liquid Film

Fig. 6.6 shows the streamlines inside the liquid slug simulated using the MFR single phase technique. As shown, the circulation center is located toward the front interface.

Same flow patterns have been reported by Mehdizadeh et al. [63]. They showed internal circulations inside a moving droplet with flat interfaces inside a circular tube. The circulations inside moving slugs bring fresh liquid from the center to the wall and this way enhance the convection heat transfer.

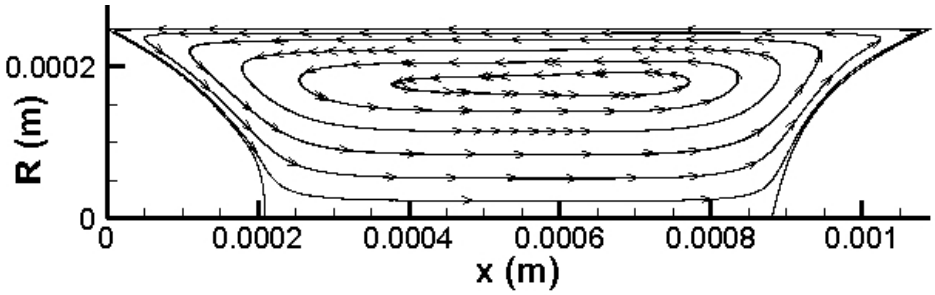

Figure 6.6: Streamlines inside the liquid slug (MFR single phase simulation).

Local and mean wall shear stress for the FFR two phase simulation and also for six single phase moving slugs at the same axial locations are shown in Fig. 6.7. As can be seen in Fig. 6.7 the MFR simulations can predict local distribution of the shear stress appropriately along the contact area between liquid and solid wall except for two front and end regions near the three-phase interfaces. In these two regions, local shear stress goes toward infinity due to the motion of the three-phase interface point. Furthermore, using the single phase MFR technique, one is not able to predict the local shear stress distribution at gas slug locations, where a thin liquid film exists between the moving gas slug and the solid wall.

The pressure drop in microtubes can be calculated using a simple force balance between shear force and pressure drop force. This way, the pressure drop in the two

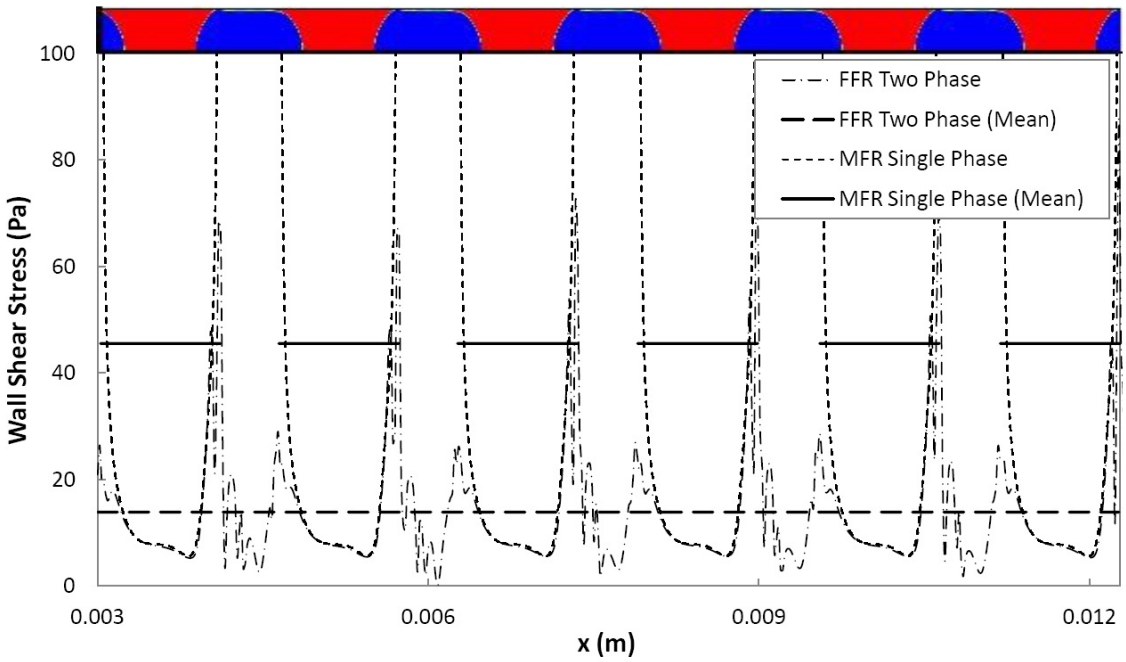

Figure 6.7: Local and average shear stress of the FFR two phase and MFR single phase simulations.

phase slug flow and single phase MFR simulations are 111,168 (Pa/m) and 364,304 (Pa/m), respectively. The pressure drop resulted from the MFR single phase simulation is significantly higher than the calculated pressure drop in the two phase flow simulation. This is due to the effects of moving three-phase interface lines which make the local shear stress increase to very large values near the front and end of moving slugs.

6.2.4 Heat Transfer at Constant Wall Temperature With and Without Liquid Film

Temperature contours for two phase flow simulation and also for six moving slugs at same axial locations are shown in Fig. 6.8. As shown in this figure, there are some differences in the general temperature distribution between two phase and single phase simulations. A significant difference is in the first slug. While the thermal boundary layer is still growing due to diffusion in the first liquid slug of the two phase flow, convection heat transport process (circulation effects) has actually started in the first single phase slug. Heated fluid has to be brought toward the center because there is a full circulation and no relation between neighboring slugs through a thin film around bubbles. Another potential reason might be the difference between applying the thermal boundary condition in the two simulations. In the FFR two phase flow simulation, a liquid slug gradually enters the heated section of the microtube and this makes a gradually feeding of the heated surface. This means that when a certain portion of the liquid slug has entered the heated section, say 30% for instance, the heat transfer occurs only in the first 30% of the slug and the rest (70%) does not contribute in the heat transfer process. On the other hand, the thermal boundary condition has been applied at all of the liquid-solid contact surface in the MFR simulation at the beginning of the simulation. The temperature distribution shown in the first single phase slug in Fig. 6.8 represents the simulation time required for the moving slug with the applied velocity to arrive at the same position of its corresponding slug in the two

phase snapshot. This distance is about half of the single phase moving slug length because the middle of this slug has an axial position of zero at the beginning of the simulation.

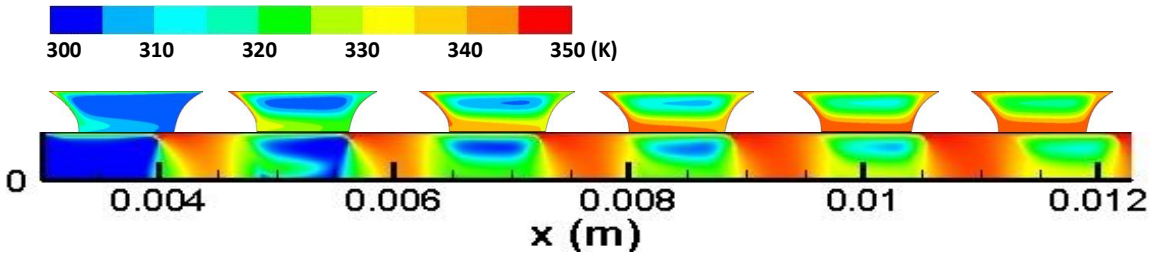

Figure 6.8: Temperature contours of both MFR single phase and FFR two phase simulations under constant wall temperature boundary condition.

The differences in the second and third slugs show that the heat convection in the MFR single phase simulation is more than the two phase slug flow because of effects of the thin liquid film around the bubble, which makes some of the liquid bypassing through this layer and does not contribute in the circulations. This bypass ratio depends on the Capillary number, Ca, and relative velocity between the bubble and the liquid [27]. Another potential reason for the difference in the temperature distribution is the thermal relationship between gas and liquid slugs, which has been ignored in the MFR single phase simulation. Since gas is going to be thermally saturated much faster than the liquid due to its lower heat capacity, this effect will vanish after a distance from the entrance and the temperature distribution of the two simulations are converging in the last slugs.

Fig. 6.9 shows the local and average wall heat flux for both of the simulations. As

discussed earlier, the difference between wall heat flux (local and average) is decreasing as the liquid slug moves forward through the microtube. Based on this figure, the average heat flux for the two phase slug flow for this specific tube length is around 419,883 (W/m^2). The average wall heat flux using the results of the MFR single phase simulation and Eq. 3.29 (see section 3.3.2, the first approach of integration) is 771,500 (W/m^2) which is almost twice the FFR two phase simulation results.

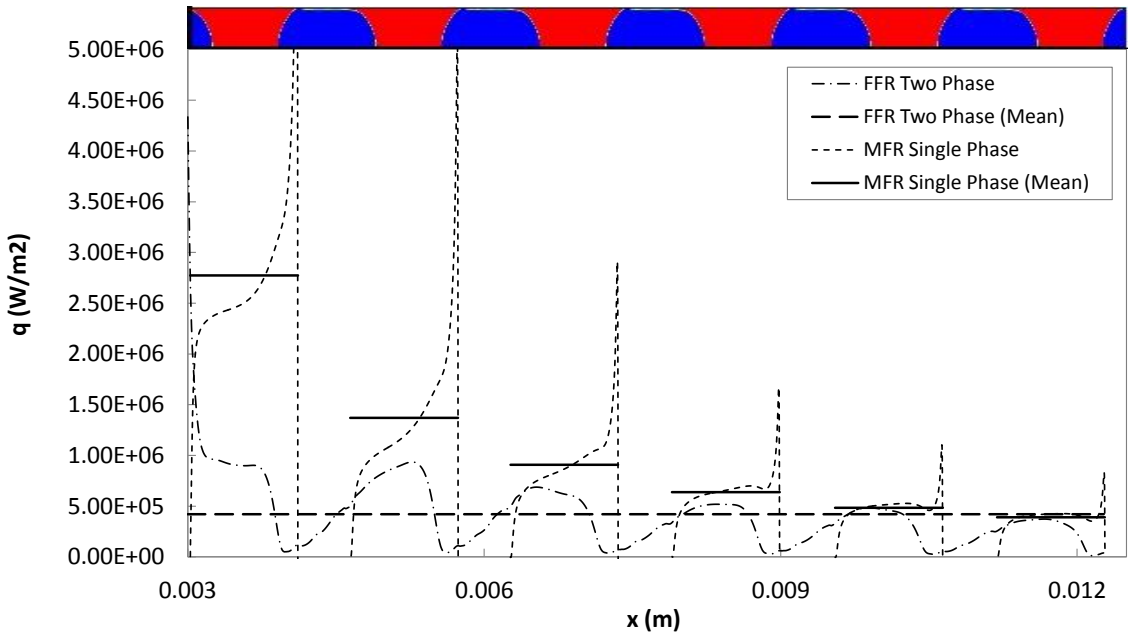

Figure 6.9: Local and mean wall heat flux of the FFR and MFR simulations for constant wall temperature.

Table 6.3 presents a quantitative comparison between the integrated single phase heat flux using Eq. 3.29 and two phase overall heat flux for different numbers of slugs including in the comparison from one slug to six slugs. As presented in the table, as the number of slugs increases the difference between predicted heat flux

using the fixed and MFR simulations decreases. More importantly, the difference between the two simulations reported in Table 6.3 is large and it cannot be only due to the simplifications discussed earlier. The possible reason for the greater mean wall heat flux under no-film condition may be neglecting the role of liquid film around the bubbles. In other words, more heat transfer can be achieved when there is no film around the bubbles. The fluid bypassing through the film will be thermally saturated before entering the next liquid slug. This is exactly where the boundary layer is renewed. Injection of hot liquid into the thin thermal boundary layer decreases the potential of heat transfer enhancement due to circulations. This shows that, in spite of what some researchers argue (e.g. [44]), liquid film around the bubble has negative effect on the total heat transfer process.

Table 6.3: Comparison between the MFR single phase (integrated using Eq. 3.29) and FFR two phase simulations heat flux results for different number of slugs including in the comparison.

Slugs	Two phase $\overline{q}\,(W/m^2)$	Single phase $\overline{q}\,(W/m^2)$	Difference (%)
1	893,676	2,712,840	+196
1, 2	675,756	1,650,905	+140
1, 2, 3	578,894	1,264,391	+118
1, 2, 3, 4	509,229	1,035,696	+107
1, 2, 3, 4, 5	461,073	881,272	+98
1, 2, 3, 4, 5, 6	419,883	771,500	+93

This conclusion is also in agreement with the very recent article published by Leung et al. [78] in 2012. They reported that in slug flows with higher Capillary numbers

heat transfer is lower, due to the decrease in circulation strength as a result of a thicker liquid film. The question is: *Is heat transfer under no film condition the maximum heat transfer can be achieved using slug flow if one keeps the same slug length, pitch, and velocity?* More studies, including experiments with hydrophobic microchannels, are required to address this question.

6.2.5 Heat Transfer at Constant Wall Heat Flux With and Without Liquid Film

Temperature contours for FFR two phase flow simulation and also for six moving liquid slugs at same axial locations to the liquid slugs of the FFR simulation are shown in Fig. 6.10. By comparing the temperature distributions of the two simulations one can observe that the circulation cores are being warmed faster in the FFR simulation. On the other hand the liquid near the circulation core remains cooler when the MFR single phase simulation has been used. This may show the effects of the liquid film around the bubbles in the heat removal process i.e. receiving heat when the liquid is in contact with the wall in the thin film region and bringing the heat to the incoming slug. This helps the circulation effects to heat up the core region. This has also been reported recently (in 2012) by Leung et al. [78] based on experimental observations (Eq. 2.14). Besides, the gas phase is going to be warmer than the liquid phase as it has a smaller heat capacity as shown in Fig. 6.10, and this might be another factor.

Fig. 6.11 shows the local wall temperature for both of the simulations of Fig. 6.10, and average wall temperature along liquid/solid contact area for discrete moving slugs

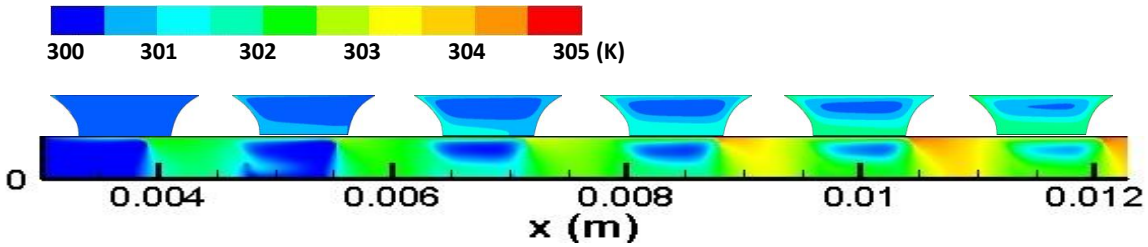

Figure 6.10: Temperature contours of both MFR single phase and FFR two phase simulations under constant wall heat flux boundary condition.

resulted from the MFR technique. As shown in this figure, a significant difference exists between the results of heat transfer simulations for constant wall heat flux boundary condition.

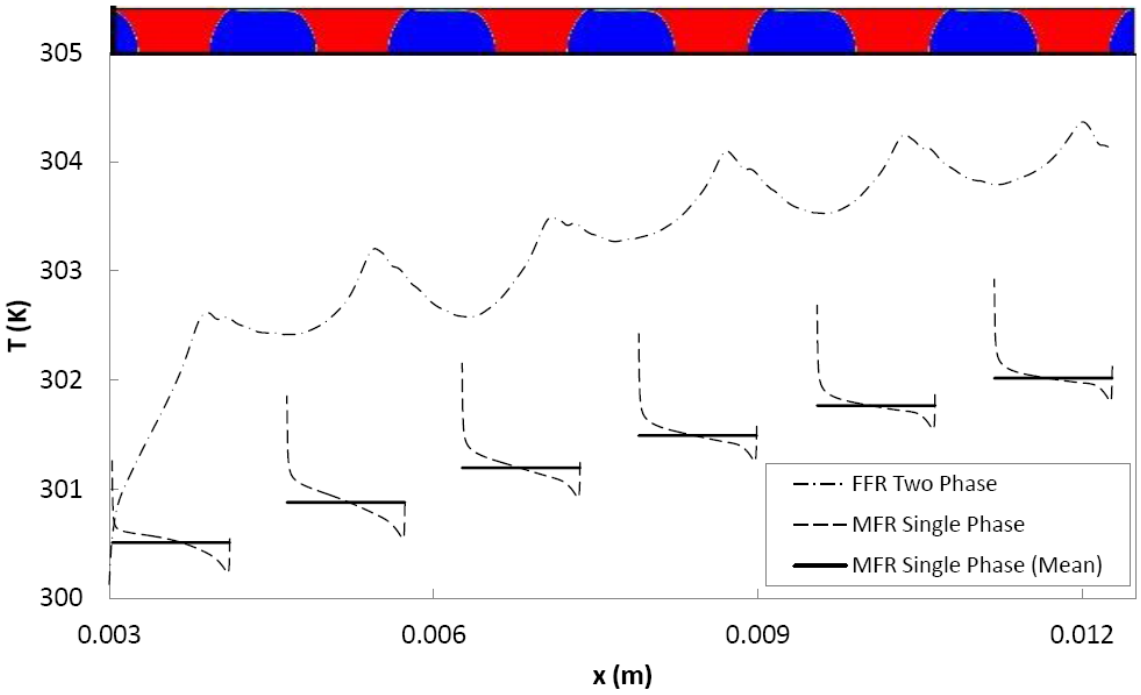

Figure 6.11: Local and mean wall temperature of the FFR and MFR simulations for constant wall heat flux.

Generally, the wall temperature is the parameter of interest in the constant wall heat flux problems, and the wall temperature at the liquid-wall contact region in the discrete slugs case is significantly lower than the case with a thin liquid film around the bubbles as shown in Fig. 6.11. This shows that the wall is cooler when there is no liquid film or dry-out conditions, which happens mainly when the microchannel surface is hydrophobic. Using hydrophobic materials for the microchannel wall causes the circulation inside the slugs to be the only mechanism of convective heat transfer between the wall and the fluid, so the liquid which is brought to the wall from the center is fresh and ready to accept more heat. On the other hand, when thin liquid films exist around the bubbles, the bypassed liquid through this film will be heated up and injected into the downstream liquid slug, which is coming after, and decreases the amount of fresh liquid from the center to be in contact with the wall, and this way decreases the heat removal capacity. There is no information on the wall temperature where the gas phase touches the wall (no liquid film), since the gas phase is not included in the present MFR simulation. The effects of this thin liquid film and its thickness on the heat transfer requires more studies (experimental and numerical) and will be dealt with in the future. As mentioned earlier, Leung et al. [78] published an article recently (2012) showing this impediment effect on heat transfer in slug flows at constant wall heat flux boundary condition.

6.2.6 Summary

The ability of MFR single phase technique for simulating pressure drop and heat transfer of two phase slug flow inside hydrophilic microtubes has been examined in this section using numerical simulation. While in most situations there is a thin liquid film around the bubbles, this film and its effects are generally neglected when a moving wall single phase simulation is desired. It has been assumed so far that the MFR single phase simulation is applicable for hydrophobic microtube wall materials where both phases touch the wall. A slug flow has been simulated numerically in this section and then a MFR single phase computational domain has been generated using the real liquid slug shapes resulting from the two phase simulation. It has been shown that the predicted pressure drop in MFR technique is higher than that predicted by FFR two phase simulation. This is the effect of moving three phase contact line which has been mentioned in the past literature as well.

A comparison between the two simulations of heat transfer for constant wall temperature and constant wall heat flux has been conducted for a different number of liquid slugs. Neglecting the contribution of liquid film around the bubbles has been discussed to be a source of difference.

In both thermal wall boundary conditions, heat transfer is observed to be greater than slug flows with liquid film around the bubbles. This leads to a higher wall heat flux and a cooler wall for isothermal and isoflux walls, respectively. The important question here is: *Is the heat transfer at no film condition the maximum heat transfer*

can be achieved using a slug flow? While this study has shown potential of slug flows with no film for a further increase in heat transfer, more studies are required in this area in the future. In this case, using hydrophobic materials in microchannels lead to complete circulations inside liquid slugs and consequently more heat transfer, but the penalty is increase in pressure drop as discussed in the present work. Understanding the effects of film thickness on heat transfer needs more detailed studies and will be performed in the next section.

When a MFR single phase simulation is desired, the following limitations should be considered:

- The MFR single phase simulation overpredicts the pressure drop for a two phase slug flow with liquid film around the bubbles. This is mainly due to the moving three phase contact line which produces high wall shear stress.
- A suddenly applied heat transfer at the wall is one of the approximations of this technique and gives different results from the real situation in the slugs which just entered the heated section. To minimize this effect, one should assure that enough slugs are included in the system which depends on microtube length, slugs length, and pitch.
- The heat transfer between liquid and gas slugs is neglected in the MFR technique. This could be important for a few slugs which have just entered a heat sink, since the gas slugs are thermally saturated very soon after due to their lower heat capacity.

6.3 Effects of Film Thickness on Heat Transfer

As discussed earlier, increases in the wall shear stress and heat transfer in slug flows are due to the internal circulations inside moving liquid slugs. A portion of liquid bypasses through the thin film around bubbles and decreases the portion of liquid in the circulations and this way has effects on pressure drop and heat transfer. The Capillary number has been included in the existing pressure drop models which implies these models consider the effects of film thickness. On the other hand, film thickness has not been considered in published models and correlations for heat transfer.

As examined in the previous section, liquid film could possibly have an impediment effect on heat transfer. In this section, three slug flows with different film thicknesses have been simulated numerically under constant wall heat flux and constant wall temperature boundary conditions to compare the heat transfer process and examine the effects of the liquid film. The surface tension coefficient between liquid and gas can be decreased by adding surfactant to the liquid phase without significant change in other properties such as density and conductivity [154, 155]. Based on the definition of Capillary number, decrease in surface tension increases Ca and consequently liquid film thickness around the bubbles. Given that the simulation in section 6.1 has been performed for pure water properties, this is the only physically possible direction of change in Ca. Walsh et al. [59] has suggested a correlation based on experimental data (Eq. 2.18). They did not include Ca in their correlation, but their experiments have been carried out for $6.6 \times 10^{-4} < Ca < 8 \times 10^{-3}$. This experimental correlation

will be used as a mean for slug flows with Capillary numbers lower than the Capillary numbers considered in this section. The different film thicknesses considered in this section are around 12, 15, and 20 (μm). The first one (12 (μm)) has been considered for pure water and larger thicknesses can be achieved using surfactant.

6.3.1 Numerical Modeling

The slug flow simulated in section 6.1 is considered as the base slug flow in this section. For direct comparison, Capillary number of this flow is changed and other simulations are performed. In total, three slug flows with same conditions and mass flow inlets but with different Ca numbers have been considered in this section. This gives three slug flows with different liquid film thicknesses and provides opportunity to study the effects of film thickness on heat transfer process. The Ca number for the first, second, and third simulations are 6.18×10^{-3}, 9.47×10^{-3}, and 14.83×10^{-3}, respectively. The film thickness based on the Bretherton's correlation (Eq. 2.3) and these Ca numbers are 11.3, 15, and 20.8 (μm) for the three simulations, respectively.

6.3.2 Grid Independency and Validation Study

The liquid film around bubbles needs to be captured correctly in numerical simulations in order to achieve valid results for pressure drop and heat transfer. As explained in section 6.1, mesh resolution in the film region (estimated using Bretherton's correlation) is increased to ensure that sufficient grids are available in the film region. Other details are same to what has been reported in section 6.1.

Table 6.4 and Fig. 6.12 present a comparison between the film thickness for all the simulations in the present study and the existing correlations based on experimental data. It has been reported by Gupta et at. [44] and Martinez and Udell [116] that Bretherton's correlation provides the best fit. As shown in Table 6.4 and Fig. 6.12, there is a very good agreement with Bretherton's correlation [43] and present simulations in all cases. The differences are 10%, 3%, and 5% for the three simulated cases, respectively. As explained in section 6.1, (and in the literature review) the best agreement is expected with Bretherton's model. This has also been reported by other researchers [44, 116].

Table 6.4: The film thickness captured in the present study versus existing correlations.

Case	*Ca*	Correlation	$\delta(\mu m)$
1	6.18×10^{-3}	Taylor [27]	9.8
		Bretherton [43]	11.3
		Aussillous and Quere [38]	10.1
		Present study	12.5
2	9.47×10^{-3}	Taylor [27]	12.1
		Bretherton [43]	15
		Aussillous and Quere [38]	13
		Present study	14.6
3	14.832×10^{-3}	Taylor [27]	15.2
		Bretherton [43]	20.8
		Aussillous and Quere [38]	16.8
		Present study	21.9

The pressure drop of the simulations are compared to the recent model suggested by Walsh et al. [139] (Eq. 2.9). Figure 6.13 shows the simulation points and the experimental model. As shown, all the simulations are in the range of Taylor flow as

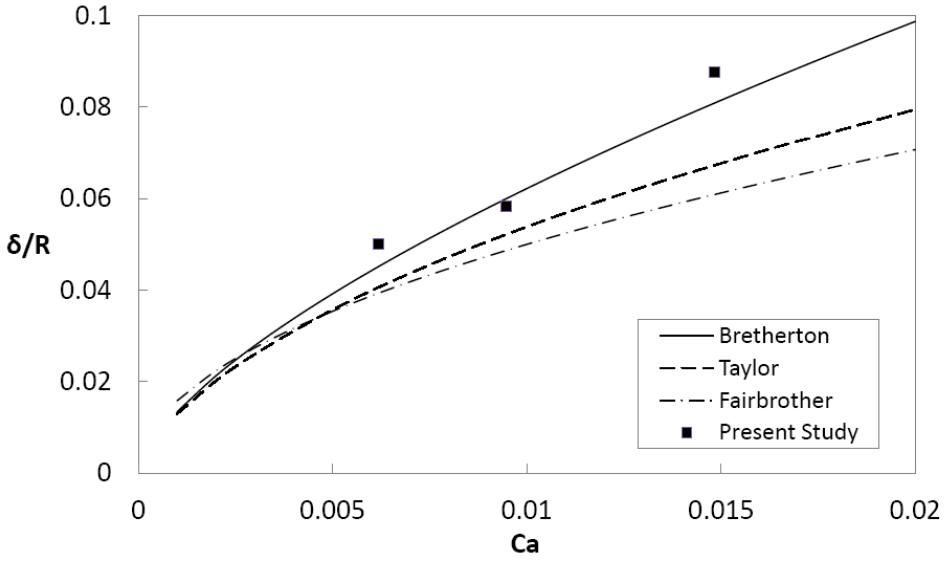

Figure 6.12: Comparison of the film thickness calculated in the present study with the available models.

discussed by Walsh et al. [139] (see Eq. 1.5). This is when $L^{\star}\left(\frac{Ca}{Re}\right)^{0.33} << 1$, and the pressure drop is significantly greater than the single phase Poiseuille flow asymptote of $fRe = 16$. As shown in Fig. 6.13, the agreement is good. The differences between present simulations and the model are 8%, 7.2%, and 5.1% for the cases 1 to 3, respectively.

The mean Nusselt number, Nu_{0-L}, for slug flows of this section are compared to the recently published correlation by Leung et al. [78] in 2012, in Fig. 6.14. As shown, the agreement is good and the differences are 5%, 2.5%, and 2% for the three simulation cases, respectively. The numerical Nusselt numbers of Fig. 6.14 are for the simulation times which will be used in graphs of the next section. However, the experimental Nusselt numbers from Leung's correlation are time averaged.

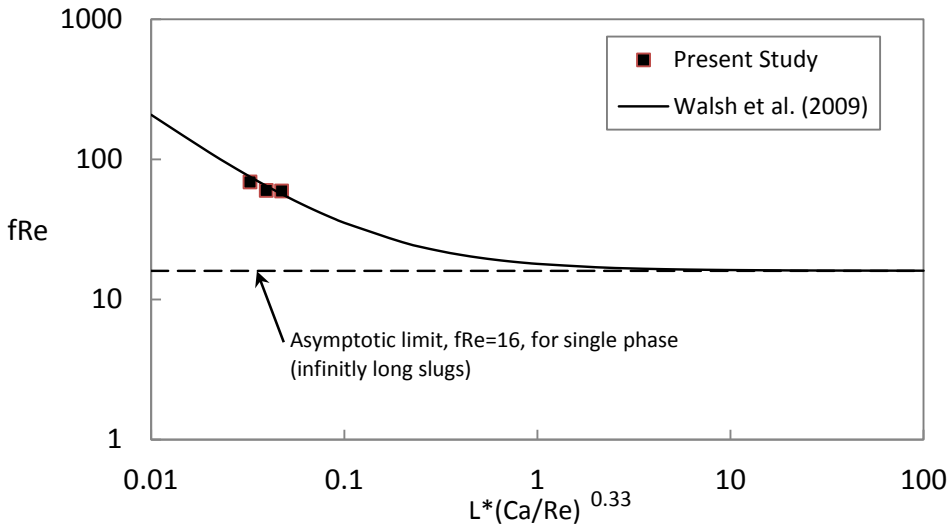

Figure 6.13: Comparison of pressure drop (fRe) from Walsh's model [139] and present simulations.

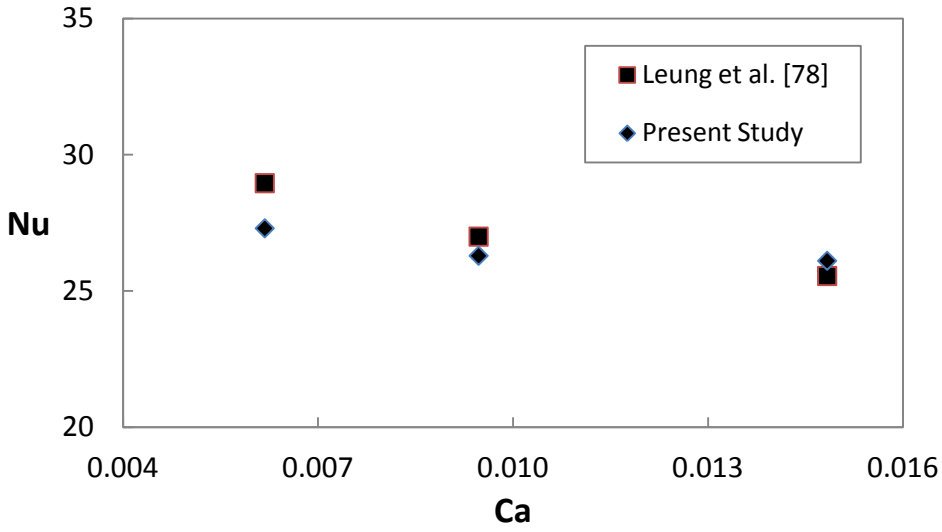

Figure 6.14: Comparison of the mean Nusselt number, Nu_{0-L}, of the simulations of this section and correlation by Leung et al. [78].

6.3.3 Heat Transfer Under Constant Wall Heat Flux

Fig. 6.15 shows the phase contours resulted from the first simulation in this section. This figure only includes a part of the computational domain in which the constant

wall heat flux has been applied to the wall. This is well after the entrance and the liquid slugs have their steady shape. The Taylor bubbles also have a stable shape and the liquid film around them has been captured successfully using the methodology discussed earlier. This portion includes six moving liquid slugs and five bubbles between them.

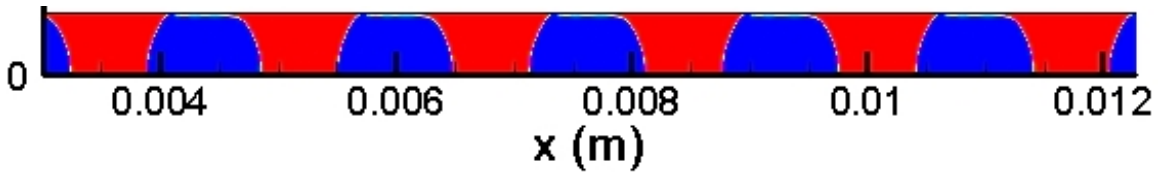

Figure 6.15: Phase contours of the present simulation (case 1, $Ca = 6.18 \times 10^{-3}$), red: water, blue: air.

Temperature contours of the window of Fig. 6.15 is presented in Fig. 6.16. As one can see, a portion of heated liquid in the slugs thermal boundary layer is circulating inside the slugs and the rest is bypassing through the thin film around the bubbles and enters the next liquid slug. This is where fresh liquid from slug center is expected to renew the thermal boundary layer and keep the its thickness low. Injection of hot liquid to this region decreases the thermal capacity and hence the cooling performance of the liquid slug.

Bubble shapes in the three slug flows simulated in this section are shown in Fig. 6.17. As shown, the film thickness is smaller in the first case (as expected) but the throat close to the bubbles end are approximately at the same thickness. This means that the jet flow from the liquid layer into the coming liquid slug might have a higher

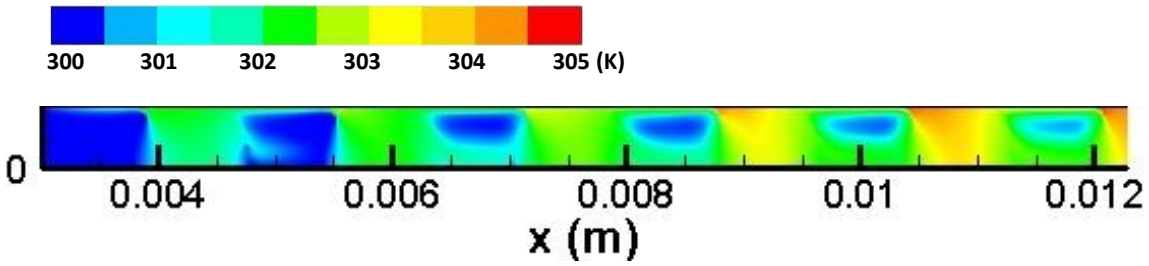

Figure 6.16: Temperature contours of the present simulation (case 1, $Ca = 6.18 \times 10^{-3}$).

velocity in the third case (thickest film), since more liquid from the film enters through a same size entrance.

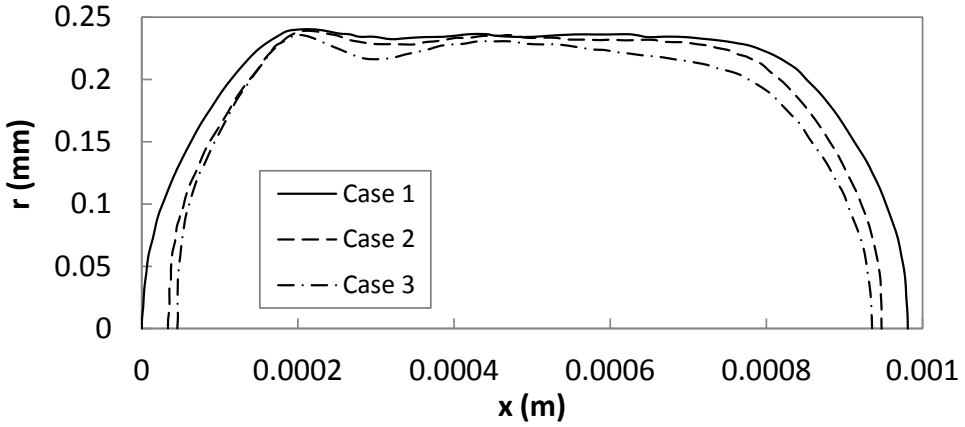

Figure 6.17: Bubble shapes from present simulations.

As shown in Fig. 6.17, bubble lengths are also different in the three cases. The third case has the shortest bubble length. When one see this fact beside the thicker liquid film which denotes lower bubble diameter, it means that the bubble volume is lower in the third case. Figure 6.18 shows a part of the slug flow of case 3, in the same microtube length as Fig. 6.15 for case 1. A comparison between these two figures

shows that the number of bubbles is more in the third case, 6, against 5.5 in the first case. This leaves 6 liquid slugs in the first case (Fig. 6.15), but around 6.5 liquid slugs in the third case (Fig. 6.17). Therefore, a change in Capillary number not only leads to a change in film thickness but also to changes in slug and bubble lengths. The present study is considered as an initial step toward studying the potential effects of the liquid film thickness on heat transfer process in two phase slug flows.

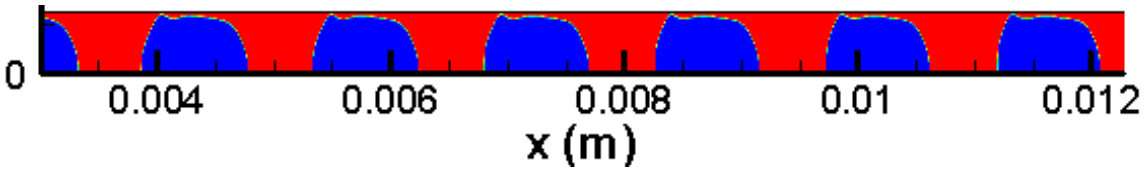

Figure 6.18: Phase contours of the present simulation (case 3), red: water, blue: air.

The wall temperature is the parameter of interest in constant wall heat flux boundary conditions. In cooling processes, the purpose is keeping wall temperature as low as possible. If the wall temperature rises up in a region it means a low heat transfer rate. Figure 6.19 shows the local wall temperature in the first case. As can be observed, there is a local hot spot just after each bubble trailing end. This means less heat removal because the hot liquid exits the film and decreases the rate of heat transfer. Besides, the wall temperature is greater close to bubble ends as compared to bubble fronts where liquid is flowing into the film. This is because the small portion of liquid bypassing through the film receives heat and its temperature rises up quickly due to the small amount of mass in the film. Heated liquid then exits the film and enters the coming slug and decreases the liquid slug heat removal capacity as mentioned above.

This shows that in spite of what has been assumed so far the contribution of the liquid film around the bubbles in heat transfer is probably an impediment.

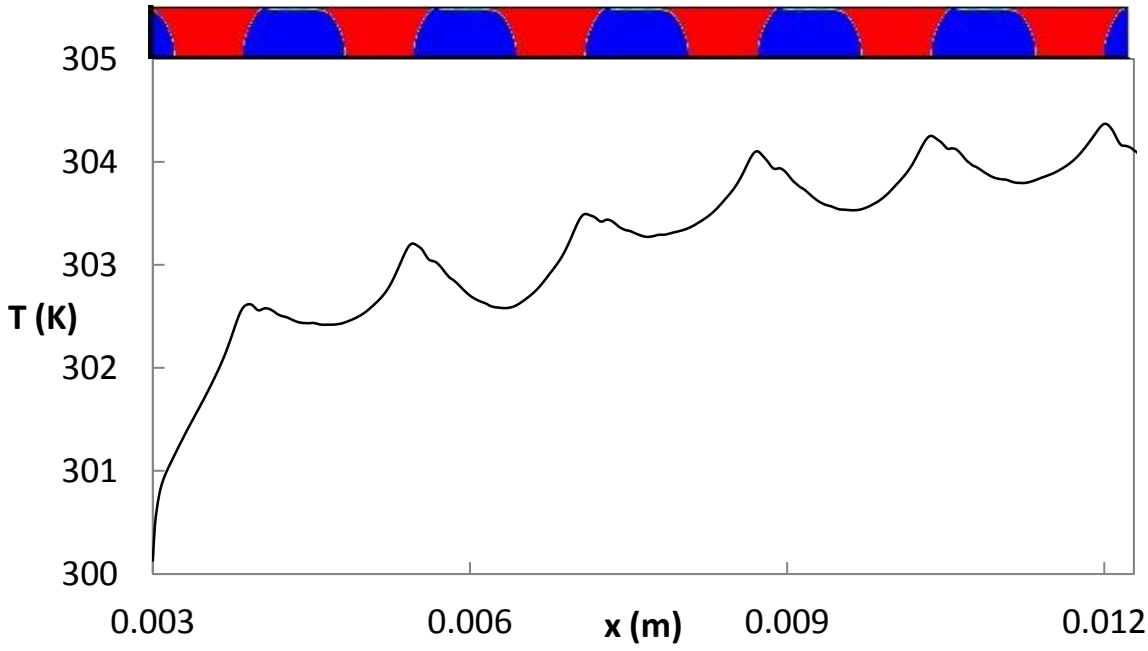

Figure 6.19: Local wall temperature for slug flow (case 1).

The local dimensionless wall temperature in the three slug flows of this section are compared to each other in Fig. 6.20. Based on the slightly different bubble lengths in the three simulations, slug locations are not approximately same after the first few slugs. Therefore, only the region including three slugs is shown in Fig. 6.20 where there is a chance to compare wall temperature directly. Figure 6.20 also includes dimensionless wall temperature simulated in section 6.2 for a similar slug flow (similar to case 1) but with no liquid film using moving frame of reference technique. As discussed earlier, the main case (case 1, $Ca = 6.18 \times 10^{-3}$) has been simulated considering pure water. In reality, by adding surfactant, one can increase Capillary

number, Ca, and hence the film thickness. The heat transfer modeled by Walsh et al. [59] is also included in Fig. 6.20. Since this model has been developed for $6.6 \times 10^{-4} < Ca < 8 \times 10^{-3}$, it can be considered as a mean for Capillary numbers lower than the base case (case 1), if one starts from a lower Capillary number with pure water.

Fig. 6.20 shows a rapid increase in all three cases at the beginning of the heated length of the microtube. This is due to the initial thermal boundary layer development in the liquid slug which just entered the heated region. After this entrance effect, there is a rise in dimensionless wall temperature with periodic fluctuations. While the axial location of local maximums are almost the same for the first slugs they separate after a few periods. As discussed, this is mainly due to the slight difference in slug and bubble lengths which can also be seen in Fig. 6.17. Different bubble lengths gives different levels of effects on the heat transfer process since longer bubbles provide longer films and consequently higher liquid temperature in the jet region. Therefore, a better comparison can be made based on the first few slugs. In the future, more simulations are required to achieve the same slug and bubble lengths with different film thicknesses.

As can be seen from the dimensionless wall temperature in Fig. 6.20, the first case gives lower wall temperature among the three simulated slug flows in this section (cases 1 to 3). This is mainly due to the difference in film thicknesses. In the first case, the film thickness is smaller so less fluid bypasses through the film and consequently

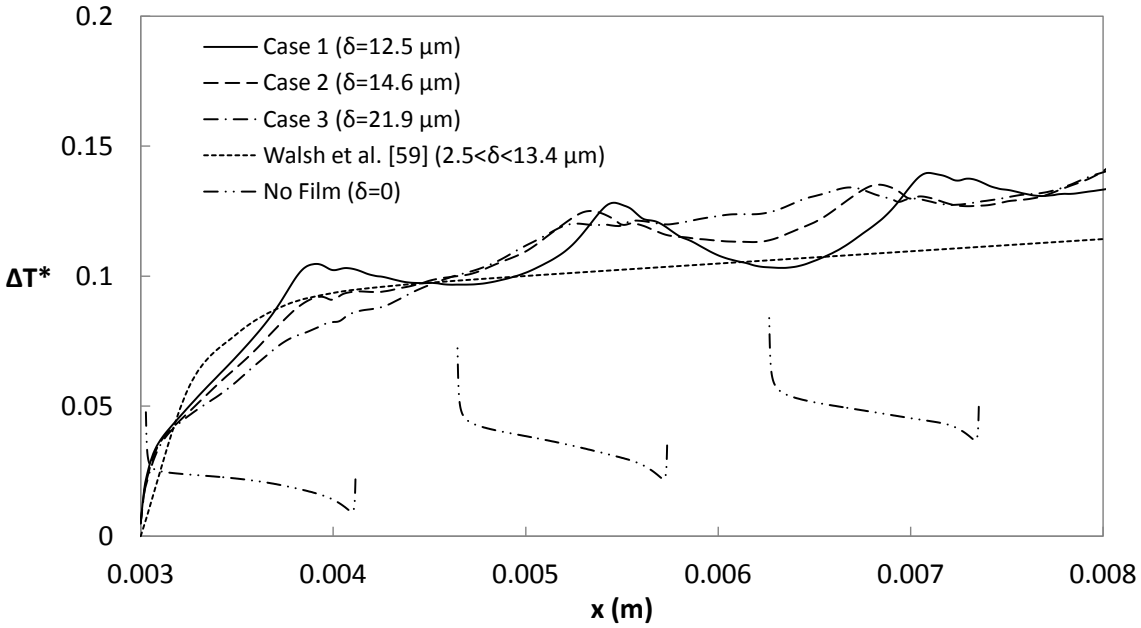

Figure 6.20: Dimensionless wall temperature for three cases of slug flows (see Table. 6.4) and slug flow with no film (see section 6.2).

there is less negative effect on the heat transfer process inside the liquid slugs. The peaks are almost at the same order of magnitude in the first and second cases. This could probably be due to the small difference in the film thicknesses. Figure 6.20 shows that by increasing film thickness, the circulation effects decrease. The fluctuations in wall temperature is dampen out in the third case (with the thickest film). This shows the effects of circulations on heat transfer have been dampen due to the decrease in the circulation strength after thickening of the liquid film.

The dimensionless wall temperature in the no-film slug flow is much lower than the slug flows with film. Detailed discussion has been reported in section 6.2. When there is no film around the bubbles, all the fluid is in circulation and hence there is

an enhancement in heat transfer process.

The liquid film thickness has been increased in this section from 12.5 (μm) to 21.9 (μm), and the reason was discussed earlier. In order to compare the results to dimensionless wall temperature at thinner films, the experimental correlation by Walsh et al. [59] is used in Fig. 6.20. This correlation corresponds mean dimensionless wall temperature for the film thicknesses between 2.5 (μm) to 13.4 (μm), based on the range of Capillary number in the experiments. As shown in the figure, the mean wall temperature is lower when a slug flow with a thinner liquid film is used, which means a higher heat transfer rate. Therefore, the experimental model is in agreement with the discussion above. As discussed earlier, the numerical simulations shown in Fig. 6.20 are for certain simulation times, but the correlation by Walsh et al. [59] is based on time averaged temperature measurements using a camera. This is why, the oscillations shown in CFD graphs are not shown in the experimental curve in this figure.

6.3.4 Heat Transfer Under Constant Wall Temperature

Fig. 6.21 shows local wall heat flux for the first and third cases and also the slug flow with no film around bubbles (from section 6.2). The axial range of this figure is the same as Fig. 6.20 in order to show only the few first liquid slugs where axial positions of the liquid slugs are approximately the same. The comparison between case 1 and the slug flow with no film has been presented in detail in section 6.2.3. In this section

the focus is on differences between cases 1 and 3.

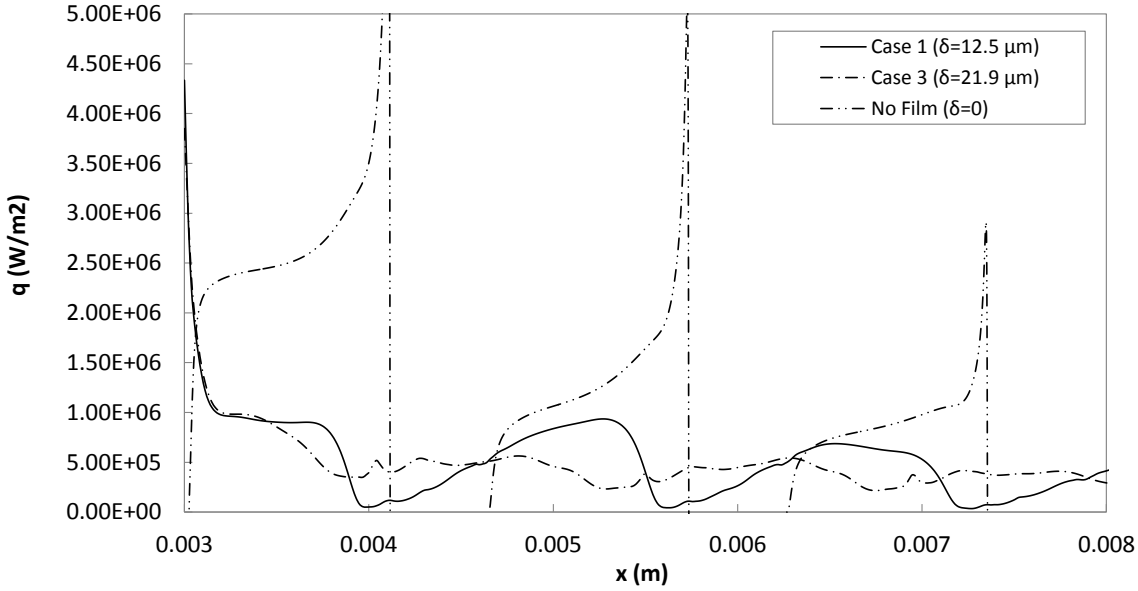

Figure 6.21: Wall heat transfer for two cases of slug flows (see Table. 6.4) and slug flow with no film (see section 6.2).

As shown in Fig. 6.21, the local heat flux curves are not very different in the beginning of the heated section of the microchannel. The local minimums in case 1 happen in the liquid slug area close to the bubble ends, where the heated liquid is injected to the liquid slug through the thin film, as discussed in in section 6.2.3. These fluctuations (local minimums and maximums) have been somehow dampen out in the third case. In other words, while the third case is a two phase slug flow with circulations in the liquid slugs, it shows a different behavior. This phenomenon might be explained as a result of a thicker liquid film in case 3, as compared to case 1. More liquid bypasses through the film when the film thickness is greater, leaves less liquid in circulation. As reported in the first chapter, the circulations are the reason for heat

transfer enhancement in two phase slug flows. This shows that the film thickness has some effects on heat transfer process and needs to be considered when one is about to develop a model for two phase slug flow heat transfer in microscales. Presenting more details and quantifying these effects has been left for future studies using experiments or more numerical simulations.

6.3.5 Summary

There is a significant number of articles stating that using slug flows at small scales provides a higher heat or mass transfer. Thickness of the liquid film around bubbles has a significant effect on flow pattern i.e. internal circulations inside liquid slugs. These circulations are the reason for enhancement in the heat or mass transfer. Possible effects of film thickness on heat transfer have not been included in the existing models on heat transfer, except the one recently published by Leung et al. [78] in 2012. In this section, three slug flows with different film thicknesses have been simulated numerically to make a direct comparison between heat transfer processes under constant wall heat flux and constant wall temperature boundary conditions. The results show that a slug flow with a thinner film thickness can probably provide a higher heat transfer due to a smaller negative effects of liquid bypass through the film on internal circulations. This could also show that using hydrophobic (or superhydrophobic) materials as microchannel wall probably provide a higher heat transfer rate (cooling performance) since there is no film around the gas phase and all of the liquid circulates

inside slugs. Future studies may include experiments for a wide range of Ca to study and quantify possible heat transfer enhancement with thinner films.

7 SUMMARY AND CONCLUSIONS

Hydrodynamics and heat transfer in two phase gas-liquid slug flows at microscales have been examined in the present thesis, using different numerical simulation techniques. In general, the circulations inside moving liquid slugs enhance fluid mixing and heat (or mass) transfer. The intensity of these circulations is a function of different parameters including flow conditions, channel geometry, and liquid slug shape and dimensions. The effects of all of these parameters on heat transfer have been studied numerically in this thesis.

7.1 Objectives of The Present Thesis

The objectives discussed in section 3.1 have been met in the present thesis, as follows:

7.1.1 Implementation of The Moving Wall Technique

Two approaches for integration of heat transfer along the channel when using the moving wall technique have been discussed in section 3.3.2. In the first approach, the slugs

heat transfer were integrated, that requires knowing exact locations and heat transfer rates of all the slugs. In the second approach, the energy balance was used based on the enthalpy difference of slug initial and final states. The second approach requires reading one data point from the dimensionless heat transfer graphs, as discussed in detail in section 3.3.2. These two approaches were assessed and compared in sections 4.1.4 and 4.2.5, for parallel plates channels and circular channels, respectively. The results were in agreement.

7.1.2 Three Dimensional Flow Pattern Effects on Heat Transfer in Moving Slugs Between Parallel Plates

The assumption of two dimensional simulation when one wants to simulate a moving slug between two parallel plates has been questioned and discussed in section 5.1. Two dimensional and three dimensional simulations for similar moving slugs (dimensions and shape) have been performed and the results have been compared. The comparison has been conducted for different slug lengths, contact angles, and Reynolds numbers, Re. It was shown that if the channel is much longer than the thermal entrance region, the results are in agreement and the 2D assumption is valid. In shorter channels or for shorter slugs, the 3D flow pattern can affect the heat transfer process, and the 2D assumption does not provide accurate results. In all cases, the two dimensional results must be nondimensionalized using the slug real contact area and volume as discussed in detail in section 5.1.

7.1.3 Potential Effects of Liquid Film on Heat Transfer in Slug Flows

As the first step, the heat transfer results from moving wall and fixed frame of reference simulations were compared. Since the liquid film around the bubbles are neglected in the moving frame of reference single phase simulations, it was expected that the total heat transfer using this type of simulation should be lower than the full two phase simulations. The results were in reverse. These comparisons have been performed for circular channels and square channels (with experimental data) in sections 6.2 and 5.2.5, respectively. It was argued that the reason is that at no-film condition, all the liquid is in circulation and this way the heat transfer in slug flows with no film is greater.

As the next step, three slug flows with different liquid film thicknesses have been simulated using fixed frame of reference technique in section 6.3. The results were compared to an available heat transfer model proposed by Walsh et al. [59] for a lower range of film thicknesses. The comparison confirms the aforementioned discussion about the circulation effects. Recently, Leung et al. [78] published a model (in 2012) based on experimental data and showed the impediment effects of liquid film thickness on heat transfer, at isoflux wall boundary condition. The results of the present thesis have been compared to this recent correlation, and a perfect agreement was observed.

7.2 Assumptions and Limitations of the Present Thesis

Different assumptions have been used in the present thesis. However, the results of this research show agreement with published experimental, analytical, and numerical results by other researchers. The more important ones are as follows:

7.2.1 Contact Angle Hysteresis

Static contact angle of a liquid slug depends on the fluids properties and wall material. When a slug moves in a channel, the advancing and receding contact angles are not similar. These angles, θ_A and θ_R, depend on the flow conditions as well, for example Reynolds number, Re. In section 4.2.4, the heat transfer in slug flow inside circular channels have been simulated including advancing and receding contact angles along with assuming only the slug static contact angle. It has been shown that the difference is insignificant, and the reason has been discussed. Therefore, in other channel geometries, one can assume static contact angle for heat transfer simulation (equal advancing and receding contact angles) if the correlations for contact angle prediction is not available in the literature.

7.2.2 Temperature Effects on Fluid Properties

It is normal in convection heat transfer problems, to assume fluid properties at mean temperature. In this thesis, the fluid(s) inlet temperature has been assumed at room temperature in all simulations. In most electronic cooling designs, there is a limit of 50 (^oC) in fluid temperature rise. Therefore, all the fluid(s) properties have been eval-

uated at the temperature of 50 (^oC) i.e. the average between the inlet and allowable exit temperatures. The agreement between numerical results and existing models (see sections 6.1.2 and 6.3.2 for example) supports this assumption.

7.2.3 Phase Change

Considering water and air as the two phases and the typical fluids and wall temperatures in the numerical simulations, boiling is not expected. However, evaporation occurs at all temperatures. In this thesis, which follows other published literature, phase change has been neglected, and results are in good agreement with experimental data or the existing models. This shows that latent heat transfer due to evaporation is insignificant. To evaluate how much heat is removed by evaporation, especially in the thin film region, one can perform two sets of simulations with and without evaporation and compare the results. This could be done in the future.

7.2.4 Effects of Wall Material Conductivity

So far, almost all the numerical simulations of convection heat transfer in two phase slug flows published in the literature have been performed considering the flow inside the microchannels along with the well accepted thermal boundary conditions of isothermal and isoflux walls, with a few exceptions. One might ask how significant are the effects of axial heat conduction inside the wall of the microchannel due to the temperature fluctuations caused by periodical nature of the two phase slug flows. Addressing this question requires conjugated numerical simulations including both the

flow and the wall, which could be pursued in the future. Again, the agreement between numerical results of the present thesis with available models shows the validity of this assumption.

7.2.5 Marangoni Effects

After adding surfactants to slug flow to change the Capillary number, Marangoni effects may cause surface tension gradient along the interface and this way can have compounding effects. Based on the agreement between numerical results in the present thesis with experimental data points, this might be insignificant in the range of applications considered here. However, Marangoni effects can be addressed in detail in future studies.

7.3 Conclusions and Remarks

The main conclusions and remarks of the present thesis are as follows:

7.3.1 Effects of Slug Shape and Dimension on Heat Transfer

The numerical simulation results of the present thesis show that liquid slug length has significant effects on heat transfer. For all the cross sections considered in this thesis, from circle to square, by a decrease in moving slug length heat transfer is enhanced (at same α_L), due to increase in circulation effects along channel.

While the difference between the advancing and receding contact angles, and the deviation between them and static contact angle can affect the flow pattern in the

corners, the effects on heat transfer has been shown to be insignificant. The reason has been discussed in section 4.2.4.

7.3.2 Effects of Flow Conditions on Heat Transfer

The effects of Reynolds number on two phase slug flow heat transfer has been investigated in this thesis. It has been shown that a change in Reynolds number can change the flow patterns and circulation shapes inside the moving liquid slugs, and this way it affects heat transfer process. A two phase slug flow with a higher Reynolds number removes heat more than a low Reynolds flow, but it will be thermally saturated at smaller $x^\star$ values, as shown in the present thesis.

7.3.3 Effects of Film Thickness on Heat transfer

As reported in section 3.3.1, a numerical simulation of two phase slug flow can be performed using different types of computational domains. Both moving and fixed computational domains have been considered in this research and results have been compared to each other. This led to a new finding which suggests that the thin liquid film around gas bubbles might have a negative effect on heat transfer. This has also been examined for different film thicknesses for isothermal and isoflux wall boundary conditions. The results are in a very good agreement with the recently published experimental model (2012) by Leung et al. [78] (see section 6.3.2). They also reported the same trend and discussed the same way. Therefore, liquid film thickness, or Capillary number, should be considered when one develops a model for heat transfer

for two phase slug flows.

7.4 Path Forward

Based on the results of the present thesis, there are still many open questions and discussions on heat transfer in two phase slug flows. The followings are the most important ones which could be considered and addressed in the future studies:

7.4.1 Experimental and Numerical Studies of the Effects on Film Thickness on Heat Transfer

It has been observed that the liquid film around bubbles could have a negative effect on heat transfer in two phase slug flows by changing the portion of liquid in circulation and bypass. Further evidence has recently been published by Leung et al. [78] in 2012, but more is required to to evaluate quantitatively the significance of this effect. Therefore, more numerical simulations and also experiments on this phenomenon are needed which could be considered in the future studies.

7.4.2 Two Phase Slug Flow Heat Transfer in Meandering Microchannels

This research and many of the published studies on heat transfer in two phase slug flows are for straight microchannels. As shown by some researchers, curvature of the flow path affects the flow pattern by generating secondary flows. The effects of channel curvature on heat transfer in two phase slug flows can be investigated in the future.

7.4.3 Liquid-Liquid Two Phase Slug Flows

Generating a gas-liquid two phase slug flow and phase separation are more straightforward than a liquid-liquid two phase slug flow. The drawback is the gas phase cannot contribute in heat transfer process significantly due to its small heat capacity compared to liquid phase. Using liquid-liquid two phase flows for heat removal at microscales can also be considered in the future studies.

References

[1] Tuckerman D. B., Pease R. F. W., 1981, "High-Performance Heat Sinking for VLSI, *IEEE Electron Device Lett. EDL-2*, 5, pp. 126-129.

[2] Shah R. K., London A. L., 1978, " Laminar Flow Forced Convection in Ducts", *Academic Press*.

[3] Krishnamurthy S., Peles Y., 2008, "Flow boiling of water in a circular staggered micro-pin fin heat sink, *International Journal of Heat and Mass Transfer*, 51, pp. 1349-1364.

[4] Escher W., Michel B., Poulikakos D., 2009, "Efficiency of optimized bifurcating tree-like and parallel microchannel networks in the cooling of electronics, *International Journal of Heat and Mass Transfer*, 52, pp. 1421-1430.

[5] Chen Y., Cheng P., 2002, "Heat transfer and pressure drop in fractal tree-like microchannel nets, *International Journal of Heat and Mass Transfer*, 45, pp. 2643-2648.

[6] Rosaguti N. R., Fletcher D. F., Haynes B. S., 2006, "Laminar flow and heat transfer in a periodic serpentine channel with semi-circular cross-section, *International Journal of Heat and Mass Transfer*, 49, pp. 2912-2923.

[7] Geyer P. E., Fletcher D. F., Haynes B. S., 2007, "Laminar flow and heat transfer in a periodic trapezoidal channel with semi-circular cross-section, *International Journal of Heat and Mass Transfer*, 50, pp. 3471-3480.

[8] Gupta R., Geyer P. E., Fletcher D. F., Haynes B. S., 2008, "Thermohydraulic performance of a periodic trapezoidal channel with a triangular cross-section, *International Journal of Heat and Mass Transfer*, 51, pp. 2925-2929.

[9] Rosaguti N. R., Fletcher D. F., Haynes B. S., 2007, "Low-Reynolds number heat transfer enhancement in sinusoidal channels, *Chemical Engineering Science*, 62, pp. 694-702.

[10] Lee P. S., Garimella S. V., 2006, "Thermally developing flow and heat transfer in rectangular microchannels of different aspect ratios, *International Journal of Heat and Mass Transfer*, 49, pp. 3060-3067.

[11] Aparecidot J. B., Cotta R. M., 1990, "Thermally developing laminar flow inside rectangular ducts, *International Journal of Heat and Mass Transfer*, 33, pp. 341-347.

[12] Tiantian Z., Li J., , 2008, "Laminar Flow Characteristics in Entry Region in Microchannels, *Proceedings of the ASME Micro/Nanoscale Heat Transfer International Conference, MNHT2008*, pp. 1257-1264.

[13] Lee J., Mudawar I., , 2007, "Assessment of the effectiveness of nanofluids for single-phase and two-phase heat transfer in micro-channels, *International Journal of Heat and Mass Transfer*, 50, pp. 452-463.

[14] Ijam A., Saidur R., Ganesan P., 2012, "Cooling of minichannel heat sink using nanofluids, *International Communications in Heat and Mass Transfer*, 39, pp. 1188-1194.

[15] Ho C. J., Wei L. C., Li Z. W., 2010, "An experimental investigation of forced convective cooling performance of a microchannel heat sink with Al2O3/water nanofluid, *Applied Thermal Engineering*, 30, pp. 96-103.

[16] Mudawar I., 2011, "Two-Phase Microchannel Heat Sinks: Theory, Applications, and Limitations", *Journal of Electronic Packaging*, 133, 041002-1.

[17] Angeli P., Gavriilidis A., 2008, "Hydrodynamics of Taylor Flow in Small Channels: A Review", *Proceedings of the IMechE Part C Journal of Mechanical Engineering Science*, 222, pp. 737-750.

[18] Gupta R., Fletcher D. F., Haynes B. S., 2010, "Taylor Flow in Microchannels: A Review of Experimental and Computational Work", *The Journal of Computational Multiphase Flow*, 2, pp. 1-31.

[19] Kreutzer M. T., Kapteijn F., Moulijn J. A., Heiszwolf J. J., 2005, "Multiphase monolith reactors: Chemical reaction engineering of segmented flow in microchannels", *Chemical Engineering Science*, 60, pp. 5895-5916.

[20] Talimi V., Muzychka Y. S., Kocabiyik S., 2012, "A Review on Numerical Studies of Slug Flow Hydrodynamics and Heat Transfer in Microtubes and Microchannels", *International Journal of Multiphase Flow*, 39, pp. 88-104.

[21] Muzychka Y.S., Walsh E., Walsh P., Egan V., 2011b, "Non-Boiling Two Phase Flow in Microchannels", *CRC Handbook of Microfluidics and Nanofluidics, (in press)*.

[22] Triplett K. A, Ghiaasiaan S. M., Abdel-Khalik S. I., Sadowski D. L., 1999, "Gas-Liquid Two-Phase flow in Microchannels Part I: Two-Phase Flow Patterns, *International Journal of Multiphase Flow*, 25, pp. 377-394.

[23] Liu, D. and Wang, S., 2008, "Flow Pattern and Pressure Drop of Upward Two Phase Flow in Vertical Capillaries, *Ind. Eng. Chem. Res.*, 47, pp. 243-255.

[24] Akbar M. K., Plummer D. A., Ghiaasiaan S. M., 2003, "On Gas-Liquid Two-Phase Flow Regimes in Microchannels, *International Journal of Multiphase Flow*, 29, pp. 855-865.

[25] Sur A., Liu D., 2012, "Adiabatic Air-Water Two-Phase Flow in Circular Microchannels, *International Journal of Thermal Sciences*, 53, pp. 18-34.

[26] Galbiati L., Andreini P., 1994, "Flow Pattern Transition for Horizontal Air-Water Flow in Capillary Tubes: a Microgravity Equivalent System Simulation, *Int. Commun. Heat Mass Transfer*, 21, pp. 461-468.

[27] Taylor G.I., 1961, "Deposition of a viscous fluid on the wall of a tube", *Journal of Fluid Mechanics*, 10, pp. 161-165.

[28] Prothero J., Burton A. C., 1961, "The Physics of Blood Flow in Capillaries: 1 The Nature of The Motion, *Biophysics Journal*, 1, pp. 565-579.

[29] Horvath C., Solomon B. A., Engasser J. M., 1973, "Measurement of Radial Transport in Slug Flow Using Enzyme Tubes", *Industrial and Engineering Chemistry Fundamentals*, 12(4), pp. 431-439.

[30] Muzychka Y.S., Walsh E. J., Walsh P., 2011, "Heat Transfer Enhancement Using Laminar Gas-Liquid Segmeted Plug Flow", *Journal of Heat Transfer*, Vol. 133.

[31] Talimi V., Muzychka Y.S., Kocabiyil S., 2011, "A Numerical Study on Shear Stress and Heat Transfer of Segmented Flow Between Parallel Plates", *Proceedings of the 9th International Conference on Nanochannels, Microchannels, and Minichannels, ICNMM2011, Edmonton, Canada.*

[32] Incropera, DeWitt, Bergman, Lavine, 2007, "Fundamentals of heat and mass transfer", 6^{th} Edition, *John Wiley and Sons.*

[33] Ren H., Fair R. B., Pollack M. G., Schayghnessy E. J., 2002, "Dynamics of electrowetting droplet transport", *Sensors Actuators*, B 87, pp. 201-206.

[34] Ghajar A. J., Tang C. C., Cook W. L., 2010, "Experimental Investigation of Friction Factor in the Transition Region for Water Flow in Minitubes and Microtubes.", *Heat Transfer Engineering*, 31(8), pp. 646-657.

[35] Churchill S. W., 1987, "Viscous Flows: The Practical Use of Theory, *Butterworth-Heinemann, Boston, MA.*.

[36] Akbar M. K., Ghiaasiaan S. M., 2006 "Simulation of Taylor Flow in Capillaries Based on the Volume-of-Fluid Technique", *Industrial and Engineering Chemistry Research*, 45, pp. 5396-5403.

[37] Shao N., Salman W., Gavriilidis A., Angeli P., 2008, "CFD simulations of the effect of inlet conditions on Taylor flow formation, *International Journal of Heat and Fluid Flow*, 29, pp. 1603-1611.

[38] Aussillous P., Quere D., 2000, "Quick deposition of a fluid on the wall of a tube", *Physics of Fluids*, 12(10), pp. 2367-2371.

[39] Han Y., Shikazono N., 2009, "Measurement of the liquid film thickness in micro tube slug flow, *International Journal of Heat and Fluid Flow*, 30(5), pp. 842-853.

[40] Warnier M. J. F., Rebrov E. V., de Croon M. H. J. M., Hessel V., Schouten J. C., 2008, "Gas hold-up and liquid film thickness in Taylor flow in rectangular microchannels", *Chemical Engineering Journal*, 135(1), pp. S153-S158.

[41] Thulasidas T. C., Abraham M. A., Cerro R. L., 1995, "Bubble-train flow in capillaries of circular and square cross section, *Chemical Engineering Science*, 50(2), pp. 183-199.

[42] Fairbrother, F., Stubbs A. E., 1935, "The bubble-tube method of measurement", *Journal of Chemical Society*, 1, pp. 527-529.

[43] Bretherton F. P., 1961, "The motion of long bubbles in tubes", *Journal of Fluid Mechanics*, 10, pp. 166-188.

[44] Gupta R., Fletcher D. F., Haynes B. S., 2009, "On the CFD modelling of Taylor flow in microchannels, *Chemical Engineering Science*, 64, pp. 2941-2950.

[45] Martinez M. J., Udell K. S., 1989, "Boundary Integral Analysis of the Creeping Flow of Long Bubbles in Capillaries", *Journal of Applied Mechanics*, 56, pp. 211-217.

[46] Chen Y., Kulenovic R., Mertz R., 2009, "Numerical study on the formation of Taylor bubbles in capillary tubes", *International Journal of Thermal Sciences*, 48, pp. 234-242.

[47] Taha T., Cui Z. F., 2006, "CFD modelling of slug flow in vertical tubes, *Chemical Engineering Science*, 61, pp. 676-687.

[48] Shen E. I., Udell K. S., 1985, "A Finite Element Study of Low Reynolds Number Two-Phase Flow in Cylindrical Tubes", *Journal of Applied Mechanics*, 52, pp. 253-256.

[49] Giavedoni M. D., Saita F. A., 1997, "The Axisymmetric and Plane Cases of a Gas Phase Steadily Displacing a Newtonian Liquid A Simultaneous Solution of the Governing Equations", *Phys. Fluids*, 9(8) , pp. 2420-2428.

[50] Edvinsson R. K., Irandoust S., 1996, "Finite-Element Analysis of Taylor Flow", *AIChE Journal*, 42 (7), pp.1815-1823.

[51] Taha T., Cui Z. F., 2004, "Hydrodynamics of slug flow inside capillaries", *Chemical Engineering Science*, 59, pp. 1181-1190.

[52] Han Y., Shikazono N., 2009, "Measurment of the Liquid Film Thickness in micro Tube Slug Flow", *International Journal of Heat and Fluid Flow*, 30, pp. 842-853.

[53] Ghidersa B. E., Worner M., Cacuci D. G., 2004, "Exploring the flow of immiscible fluids in a square vertical mini-channel by direct numerical simulation", *Chemical Engineering Journal*, 101, pp. 285-294.

[54] Taha T., Cui Z. F., 2006, "CFD modelling of slug flow inside square capillaries, *Chemical Engineering Science*, 61, pp. 665-675.

[55] Onea A., Worner M., Cacuci D. G., 2009, "A qualitative computational study of mass transfer in upward bubble train flow through square and rectangular mini-channels", *Chemical Engineering Science*, 64, pp. 1416-1435.

[56] Liu D., Wang S., 2008, "Hydrodynamics of Taylor flow in noncircular capillaries", *Chemical Engineering and Processing*, 47, pp. 2098-2106.

[57] Yu Z., Hemminger O., Fan L. S., 2007, "Experiment and lattice Boltzmann simulation of two-phase gas-liquid flows in microchannels, *Chemical Engineering Science*, 62, pp. 7172-7183.

[58] Kreutzer M. T., Kapteijn F., Moulijn J. A., 2005, "Internal and Interfacial Effects on Pressure Drop of Taylor Flow in Capillaries", *AIChE Journal*, 51(9), pp. 2428-2440.

[59] Walsh P., Walsh E., Muzychka Y. S., 2010, "Heat transfer model for gas-liquid slug flows under constant flux", *International Journal of Heat and Mass Transfer*, 53, pp. 3193-3201.

[60] He Q., Fukagata K., Kasagi N., 2007, "Numerical simulation of gas-liquid two-phase flow and heat transfer with dry-out in a micro tube, *6th International Conference on Multiphase flow, ICMF 2007, Leipzig, Germany, July 9-13.*

[61] He Q., Kasagi N., 2008, "Numerical Investigation on Flow Pattern and Pressure Drop Characteristics of Slug Flow in a Microtube", *Proceedings of the sixth Inter-*

national ASME Conference on Nanochannels, Microchannels, and Minichannels, ICNMM2008, Darmstadt, Germany, pp. 327-335.

[62] Fries D. M., von Rohr Ph. R., 2009, "Liquid mixing in gas-liquid two-phase flow by meandering microchannels", *Chemical Engineering Science*, 64, pp. 1326-1335.

[63] Mehdizadeh A., Sherif S. A., Lear W. E., 2009, "Numerical Simulation of Two-Phase Slug Flow in Microchannels", *Proceedings of the ASME 2009 Heat Transfer Summer Conference, HT2009, July 2009, San Francisco, California, USA*.

[64] Gupta R., Fletcher D. F., Haynes B. S., 2010, "CFD Modeling of Flow and Heat Transfer in the Taylor Flow Regime, *Chemical Engineering Science*, 65, pp. 2094-2107.

[65] Qian D., Lawal A., 2006, "Numerical study on gas and liquid slugs for Taylor flow in a T-junction microchannel", *Chemical Engineering Science*, 61, pp. 7609-7625.

[66] Baird E. S., 2008, "Hydrodynamic and thermal modeling of two-dimensional microdroplet arrays for digitized heat transfer", *PhD Thesis, University of Colorado.*

[67] Kashid M. N., Renken A., Kiwi-Minsker L., 2010, "CFD Modeling of Liquid-Liquid Multiphase Microstructured Reactor: Slug Flow Generation", *Chemical Engineering Research and design*, 88, pp. 362-368.

[68] Oliver D. R., Wright S. J., 1964, "Pressure Drop and Heat Transfer in Gas-Liquid Slug Flow in Horizontal Tubes", *Brazilian Journal of Chemical Engineering*, 9, pp. 590-596.

[69] Oliver D. R., Young-Hoon A., 1968, "Two-Phase Non-Newtonian Flow: Part 1 Pressure Drop and Holdup", *Transactions of the Institution of Chemical Engineers*, 46, pp. 106-115.

[70] Oliver D. R., Young-Hoon A., 1968, "Two-Phase Non-Newtonian Flow: Part 2 Heat Transfer", *Transactions of the Institution of Chemical Engineers*, 46, pp. 116-122.

[71] Hughmark G. A., 1965, "Holdup and Heat Transfer in Horizontal Slug Gas Liquid Flow", *Chemical Engineering Science*, 20, pp. 1007-1010.

[72] Vrentas J. S., Duda J. L., Lehmkuhl G. D., 1978, "Characteristics of Radial Transport in Solid-Liquid Slug Flow", *Industrial and Engineering Chemistry Fundamentals*, 17(1), pp. 39-45.

[73] Ua-arayaporn P., Fukagata K., Kasagi N., Himeno T., 2005, "Numerical simulation of gas-liquid two-phase convective heat transfer in a micro tube, *ECI International Conference on Heat Transfer and Fluid Flow in Microscale, Castelvecchio Pascoli, 25-30 September*.

[74] Lakehal D., Larrignon G., Narayanan C., 2008, "Computational heat transfer and two-phase flow topology in miniature tubes, *Microfluid Nanofluid*, 4, pp. 261-271.

[75] Narayanan C., Lakehal D., 2008, "Two-phase convective heat transfer in miniature pipes under normal and microgravity conditions", *Journal of Heat Transfer*, July 2008, Vol. 130.

[76] Fei K., Chen T. S., Hong C. W., 2010, "Direct Methanol Fuel Cell Bubble Transport Simulations via Thermal Lattice Boltzmann and Volume of Fluid Methods", *Journal of Power Sources*, doi:10.1016/ j.jpowsour.2009.10.025.

[77] Leung S. S. Y., Liu Y., Fletcher D. F., Haynes B. S, 2010, "Heat Transfer in Well-Characterized Taylor Flow, *Chemical Engineering Science*, 65, pp. 6379-6388.

[78] Leung S. S. Y., Gupta R., Fletcher D. F., Haynes B. S, 2012, "Effect of Flow Characteristics on Taylor Flow Heat Transfer, *Industrial and Engineering Chemistry Research*, 51, pp. 2010-2020.

[79] Young P., Mohseni K., 2008, "The Effect of Droplet Length on Nusselt numbers in Digitized Heat Transfer, Proceedings of I-THERM, 2008, *11th IEEE Intersociety Conference on Thermal and Thermomechanical Phenomena in Electronic Systems*, pp. 352-359.

[80] Oprins H., Danneels J., Van Ham B., Vandevelde B., Baelmans M., 2008, "Convection heat transfer in electrostatic actuated liquid droplets for electronics cooling, *Microelectronics Journal*, 39, pp. 966-974.

[81] Mehdizadeh A., Sherif S. A., Lear W. E., 2011, "Numerical Simulation of Thermofluid Characteristics of Two-Phase Slug Flow in Microchannels", *International Journal of Heat and Mass Transfer*, 54, pp.3457-3465.

[82] Talimi V., Muzychka Y. S., Kocabiyik S., 2011, "On the Validity of Two-Dimensional Heat Transfer Simulation of Moving Droplets Between Parallel Plates", *Proceedings of the 9th International Conference on Nanochannels, Microchannels, and Minichannels, ICNMM9, June 2011, Edmonton, Canada.*

[83] Fukagata K., Kasagi N., Ua-arayaporn P., Himeno T., 2006, "Numerical simulation of gas-liquid two-phase flow and convective heat transfer in a micro tube", *International Journal of Heat and Fluid Flow*, 28, pp. 72-82.

[84] Asadolahi A. N., Gupta R., Fletcher D. F., Haynes B. S., 2011, "CFD Approaches for the Simulation of Hydrodynamics and Heat Transfer in Taylor Flow", *Proceedings of the IMechE Part C Journal of Mechanical Engineering Science*, 222, pp. 737-750.

[85] Asadolahi A. N., Gupta R., Fletcher D. F., Haynes B. S., 2011, "CFD Approaches for the Simulation of Hydrodynamics and Heat Transfer in Taylor Flow", *Chemical Engineering Science*, 66, pp. 5575-5584.

[86] Asadolahi A. N., Gupta R., Leung S. S. Y., Fletcher D. F., Haynes B. S., 2012, "Validation of a CFD Model of Taylor Flow Hydrodynamics and Heat Transfer", *Chemical Engineering Science*, 69, pp. 541-552.

[87] Howard J. A., Walsh P. A., Wlash E. J., 2011, "Prandtl and Capillary Effects on Heat Transfer Performance Within Laminar Liquid-Gas Slug Flows", *International Journal of Heat and Mass Transfer*, 54, pp. 4752-4761.

[88] Talimi V., Muzychka Y. S., Kocabiyik S., 2013, "Slug Flow Heat Transfer in Square Microchannels", *International Journal of Heat and Mass Transfer*, 62, pp. 752-760.

[89] Leung S. S. Y., Gupta R., Fletcher D. F., Haynes B. S., 2012, "Gravitational Effect on Taylor Flow in Horizontal Microchannels", *Chemical Engineering Science*, 69, pp. 553-564.

[90] Versteeg H. K., Malalasekera W., 1995, "An introduction to computational fluid dynamics, 1^{st} Edition, *Longman Scientific and Technical*.

[91] Barth T. J., Jespersen D., 1989, "The design and application of upwind schemes on unstructured meshes", *Technical Report AIAA-89-0366, AIAA 27th Aerospace Sciences Meeting, Reno, Nevada, USA*.

[92] "Fluent 6.3 User Guide", 2006, *FLUENT INC.*.

[93] Patankar S. V., 1980, "Numerical Heat Transfer and Fluid Flow", *Hemisphere Publishing Corporation, Taylor and Francis Group, New York.*

[94] Leonard B. P., 1979, "A Stable and Accurate Convective Modelling Procedure Based on Quadratic Upstream Interpolation", *Computer Methods in Applied Mechanics and Engineering*, 19, pp. 59-98.

[95] Patankar S. V., Spalding D. B., 1972, "A Calculation Procedure for Heat, Mass, and Momentum Transfer in Three Dimensional Parabolic Flows", *International Journal of Heat and Mass Transfer*, 15, pp.1787.

[96] Van Doormal J. P., Raithby G. D., 1984, "Enhancements of the SIMPLE Method for Predicting Incompressible Fluid Flows", *Numerical Heat Transfer*, 7, pp. 147-163.

[97] Issa R. I., 1986, "Solution of the Implicitly Discretised Fluid Flow Equations by Operator Splitting", *Journal of Computational Physics*, 62, pp. 40-65.

[98] Hirt C. W., Nichols B. D., 1981, "Volume of fluid (VOF) method for the dynamics of free boundaries, *Journal of Computational Physics*, 39 (1).

[99] Carlson A., Kudinov P., Narayanan C., 2008, "Prediction of two-phase flow in small tubes: A systematic comparison of state-of-the-art CMFD codes", *5th European Thermal-Sciences Conference, The Netherlands.*

[100] Brackbill J. U., KotheD. B., Zemach C., 1992, "A continuum method for modeling surface tension", *Journal of Computational Physics*, 100, pp. 335-354.

[101] Kashid M. N., Platte F., Agar D. W., Turek S., 2007, "Computational modelling of slug flow in a capillary microreactor, *Journal of Computational and Applied Mathematics*, 203, pp. 487-497.

[102] Wu L., Tsutahara M., Kim L. S., Ha M. Y., 2008, "Three-dimensional lattice Boltzmann simulations of droplet formation in a cross-junction microchannel, *International Journal of Multiphase Flow*, 34, pp. 852-864.

[103] Kumar V., Vashisth S., Hoarau Y., Nigam K. D. P., 2007, "Slug flow in curved microreactors: Hydrodynamic study, *Chemical Engineering Science*, 62, pp. 7494-7504.

[104] Muradoglu M., Gunther A., Stone H. A., 2007, "A computational study of axial dispersion in segmented gas-liquid flow, *PHYSICS OD FLUIDS*, 19, 072109.

[105] Worner M., Ghidersa B., Onea A., 2007, "A model for the residence time distribution of bubble-train flow in a square mini-channel based on direct numerical simulation results, *International Journal of Heat and Fluid Flow*, 28, pp. 83-94.

[106] Rosengarten G., Harvie D. J. E., Cooper-White J., 2006, "Contact Angle Effects on Microdroplet Deformation using CFD", *Applied Mathematical Modeling*, 30, pp. 1033-1042.

[107] Raimondi N. D. M., Prat L., 2011, "Numerical Study of the Coupling Between Reaction and Mass Transfer for Liquid-Liquid Slug Flow in Square Microchannels", *AIChE Journal*, 57(7), pp. 1719-1732.

[108] Goel D., Buwa V. V., 2009, "Numerical Simulations of Bubble Formation and Rise in Microchannels", *Industrial and Engineering Chemistry Research*, 48, pp. 8109-8120.

[109] Cherlo S. K. R., Kariveti S., Pushpavanam S., 2010, "Experimental and Numerical Investigations of Two-Phase (Liquid-Liquid) Flow Behavior in Rectangular Microchannels", *Ind. Eng. Chem. Res.*, 49, pp. 893-899.

[110] Van Baten J. M., Krishna R., 2005, "CFD simulations of wall mass transfer for Taylor flow in circular capillaries", *Chemical Engineering Science*, 60, pp. 1117-1126.

[111] Renardy M., Renardy Y., Li J., 2001, "Numerical Simulation of Moving Contact Line Problems Using a Volume-of-Fluid Method", *Journal of Computational Physics*, 171, pp. 243-263.

[112] Spelt P. D. M., 2005, "A level-set approach for simulations of flows with multiple moving contact lines with hystersis", *Journal of Computational Physics*, 207, pp. 389-404.

[113] Dai L., Cai W., Xin F., 2009, "Numerical Study on Bubble Formation of a Gas Liquid Flow in a T-junction Microchannel", *Chemical Engineering and Technology*, 32(12), pp. 1984-1991.

[114] Ilnicki F., Sobieszuk P., Pohorecki R., 2009, "Simulations of a Two Phase Flow in a Closed Microchannel", *Chemical and Process Engineering*, 30, pp. 205-216.

[115] Edvinson R. K., Irandoust S., 1996, "Finite-element analysis of Taylor Flow", *AIChE Journal*, 42(7), pp. 1815-1823.

[116] Martinez M. J., Udell K. S., 1989, "Boundary Integral Analysis of the Creeping Flow of Long Bubbles in Capillaries", *Journal of Applied Mechanics*, 56, pp. 211-217.

[117] Armand A.A., Treschev G. G., 1946, "The Resistance During the Movement of a Two-Phase System in Horizontal Pipe", *Izvestia Vses Teplo. Inst*, 1, pp. 16-23.

[118] Salman W., Gavriilidis A., Angeli P., 2004, "A Model for Predicting Axial Mixing During Gas-Liquid Taylor Flow in Microchannels at Low Bodenstein Numbers", *Chemical Engineering Journal*, 101, pp. 391-396.

[119] Santos R. M., Kawaji M., 2010, "Numerical Modeling and Experimental Investigation of Gas-Liquid Slug Flow Formation in Microchannel T-junction", *International Journal of Multiphase Flow*, 36, pp. 314-323.

[120] Guo F., Chen B., 2009, "Numerical Study on Taylor Bubble Formation in a Microchannel T-junction Using VOF Method", *Microgravity Science and Technology*, 21(1), pp. S51-S58.

[121] Raimondi N. M., Prat L., Gourdon C., Cognet P., 2008, "Direct Numerical Simulations of Mass Transfer in Square Microchannels for Liquid-Liquid Slug Flow", *Chemical Engineering Science*, 63, pp. 5522-5530.

[122] Reznik S. N., Yarin A. L., 2002, "Strong Squeezing Flow Between Parallel Plates Leads to Rolling Motion at the Contact Line", *International Journal of Multiphase Flow*, 28, pp. 911-925.

[123] Onea A., Worner M., Cacuci D. G., 2009, "A Quantitative Computational Study of Mass Transfer in Upward Bubble Train Flow Through Square and Rectangular Minichannels", *Chemical Engineering Science*, 64, pp. 1416-1435.

[124] Zaloha P., Kristal J., Jiricny V., Volkel N., Xuereb C., Aubin J, 2012, "Characteristics of Liquid Slugs in Gas-Liquid Taylor Flow in Microchannels", *Chemical Engineering Science*, 68, pp. 640-649.

[125] Kashid, M.N., Gerlach, I., Goetz, S., Franzke, J., Acker, J.F., Platte, F., Agar, D.W., Turek, S., 2005, "Internal circulation within the liquid slugs of a liquidliquid slug-flow capillary microreactor", *Industrial and Engineering Chemistry Research*, 44, 5003-5010.

[126] Kashid, M.N., Agar, D.W., Turek, S., 2007, "CFD modeling of mass transfer with and without chemical reaction in the liquid-liquid slug flow microreactor", *Chemical Engineering Science*, 62, 5102-5109.

[127] Kashid, M.N., Rivas, D.F., Agar, D.W., Turek, S., 2008, "On the hydrodynamics of liquid-liquid slug flow capillary microreactors", *Asia-Pacific Journal of Chemical Engineering*, 3, 151-160.

[128] Kashid, M.N., Renken, A., Kiwi-Minsker, L., 2010, "CFD Modeling of liquid-liquid multiphase microstructured reactor: slug flow generation", *Chemical Engineering Research and Design*, 88, 362-368.

[129] Wu, L., Tsutahara, M., Kim, L., Ha, M.Y., 2007, "Numerical simulations of droplet formation in a cross-junction microchannel by the lattice Boltzmann method", *International Journal for Numerical Methods in Fluids*, 57, 793-810.

[130] Aliasghar Zadeh, S., Radespiel, R., 2010, "Numerical study on droplet formation in a microchannel T-junction using the VOF method", *Proceeding of 8th International Conference on Nanochannels, Microchannels, and Minichannels, FEDSM-ICNMM2010, Montreal, Canada.*

[131] Raj, R., Mathur, N., Buwa, V.V., 2010, "Numerical simulations of liquid-liquid flows in microchannels", *Industrial and Engineering Chemistry Research*, 49, 10606-10614.

[132] Bonn D., Eggers J., Indekeu J., Meunier J., Rolley E., 2009, "Wetting and Spreading", *Reviews of Modern Physics*, 81, pp. 739-805.

[133] Ghia U., Ghia K. N., Shin C. T., 1982, "High-Re Solutions for Incompressible Flow Using Navier-Stokes Equations and a Multigrid Method", *Journal of Computational Physics*, 43, pp. 387-411.

[134] Y.S. Muzychka, E. Walsh, and P. Walsh, 2010, Simple Models for Thermally Developing Slug Flow in Non-circular Ducts and Channels, *ASME Journal of Heat Transfer*, 132, 10 pages.

[135] Oztaskin, M.C., Worner, M., Soyhan, H.S., 2009, "Numerical investigation of the stability of bubble train flow in a square minichannel", *Physics of Fluids*, 21, 042108.

[136] Hetsroni G., 1982, "Handbook of Multiphase Systems", *McGraw-Hill*.

[137] Youngs D. L., 1982, "Time-Dependent Multi-Material Flow with Large Fluid Distortion", In K. W. Morton and M. J. Baines, editors, Numerical Methods for Fluid Dynamics*Academic Press*.

[138] Heil M., 2001, "Finite Reynolds Number Effects in the Bretherton Problem", *Physics of Fluid*, 13(9), pp. 2517-2521.

[139] Walsh E., Muzychka Y. S., Walsh P., Egan V., Punch J., 2009, "Pressure drop in two phase slug/bubble flows in mini scale capillaries", *International Journal of Multiphase Flow*, 35, pp. 879-884.

[140] Paik P., Pamula V. K., Chakrabarty K., 2005, "Adaptive hot-spot cooling of integrated circuits using digital microfluidics", *Proceedings of IMECE, IMECE2005-81081, Florida, USA*.

[141] Baird E. S., Mohseni K., 2007, "A Unified Velocity Model for Digital Microfluidics", *Nanoscale and Microscale Thermophysical Engineering*, 11(1)(222), pp. 109-120.

[142] Mohseni K., Baird E. S., 2007, "Digitized Heat Transfer Using Electrowetting on Dielectric", *Nanoscale and Microscale Thermophysical Engineering*, 11(1)(222), pp. 99-108.

[143] Sammarco T. S., Burns M. A., 2000, "Heat-transfer analysis of microfabricated thermocapillary pumping and reaction devices, *Journal of Micromechanics and Microengineering*, 10, pp. 42-55.

[144] Suzuki S., Nakajima A., Sakai M., Hashimoto A., Yoshida N., Kameshima Y., Okada K., 2008, "Rolling and slipping motion of a water droplet sandwiched between two parallel plates coated with fluoroalkylsilanes", *Applied Surface Science*, 255, pp. 3414-3420.

[145] Clime L., Brassard D., Veres T., 2010, "Numerical modeling of electrowetting process in digital microfluidic devices", *Computers and Fluids*, 39, pp. 1510-1515.

[146] Kumari N., Garimella S. V., 2011, "Characterization of the heat transfer accompanying electrowetting or gravity-induced droplet motion", *International Journal of Heat and Mass Transfer*, 54, pp. 4037-4050.

[147] Yu D., Choi Ch., Kim M. H., 2012, "Pressure Drop and Dynamic Contact Angle of Triple-Line Motion in a Hydrophobic Microchannel", *Experimental Thermal and Fluid Science*, 39, pp. 60-70.

[148] Pamula V. K., Chakrabarty K., 2003, "Colling of integrated circuits using droplet-based microfluidics", *Proceedings of the ACM Great Lakes Symposium on VLSI*, pp. 84-87.

[149] Walker S. W., Shapiro B., 2006, "Modeling the Fluid Dynamics of Electrowetting on Dielectric (EWOD)", *Journal of Microelectromechanical Systems*, 15(4), pp. 986-1000.

[150] Zeng J., Korsmeyer T., 2004, "Principles of droplet electrohydrodynamics for lab-on-a-chip", *Miniaturisation for Chemistry, Biology and Bioengineering*, 4, pp. 265-277.

[151] Jang L. S., Lin G. H., Lin Y. L., Hsu C. Y., Kan W. H., Chen C. H., 2007, "Simulation and experimentation of a microfluidic device based on electrowetting on dielectric", *Biomed Microdevices*, 9, pp. 777-786.

[152] Rosenhead L., 1988, "Laminar Boundary Layers", *Dover*, 9, pp. 777-786.

[153] Betz A. R., Attinger D., 2010, "Can segmented flow enhance heat transfer in microchannel heat sinks?", *International Journal of Heat and Mass Transfer*, 53, pp. 3683-3691.

[154] Somasundaran P., Zhang L., 2006, "Adsorption of surfactants on minerals for wettability control in improved oil recovery processes", *Journal of Petroleum Science and Engineering*, 52, pp. 198-212.

[155] Standnes D. C., Austad T., 2003, "Wettability alteration in carbonates Interaction between cationic surfactant and carboxylates as a key factor in wettability alteration from oil-wet to water-wet conditions", *Colloids and Surfaces A: Physicochem. Eng. Aspects*, 216, pp. 243-259.

APPENDICES

APPENDIX 1- EXPERIMENTAL DATA ADOPTION

As mentioned in section 5.2.5, experiments by Betz and Attinger [153] have been conducted under constant wall heat flux boundary condition. However, a constant wall temperature boundary condition was of interest in the present study, therefore, there was a need to adopt isoflux experimental data to isothermal condition. As mentioned, the microchannel wall material in Betz and Attinger [153] is highly conductive hence a small temperature gradient in axial direction is expected. Based on the aforementioned assumptions, a goal seek method has been applied to find wall temperatures (constant) which give same Nu numbers under same flow condition.

Based on Leveque solution, the Nu number under constant wall temperature is [2]:

$$Nu_T = 0.641 \frac{(fRe)^{\frac{1}{3}}}{L^{\star\frac{1}{3}}} \tag{A1.1}$$

where:

$$L^{\star} = \frac{L}{D_h Pe} \tag{A1.2}$$

and the local Nu number under constant wall heat flux is:

$$Nu_H = 0.517 \frac{(fRe)^{\frac{1}{3}}}{x^{\star\frac{1}{3}}} \tag{A1.3}$$

where:

$$x^{\star} = \frac{x}{D_h Pe} \tag{A1.4}$$

If one uses the definition of Nu number, then:

$$Nu_H = \frac{q_w D_h}{k\Delta T} \tag{A1.5}$$

Combining Eqs. A1.3 and A1.5 the local wall to bulk temperature difference is:

$$\Delta T = 1.93 \frac{q_w D_h x^{\star \frac{1}{3}}}{k\left(fRe\right)^{\frac{1}{3}}} \tag{A1.6}$$

which could be expanded using Eq. A1.3 as follows:

$$\Delta T = 1.93 \frac{q_w D_h}{k\left(fRe\right)^{\frac{1}{3}}} \left(\frac{x}{D_h Pe}\right)^{\frac{1}{3}} \tag{A1.7}$$

Integrating the expression above over $0 \rightarrow L$ one can determine the mean wall to bulk temperature difference. In general, in the boundary layer region (thermal entrance length in internal flows) the bulk temperature does not vary significantly from inlet temperature, therefore $(T_w - T_m)$ approaches to $(T_w - T_i)$ as $x \rightarrow 0$. Based on the small values of $L^{\star}$ in the present study (see Fig. 5.22), it could be assumed that the boundary layer theory is applicable. Integrating ΔT using:

$$\Delta T_{mean} = \frac{1}{L} \int_0^L \Delta T dx \tag{A1.8}$$

gives:

$$\overline{Nu}_H = 0.689 \frac{(fRe)^{\frac{1}{3}}}{L^{\star\,\frac{1}{3}}} \tag{A1.9}$$

which is only 7% different from Nu_T in Eq. A1.1.